Modelling Atom Interferometry with a Quasi-Bragg Beam-Splitter for All-Optical Waveguides

JAN-OLE RISSKE

PHD

UNIVERSITY OF YORK

Physics

September 2019

Declaration of Authorship

I, Jan-Ole RISSKE, declare that this thesis titled, " Modelling Atom Interferometry with a Quasi-Bragg Beam-Splitter for All-Optical Waveguides " and the work presented in it are my own. I confirm that:

- This work was done wholly while in candidature for a research degree at this University.
- Where I have consulted the published work of others, this is always clearly attributed.
- Where I have quoted from the work of others, the source is always given. With the exception of such quotations, this thesis is entirely my own work.

“”

“”

UNIVERSITY OF YORK

Abstract

York Centre for Quantum Technologies
Physics

Doctor of Philosophy

Modelling Atom Interferometry with a Quasi-Bragg Beam-Splitter for All-Optical Waveguides

by Jan-Ole RISSKE

Atom interferometry allows for new precision limits in measurement and a key component of it is the beam-splitter. In this thesis we look at the properties of an all optical beam-splitter, which is created by the overlap of two Gaussian laser beams, which also function as waveguides for the Bose-Einstein condensate. For this mainly the split-step Fourier method is used to model the propagation of a low density Bose-Einstein condensate of atoms. The two main areas of interest are the splitting and recombination properties.

The splitting is studied both in two and one dimensions. For the one-dimensional case both standing and propagating waves are used to find the ideal splitting conditions of a balanced splitting and transmission. The result of these methods are in general agreement with the exception that for the propagating wave some of the atoms can become localised inside the beam-splitter. For the propagation it was found that the splitting is not perfectly coherent as the outputs are slightly deformed. However, when looking at the two-dimensional case we see that the splitting is not even close to being coherent. This is because the beam-splitter excites the incoming wave into higher transverse modes of the waveguides. To compensate for this the depth of the waveguides was lowered and the width narrowed to reduce the potential kinetic energy that the atoms could acquire and to increase the separation between the eigenstates to lower the probability of excitation into higher modes, respectively. Nonetheless, these investigations improved the splitting balance but it is still not coherent. Another method investigated was the introduction of a third laser which acts as a filling to reduce the depth of the potential well where the lasers generate the beam-splitter. This approach does not improve the splitting.

Hence instead of recombining single mode waves we used a multimode approach. For this we found that the mirror position is crucial for certain parameters as the longitudinal momentum is not necessarily the same in the reflection and transmission waveguide. Our investigations have generated interference fringes in this model system with a fractional height up to 33%.

Acknowledgements

I acknowledge the funding support I've received from the National Physical Laboratory(NPL) and the University of York.

Firstly, I like to thank my academic supervisor Prof. Tim Spiller. For offering this project to me and for not giving up on me. I've learned so much during my project and I cannot stress enough of how grateful I'm to him. And hopefully we are able to get a few papers out of this thesis.

Secondly I like to thank my NPL supervisor Prof. Yuri Ovchinnikov and his group for their support and valuable feedback and the opportunity to get outside of York and visit their laboratory.

I also like thank Dr Ryan Parker as my dictionary when I was unsure about the structure of the English grammar and spelling and for convincing my to take small breaks outside to get them fresh air.

Furthermore, I like to thank Dr Marta Estarellas for helping me out with technical issues when simply entering sudo did not.

I would also like to offer my gratitude to my family and their never ending love and support.

Alas, writing this thesis only confirmed to me that I did not become a physicist because I like writing.

Contents

List of Figures

List of Tables

List of Abbreviations

BEC	Bose-Einstein condensate
NPL	National Physical Laboratory
Fig.	Figure
Eq.	Equation
Sec.	Section
Tab.	Table

List of Symbols

ω_0	Gaussian Beam Waist
U_0	Gaussian Potential Depth
θ	Crossing Angle between the Gaussian Beam
ε	Polarisation Difference between the Gaussian Beam
λ	Wavelength of the Gaussian Beams
σ_x	Wave-Packet Variance along the Propagation Direction
F	Filling
k_R	Recoil Wavenumber
E_R	Recoil Energy
v_R	Recoil Velocity
x_R	Recoil Distance
ω_R	Recoil Angular Frequency
h	Planck's constant
$\hbar$	Reduced Planck constant
I_1	Probability if the atoms being in the Atom Input
I_2	Probability if the atoms being in the Vacuum Input
T	Transmission Probability
R	Reflection Probability
BS	Beam-Splitter

Throughout this work hats (ˆ) will be used to denote mathematical operators.

Chapter 1

Introduction

It has been nearly a century since Schrödinger published his paper on the quantisation of eigenvalue problems[1], which revolutionised our perception of the fundamental behaviour of particles. Since then our knowledge of such fundamental behaviour has increased drastically and is now close to creating practical devices outside the laboratories in the areas such as quantum computing[2–4], quantum imaging[5–7], quantum communication[4, 8] and quantum metrology[9–14].
A very important discovery and achievement has been that of the Bose-Einstein condensate(BEC), which is the state of matter where all integer spin atoms, bosons, occupy the ground state, which can not happen for half spin atoms called fermions as they are bound by the Pauli exclusion principle. It was first predicted by A. Einstein[15] using the statistical tool from S. Bose[16]. The first experimental realisation of it was done by Anderson et al. using using Rb[17], which was achieved by a mixture of laser and evaporative cooling. Beside the case for rubidium there are have been other atoms used for the creation of a BEC, such as Na[18], Li[19] and H[20]. Having all of the atoms in a single momentum state gives rise to incredible coherence for atoms and thus the desire to exploit this behaviour to create the atom analogue to the laser, the atom laser, producing a coherent atom beam. It was firstly realised by Mewes et al.[21], which creates the atom-laser by using radio frequency output coupling. This frequency is applied to transition from a state that is trapped inside the potential to one that is free, which then could get pulled away by gravity or some other external force. The pulses for this atom laser come from fluctuations of the trap, which were compensated by using radio frequency pulses, reducing the coherence length, which is the distance over which the atom laser stays coherent. These issue can be fixed by using a very stable trap, which was demonstrated by Bloch et al.[22]. Besides radio frequency output coupling, there exist others like the Raman output coupling, which uses photon Raman transitions of the atoms and gives the BEC a momentum kick. It was first achieved by Hagley et al.[23]. However, there are still a major issues with the atom laser and that is that eventually the BEC runs out during the output coupling process and therefore it is necessary to develop a dumping method to have a continuous atom laser[24, 25].
Such atom lasers are especially useful for atom interferometry, which a sub-topic of quantum metrology which utilises coherent manipulation of both the translational

and internal state of the matter wave[26, 27]. Atom interferometers are devices that are able to measure the interference patterns of matter waves and thus allow the user to study any external forces that generate phase shift in the interferometer. This is done by splitting up the incoming matter wave beam through a beam-splitter and letting it evolve along at least two different paths, which are recombined in the end. The different evolution of the paths will create the phase difference which can be measured in the intensity pattern. From this interference pattern we can deduce conclusions about the external forces. One of the earliest examples of matter-wave interferometry was performed by Marton for electrons[28]. The first interferometer for atoms followed later by Carnal et al. using a double slit [29] and Keith et al. with three nano-structured gratings[30]. Atom interferometers have a high sensitivity compared to their light counterparts due to the nature that atoms travel a lot slower leaving them exposed to the external forces for longer[31]. Thus they could be used to measure the rotation of the atom interferometer due to the phase shifts between the two paths. Thus, they can make excellent gyroscopes for navigation[32–34]. Another application is the study of gravity because each of the arms could be subjected to different gravitational fields, which leads to a phase difference between the two arms[35–41]. They could also be used to gain insight on fundamentals like dark matter[42], dark energy[43–46], gravitational waves [47] or fundamental constants[48]. One of the most important parts of an atom interferometer is the beam-splitter, which can take many forms, like the splitting of a waveguide, a nanostructure or of optical lattices[26, 27, 49–55].

1.1 Background

1.1.1 Bose-Einstein Condensate

The ideal BEC consists of integer spin atoms called bosons and has a thermodynamical phase transition, which does not occur from particle interaction but from the particle statistics, for our purposes we are only we are only going to discuss a homogeneous BEC in this thesis. The average number of atoms, $\langle N_k \rangle$, occupying a specific state is given by Bose-Einstein distribution for non-degenerate energy levels results

$$\langle N_k \rangle = \frac{1}{e^{\beta(\epsilon_k - \mu)} - 1}, \tag{1.1}$$

where

$$\beta = \frac{1}{k_B T}, \tag{1.2}$$

T is the temperature, k_B is Boltzmann constant, ϵ_k is the energy of the specific state and μ is the chemical potential of this many-particle system. This phase transition

happens at the critical temperature,

$$T_c = \frac{2\pi\hbar^2}{k_B m}\left(\frac{\rho_a}{2.612}\right)^{\frac{2}{3}}, \tag{1.3}$$

where m is the mass of an atom and ρ_a is the density[56, 57]. The population of all the excited states goes to zero at this temperature and the fraction of atoms in the ground state reaches almost unity, Fig. 1.1, which results in the phase transition. The number of atoms in the ground state for a homogeneous BEC is

$$\frac{\langle N_0\rangle}{N} = 1 - \left(\frac{T}{T_c}\right)^{\frac{3}{2}}, \tag{1.4}$$

where N is the total number of atoms. The remarkable properties of the ideal BEC are that the atoms do not interact with each other and are not governed by the Pauli exclusion principle[56, 57]. Leading to the fact that all the particles in a BEC behave essentially in the same way allowing one to create an atom laser, which can be used for atom interferometry.

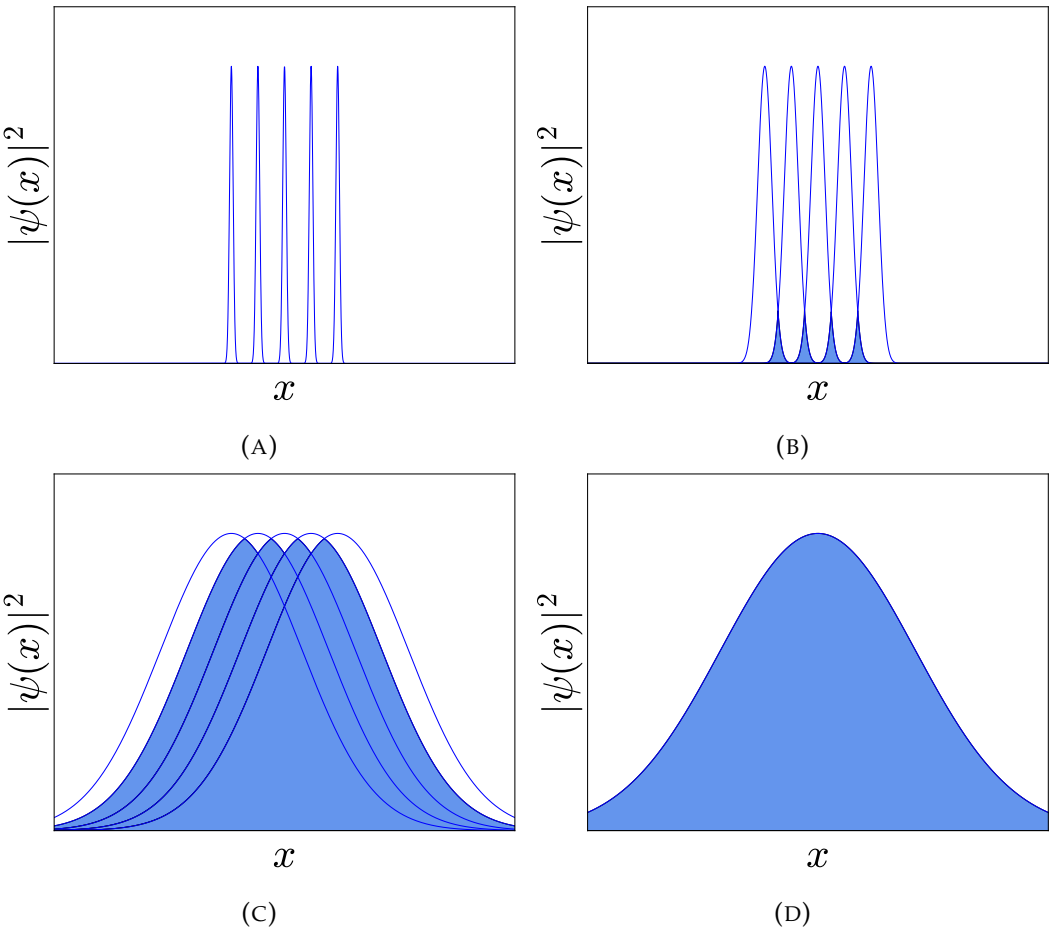

FIGURE 1.1: Schematic one-dimensional depiction of the atom probability densities that begin independently(A) and get cooled down. Cooling them down increases their wavelength and thus they start overlapping(B). The further cooled down it gets the bigger the overlap(C) until it goes below the critical temperature and become a Bose-Einstein condensate(D).

To create a BEC one needs to bring the atoms below the critical temperature. This can be achieved by a combination of laser cooling and potential trapping. The first step is to apply a laser towards the trapped atoms so that the emitted photons are absorbed with a high percentage when the atoms are travelling in the opposite direction of the photons instead of travelling in the same direction. These different absorption rates are gained from the Doppler shift, where the photons moving in the opposite direction get blue-shifted towards the atom's resonance frequency and the ones travelling in the same direction get red-shifted away[57–61], see Fig.1.2 . However, there is a limit to this due to spontaneous emission of the excited atoms. Thus this method can only reach temperatures of

$$T_R = \frac{\hbar^2 k^2}{2mk_B}, \tag{1.5}$$

where m is the mass of the atoms and k is the spontaneously emitted photon wavenumber[62]. It is called the recoil temperature.

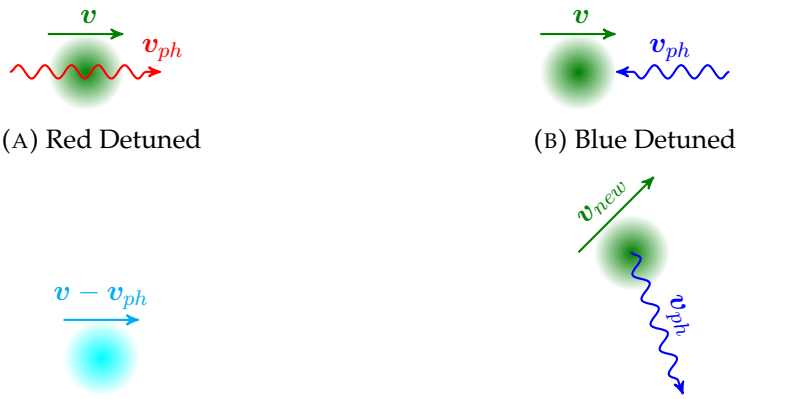

(A) Red Detuned (B) Blue Detuned

(C) Excited Atom (D) Spontaneous Emission

FIGURE 1.2: These figure depict the process of laser cooling. The laser is so detuned that atoms travelling in the same direction as the photon, red detuned, are less likely to absorb the photon(A) while photons travelling in the opposite direction have a higher absorption rate(B). When a blue detuned photon is absorbed and the momentum of the atom is reduced(C). It then spontaneously emits the photon in a random direction(D), on average reducing its overall velocity.

After laser cooling to T_R, evaporative cooling is then effected by steadily reducing the strength of the potential trap so that atoms with higher energy can escape the trap until only atoms below the critical temperature remain trapped [56, 57]. However, this could take a considerable time. Hence, it is more common to induce the evaporative process with a radio frequency to flip the spin of the atoms allowing higher energy atoms to escape. The forming of the BEC can be seen in Fig. 1.3.

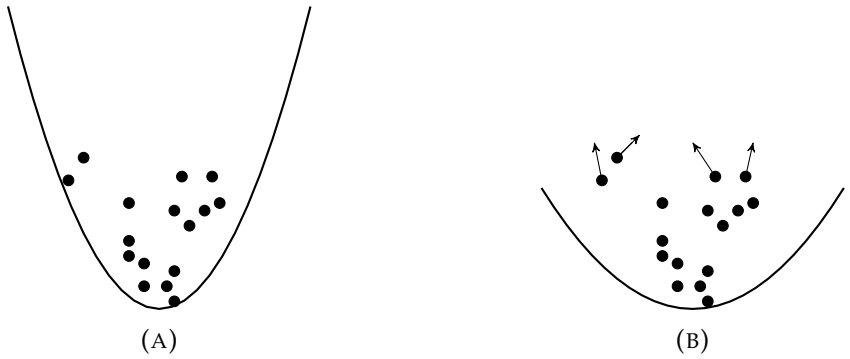

FIGURE 1.3: These figures show the trapped atoms in a one-dimensional potential against the position(A) and how it start to evaporate when the boundary is lowered(B) to create the BEC.

Lastly, the ideal BEC has no interaction with itself, though this is not the case for a real one[63]. The BEC can then be used for the creation of an atom laser. By output-coupling the BEC. There are several different ways to do this though only radio frequency and Raman output-coupling will be discussed here. Radio frequency output-coupling works by switching a trapped mode inside the BEC to a free one, which then get pulled away by a force, such as gravity. However, this method requires the use of weak radio frequency fields, where the transition to the unbound state goes via Zeeman transitions [25, 64], as BECs are generally trapped in magnetic traps, which cause Zeeman splitting of levels.. For these weak fields the flux of the atoms is roughly proportional to the field strength[65]. If the the field becomes too strong bound states start to appear[66, 67]. Thus disabling the atom laser. Nonetheless, it is possible to use a strong field as shown by Bolpasi et al.[64], where they used the field to deform the trap to let the atoms spill out of a hole, created by lowering the potential height in the region of the hole. Another coupling method is the Raman output-coupling, which is based on Raman transitions[23, 25, 68, 69]. For this method two detuned lasers are pointed at the atoms where the first one excites an atom from the ground state to an excited state, and the second one induces stimulated emission to a lower state which is not trapped and from which it also gets a momentum kick[25, 69].

1.1.2 Difference between Optics and Atom Optics

To understand the difference between light and atom interferometers we first need to consider their underlying equations. The equations which govern the wave properties of light are Maxwell's equations

$$\nabla \cdot \boldsymbol{D}\left(\boldsymbol{r}, t\right) = \rho_e, \tag{1.6}$$

$$\nabla \cdot \boldsymbol{B}\left(\boldsymbol{r}, t\right) = 0, \tag{1.7}$$

$$\nabla \times \boldsymbol{E}(\boldsymbol{r},t) = -\frac{\partial \boldsymbol{B}(\boldsymbol{r},t)}{\partial t}, \tag{1.8}$$

$$\nabla \times \boldsymbol{H}(\boldsymbol{r},t) = \mathbf{J}(\boldsymbol{r},t) + \frac{\partial \boldsymbol{D}(\boldsymbol{r},t)}{\partial t}, \tag{1.9}$$

where $\boldsymbol{E}(\boldsymbol{r},t)$ is the electric field, $\boldsymbol{B}(\boldsymbol{r},t)$ is the magnetic flux density, $\boldsymbol{D}(\boldsymbol{r},t)$ is the electric flux density $\boldsymbol{H}(\boldsymbol{r},t)$ is the magnetic field, $\boldsymbol{J}$ is the electric current density and ρ_e is the electric charge density. For a linear isotropic material they are related by $\boldsymbol{D}(\boldsymbol{r}) = \epsilon_r\epsilon_0\boldsymbol{E}(\boldsymbol{r})$ and $\boldsymbol{B}(\boldsymbol{r}) = \mu_r\mu_0\boldsymbol{H}(\boldsymbol{r})$, where ϵ_0, ϵ_r, μ_0 and μ_r are the vacuum permittivity, relative permittivity, vacuum permeability and relative permeability, respectively. These can be rewritten into the wave-equations for light

$$\left(\nabla^2 - \frac{n^2}{c_0^2}\frac{\partial^2}{\partial t^2}\right)\boldsymbol{E}(\boldsymbol{r},t) = 0, \tag{1.10}$$

$$\left(\nabla^2 - \frac{n^2}{c_0^2}\frac{\partial^2}{\partial t^2}\right)\boldsymbol{B}(\boldsymbol{r},t) = 0, \tag{1.11}$$

where $n = \sqrt{\epsilon_r\mu_r}$ denotes the refractive index of the propagation medium, and c_0 is the speed of light in vacuum[27]. The equation which governs the behaviour of nonrelativistic matter waves is the Schrödinger equation

$$\left(-\frac{\hbar^2}{2m}\nabla^2 + V\right)\psi(\boldsymbol{r},t) = i\hbar\frac{\partial}{\partial t}\psi(\boldsymbol{r},t), \tag{1.12}$$

with m being the mass of the atom and V being the potential. The difference between the equations governing the electromagnetic wave and matter wave is the order of time derivatives[27], which would suggest that matter and light wave behave fundamentally differently. However, for a time-independent problem, like the propagation of the matter wave through a time-independent potential $V(\boldsymbol{r})$, the Schrödinger equation can be simplified by substituting $\psi(\boldsymbol{r},t) = \psi(\boldsymbol{r})e^{-i\frac{Et}{\hbar}}$, E denoting the total energy, which is used for time-independent problems set equal to a constant. Thus, leaving us with the time-independent Schrödinger equation

$$\left(-\frac{\hbar^2}{2m}\nabla^2 + V(\mathbf{r}) - E\right)\psi(\boldsymbol{r}) = 0. \tag{1.13}$$

On the other hand using $\boldsymbol{E}(\boldsymbol{r},t) = \boldsymbol{E}(\boldsymbol{r})e^{-i\omega t}$ for linear polarised light gives

$$\left(\nabla^2 + \frac{n^2\omega^2}{c^2}\right)\boldsymbol{E}(\boldsymbol{r}) = 0. \tag{1.14}$$

Thus time-independent matter waves behave similarly to time-independent light. If identical boundary conditions are allied to time-independent matter waves and

light wave problems, they will yield the same results. However, additional atomic non-linearities, from self-interactions, can be rather larger than those of light. In most media non-linear effects for light are negligible. This intrinsic non-linearity of matter waves has a simple description in the region of weak interaction, which is the case if the mean particle spacing is much larger than a, where a is the mean scattering distance and ρ is the density. Its internal interaction can be modelled using mean field theory and thus gives rise to the Gross-Pitaevskii equation[27, 63, 70]

$$\left(-\frac{\hbar^2}{2m}\nabla^2 + V(\mathbf{r},t) + \frac{4\pi\hbar a}{m}\left|\psi(\mathbf{r},t)\right|^2\right)\psi(\mathbf{r},t) = i\hbar\frac{\partial}{\partial t}\psi(\mathbf{r},t). \tag{1.15}$$

This is the Schrödinger equation with a nonlinear term describing the self-interaction between the atoms. This equation is especially relevant for a BEC trapped in a potential or waveguide. In the case where the BEC is free, the dispersion,due to the standard Schroedinger evolution, is generally fast enough so that the self-interaction can be neglected.

Optical Dipole Trap

When dealing with atoms one of the important aspects is to keep them confined to be able to control them. There are several different ways to trap neutral atoms like resonance or magnetic trapping[59, 69, 71–73]. The one that is going to be discussed here is the optical dipole trap. This works by the creation of an induced electrical dipole when the atoms are placed inside a laser beam. Due to this dipole the atoms feel the potential

$$U_{ODP}\left(\boldsymbol{r}\right) = \frac{3\pi c_0^2}{2\omega_0^2}\frac{\Gamma}{\Delta}I(r), \tag{1.16}$$

where

$$\Delta = \omega - \omega_0, \tag{1.17}$$

is the detuning of the laser with a driving frequency of ω from the resonant frequency of the atom ω_0. The damping rate for a two-level system is

$$\Gamma = \frac{\omega_0^3}{3\pi\epsilon_0\hbar c_0^2}\left\langle e|\mu|g\right\rangle, \tag{1.18}$$

which is also the rate of spontaneous emission and can be approximated, where μ is the dipole matrix element between the excited state $|e\rangle$ and the ground state $|g\rangle$. Lastly, there is the intensity of the laser beam[72]

$$I(\boldsymbol{r}) = 2\epsilon_0 c_0 |\boldsymbol{E}(\boldsymbol{r})|^2, \tag{1.19}$$

If the light is far detuned into the red the potential will give rise to an attractive potential while if it is detuned to the blue it will be reflective. Allowing it to be used for a waveguide[74]. However, it should be noted that these waveguides have the problem that they heat the atoms due to photon recoil from scattered laser light, there are proposals and experiments to reduce this by introducing cooling lasers[75].

Beam-Splitter

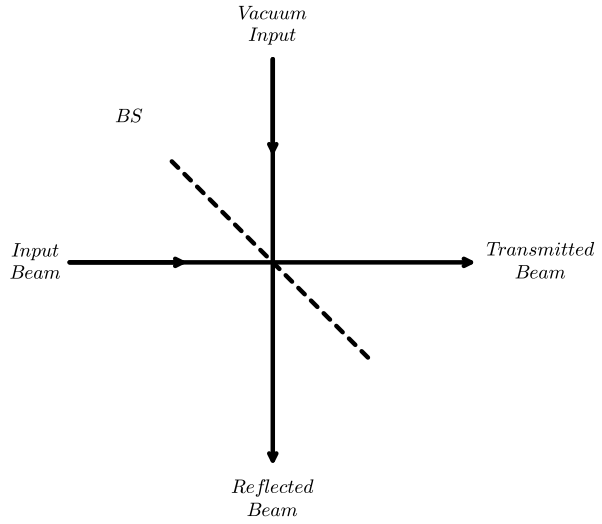

FIGURE 1.4: Schematic of a beam-splitter

One of the most important operations in interferometry is the coherent splitting of the incoming atom beams. This splitting is done via a beam-splitter, which splits the incoming beam into at least two, see Fig. 1.4. The incoming wave into the beam-splitter is in the transverse ground state of the waveguide, which is orthogonal to the direction of the waveguide, and in the longitudinal momentum state k long the waveguide direction, $|g,k\rangle$ while in the other is vacuum $|0,0\rangle$. Our desire is to split the beam coherently so that atoms occupy the transverse ground state and the longitudinal momentum state of their respected waveguide, such as

$$|g,k;0,0\rangle \rightarrow \frac{1}{\sqrt{2}}\left(|g,k;0,0\rangle + |0,0;g,k\rangle\right), \tag{1.20}$$

which clearly shows that occupied modes get entangled with the vacuum. For classical light interferometers this is easily achieved by the use of partially reflecting mirrors. However, there is not such a convenient case for atom optics. Hence, it is necessary to build an atomic beam-splitter using the diffraction properties of waves, where diffraction describes how a the matter wave's amplitude and phase

are changed when it interacts with an object, as the early case of the double slit experiment for electrons carried out by C. Jönsson demonstrates[76, 77]. Diffraction gratings are periodic diffraction areas, which modulate the spatial components of the propagating wave. Giving rise to constructive interference in a particular direction defined by the grating condition

$$m_r \lambda_{db} = d \sin \theta_n, \tag{1.21}$$

where $\lambda_{db} = \frac{h}{p}$ is the deBroglie wavelength for a atom of the momentum p, d is the grating spacing and m_r is an integer specifying the diffraction order. There are a generally speaking two types of grating with the first one being based on the modulation of the amplitude. An example of this would be a multi-slit nanostructure for this case it is necessary that the deBroglie wavelength is bigger than the grating spacing so that the diffraction happens from multiple slits[26, 27, 59, 78, 79]. The other approach is to modulate the phases by keeping the wave together travelling through the grating, where its phase is then modulated locally depending on the region of the grating. An example of this would be the optical lattice[26, 27, 51, 80–82]. These lattices are produced by the crossing of two light beams whose interference with each other creates a standing wave with a reciprocal lattice vector $\mathbf{G} = \mathbf{k}_1 - \mathbf{k}_2$ and $G = 2\pi/d$, where $\mathbf{k}_1$ is the wave vector of the first laser and $\mathbf{k}_2$ of the second laser. Diffraction gratings create several different momentum components shifted by

$$p = \pm m_r \hbar G, \tag{1.22}$$

[26, 27]. For an optical grating this can be understood to come from stimulated emission, where the atom absorbs a photon from one of the beams and emits it into the other one[59]. The light beams used to define the grating are classical beams, of uncertain photon number.

Optical lattices function either as thick or thin optical devices and have thus different scattering properties. In the case of thin gratings we can neglect the influence of the lattice along the axis of propagation. In this limit the behaviour follows the grating condition Eq. 1.21, where the diffraction splits the incoming wave into many momentum states and it is called Kapitza-Dirac diffraction[26, 27], see Fig. 1.5, which was firstly observed for BECs by Ovchinnikov et al. [80]. However, it should be noted that for matter waves their diffraction pattern can be blurred due to spontaneous emission from the atoms[59]. This can be mitigated by detuning the lasers far from the resonance frequencies of the atoms, which leads also to a reduction of interaction strength between the atoms and the lattice. This splitting is undesirable for us as we only want two momentum states.

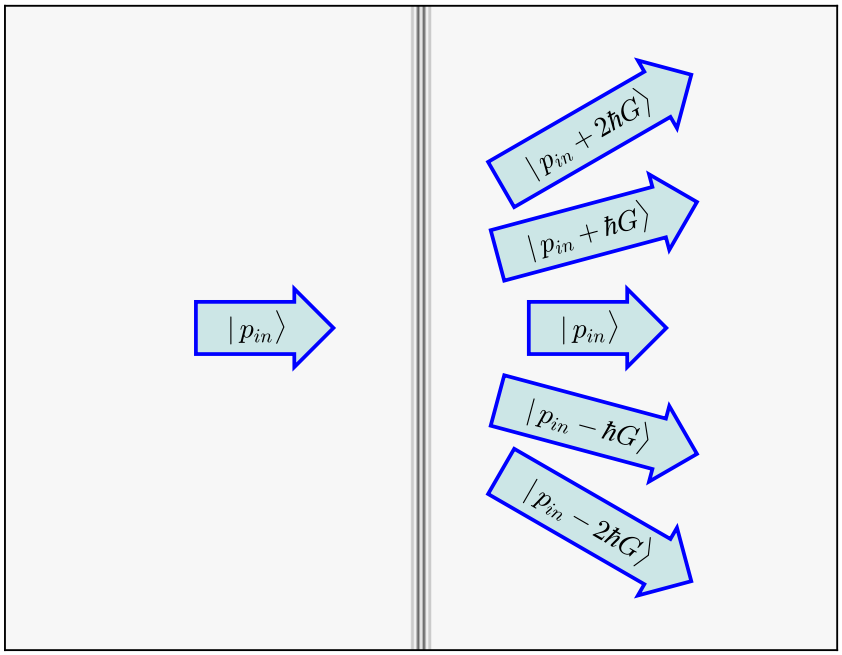

FIGURE 1.5: Depiction of Kapitza-Dirac diffraction, which splits the incoming atoms into several momentum states.

Hence we will focus on the thick optical lattices. For these lattices it its necessary to consider the whole propagation of the beam. Due to the long interaction time, atoms in them will undergo multiple optical transitions, where they experience Bragg diffraction if the potential of the lattice is weak in comparison to the characteristic energy of the grating

$$E_G = \frac{\hbar^2 G^2}{2m}, \tag{1.23}$$

while the potential needs to be higher than this for channelling[26, 27], where the atoms are guides through the optical lattice and interfere afterwards[26]. Continuing, we will focus on the thick optical lattices which have Bragg scattering because they are more suitable to work as a beam-splitter because we only want two output states. The Bragg diffraction only occurs at specific angles, θ_B, which are defined by the Bragg condition

$$m_r \lambda_{dB} = 2dsin\theta_B. \tag{1.24}$$

If this condition is fulfilled the initial momentum from the propagating wave, p_in, is transferred to a new momentum state $p_{in} = p_{in} + \hbar G$[26, 27, 83]. This can also occur for a higher order Bragg diffraction which will transform the momentum by a multiple of $\hbar G$, see Fig. 1.6. One example for this type of Bragg scattering example is achieved by Fabre et al.[51] and the first one was observed by Martin et al. [52].

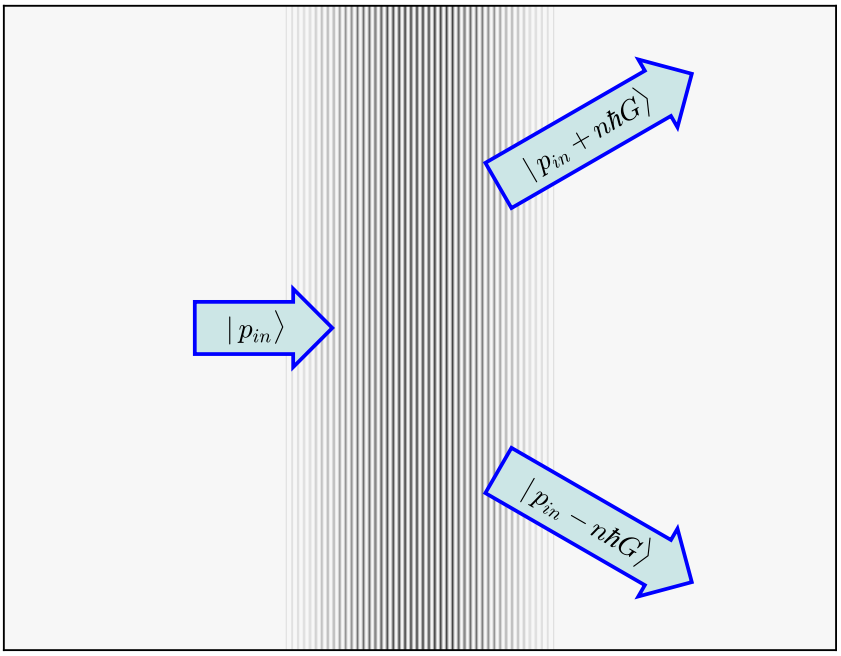

FIGURE 1.6: Simple depiction of a thick optical lattice splitting the incoming beam into two momentum states.

1.1.3 Contrast

To gain better control over the splitting properties of an optical lattice it is also necessary to control the fringe amplitude of these lattices. For this we look at the case where two electric fields

$$\boldsymbol{E}_1 = \boldsymbol{A}_1 e^{ikz}, \tag{1.25}$$

$$\boldsymbol{E}_2 = \boldsymbol{A}_2 e^{-ikz}, \tag{1.26}$$

are interfere and create an intensity

$$I \approx |\boldsymbol{E}_1 + \boldsymbol{E}_2|^2 = |\boldsymbol{E}_1|^2 + |\boldsymbol{E}_2|^2 + \boldsymbol{E}_1^* \cdot \boldsymbol{E}_2 + \boldsymbol{E}_1 \cdot \boldsymbol{E}_2^*, \tag{1.27}$$

$$= \langle I \rangle + \boldsymbol{A}_1 \cdot \boldsymbol{A}_2 \left(e^{2ikz} + e^{-2ikz} \right), \tag{1.28}$$

$$= \langle I \rangle \left(1 + C\varepsilon \cos 2kz \right), \tag{1.29}$$

where the interference contrast is

$$C = \frac{2A_1 A_2}{A_1^2 + A_2^2}, \tag{1.30}$$

the average intensity

$$\langle I \rangle = A_1^2 + A_2^2 \tag{1.31}$$

and

$$\varepsilon = \cos\theta, \tag{1.32}$$

which comes from the polarisation angle difference between the two fields and is simply labelled as the polarisation in this thesis. It comes from the angle between the two polarisations. This allows for the control of the amplitude of the lattice fringes by controlling the the polarisation difference.

1.1.4 Interferometer

Atom interferometers are devices which create a superposition of the propagation wave and measure it through a final intensity pattern. This is often done by measuring the number of atoms in the outputs[27]. The the incoming wave, ψ, is split up into into at least two different states, $\psi_1, \psi_2, ...$,

$$\psi_{in} \rightarrow \psi_1 + \psi_2, \tag{1.33}$$

which evolve along different paths, develop a phase difference φ

$$\psi_1 + \psi_2 \rightarrow \psi_1 + e^{i\varphi}\psi_2, \tag{1.34}$$

and are then recombined into ψ_{out} [26, 27]. From which the measured interference can be seen as fringes on the intensity pattern

$$\begin{aligned} I = |\psi_{out}|^2 &= \left|\psi_1 + \psi_2 e^{i\varphi}\right|^2, \\ &= A_1^2 + A_2^2 + 2A_1A_2\cos(\varphi), \\ &= \langle I\rangle\left(1 + C\cos(\varphi)\right), \end{aligned} \tag{1.35}$$

where $A_1 = |\psi_1|$, $A_2 = |\psi_2|$ are the amplitudes and the notation is chosen to highlight the similarities to the electric field example discussed in the previous section. This allows one to fully express the interference via the phase φ and by a combination following two properties: the amplitude $2A_1A_2$, the average intensity $\langle I\rangle = A_1^2 + A_2^2$ or its contrast C, which is described by

$$C = \frac{2A_1A_2}{A_1^2 + A_2^2}. \tag{1.36}$$

An explicit example would we be that of the coherent state of an optical mode $|\alpha\rangle$, as described by C. C. Gerry and P. L. Knight[84], which can be written as a superposition of the photon number states, $|n\rangle$,

$$|\alpha\rangle = e^{\frac{|\alpha|^2}{2}} \sum_{n=0}^{\infty} \frac{\alpha^n}{\sqrt{n!}} |n\rangle \tag{1.37}$$

that gets split using a 50:50 beam-splitter to

$$|0\rangle\,|\alpha\rangle \rightarrow |\frac{i\alpha}{\sqrt{2}}\rangle\,|\frac{\alpha}{\sqrt{2}}\rangle\,, \tag{1.38}$$

where $|0\rangle$ is the vacuum. This now experiences a phase shift

$$|\frac{i\alpha}{\sqrt{2}}\rangle\,|\frac{\alpha}{\sqrt{2}}\rangle \rightarrow |\frac{ie^{i\varphi}\alpha}{\sqrt{2}}\rangle\,|\frac{\alpha}{\sqrt{2}}\rangle\,. \tag{1.39}$$

These states are then recombined at a second 50:50 beam-splitter

$$|\frac{ie^{i\varphi}\alpha}{\sqrt{2}}\rangle\,|\frac{\alpha}{\sqrt{2}}\rangle \rightarrow |\frac{i\left(e^{i\varphi}+1\right)\alpha}{\sqrt{2}}\rangle\,|\frac{\left(1-e^{i\varphi}\right)\alpha}{\sqrt{2}}\rangle\,. \tag{1.40}$$

The two output modes can then be measured using the detectors for the number operator $\hat{D}_a = \hat{a}^\dagger\hat{a}$ and $\hat{D}_b = \hat{b}^\dagger\hat{b}$, where $\hat{a}^\dagger$ is the creation operator and $\hat{a}$ is the annihilation operator. They work on the number state such that $\hat{a}^\dagger\,|n\rangle = \sqrt{n+1}\,|n+1\rangle$ and $\hat{a}\,|n\rangle = \sqrt{n}\,|n-1\rangle$. Correspondingly for the b operators in the other mode. Combining the detector outputs $\hat{O} = \hat{D}_a - \hat{D}_b$, which is a operator giving the difference number between the outputs and has the expectation value $\langle\hat{O}\rangle = |\alpha|^2\cos\varphi$. From this one can see that a beam-splitter with 50:50 the transmissions can be complete so that that the output can end up entirely in one arm or the other, depending on the phase. There are several different ways to implement this [26, 27, 50, 82, 85–87]. The Michelson[88], see Fig. 1.7b and Mach-Zehnder interferometer[88], Fig. 1.7a. The Michelson splits the beam which evolves along two different paths and then gets reflected backwards into the same beam-splitter. The disadvantage of this method is that the atoms going into the input from which they came are not measured and contribute to the loss and that there will be interactions between the atoms going towards the mirror and the ones coming back, creating noise. For Mach-Zehnder the beams is split as well and evolves along two different paths which then get reflected into another beam-splitter. It is harder to implement than the Michelson but allows for two independent inputs as ideally the waveguides enter the second beam-splitter with the same angle.

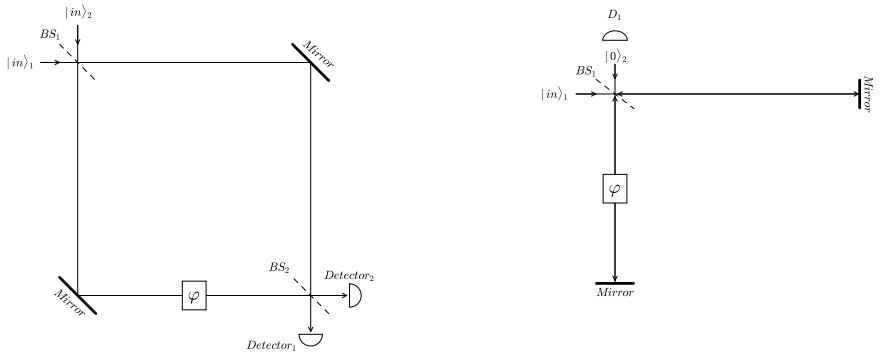

(A) Mach-Zehnder interferometer (B) Michelson interferometer

FIGURE 1.7: These Figures show the depiction of a Mach-Zehnder(A) and Michelson(B) interferometer. For both cases the beam gets split by a beam-splitter(BS) and evolves along two different path. The main difference is that they are recombined using the same beam-splitter for the Michelson and a different for the Mach-Zehnder.

1.1.5 Shot Noise Limit

Typically, interferometers measure the number of particles at their respective outputs, where for N atoms the probability of finding the number of atoms in an output is dependent on the phase difference. For this we recap the arguments from Schaff et al. [27], where the mean number of atoms inside an output is

$$\langle n_o \rangle = \frac{N}{2} \left(1 + \sin \vartheta\right), \tag{1.41}$$

where for $\vartheta = 0$ the probability of finding the atoms in one output or the other is 50:50, which has a variance for a single atom, $N = 1$, of

$$\begin{aligned} Var\left(\langle n_o \rangle^{(1)}\right) &= Ex\left(\left(\langle n_o \rangle^{(1)}\right)^2\right) - Ex\left(\left(\langle n_o \rangle^{(1)}\right)\right)^2 \\ &= \frac{0^2}{2} + \frac{1^2}{2} - \left(\frac{1}{2}\right)^2 = \frac{1}{4}, \end{aligned} \tag{1.42}$$

where Ex is the function for the expectation value. From which for $N > 1$ atoms can be calculated via

$$Var\left(\langle n_o \rangle\right) = NVar\left(\langle n_o \rangle^{(1)}\right) = \frac{N}{4} = \Delta n_o^2. \tag{1.43}$$

Thus the sensitivity

$$\Delta\vartheta = \frac{\Delta n}{\left.\frac{\partial \langle n \rangle}{\partial \vartheta}\right|_{\vartheta=0}} = \frac{1}{\sqrt{N}}, \tag{1.44}$$

which is the shot noise limit. In this derivation the atoms are uncorrelated and thus this limit can be beaten. The ultimate sensitivity limit for interferometry is considered to be theHeisenberg limit [89],

$$\Delta\vartheta = \frac{1}{N}. \tag{1.45}$$

However, there have been arguments presented by Zwierz et al. [90] that it might not be the limit due to Heisenberg's uncertainty[91] but stemming from the the Margolus-Levitin bound[92], which is the lower bound of time it takes to change a state into an orthogonal one[90]. As there have been reported schemes to go below it[93]. However if one does the proper accounting for all the available resources, the results come back to agreement with the Heisenberg limit[10], as shown by M. Zwierz et al. [90].

1.1.6 Units

It is more convenient for our purposes to work in non-SI units, which are based on the wavelength of our lasers, which are called recoil units. The starting point for these units is the wavenumber of the laser:

$$k_R = \frac{2\pi}{\lambda}. \tag{1.46}$$

From this one can calculate the recoil energy

$$E_R = \frac{\hbar^2 k_R^2}{2m}, \tag{1.47}$$

the position

$$x_R = \frac{1}{k_R}, \tag{1.48}$$

the velocity

$$v_R = \frac{k_R \hbar}{m}, \tag{1.49}$$

and angular frequency

$$\omega_R = k_R v_R = \frac{k_R^2 \hbar}{m}. \tag{1.50}$$

More associated definitions could be made but these are the ones used in this thesis. A conversion from them into SI units can be seen in Tab. 1.1b for two different laser beams.

SI	$\lambda = 1064nm$	$\lambda = 720nm$
$1/\mu m$	$0.169k_R$	$0.115k_R$
$1ev$	$120GE_R$	$54GE_R$
$1\mu m$	$5.9x_R$	$8.7x_R$
$1mm/s$	$0.23v_R$	$0.16v_R$
$1/\mu s$	$35\omega_R$	$18\omega_R$

(A) SI to Recoil

Recoil	$\lambda = 1064nm$	$\lambda = 720nm$
$1k_R$	$\frac{5905}{mm}$	$\frac{8726}{mm}$
$1E_R$	$8.3pev$	$18.3pev$
$1x_R$	$169nm$	$115nm$
$1v_R$	$4.3mm/s$	$6.4mm/s$
$1\omega_R$	$28482/s$	$55648/s$

(B) Recoil to SI

TABLE 1.1: Conversion table for SI to Recoil units(A) and the reverse(B).

1.2 This Thesis

In this thesis we will model a novel beam-splitter for all-optical waveguides, which is created by the interference of the waveguides themselves[94], giving rise to continuous splitting instead of the need to use pulses. Furthermore, this also reduces the size required to create the interferometer as only the waveguides are necessary as the mirror and beam-splitters are created by their interference. Our desire is to find parameters for which the beam-splitter exhibits quasi Bragg scattering where the properties of the propagating matter wave and optical lattice need to be tuned so that the two scattered waves have equal probability. For this we will look at the splitting abilities in one dimension, chapter 3, two dimensions, chapter 4 and its ability to recombine the beams, chapter 5. Beside the modelling there are experiments carried out by Prof. Yuri B. Ovchinnikov's group at the National Physical Laboratory(NPL,UK)[95], the fixed parameters are chosen in connection with their capabilities and needs. The overall goal is the creation of a Mach-Zehnder style interferometer where the waveguides cross at 90° to give it a small area. However, to model and analyse the recombination ability we will use a Michelson style interferometer. Additionally, it should be noted that only low density BECs are used for the modelling allowing the neglect of the nonlinear terms in the Gross-Pitaevskii equation. However, this reduces the precision limits for both the shot noise and the Heisenberg as both these limits are dependent on the number of atoms.

Chapter 2

Methods

This chapter is focused on the derivation of the novel beam-splitter and methods to analyse its behaviour.

2.1 Beam-Splitter

The optical lattices which we are using come from the experiment conducted at the National Physical Laboratory(NPL), which consists of a wave package travelling along a waveguide towards a potential, functioning as a beam-splitter [94, 95]. The potential which functions as the splitter is created by two Gaussian beams with an electric field of the form

$$E(x,y) = E_0 \frac{\omega_0}{\omega(x)} e^{-\frac{y^2}{\omega(x)}} e^{-ik_R x} e^{-ik_R \frac{y^2}{2R(x)}} e^{i\xi(x)}, \tag{2.1}$$

where E_0 is the peak amplitude of the beam, $\omega(x)$ is the beam radius, ω_0 is the radius at the beam waist, k_R is the recoil wavevector, $R(x)$ is the curvature of the beam and $\xi(x)$ is the Gouy phase[96],see Fig. 2.1 for a Sketch of the profile and . Furthermore, we can make the assumption that $\omega_0 \gg \frac{2\pi}{k_R}$, resulting in $w(x) \sim w_0$, $R(x) \gg \omega_0$ and $\xi(x) \sim 0$.

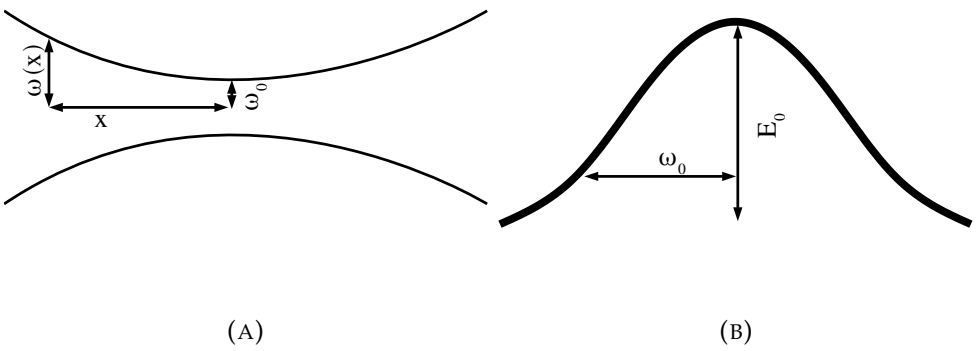

(A) (B)

FIGURE 2.1: A shows the change of the beam waist in regards to the position and B shows the 1D electric field profile.

The two beams are crossing at an angle θ, resulting in the electric field for the respective beams

$$E_1(x,y) = E_0 e^{-\frac{y^2}{\omega_0^2}} e^{-ik_R x}, \tag{2.2}$$

$$E_2(x,y) = E_0 e^{-\frac{(\cos(\theta)y - \sin(\theta)x)^2}{\omega_0^2}} e^{-ik_R(\cos(\theta)x - \sin(\theta)y)}. \tag{2.3}$$

Defining the normalized beam intensity as

$$\mathcal{I}(x,y) \equiv \left| \frac{E_1(x,y) + E_2(x,y)}{E_0} \right|^2. \tag{2.4}$$

Into this we substitute Eq. 2.2 and Eq. 2.3 and perform a change of coordinates via a rotation of $\frac{\theta}{2}$ which is described by

$$\begin{pmatrix} x' \\ y' \end{pmatrix} = \begin{pmatrix} \cos\left(\frac{\theta}{2}\right) & \sin\left(\frac{\theta}{2}\right) \\ -\sin\left(\frac{\theta}{2}\right) & \cos\left(\frac{\theta}{2}\right) \end{pmatrix} \begin{pmatrix} x \\ y \end{pmatrix}. \tag{2.5}$$

This is done to simplify the normalized intensity to

$$\begin{aligned} \mathcal{I}(x',y') =& 2e^{-\frac{(1-\cos(\theta)\cos(2\theta))x'^2 + (1+\cos(\theta)\cos(2\theta))y'^2}{\omega_0^2}} \\ & \times \left[2\cos\left(2\sin(\theta)\frac{x'y'}{\omega_0^2} \right) + \varepsilon \cos\left(2\sin\left(\frac{\theta}{2}\right) k_R y' \right) \right], \end{aligned} \tag{2.6}$$

where the effective wavevector is $k_R^{eff}(\theta) = 2\sin\left(\frac{\theta}{2}\right) k_R$ and its associated effective recoil energy $E_R^{eff}(\theta) = 2\left(1 - \cos(\theta)\right) E_R$. Also, the polarisation ε, Sec. 1.1.3 which depends on the relative polarization of the two beams has been included. Now the potential for the scattering can be calculated via its relation to the normalized intensity

$$U(x',y') = -\frac{1}{2\varepsilon_0 c}\alpha |E_0|^2 \mathcal{I}, \tag{2.7}$$

where α is the polarizability, c the speed of light and ε_0 is representing the permittivity of free space. Thus the beam splitter potential takes the form

$$U(x',y') = -U_G(x',y')[A(x',y') + \varepsilon \cos(k_R^{eff}(\theta)y')], \tag{2.8}$$

where

$$U_G(x',y') = \frac{1}{\varepsilon_0 c}\alpha |E_0|^2 e^{-\frac{(1-\cos(\theta)\cos(2\theta))x'^2 + (1+\cos(\theta)\cos(2\theta))y'^2}{\omega_0^2}}, \tag{2.9}$$

and

$$A(x', y') = 2\cos\left(2\sin(\theta)\,\frac{x'y'}{\omega_0^2}\right). \tag{2.10}$$

The beams at the current NPL experiment cross at an angle of $\theta = \frac{\pi}{2}$ changing Eq. 2.9 and Eq. 2.10 to

$$U_G(x', y') = \frac{1}{\varepsilon_0 c}\alpha|E_0|^2 e^{\frac{x'^2+y'^2}{\omega_0^2}}, \tag{2.11}$$

and

$$A(x', y') = 2\cos\left(2\frac{x'y'}{\omega_0^2}\right). \tag{2.12}$$

respectively. The effective wavevector can now be written as $k_R^{eff} = \sqrt{2}\,k_R$. Following from here the task is to analyse the beam-splitter properties of this potential.

2.2 Band-Gap Analysis

One way to analyse the splitting behaviour of the beam-splitter is by analysing its band-gap structure, as shown by Damon et al.[97]. For this analysis the atoms can be described by starting with the Bloch formalism for a quantum state in a periodic potential $U(z+d) = U(z)$, where d is the period. This is described by the Schrödinger equation,

$$\hat{H}\psi(z) = \left(\frac{\hat{P}}{2m} + U(z)\right)\psi(z) = E\psi(z). \tag{2.13}$$

According to the Bloch theorem[83] we can write the eigenstates of a periodic Hamiltonian as a product plane wave function with wave vector q and a function $u_{n,q}$ with the same periodicity as the potential:

$$\psi_{n,q}(z) = e^{iqz}u_{n,q}(z), \tag{2.14}$$

and

$$u_{n,q}(z+d) = u_{n,q}(z). \tag{2.15}$$

The eigenenergies $E_n(q)$ are periodic, $E_n(q) = E_n(q+q_R)$, with $q_R = \frac{2\pi}{d}$. Substituting Eq. 2.14 into Eq. 2.13 yields

$$\hat{H}_k = \frac{(\hat{p}+\hbar q)^2}{2m} + U(z). \tag{2.16}$$

We can expand the periodic Bloch functions from Eq. 2.15 as a Fourier series into

$$\psi_{n,q}(z) = e^{iqz}u_{n,q}(z) = \sum_{l=-\infty}^{\infty} v_{q+lq_R}e^{i(q+lq_R)z}, \tag{2.17}$$

and similarly for the potential:

$$U(z) = \sum_{p=-\infty}^{\infty} \tilde{U}_p e^{ipq_R z}, \tag{2.18}$$

where l and p are integers. Substituting Eq. 2.17 and 2.18 into 2.13 we get

$$\frac{\hbar^2}{2m}(q+lq_R)^2 v_{q+lq_R} + \sum_p \tilde{U}_p v_{q+(l-p)q_R} = E v_{q+lq_R}. \tag{2.19}$$

The 1D case of the potential can be approximated into

$$U(z) = -U_G[A + \varepsilon\cos(q_R z)], \tag{2.20}$$

where $q_R \equiv k_R^{eff}(\theta)$ and $z \equiv y'$. This approximation is feasible because we have assumed that the radius of the beam waist is $\omega_0 \gg \frac{2\pi}{k_R}$. Using Eq. 2.19 we can turn the Schrödinger equation into an eigenvalue equation as shown by Damon et al.[97]

$$\mathbf{M}\cdot\mathbf{V} = E\mathbf{V}, \tag{2.21}$$

where $\mathbf{V}$ is the vector representation of v and the matrix $\mathbf{M}$ is chosen so that it fulfils the Eq. 2.19. Hence $\frac{\hbar^2}{2m}(q+lq_R)^2$ corresponds only to the diagonal of the matrix, while we need to calculate $\tilde{U}_p$ using

$$\tilde{U}_p = \frac{1}{2\pi}\int_{-\pi}^{\pi} U(z)e^{-ipz}dz, \tag{2.22}$$

making it easier for us to choose the right integration limit for the Fourier series as this function will be periodic from $-\pi$ to π. We evaluate the Fourier coefficient as

$$\tilde{U}_p = \frac{1}{2\pi}\int_{-\pi}^{\pi}(-U_G[A + \varepsilon\cos(z)])e^{-ipz}dz. \tag{2.23}$$

This can be easily solved by rearranging to

$$\tilde{U}_p = \frac{1}{4\pi}\int_{-\pi}^{\pi} -U_G\varepsilon(e^{i(1-p)z} + e^{-i(1+p)z})dz + \frac{1}{2\pi}\int_{-\pi}^{\pi}(-U_G A)e^{-ipz}dz, \tag{2.24}$$

which we can then integrate to give

$$\tilde{U}_p = \frac{-U_G\varepsilon}{2\pi}\left(\frac{e^{i(1-p)\pi} - e^{-i(1-p)\pi}}{2i(1-p)} + \frac{e^{-i(1+p)\pi} - e^{i(1+p)\pi}}{-2i(1+p)}\right) + \frac{-U_G A}{\pi}\frac{e^{ip\pi} - e^{-ip\pi}}{-2ip}, \tag{2.25}$$

and simplified to

$$\tilde{U}_p = \frac{-U_G\varepsilon}{2\pi}\left(\frac{\sin((1-p)\pi)}{(1-p)} + \frac{\sin((1+p)\pi)}{(1+p)}\right) + \frac{-U_G A}{\pi}\frac{\sin(p\pi)}{p}. \tag{2.26}$$

Now we need to calculate the coefficient for specific values of the integer p starting with 0 giving us

$$\tilde{U}_G = \frac{-U_G\varepsilon}{2\pi}(\sin(\pi) + \sin(\pi)) + \lim_{p\to 0}\frac{-U_G A}{\pi}\frac{\sin(p\pi)}{p}. \tag{2.27}$$

For which we need to apply L'Hôpital's rule

$$\lim_{z\to 0}\frac{g_1(z)}{g_2(z)} = \lim_{z\to 0}\frac{g_1'(z)}{g_2'(z)}, \tag{2.28}$$

to solve it. Using this we can solve now Eq. 2.27 to gain

$$\tilde{U}_0 = \lim_{p\to 0}\frac{-U_G A}{\pi}\frac{\pi\cos(p\pi)}{1} = -U_G A. \tag{2.29}$$

We can do this as well for $p = 1$

$$\tilde{U}_1 = \lim_{p\to 1}\frac{-U_G\varepsilon}{2\pi}\frac{\sin((1-p)\pi)}{(1-p)} = \lim_{p\to 1}\frac{-U_G\varepsilon}{2\pi}\frac{\pi\cos((1-p)\pi)}{1} = \frac{-U_G\varepsilon}{2}, \tag{2.30}$$

and for $p = -1$

$$\tilde{U}_{-1} = \lim_{p\to -1}\frac{-U_G\varepsilon}{2\pi}\frac{\sin((1+p)\pi)}{(1+p)} = \lim_{p\to -1}\frac{-U_G\varepsilon}{2\pi}\frac{\pi\cos((1+p)\pi)}{1} = \frac{-U_G\varepsilon}{2}. \tag{2.31}$$

For all other values of p

$$\tilde{U}_p = 0 \quad \text{for } |p| > 1. \tag{2.32}$$

Now we can create the matrix

$$M = \begin{pmatrix} b_{-N} & u & & & \\ u & b_{-N+1} & u & & \\ & \ddots & \ddots & \ddots & \\ & & u & b_{N-1} & u \\ & & & u & b_N \end{pmatrix}, \tag{2.33}$$

with $b_l = E_Q(q/q_R + l)^2 - U_G A$, $u = -U_G\varepsilon/2$ and $E_Q = \hbar^2 q_R^2/2m = 4E_R sin^2\left(\frac{\theta}{2}\right)$. This then needs to be rearranged into

$$\mathbf{A}_M \cdot \mathbf{V} = 0, \tag{2.34}$$

with

$$A_M = \begin{pmatrix} 1 & \xi_{-N} & & & \\ \xi_{-N+1} & 1 & \xi_{-N+1} & & \\ & \ddots & \ddots & \ddots & \\ & & \xi_{N-1} & 1 & \xi_{N-1} \\ & & & \xi_N & 1 \end{pmatrix}, \tag{2.35}$$

where $\xi_l = \frac{-U_G\epsilon}{2E_Q\left(\left(\frac{\kappa}{q_R}+l\right)^2-\zeta\right)}$, $\zeta = \frac{U_G A+E}{E_Q}$ and κ is Mathieu characteristic exponent. The solution for this equation is

$$\cos\left(\frac{2\pi\kappa}{q_R}\right) = 1 - \Delta(0)\left(1 - \cos\left(2\pi\sqrt{\zeta}\right)\right), \tag{2.36}$$

where $\Delta(0) = \det(A_M(\kappa = 0))$[98]. Real solutions of this equation provide the equations for the energy bands$E(q)$, while those with an imaginary part account for the evanescent modes in the gaps. These gaps are regions of forbidden energy. The transmission probability $T(E)$ of the these band-gaps in the interval $[z_1 : z_2]$can be calculated via

$$T(E) = e^{-2\int_{z_2}^{z_1} Im[\kappa(z,E)dz]}, \tag{2.37}$$

as shown by Damon et al.[97]. This analysis will be used in Sec. 3.1.

2.3 Computational Method

2.3.1 Discrete Fourier Transform

The numerical time evolution of the atoms will be calculated to understand the behaviour and performance of the beam-splitter and interferometer. The algorithm to model the time evolution is based on series of Fourier transforms. However, a computer only deals with discrete values and it is thus necessary to determine an approximation for numerical analyses. It can be approximated by something resembling a Fourier series on a time interval of $0 < t < T$[99]. The exponential Fourier series for this interval has the form of

$$f(t) = \sum_{n=-\infty}^{\infty} c_n e^{i2\pi n\frac{t}{T}}, \tag{2.38}$$

with its coefficients defined by the integral

$$c_n = \frac{1}{T}\int_0^T f(t)e^{-i2\pi n\frac{t}{T}}dt. \tag{2.39}$$

This function is periodic in t with period T. To make it more similar to the Fourier transform let us define

$$\Delta\omega = \frac{2\pi}{T}. \tag{2.40}$$

The Eq. 2.39 can now be approximated by the trapezoid rule[99], allowing us to define the discrete Fourier transform as

$$g(n\Delta\omega) = \sum_{m=0}^{N-1} f(m\Delta t)e^{-in\Delta\omega m\Delta t} = \sum_{m=0}^{N-1} f(m\Delta t)e^{-i2\pi n\frac{m}{N}}. \tag{2.41}$$

It has an inherent periodicity from the Fourier series. Furthermore, n and m are always positive as well as $\Delta\omega$ and Δt and thus it is only viable in positive ranges, where $\Delta\omega = \frac{2\pi}{T}$ and $\Omega = N\Delta\omega$ are the interval of the frequencies. Its inverse can be calculated exactly via orthogonality relations between the two transforms:

$$f(m\Delta t) = \frac{1}{N}\sum_{n=0}^{N-1} g(n\Delta\omega)e^{i2\pi m\frac{n}{N}}. \tag{2.42}$$

2.3.2 Relationship between the Fourier Transform and the Discrete Fourier Transform

In the previous section we defined the discrete Fourier transforms using the relationship between time and frequencies. Now we change to position and wavenumber. In addition, it is necessary to explore its relation to the analytical Fourier transform to see how one can deal with negative positions and wavenumbers[100, 101] Starting off with the Fourier transform over a finite dimension

$$\tilde{\psi}(k,t) = \mathcal{F}(\psi(x,t)) = \frac{1}{\sqrt{2\pi}}\int_{x_{min}}^{x_{max}} \psi(x,t)e^{-ikx}dx. \tag{2.43}$$

This expression can be approximated as a sum of N terms

$$\tilde{\psi}(k,t) \simeq \frac{1}{\sqrt{2\pi}}\sum_{m=0}^{N-1} \psi(x_m,t)e^{-ikx_m}\Delta x, \tag{2.44}$$

where $\Delta x = \frac{x_{max}-x_{min}}{N}$ and $x_m = x_{min} + m\Delta x$. Defining $\Delta k = \frac{2\pi}{N\Delta x}$ and $k_n = k_{min} + n\Delta k$ allows one to rewrite it as

$$\tilde{\psi}(k_n, t) \simeq \frac{1}{\sqrt{2\pi}} \sum_{m=0}^{N-1} \psi(x_m, t) e^{-ik_n x_m} \Delta x. \tag{2.45}$$

Substituting the expressions for Δx, x_m, k_m and Δk gives

$$\tilde{\psi}(k_n, t) e^{inx_{min}\Delta k} \simeq \frac{1}{\sqrt{2\pi}} \sum_{m=0}^{N-1} \Delta x \psi(x_m, t) e^{-ik_{min}x_m} e^{-i2\pi n \frac{m}{N}}. \tag{2.46}$$

The exponential term $e^{-i2\pi n \frac{m}{N}}$ shifts the original starting point away from zero towards k_{min}, which represents the lower limit of the wavevector space. Similar analysis can be applied to the inverse Fourier transform

$$\psi(x, t) = \mathcal{F}^{-1}(\tilde{\psi}(k, t)) = \frac{1}{\sqrt{2\pi}} \int_{k_{min}}^{k_{max}} \tilde{\psi}(k, t) e^{ikx} dk, \tag{2.47}$$

resulting in

$$\frac{\Delta x}{\sqrt{2\pi}} \psi(x_m, t) e^{-ik_{min}x_m} \simeq \sum_{n=0}^{N-1} \tilde{\psi}(k_n, t) e^{inx_{min}\Delta k} e^{i2\pi m \frac{n}{N}}. \tag{2.48}$$

Comparing the two Fourier transforms, one finds that the continuous Fourier transform has a corresponding pair of

$$\psi(x, t) \Longleftrightarrow \tilde{\psi}(k, t), \tag{2.49}$$

while the pair of the discrete Fourier transforms have extra terms due to normalization and the shift of the lower limit of the spaces in order to adjust them to the problem at hand[100, 101]:

$$\frac{\Delta x}{\sqrt{2\pi}} \psi(x_m, t) e^{-ik_{min}x_m} \Longleftrightarrow \tilde{\psi}(k_n, t) e^{inx_{min}\Delta k}. \tag{2.50}$$

2.3.3 The Split-Step Fourier Method for the Schrödinger Equation

The algorithm used to solve the nonlinear quantum mechanics equation like the Gross–Pitaevskii equation, is called the split-step Fourier method[100–102]. However, before applying it to a nonlinear equation we test it out on the Schrödinger equation. The reason for this is that it allows us to test the algorithm using problems which have analytical solutions. The numerical solutions from the algorithm and the analytical ones can then be compared to get a better understanding of the numerical errors. Beginning with the Schrödinger equation,

$$i\hbar \frac{\partial \psi(x, t)}{\partial t} = \frac{-\hbar^2}{2m} \frac{\partial^2 \psi(x, t)}{\partial x^2} + V(x)\psi(x, t), \tag{2.51}$$

and the Schrödinger equation in k-space

$$i\hbar\frac{\partial\tilde{\psi}(k,t)}{\partial t} = \frac{\hbar^2k^2}{2m}\tilde{\psi}(k,t) + V\left(i\frac{\partial}{\partial k}\right)\tilde{\psi}(k,t). \tag{2.52}$$

These two equations are to be solved separately. The normal Schrödinger equation is used to model the effects of the potential on the wave function, while the kinematics are neglected for this case. This results in a simplified version

$$i\hbar\frac{\partial\psi(x,t)}{\partial t} = V(x)\psi(x,t), \tag{2.53}$$

with the analytical solution of

$$\psi(x,t+\Delta t) = \psi(x,t)e^{-iV(x)\frac{\Delta t}{\hbar}}. \tag{2.54}$$

Similarly, in the k-space the effects of the potential are neglected and the Eq.2.52 takes the form

$$i\hbar\frac{\partial\tilde{\psi}(k,t)}{\partial t} = \frac{\hbar^2k^2}{2m}\tilde{\psi}(k,t). \tag{2.55}$$

The solution of this equation is

$$\tilde{\psi}(k,t+\Delta t) = \tilde{\psi}(k,t)e^{-i\hbar k^2\frac{\Delta t}{2m}}. \tag{2.56}$$

The algorithm for modelling the evolution is as follows for a single step[100–102]

$$\psi(x,t+\Delta t) = \mathcal{F}^{-1}\left(\mathcal{F}\left(\psi(x)e^{-iV(x)\frac{\Delta t}{2\hbar}}\right)e^{-i\hbar k^2\frac{\Delta t}{2m}}\right)e^{-iV(x)\frac{\Delta t}{2\hbar}}. \tag{2.57}$$

The reason behind the splitting of the step in position space is to reduce the error from $\mathcal{O}(\Delta t^2)$ to $\mathcal{O}(\Delta t^3)$[102], giving us the symmetric split-step Fourier Method. This can be seen by Taylor expanding the proper unity operator responsible for the time evolution

$$\begin{aligned} e^{h(\hat{A}+\hat{B})} &= \hat{I} + h(\hat{A}+\hat{B}) + \frac{h^2}{2!}(\hat{A}^2+\hat{B}^2+\hat{A}\hat{B}+\hat{B}\hat{A}) \\ &+\frac{h^3}{3!}(\hat{A}^3+\hat{B}^3+\hat{A}^2\hat{B}+\hat{B}^2\hat{A}+\hat{A}\hat{B}\hat{A}+\hat{B}\hat{A}^2+\hat{A}\hat{B}^2+\hat{B}\hat{A}\hat{B}) + \ldots, \end{aligned} \tag{2.58}$$

and compare it with the split operator firs

$$\begin{aligned} e^{h\hat{A}}e^{h\hat{B}} &= (\hat{I} + h(\hat{A}) + \frac{h^2}{2!}(\hat{A}^2) + \frac{h^3}{3!}(\hat{A}^3) + \ldots) \\ &\quad (\hat{I} + h(\hat{B}) + \frac{h^2}{2!}(\hat{B}^2) + \frac{h^3}{3!}(\hat{B}^3) + \ldots) \\ &= \hat{I} + h(\hat{A}+\hat{B}) + \frac{h^2}{2!}(\hat{A}^2+\hat{B}^2+2!\hat{A}\hat{B}) + \ldots. \end{aligned} \tag{2.59}$$

This shows clearly that the error is of $\mathcal{O}(\Delta t^2)$. Now doing in the same for the symmetric split-step method

$$\begin{aligned} e^{\frac{h}{2}\hat{A}}e^{h\hat{B}}e^{\frac{h}{2}\hat{A}} &= (\hat{I} + h\frac{1}{2}(\hat{A}) + \frac{h^2}{2!}\frac{1}{4}(\hat{A}^2) + \frac{h^3}{3!}\frac{1}{8}(\hat{A}^3) + \ldots) \\ &\quad (\hat{I} + h(\hat{B}) + \frac{h^2}{2!}(\hat{B}^2) + \frac{h^3}{3!}(\hat{B}^3) + \ldots) \\ &\quad (\hat{I} + h\frac{1}{2}(\hat{A}) + \frac{h^2}{2!}\frac{1}{4}(\hat{A}^2) + \frac{h^3}{3!}\frac{1}{8}(\hat{A}^3) + \ldots) \\ &= \hat{I} + h(\hat{A} + \hat{B}) + \frac{h^2}{2!}(\hat{A}^2 + \hat{B}^2 + \hat{A}\hat{B} + \hat{B}\hat{A}) + \\ \frac{h^3}{3!}(\hat{A}^3 + \hat{B}^3 + \frac{3}{2}\hat{A}\hat{B}^2 + \frac{3}{2}\hat{B}^2\hat{A} + \frac{3}{4}\hat{A}^2\hat{B} + \frac{3}{4}\hat{B}\hat{A}^2 + \frac{3}{2}\hat{A}\hat{B}\hat{A}) + \ldots, \end{aligned} \tag{2.60}$$

shows the improved error of $\mathcal{O}(\Delta t^3)$. The desired time can be archived by repetition. From this method animations showing the probability density are created and only chosen time stamps of them are shown in the thesis, where to find the full animations list is explained in appendix A.

Evolution of a free Gaussian Particle

The first test for the algorithm is the evolution of a free Gaussian wave packet described as

$$\psi(x,0) = \frac{1}{\sqrt{\sigma\sqrt{\pi}}} e^{-\frac{(x-x_0)^2}{2\sigma^2}} e^{ik_0 x}, \tag{2.61}$$

where σ is the variance of the Gaussian wave packet, x_0 the starting position and k_0 the initial wave number. The straightforward way to solve it analytically is by solving the Schrödinger equation in k-space where the initial wave function is

$$\tilde{\psi}(k,0) = \sqrt{\frac{\sigma}{\sqrt{\pi}}}\, e^{-\frac{(k-k_0)^2\sigma^2}{2}} e^{ix_0(k-k_0)} \tag{2.62}$$

The potential for a free Gaussian wave packet is zero and the evolution is therefore described by Eq. 2.55. The result is

$$\tilde{\psi}(k,t) = \sqrt{\frac{\sigma}{\sqrt{\pi}}}\, e^{-\frac{(k-k_0)^2\sigma^2}{2}} e^{ix_0(k-k_0)} e^{-i\hbar k^2 \frac{\Delta t}{2m}}, \tag{2.63}$$

which then needs to be inverse Fourier transformed. Leaving us with the final result of[103]

$$\tilde{\psi}(x,t) = \sqrt{\frac{\sigma}{\alpha\sqrt{\pi}}}\, e^{-\frac{\beta^2}{\alpha}} e^{ik_0 x} e^{-i\hbar k_0^2 \frac{t}{2m}}, \tag{2.64}$$

where

$$\alpha = \sigma^2 + i\hbar\frac{t}{m}, \tag{2.65}$$

and

$$\beta = x_0 - x + k_0 \hbar \frac{t}{m}. \tag{2.66}$$

Eq. 2.64 shows that the wave packet moves and diffuses over time. Following from here we use the split-step Fourier method to solve this case numerically, see Fig. 2.2. In this case the Gaussian wave packet of ^{87}Rb starts of at $x_0 = -0.0001m$, with a velocity $v = 0.005ms^{-1}$ and a variance $\sigma = 10^{-5}m$ represented by a red solid line. The evolution of the analytical solution, blue dotted line, and the numerical, green dashed line, are nearly identical after a propagation time of 0.1s.

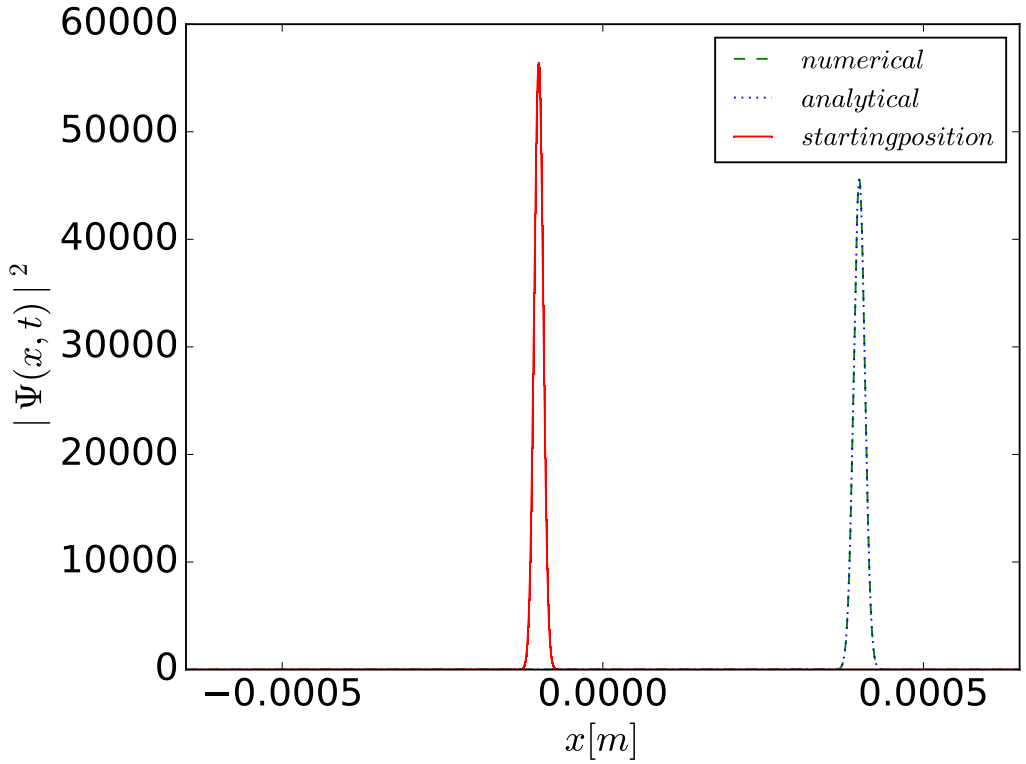

FIGURE 2.2: The initial wave function starts of at $x_0 = -0.0001m$, with a velocity $v = 0.005m/s$ and a variance $\sigma = 10^{-5}m$(red solid line) and is then numerically evolved via time steps of the size of $\Delta t = 10^{-6}s$ giving the final numerical result after $0.1s$(green dashed line). This is then compared with the analytical solution from Eq. 2.64.

The absolute difference between these two solutions can be seen in Fig. 2.3. It can be clearly seen that the difference is minimal. Another way to analyse the difference is to determine the inner product of these two, which turns out to be close to unity. The time step for this calculation is $\Delta t = 10^{-6}s$, the initial wave function is discretized into 100000 data points evenly distributed and a k-range with $k_{max} = -k_{min}$. The same calculations have been done for a variety of systems, producing similar results.We therefore conclude that the method works well for a free wave packet.

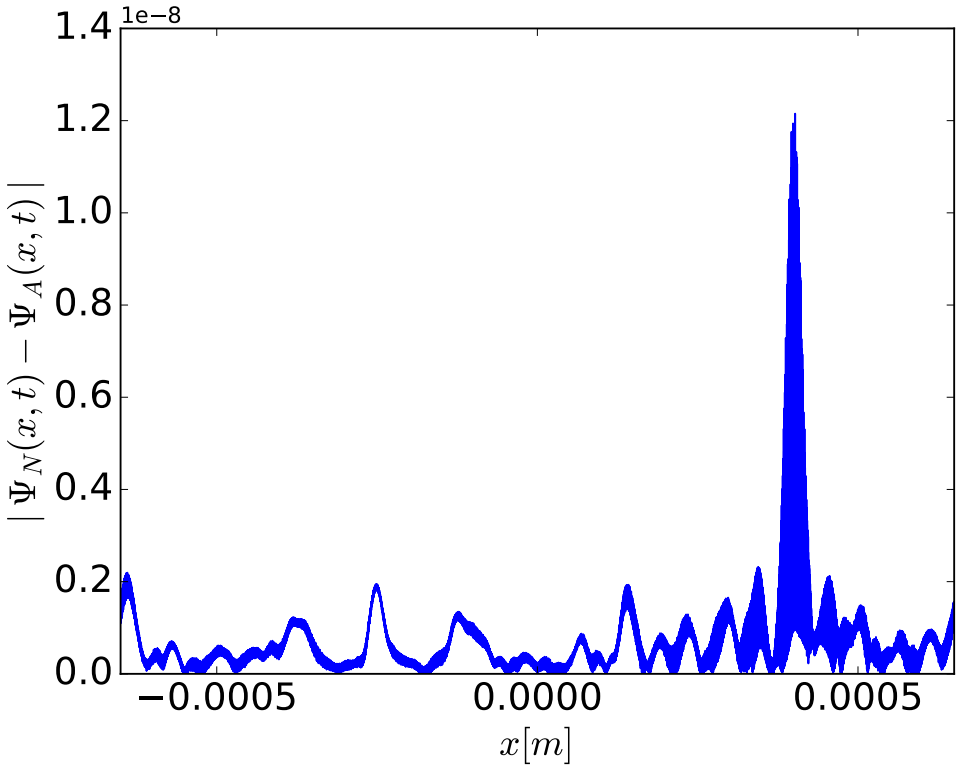

FIGURE 2.3: This figure depicts the absolute difference of the numerical, represented by $\psi_N(x,t)$ and the analytical solution, $\psi_A(x,t)$. For a Gaussian wave function starting with $x_0 = -0.0001m$, with a velocity $v = 0.005m/s$, a variance $\sigma = 10^{-5}m$, time step size $\Delta t = 10^{-6}s$ and a propagation time $t = 0.1s$. The maximum of this peak lies around 1.3×10^{-8}.

Evolution of a Coherent State in a Harmonic Oscillator

The next test for the split-step Fourier method is the evolution of a coherent state in a harmonic oscillator. The evolution of the coherent state inside a harmonic oscillator:

$$|\alpha(t)\rangle = e^{-i\omega\frac{t}{2}} e^{-\frac{|\alpha_0|^2}{2}} \sum_n \frac{\alpha_0^n e^{-in\omega t}}{\sqrt{n!}} |n\rangle \,, \tag{2.67}$$

where, ω is the frequency and t the time [84, 103]. They resemble very closely to the behaviour of classical systems in the sense that the expectation values for the position and momentum oscillate in a quantum harmonic oscillator similarly to how momentum and position change with time in a classical harmonic oscillator.The real part of a coherent state represents its position and the imaginary part its momentum. In a harmonic oscillator with the potential

$$V(x) = \frac{1}{2} m\omega^2 \hat{x}^2, \tag{2.68}$$

where m is the mass of the particle and $\hat{x}$ the position operator, the wave function for the coherent state in position space can be written as

$$\psi(x,t) = e^{i\theta_\alpha(t)} \left(\frac{m\omega}{\pi\hbar}\right)^{\frac{1}{4}} e^{i\frac{x\langle P(t)\rangle}{\hbar}} e^{-\left[\frac{x-\langle X(t)\rangle}{2\Delta}\right]^2}, \tag{2.69}$$

where the phase $\theta_\alpha(t)$ is described by

$$e^{i\theta_\alpha} = e^{\frac{\alpha^*(t)^2-\alpha(t)}{4}}, \tag{2.70}$$

the mean momentum by

$$\langle P(t)\rangle = \sqrt{\frac{2\hbar}{m\omega}}\, Re\left[\alpha_0 e^{-i\omega t}\right], \tag{2.71}$$

and the mean position

$$\langle X(t)\rangle = \sqrt{2\hbar m\omega}\, Im\left[\alpha_0 e^{-i\omega t}\right]. \tag{2.72}$$

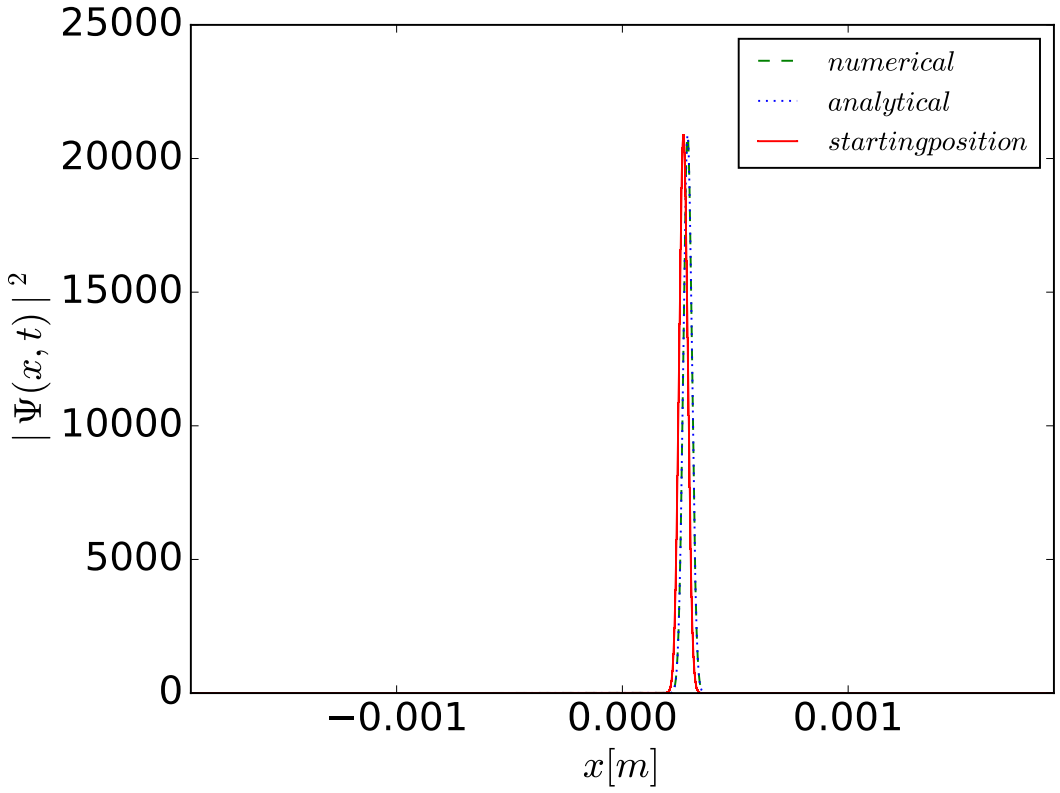

FIGURE 2.4: The evolution of the coherent state with $|\alpha| = 10$ in the x-space is depicted in a harmonic oscillator with an angular frequency of $\omega = 1rad/s$. The red solid line shows the initial position of the coherent state starting $\alpha = 10 * e^{i\frac{\pi}{4}}$. This is then numerically evolved with a time step size $\Delta t = 10^{-6}s$ over a period of $1.5s$. Resulting in the wave function shown as the green dashed dotted line which is very close to the analytical solution, the blue dotted line.

Now starting of with an initial coherent state of $\alpha = 10e^{i\frac{\pi}{4}}$, an angular frequency of $\omega = 1 \quad rad/s$ and a mass of ^{87}Rb atom, we discretize the initial wave function into 100000 data points and let it evolve via a time step size of $\Delta t = 10^{-6}s$ for a period of $1.5s$. The Fig. 2.4 shows the numerical solution as a green dashed line and the analytical one as a blue dotted line. Like for the free Gaussian wave packet these two are nearly identical neglecting the numerical error.
The absolute difference is shown in Fig.2.5 which is not bigger than 4×10^{-8}. This shows that this algorithm is suitable to model the evolution of wave functions which are interacting with a potential. Also, the inner product between the analytical solution and the numerical one is very close to unity. The same calculations have been carried out for a variety of times and coherent states, leading to similar solutions. Thus the split-step Fourier method is a good way so solve the Schrödinger and Gross–Pitaevskii equation.

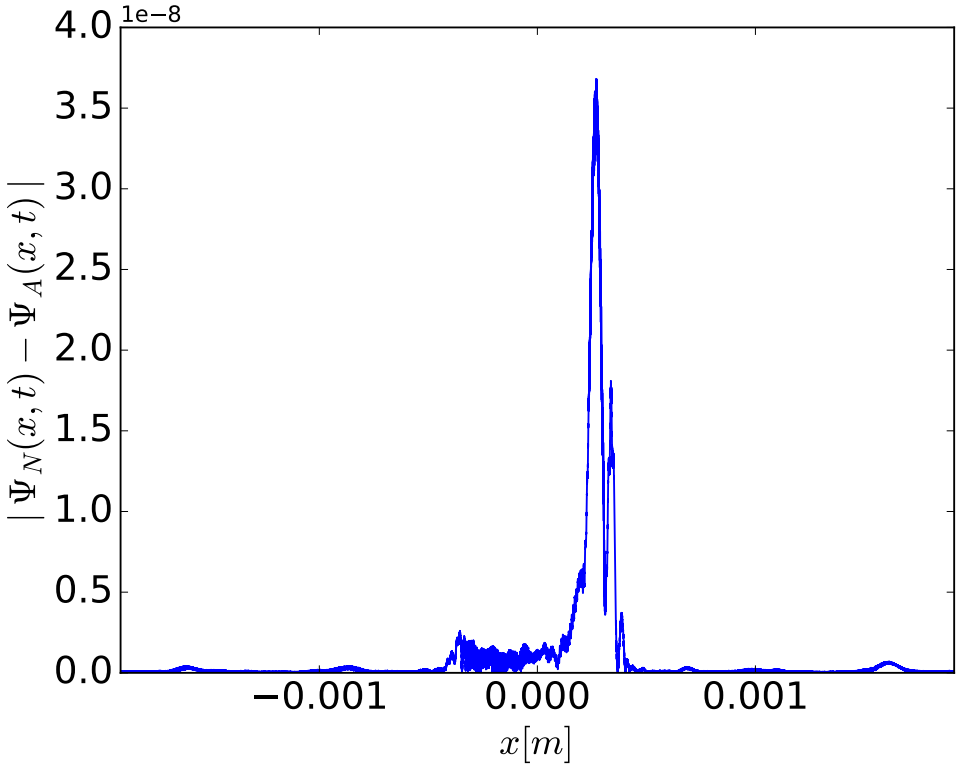

FIGURE 2.5: This figure shows the absolute difference between the numerical, $\psi_N(x,t)$ and analytical solution, $\psi_A(x,t)$. The maximum difference is approximately 3.6×10^{-8}.

Free Gaussian

Another example to test the split-step Fourier method is the evolution of two free Gaussian wave packets moving in opposite directions. Starting with the normalised wave-function for a single moving Gaussian

$$\psi(x,0) = \frac{1}{\sqrt{\sigma\sqrt{\pi}}}\left(e^{-\frac{(x-x_0)^2}{2\sigma^2}}e^{ik_0x}\right), \tag{2.73}$$

from which we create a superposition of two Gaussians with one starting at x_0 with a wavenumber k_0 and the other with $-x_0$ and $-k_0$.

$$\Psi(x,0) = \frac{1}{\sqrt{2\sigma\sqrt{\pi}}}\left(e^{-\frac{(x-x_0)^2}{2\sigma^2}}e^{ik_0x} + e^{-\frac{(x+x_0)^2}{2\sigma^2}}e^{-ik_0x}\right). \tag{2.74}$$

For this case it is easier to calculate the evolution in k-scape and thus the Fourier transform of wave-function is

$$\tilde{\Psi}(k,0) = \sqrt{\frac{\sigma}{2\sqrt{\pi}}}\left(e^{-\frac{(k-k_0)^2}{2\sigma^2}}e^{-i(k-k_0)x_0} + e^{-\frac{(k+k_0)^2}{2\sigma^2}}e^{i(k+k_0)x_0}\right). \tag{2.75}$$

This wave-function obeys the Schrödinger equation and evolves according to

$$\tilde{\Psi}(k,t) = \tilde{\Psi}(k,0)e^{-\frac{i\hbar k^2 t}{2m}}, \tag{2.76}$$

into which we substitute our wave-function to get

$$\tilde{\Psi}(k,t) = e^{-\frac{i\hbar k^2 t}{2m}}\sqrt{\frac{\sigma}{2\sqrt{\pi}}}\left(e^{-\frac{(k-k_0)^2\sigma^2}{2}}e^{-i(k-k_0)x_0} + e^{-\frac{(k+k_0)^2\sigma^2}{2}}e^{i(k+k_0)x_0}\right). \tag{2.77}$$

As this is is already the solution in k-space we just need to Fourier transform it back into position space to obtain

$$\Psi(x,t) = \sqrt{\frac{\sigma}{2\alpha\sqrt{\pi}}}\,e^{\frac{-i\hbar k_0^2 t}{2m}}\left(e^{-\frac{\left(x-x_0-\frac{k_0\hbar t}{m}\right)^2}{2\alpha}}e^{ik_0x} + e^{-\frac{\left(x+x_0+\frac{k_0\hbar t}{m}\right)^2}{2\alpha}}e^{-ik_0x}\right), \tag{2.78}$$

where

$$\alpha = \left(\sigma^2 + \frac{i\hbar t}{m}\right). \tag{2.79}$$

Now that we have our analytical solution, we are comparing to the numerical one. For this we set $m = 1$, $k_0 = 1$, $\hbar = 1$, $\sigma = 1$ and $\pi = 1$, simplifying our wave function to

$$\Psi(x,t) = \sqrt{\frac{1}{2\,(1+it)}}\,e^{\frac{-it}{2}}\left(e^{-\frac{(x-x_0-t)^2}{2(1+it)}}e^{ix} + e^{-\frac{(x+x_0+t)^2}{2(1+it)}}e^{-ix}\right). \tag{2.80}$$

The other parameter we use for testing are the run time of $t = 6$ the starting position of $x_0 = 6$, the number of data points $N_x = 10000$, the step size in time $\delta t = 10^{-4}$ and the area of our simulation ranging from $x_{min} = -20$ to $x_{max} = 20$. They are unitless for these calculations. Looking at Fig. 2.6, we see the starting position of a red dotted line and the final form at the end of the simulation for the split-step Fourier method in a green dashed line and the analytical solution in a blue dotted line for compression.

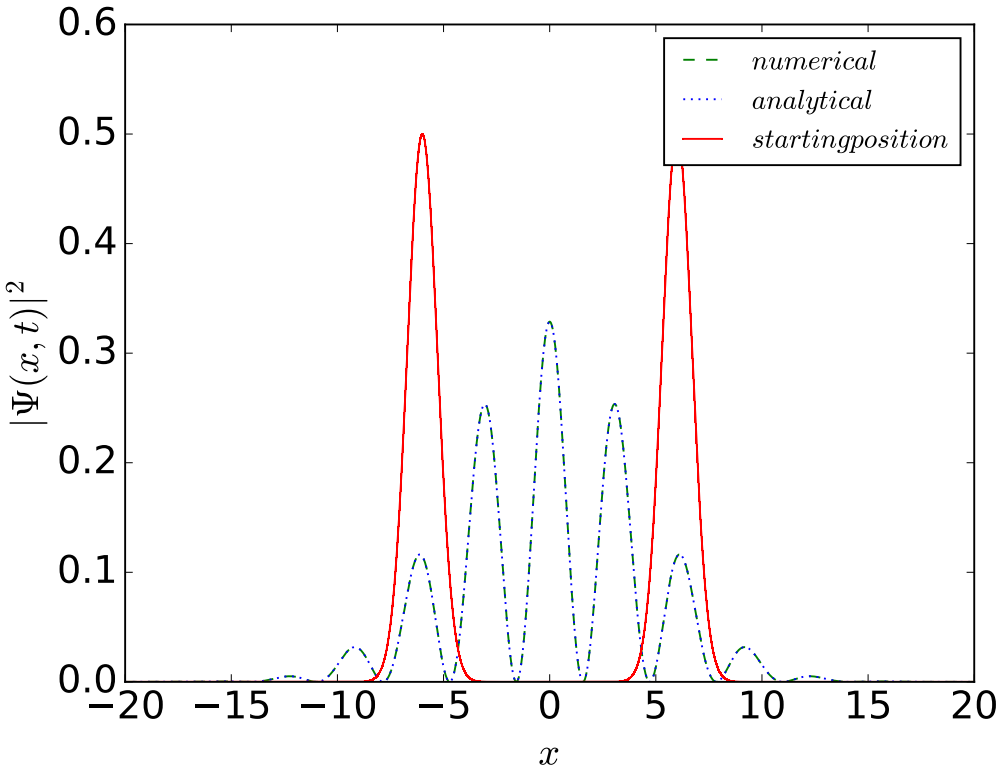

FIGURE 2.6: The overlap of two free Gaussian wave-packets that started off at $x_0 = 6$(red solid line) and then evolved moving towards each other finishing at $t = 6$ with an analytical(blue dotted line) and numerical solution(green dashed line), where all variables are unitless.

The analytical and numerical solution overlap extremely well as seen by the errors in Fig. 2.7. The error in the error graph show period behaviour. This comes from the nature of the discrete Fourier transform and its periodic boundaries. Hence it is clear to see that these errors come from the remnants of the numerical solution that left the boundary on one site and entered the simulation back on the other side. Hence, from this we can see that we need to give sufficient space between the wave-function and the boundary to avoid such error. As long as we satisfy this boundary constraint, we conclude that our numerical method works well for wave-functions comprising packets with different motions. Furthermore, their are potential boundaries around the simulation in the subsequent chapters, in the shape of Gaussian barriers to avoid this behaviour, which are referred to as the cage.

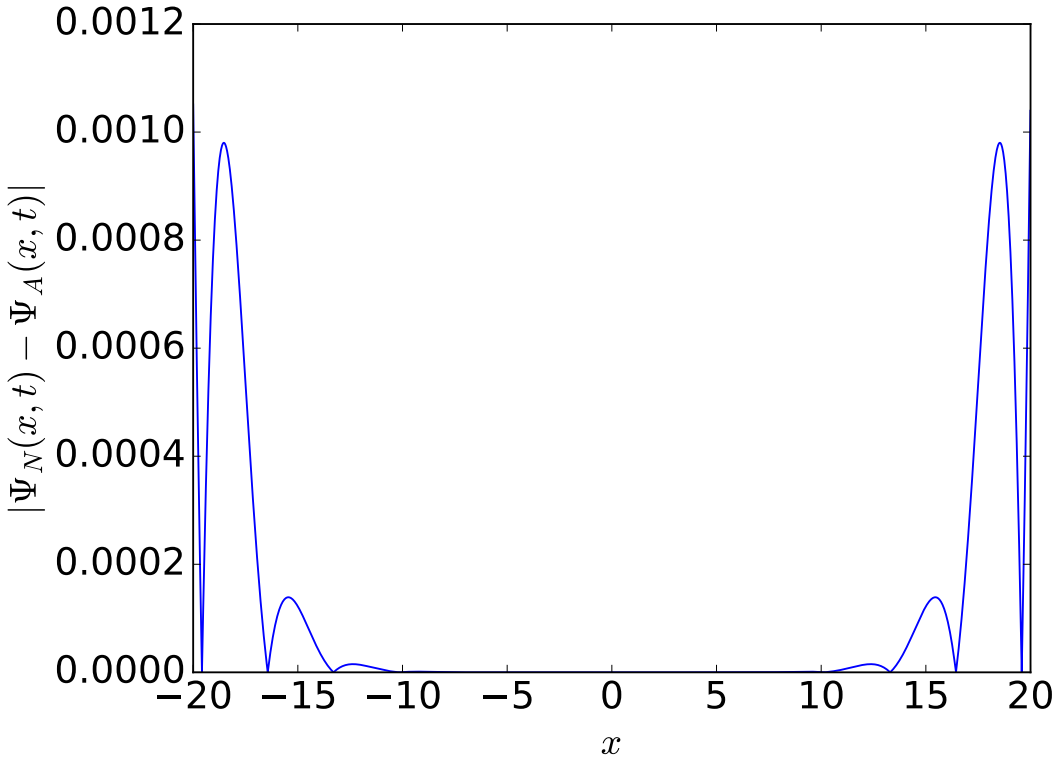

FIGURE 2.7: The error between the numerical and analytical solution for two free overlapping Gaussian.

Cat State

The last example we are looking at will be the cat state[102] in a harmonic oscillator. Starting off with the wave-function for a coherent state,

$$\psi_\alpha(x,t) = \langle x|\alpha\rangle = e^{i\theta_{\alpha(t)}} \left(\frac{m\omega}{\pi\hbar}\right)^{\frac{1}{4}} e^{-\left(\frac{x-\langle X\rangle_{\alpha(t)}}{2\Delta X}\right)^2} e^{i\langle K\rangle_{\alpha(t)}x}, \tag{2.81}$$

where

$$e^{i\theta_{\alpha(t)}} = e^{\frac{\alpha^{*2}(t)-\alpha^2(t)}{4}}, \tag{2.82}$$

$$\langle X\rangle_{\alpha(t)} = \sqrt{\frac{2\hbar}{m\omega}}\, Re\left(\alpha\left(t\right)\right), \tag{2.83}$$

$$\langle K\rangle_{\alpha(t)} = \sqrt{\frac{2m\omega}{\hbar}}\, Im\left(\alpha\left(t\right)\right), \tag{2.84}$$

$$\Delta X = \sqrt{\frac{\hbar}{2m\omega}}, \tag{2.85}$$

$$\Delta K = \sqrt{\frac{m\omega}{2\hbar}}, \tag{2.86}$$

$$\alpha\left(t\right) = \alpha\left(0\right) e^{-i\omega t}, \tag{2.87}$$

From this we can create a cat state via the superposition of coherent states as

$$|cat\rangle = \frac{1}{\sqrt{2\left(1+e^{-2|\alpha|^2}\right)}}\left(|\alpha\rangle + |-\alpha\rangle\right), \tag{2.88}$$

which takes the form in position space of

$$\begin{aligned}\psi_{cat}(x,t) &= \frac{1}{\sqrt{2\left(1+e^{-2|\alpha|^2}\right)}}\left(\psi_{\alpha}(x,t) + \psi_{-\alpha}(x,t)\right), \\ &= \frac{1}{\sqrt{2\left(1+e^{-2|\alpha|^2}\right)}}\left(\frac{m\omega}{\pi\hbar}\right)^{\frac{1}{4}} e^{i\theta_{\alpha(t)}}\left(e e^{-\left(\frac{x-\langle X\rangle_{\alpha(t)}}{2\Delta X}\right)^2} e^{i\langle K\rangle_{\alpha(t)}x}\right. \\ &\left. + e^{-\left(\frac{x-\langle X\rangle_{-\alpha(t)}}{2\Delta X}\right)^2} e^{i\langle K\rangle_{-\alpha(t)}x}\right).\end{aligned} \tag{2.89}$$

Now we can compare this analytical solution with the numerical one, using only unitless parameters. For this we set $m = 1$, $\omega = 1$ and $\hbar = 1$ as we are only concerned about how well the numerical matches the analytical, leading to

$$\begin{aligned}\psi_{cat}(x,t) = \frac{1}{\sqrt{2\left(1+e^{-2|\alpha|^2}\right)}} e^{i\theta_{\alpha(t)}}\left(e^{-\frac{\left(x-\sqrt{2}\,Re(\alpha(t))\right)^2}{2}} e^{i\sqrt{2}\,Im(\alpha(t))x}\right. \\ \left. + e^{-\frac{\left(x+\sqrt{2}\,Re(\alpha(t))\right)^2}{2}} e^{-i\sqrt{2}\,Im(\alpha(t))x}\right).\end{aligned} \tag{2.90}$$

From this we can now do a comparison between our numerical method and our analytical solution for a cat state in a harmonic oscillator. For this we set the other parameters in our simulation to a run time of $t = 4.5\pi$, the starting α position of $\alpha_0 = 5$, the number of data points $N_x = 10000$, the step size in time $\Delta t = 10^{-4}$ and the area of our simulation ranging from $x_{min} = -15$ to $x_{max} = 15$. This can be seen in Fig. 2.8, where the red line is the starting position and the position at the end of the simulation is in green dotted for the numerical and blue dotted for the analytical solution. The time of $t = 4.5\pi$ is chosen as this allows for more than two whole rotations of the cat state letting it finish at an $90°$ angle from its starting position and thus showing us the expected fringes. Furthermore, the error between numerical and analytical are very small as seen in Fig. 2.9.

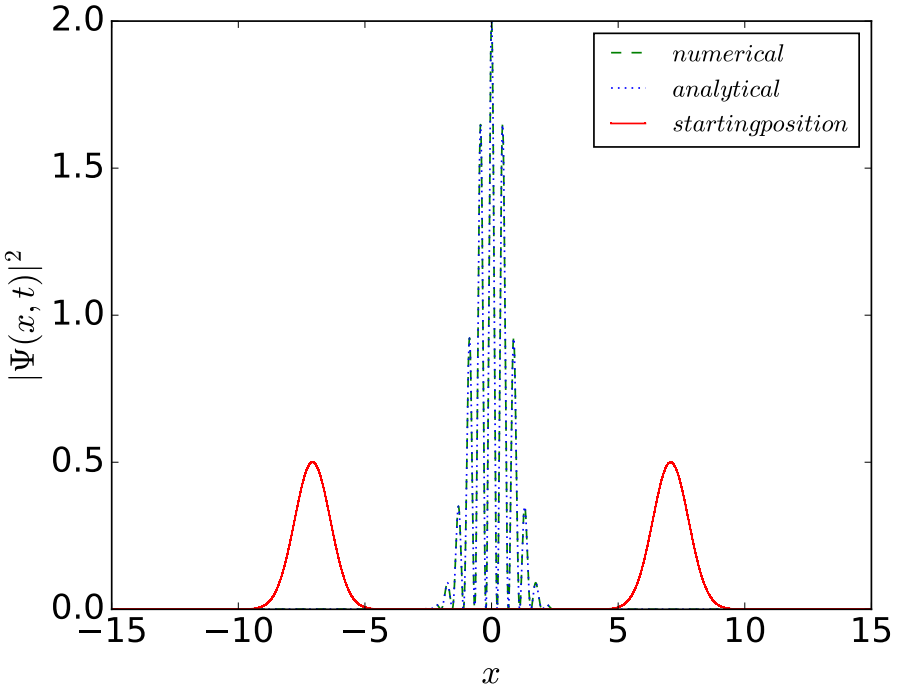

FIGURE 2.8: The evolution of at cat state starting of from $\alpha_0 = 5$(red solid line) and finishing at an $90°$ angle after a run time of $t = 4.5\pi$(green dashed) and the analytical solution as a comparison. Using unitless parameters

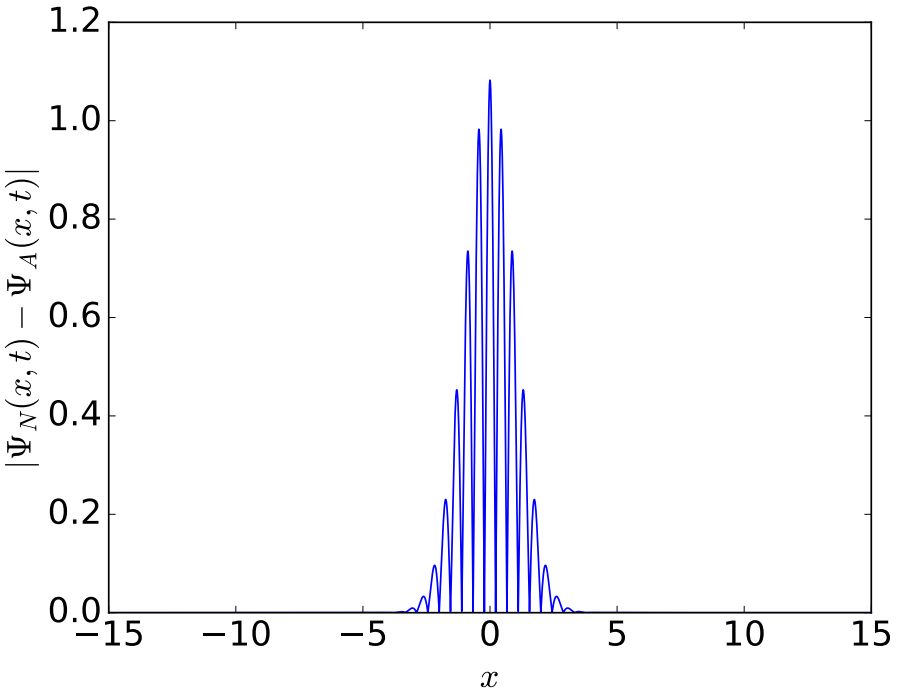

FIGURE 2.9: The error between the analytical and numerical solution for a run time of $t = 4.5\pi$, the starting α position of $\alpha_0 = 5$, the number of data points $N_x = 10000$, the step size in time $\Delta t = 10^{-4}$ and the area of our simulation ranging from $x_{min} = -15$ to $x_{max} = 15$

2.3.4 Shooting Method

The shooting method is a method for the calculations of eigenstate energies and their respective wave-functions[99]. Starting off with the time-independent Schrödinger equation

$$\frac{\hbar^2}{2m}\frac{\partial^2\psi(x)}{\partial x^2} + (E - V(x))\psi(x) = 0, \tag{2.91}$$

which can be rewritten into

$$\frac{\partial\psi(x)}{\partial x} = z(x) = f_1(\psi, x, z), \tag{2.92}$$

$$\frac{\partial^2\psi(x)}{\partial x^2} = \frac{\partial z(x)}{\partial x} = -\frac{2m}{\hbar^2}(E - V(x))\psi(x) = f_2(\psi, x, z). \tag{2.93}$$

Using the Euler Method[99] to solve it with step size Δz we get

$$\psi_{i+1} = \psi_i + f_1(\psi, x, z)\,h = \psi_i + z_i\Delta z \tag{2.94}$$

$$z_{i+1} = z_i + f_2(\psi, x, z)\,h = z_i - \frac{2m}{\hbar^2}(E - V(x))\psi(x)\Delta z, \tag{2.95}$$

with the boundary condition for an even function being

$$\psi(0) = \psi_0 = R, \tag{2.96}$$

$$\frac{\partial\psi(0)}{\partial x} = z_0 = 0, \tag{2.97}$$

and for an odd function

$$\psi(0) = \psi_0 = 0, \tag{2.98}$$

$$\frac{\partial\psi(0)}{\partial x} = z_0 = R, \tag{2.99}$$

where R is a random number. Its value is not important as it will be changed due to normalisation. The other boundary condition is that the $\psi(\infty) = 0$ or for a numerical case it should approach zero far away from the centre as possible. To find the ground state we start off at a random value for E which is chosen to be less than the energy of the actual ground state, by setting it to the minimum of the potential, and the boundary condition for an even state. Then we integrate numerically from the centre to see if the wave-function converges at the boundary. If not, we note whether the wave-function diverges positively or negatively, and store this information. Then we increase the initial estimate of the energy by a small amount ΔE and repeat this process until we achieve convergence of the wave-function, or we observe a change in the direction of the divergence. If it the direction changes we will go back to the previous energy estimate and increase this by $\Delta E/2$ instead of just ΔE. These steps will be repeated until our wave-function converges. From this we could calculate the first excited state by choosing the boundary condition of an odd state and have

the energy for the first estimate slightly above the ground state. All other eigenstates could be found in a similar fashion if desired. To increase precision one could reduce Δz or go from Euler method to a more precise like Runge-Kutta[99]. This is used in Sec. 4.2.

2.3.5 Transmission Probability for Arbitrary Potentials

The previously discussed band-gap method, gives us a detailed look into the splitting properties of our beam-splitter. However, it relies on a certain number of fringes and fringe density, which is not always the case. Hence, we will discuss an alternative method for calculating the transmission probability, as demonstrated by Rundquist[104]. For this we will have three potential regions: the first on with $V_I = 0$, the second region where $V_{II} = V(x)$ is the actual potential of our beam-splitter and the third region with $V_{III} = 0$. These calculations are performed using standing waves, where the wave-function for the first region is

$$\psi_I = Ae^{ikx} + Be^{-ikx}, \tag{2.100}$$

and its first derivative

$$\frac{d\psi_I}{dx} = ikAe^{ikx} - ikBe^{-ikx}. \tag{2.101}$$

The same can be done for region three, where the wave-function has the form

$$\psi_{III} = Ce^{ikx}, \tag{2.102}$$

and its derivative is

$$\frac{d\psi_{III}}{dx} = ikCe^{ikx}. \tag{2.103}$$

The wave number for both wave-functions is

$$k = \sqrt{\frac{2m^2}{\hbar^2}\left(E - V_{III}\right)}. \tag{2.104}$$

To calculate the transmission probability we need to integrate backwards from the boundary between region II and III to the boundary between region I and II. The rationale behind integrating backwards instead of forwards is that forwards integration would require us to have some understanding about the phase difference between the incoming wave Ae^{ikx} and the reflected one Be^{-ikx}. Any phase in regards to the transmitted wave Ce^{ikx} would be a global one and hence would not alter the transmission probability. Therefore we can simply set its coefficient to $C = 1$. For this calculation we are using recoil units as these allow us to simplify the

procedure. Starting off with the initial values

$$\frac{d\psi\left(x\right)}{dx} = g_{\psi}(\psi, z, x) = z\left(x\right), \tag{2.105}$$

$$\psi\left(L\right) = e^{ikL}, \tag{2.106}$$

$$\frac{dz\left(x\right)}{dx} = g_{z}(\psi, z, x) = \left(V(x) - E\right)\psi\left(x\right), \tag{2.107}$$

$$z\left(L\right) = ike^{ikL}. \tag{2.108}$$

From here on we will take a step backwards to calculate the previous values of ψ and z. The step size is given by Δx and it must be $\Delta x > 0$. We will be using the Runge-Kutta method which is generally referred to as "RK4" to do this[99]. Using,

$$\psi_{n-1} = \psi_{n} - \left(k1 + k2 + k3 + k4\right), \tag{2.109}$$

$$z_{n-1} = z_{n} - \left(l1 + l2 + l3 + l4\right), \tag{2.110}$$

where

$$k_{1} = \Delta x g_{\psi}(\psi_{n}, z_{n}, x_{n}), \tag{2.111}$$

$$l_{1} = \Delta x g_{z}(\psi_{n}, z_{n}, x_{n}), \tag{2.112}$$

$$k_{2} = \Delta x g_{\psi}\left(\psi_{n} - \frac{k_{1}}{2}, z_{n} - \frac{l_{1}}{2}, x_{n} - \frac{\Delta x}{2}\right), \tag{2.113}$$

$$l_{2} = \Delta x g_{z}\left(\psi_{n} - \frac{k_{1}}{2}, z_{n} - \frac{l_{1}}{2}, x_{n} - \frac{\Delta x}{2}\right), \tag{2.114}$$

$$k_{3} = \Delta x g_{\psi}\left(\psi_{n} - \frac{k_{2}}{2}, z_{n} - \frac{l_{2}}{2}, x_{n} - \frac{\Delta x}{2}\right), \tag{2.115}$$

$$l_{3} = \Delta x g_{z}\left(\psi_{n} - \frac{k_{2}}{2}, z_{n} - \frac{l_{2}}{2}, x_{n} - \frac{\Delta x}{2}\right), \tag{2.116}$$

$$k_{4} = \Delta x g_{\psi}(\psi_{n} - k_{3}, z_{n} - l_{3}, x_{n} - \Delta x), \tag{2.117}$$

$$l_{4} = \Delta x g_{z}(\psi_{n} - k_{3}, z_{n} - l_{3}, x_{n} - \Delta x). \tag{2.118}$$

These steps are repeated until the boundary between region I and region II is reached. From this we can calculate the transmission probability via

$$T = \left|\frac{C}{A}\right|^{2} = \left|\frac{1}{A}\right|^{2}. \tag{2.119}$$

To do this we need to determine the value of $|A|$ which can be done by evaluating Eq. 2.100 and 2.101 at the boundary,

$$\left|\psi_{I}\left(x_{b}\right) - \frac{i}{k}\frac{d\psi_{I}\left(x_{b}\right)}{dx}\right| = \left|2Ae^{ikx_{b}}\right| = 2|A|, \tag{2.120}$$

where x_b is the position of the boundary. Now substituting Eq. 2.120 into 2.119 yields,

$$T = \frac{4}{\left|\psi_I\left(x_b\right) - \frac{i}{k}\frac{d\psi_I(x_b)}{dx}\right|^2}. \tag{2.121}$$

This method can be used for arbitrary potentials. However, to number of datapoints required can vary greatly between different problems. The total error of "RK4" is $\mathcal{O}\Delta x^4$. This is used in Sec. 3.2. As an example, we could recreate a test from Rundquist[104] by calculating the tunnelling probability through a parabolic potential, which is limited to the central region with the potential

$$V(x) = \begin{cases} 10(x-1)^2, & \text{if } 0 < x < 2. \\ 0, & \text{otherwise,} \end{cases} \tag{2.122}$$

which has eigenstates energies for the non-truncated case of

$$E_n = \left(n + \frac{1}{2}\right) 1.232eV \text{ where } n = 0, 1, 2, \ldots. \tag{2.123}$$

The transmission probability can be seen in Fig. 2.10. It clearly shows that we always observe total transmission at the eigenstate energies. However, for lower energy one needs to hit the eigenstate energy nearly exactly to see any transmission, while for higher energy the range energies is broader. This is because at lower energy the wave needs to tunnel through a thicker barrier.

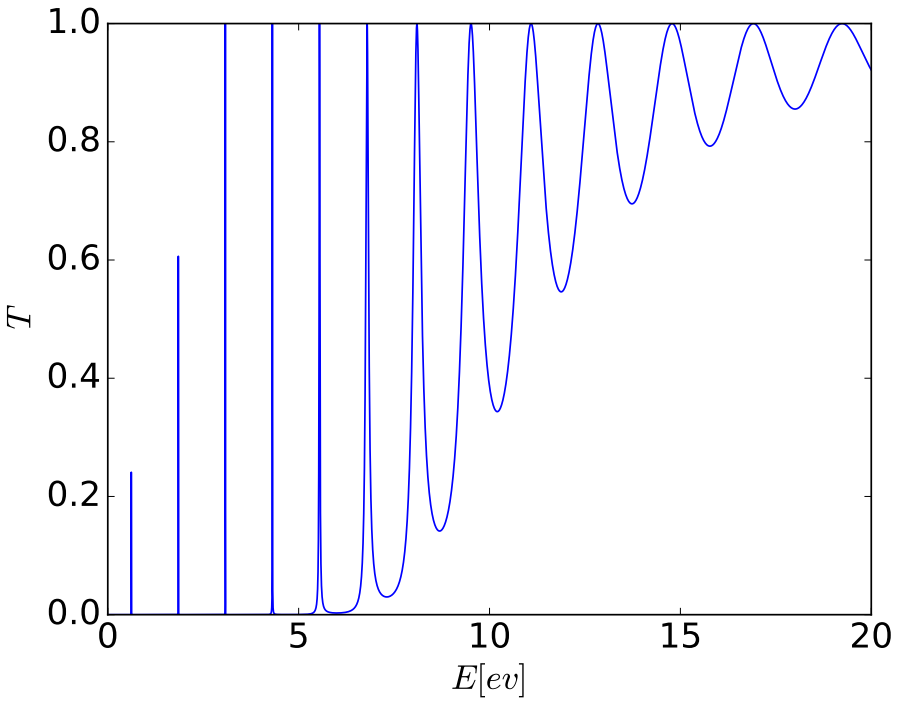

FIGURE 2.10: The tunnelling probability for the parabolic potential.

Chapter 3

Beam-Splitter Properties in One-Dimension

This chapter is focused on the beam-splitter properties in one dimension, see Fig. 3.1. This figure shows the 2D potential(A) and its corresponding 1D potential(B). The pattern inside the beam-splitter are the fringes of the optical lattice. For this we will investigate the band-gap structure of our beam-splitter, solving the time-independent Schrödinger equation for a standing wave and calculating its transmission probability. Lastly, we are going to solve the time-dependent Schrödinger equation for a Gaussian wave packet. These three methods will be applied to beam-splitter with the same parameter and their solution will be compared. This is done to counter check the validity of each solution as some of them require that a certain type of approximation is fulfilled.

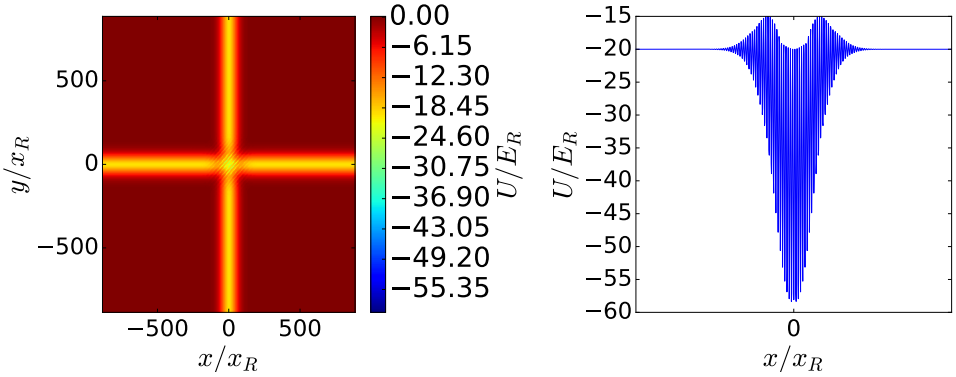

(A) 2D potential (B) 1D potential

FIGURE 3.1: 2D(A) and 1D(B) potential of the beam-splitter.

3.1 Band-Gaps Calculations

The first step to analyse the splitting behaviour of our beam-splitter in one dimensions is to calculate the band-gaps, for which the method is shown in Sec. 2.2[49, 97] where the solution for the Mathieu characteristic exponent, κ, is given in Eq. 2.36

which for a angle of $\theta = 90°$, is in recoil units defined in the Sec.1.1.6

$$\kappa(x) = \frac{\arccos(1 - \Delta\left(\kappa = 0, x\right)\left(1 - \cos\left(2\pi\sqrt{\zeta(x)}\right)\right))}{\sqrt{2}\,\pi}, \tag{3.1}$$

where

$$\Delta\left(0, x\right) = \det(A_M(\kappa = 0), x), \tag{3.2}$$

$$A_M = \begin{pmatrix} 1 & \xi_{-N} & & & \\ \xi_{-N+1} & 1 & \xi_{-N+1} & & \\ & \ddots & \ddots & \ddots & \\ & & \xi_{N-1} & 1 & \xi_{N-1} \\ & & & \xi_N & 1 \end{pmatrix}, \tag{3.3}$$

using

$$\xi_l(x) = \frac{-U_G(x)\epsilon}{4\left(\left(\frac{\kappa}{\sqrt{2}} + l\right)^2 - \zeta(x)\right)}, \tag{3.4}$$

and

$$\zeta(x) = \frac{U_G(x)A(x) + E}{2}, \tag{3.5}$$

where E is the energy. For $U_G(x)$ and $A(x)$ we look at the cross-section of the beam-splitter, Eq. 2.8 which is given by

$$U(x) = -U_G(x)[A(x) + \varepsilon\cos(k_R x)], \tag{3.6}$$

where

$$U_G(x) = -2U_0 e^{-\left(\frac{x^2}{\omega_0^2}\right)}, \tag{3.7}$$

$$A(x) = \cosh\left(\frac{x^2}{w_0^2}\right). \tag{3.8}$$

From these expressions we can calculate the band-gaps as these are the imaginary solutions for κ, which correspond to barriers through which the atoms must tunnel. Also, we need to calculate $\det(A_M(\kappa = 0), x)$ where A_M is a very large matrix, see Fig. 3.2 for an example of how the determinant is calculated over a variety of l values. However, the solution can be approximated by giving it a finite size as the solution for the matrix starts to converge for increasing its size. Thus it has been found that it is enough to let l for $\xi_l(x)$ vary from $l = -10$ to $l = 10$.

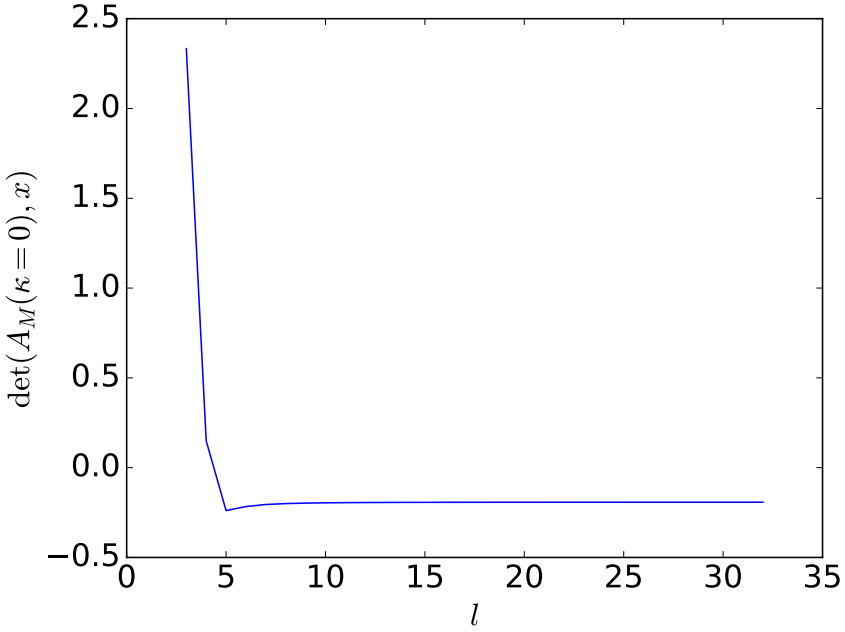

FIGURE 3.2: Shows an example solution of $\det(A_M(\kappa=0),x)$ for increasing matrix sizes. This parameters are for this example are $v = 1v_R$, $\varepsilon = 0.25$, $U_0 = -20E_R$ and $\omega_0 = 15\mu m$. The solution starts to converge before $l = 10$.

3.1.1 Band-Gaps' Structure

It is now necessary to look at the parameters that will vary in our calculations. These are the velocity of the atoms and the polarisation of the lasers. The velocity of the atoms is varied from $v = 0$ to $v = 6v_R$ with a step size of $0.1v_R$ given us 61 different velocities. The same is done for the polarisation which goes from $\varepsilon = 0$ to $\varepsilon = 1$ in 0.05 steps having 21 different values. The energy of the atoms is $E = T + V$, where T is the kinetic energy and V the potential. For the incident wave the kinetic energy is $T = \frac{k_0^2\hbar^2}{2m}$, which is in recoil units $T = \frac{\frac{k_0^2\hbar^2}{2m}}{E_R} = \frac{k^2}{k_R^2} = \frac{v^2}{v_R^2}$, allowing us to easily calculate it from just the atom velocity. The potential energy comes from the depth of the waveguide U_0, which is $U_0 = -20E_R$ for this case. The other laser parameters are the wavelength of $\lambda = 1064nm$ and the variance of the beam $\omega_0 = 15\mu m$.

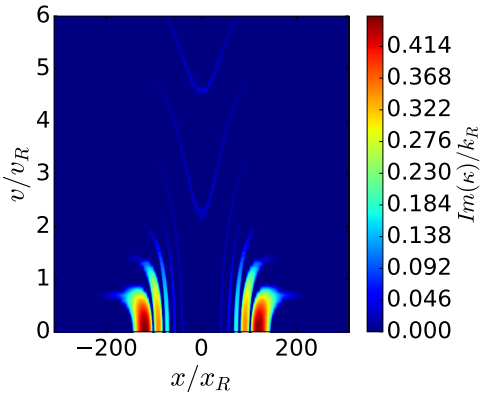

(A) Band-Gap Structure for $\varepsilon = 0.25$

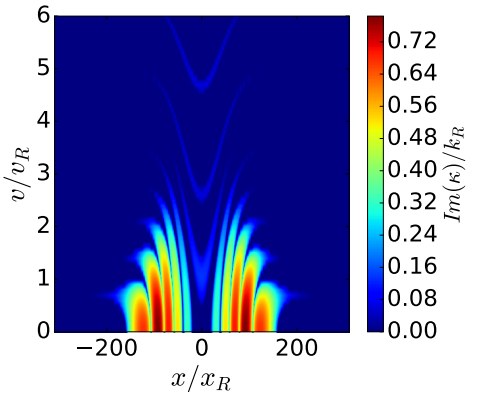

(B) Band-Gap Structure for $\varepsilon = 0.5$

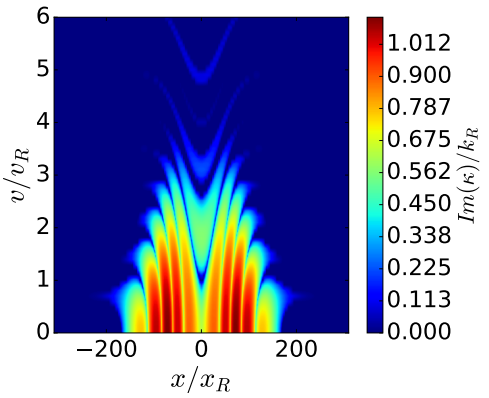

(C) Band-Gap Structure for $\varepsilon = 0.75$

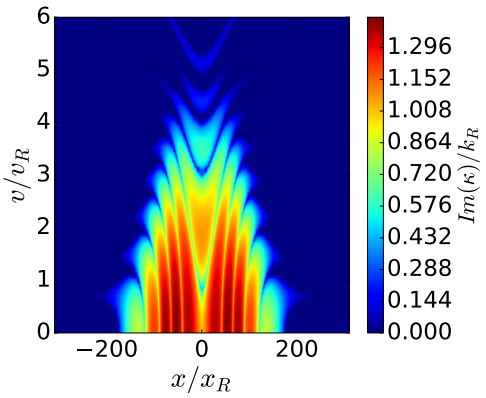

(D) Band-Gap Structure for $\varepsilon = 1$

FIGURE 3.3: These Figures show the band-gap structure for $\varepsilon = 0.25$(A), $\varepsilon = 0.5$(B), $\varepsilon = 0.75$(C) and $\varepsilon = 1$ (D). By increasing the polarisation we increase the strength, width and number of band-gaps. The other parameters for these figures are a potential depth of $U_0 = -20E_R$, a laser variance of $\omega_0 = 15\mu m$, a wavelength for the lasers of $\lambda = 1064nm$ and angle of $\theta = 90°$.

From these values, we can calculate now the band-gaps via Eq. 3.1. Selected examples of these solutions, together with their potentials can be seen in Fig. 3.3. The examples show four different band-gaps structures for polarisation of $\varepsilon = 0.25$(3.3a), $\varepsilon = 0.5$(3.3b), $\varepsilon = 0.75$(3.3c) and $\varepsilon = 1$(3.3d). For $\varepsilon = 0.25$ the band-gaps are the strongest for velocities ranging from $v = 0$ to roughly $v = 1v_R$ as there are 8 distinct band-gaps through which atoms need to tunnel. Furthermore, none of these band-gaps are in the centre of the beam-splitter. Thus leading to non-central splitting. However, central splitting is preferable as this allows for easier recombination. Hence, the best position for splitting would be roughly for $v = 2v_R$ or $v = 5v_R$. However, it is also undesirable for the atoms to travel through more than one band-gap as this will lead to atoms being reflected back and forth between the band-gaps and thus creating distortion in the outcoming atomic wave-packet and thus only $v = 5v_R$ is a good choice. The next polarisation is $\varepsilon = 0.5$. Looking at this it is becoming clear that the band-gaps for the lower polarisation have become stronger and new ones have appeared. A velocity of $v = 5v_R$ is the preferred solution for this case as well. From looking at $\varepsilon = 0.75$ and $\varepsilon = 1$ we see that the number and strength of the band-gaps are directly related to the polarisation. However, for band-gaps already

present at lower velocities their position does not really change, only their width changes and strength. Thus a good choice of splitting velocity for our chosen region would be $v = 5v_R$. From this, we need to calculate the transmission probability via Eq. 2.37, which can be seen in Fig. 3.4.

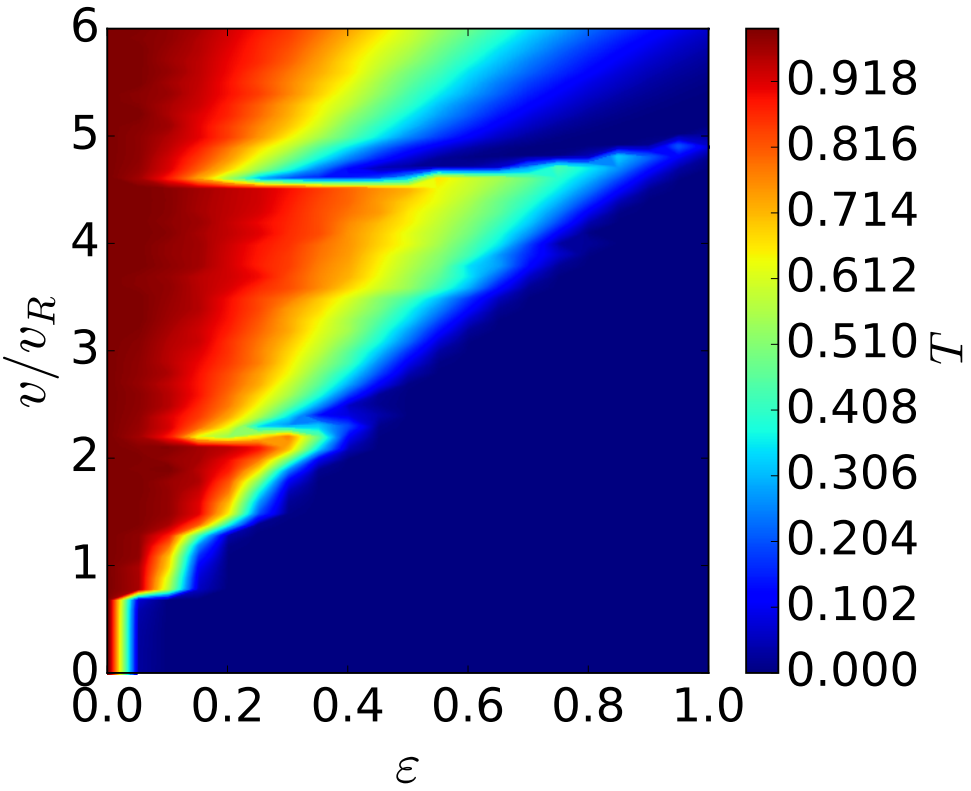

FIGURE 3.4: The transmission probability as a function of the atom velocity v and the polarisation ε calculated directly from the band-gaps. The parameters for these figures are a potential depth of $U_0 = -20E_R$, a laser variance of $\omega_0 = 15\mu m$, a wavelength for the lasers of $\lambda = 1064nm$ and angle of $\theta = 90°$.

This figure clearly demonstrates the increased strength and width of the band-gaps as we increase the polarisation, which leads to a reduction in the transmission probability. Also, the spike structure comes clearly from the areas in the band-gap structure where there are only weak band-gaps. To find the most suitable splitting parameters we need to use the band-gap structure, Fig. Fig. 3.3 and the transmission probability together Fig. 3.4. By picking suitable parameters for a roughly $50 : 50$ of the input probability, two examples would $v = 5v_R$ and $\varepsilon = 0.5$ and $v = 4v_R$ and $\varepsilon = 0.75$. Next, we look at the band-structure to see the position and number of the band-gaps. The most desired band-gap is a single central one. An example would be in Fig. 3.3c for the velocity $v = 5v_R$ and polarisation $\varepsilon = 0.5$, where the splitting would happen at the bottom of the v shape band-gap. Hence these parameters would make the ideal splitting choices, while the splitting from the parameters $v = 4v_R$ and $\varepsilon = 0.75$ would go through 3 band-gaps, see Fig. 3.3d each of which split the wave, thus creating a multitude of smaller waves.

3.1.2 Band-Gaps with Filling

Besides the previously discussed beam-splitter we can also create a beam-splitter with an additional third laser. The reasoning behind this is going to be discussed in the next chapter in Sec 4.7. However, to analyse the band-gaps we first need to look at our beam-splitter potential, where we set $U_G(x)$ to U_G, $A(x)$ to A and $f(x)$ to f, where f is the potential from the third laser, as they vary little locally in comparison to the fringes which create the band-gaps, with

$$f(x) = -FU_0 e^{-2\frac{x^2}{w_0^2}}, \tag{3.9}$$

and F is the strength of the third laser and it can be varied between 0 and 1. Giving us

$$U(z) = -U_G[A + \varepsilon\cos(q_R z)] + f = \sum_p \tilde{U}_p e^{ipq_R z}. \tag{3.10}$$

To solve this we need to make a change in variables to $z' = q_R z$

$$U(z') = -U_G[A + \varepsilon\cos(z')] + f = \sum_p \tilde{U}_p e^{ipz'}, \tag{3.11}$$

where

$$\tilde{U}_p = \frac{1}{2\pi}\int_{-\pi}^{\pi} U(z)e^{-ipz'}dz', \tag{3.12}$$

which is solved like the case without filling in Sec. 2.2. Giving us for $p = 0$

$$\tilde{U}_0 = -U_G A + f, \tag{3.13}$$

$p = 1$

$$\tilde{U}_1 = \frac{-U_G\varepsilon}{2}, \tag{3.14}$$

and $p = -1$

$$\tilde{U}_{-1} = \frac{-U_G\varepsilon}{2}. \tag{3.15}$$

For all other values of p

$$\tilde{U}_p = 0 \quad for \;\; |p| > 1. \tag{3.16}$$

Now we can create the Matrix to solve Eq. 2.21

$$M = \begin{pmatrix} b_{-N} & u & & & \\ u & b_{-N+1} & u & & \\ & \ddots & \ddots & \ddots & \\ & & u & b_{N-1} & u \\ & & & u & b_N \end{pmatrix}, \tag{3.17}$$

with $b_L = E_Q(q/q_R+l)^2 - U_G A + f$, $u = -U_G\varepsilon/2$ and $E_Q = \hbar^2 q_R^2/2m = 4E_R \sin^2\left(\frac{\theta}{2}\right)$. The matrix Eq. 3.17 is then arranged into

$$\mathbf{A}_M \cdot \mathbf{V} = 0, \tag{3.18}$$

with

$$A_M = \begin{pmatrix} 1 & \xi_{-N} & & & \\ \xi_{-N+1} & 1 & \xi_{-N+1} & & \\ & \ddots & \ddots & \ddots & \\ & & \xi_{N-1} & 1 & \xi_{N-1} \\ & & & \xi_N & 1 \end{pmatrix}, \tag{3.19}$$

where $\xi_l = \frac{-U_G\epsilon}{2E_Q\left(\left(\frac{\kappa}{q_R}+l\right)^2-\zeta\right)}$, $\zeta = \frac{U_G A - f + E}{E_Q}$. This can also be written in recoil units $\xi_l = \frac{U_G\epsilon}{8\sin^2\left(\frac{\theta}{2}\right)\left(\left(\frac{\kappa}{4\sin^2\left(\frac{\theta}{2}\right)}+l\right)^2-\zeta\right)}$, $\zeta = \frac{U_G A - f + E}{4\sin^2\left(\frac{\theta}{2}\right)}$. The solution for this equation is Eq. 3.1 for $\theta = 90°$. Using $U(x)$ and $A(x)$, given by Eq. 3.7 and 3.8, we can calculate the band-gaps, for the potential depth of $U_0 = -20E_R$, the laser width $\omega_0 = 15\mu m$ and the laser wavelength of $\lambda = 1064nm$. The velocity of the atoms is varied from $v = 0$ to $v = 6v_R$ in $0.1v_R$ increments, while the polarisation is varied from $\varepsilon = 0$ to $\varepsilon = 0$ in 0.05 increments and the filling goes from $F = 0$ to $F = 1$ in 0.1 steps. To see how the band-gaps themselves change we set the polarisation constant to $\varepsilon = 0.5$. The result of these band-gaps can be seen in Fig. 3.5. In A(3.5a) we see the band-gaps for $F = 0.1$ and when we increase this to $F = 0.2$ as seen in B(3.5b), we notice that the strength and area of the band-gap structure increases for the lower half of the velocity. If we increase the filling even more the band-gaps start to merge. However, their overall shape also changes which can best be seen in the V shaped band-gaps in the upper spectrum the the observed velocity which have been forced together for high fillings as seen in Fig. 3.5f.

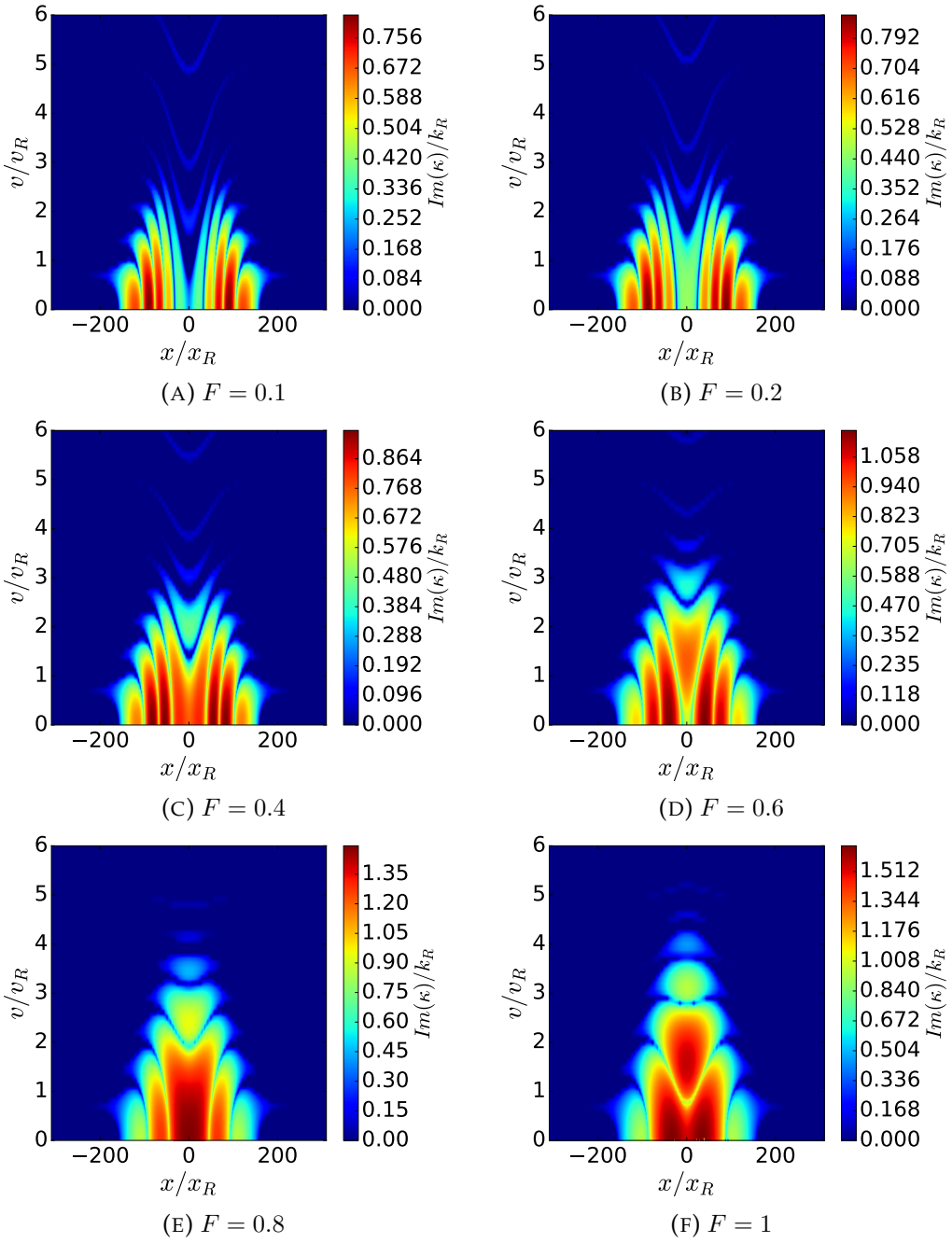

(A) $F = 0.1$ (B) $F = 0.2$

(C) $F = 0.4$ (D) $F = 0.6$

(E) $F = 0.8$ (F) $F = 1$

FIGURE 3.5: These figures show how the band-gap structure changes when the filling is increased. The overall shape changes significantly from filling as the band-gaps for lower velocities merge while the ones for higher velocity get squished, allowing only narrower areas for the atoms to travel trough. The parameters for these calculations are potential depth of $U_0 = -20E_R$, the laser width $\omega_0 = 15\mu m$, the laser wavelength of $\lambda = 1064nm$ and a polarisation of $\varepsilon = 0.5$.

From these we can then calculate the transmission probabilities as shown in Fig. 3.6. In these we see that the areas of equal transmission and reflection get reduced when the filling is increased. Instead we see a stronger contrast between total reflection and total transmission with a smaller viable parameter range for equal splitting.

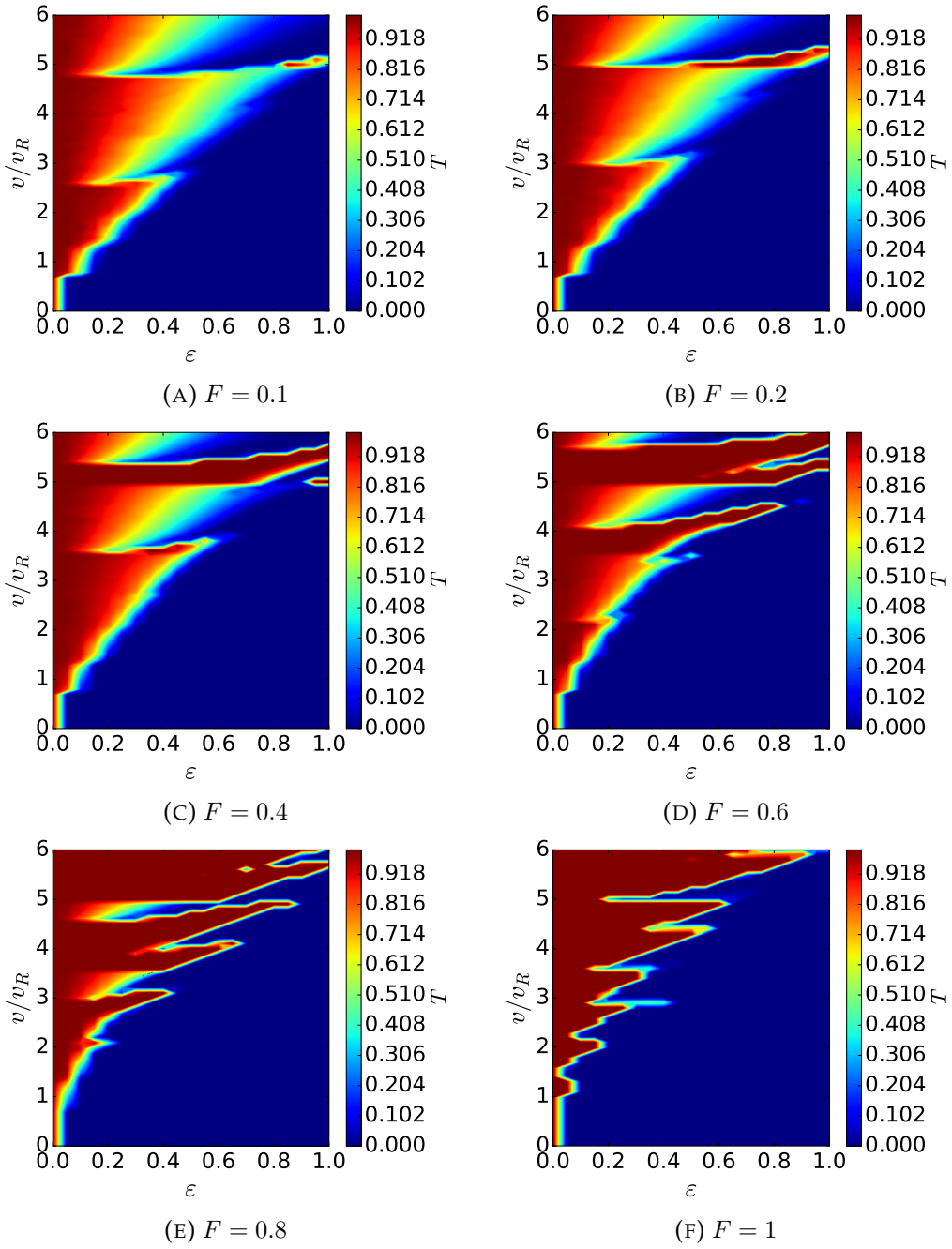

(A) $F = 0.1$ (B) $F = 0.2$

(C) $F = 0.4$ (D) $F = 0.6$

(E) $F = 0.8$ (F) $F = 1$

FIGURE 3.6: These figures show how the transmission probabilities change when filling is introduced. The filling generally changes the areas of the reflection and transmission. Furthermore, it reduces the area of equal splitting drastically. Leaving, only narrow margins for a high filling.

3.2 Standing Waves

The calculations for the band-gaps requires a sufficient number of fringes in the beam-splitter to work. However, as this is parameter dependent on the laser wavelength, we might not have of them. Therefore, we are using the method described in the Sec. 2.3.5 to calculate the transmission probability for standing waves and compare them to the cases discussed in the previous section to see if the band-gap

method is suitable for our parameters[104]. The wavenumber of the transmitted wave is given by Eq. 2.104 which is in recoil units and a potential depth U_0

$$k = \sqrt{(E + U_0)}\,. \tag{3.20}$$

From this we will integrate backwards through the beam-splitter with has the potential

$$U(x) = 2U_0 e^{-\left(\frac{x}{\omega_0}\right)^2}\left(\cosh\left(\left(\frac{x}{\omega_0}\right)^2\right) + \varepsilon\cos(x)\right) - FU_0 e^{-2\left(\frac{x}{\omega_0}\right)^2}, \tag{3.21}$$

which is a one-dimensional cut through the two-dimensional potential, Eq. 2.8, where the lasers cross at $\theta = 90°$ in recoil units. Thus our f and g functions to integrate backwards via the Runge–Kutta method are

$$g_\psi(\psi, z, x) = z\,(x)\,, \tag{3.22}$$

$$g_z(\psi, z, x) = (U(x) - E)\,\psi\,(x)\,, \tag{3.23}$$

$$\tag{3.24}$$

where the energy of the atoms is

$$E = v^2 + U_0, \tag{3.25}$$

in recoil units. The numerical value of the wave number and the velocity are the same when one uses recoil units. From this we calculate now the transmission probability via Eq. 2.121.

3.2.1 Parameters: $U_0 = -20E_R$ and $\omega_0 = 15\mu m$

The first case we are looking at is the one where the depth of the laser beam potential is $U_0 = -20E_R$, their variance is $\omega_0 = 15\mu m$, filling of $F = 0$ and their wavelength is $\lambda = 1064nm$. For these calculations we vary the velocity of our atoms from $v = 0v_R$ to $v = 6v_R$ in a step size of $0.1v_R$ and the polarisation is also varied from $\varepsilon = 0$ to $\varepsilon = 1$ with a step size of 0.01. This leads to the transmission probability as shown in Fig. 3.7. This figure clearly shows that there is a generally linear correlation for areas of good splitting probabilities with regards to the velocity and polarisation. However, the region of approximate 50:50 splitting is not smooth. Nonetheless, due to this nature a Gaussian wave-packet should smooth out the transmission probability as it can be understood as a sum of standing waves and thus its transmission probability can be thought of as an average over all the relevant standing wave transmission probabilities. Comparing this result with the one from the band-gaps we see a stark contrast as they are distinct. Thus we assume that this beam-splitter has insufficient fringes to actually calculate the transmission probability via the band-gaps.

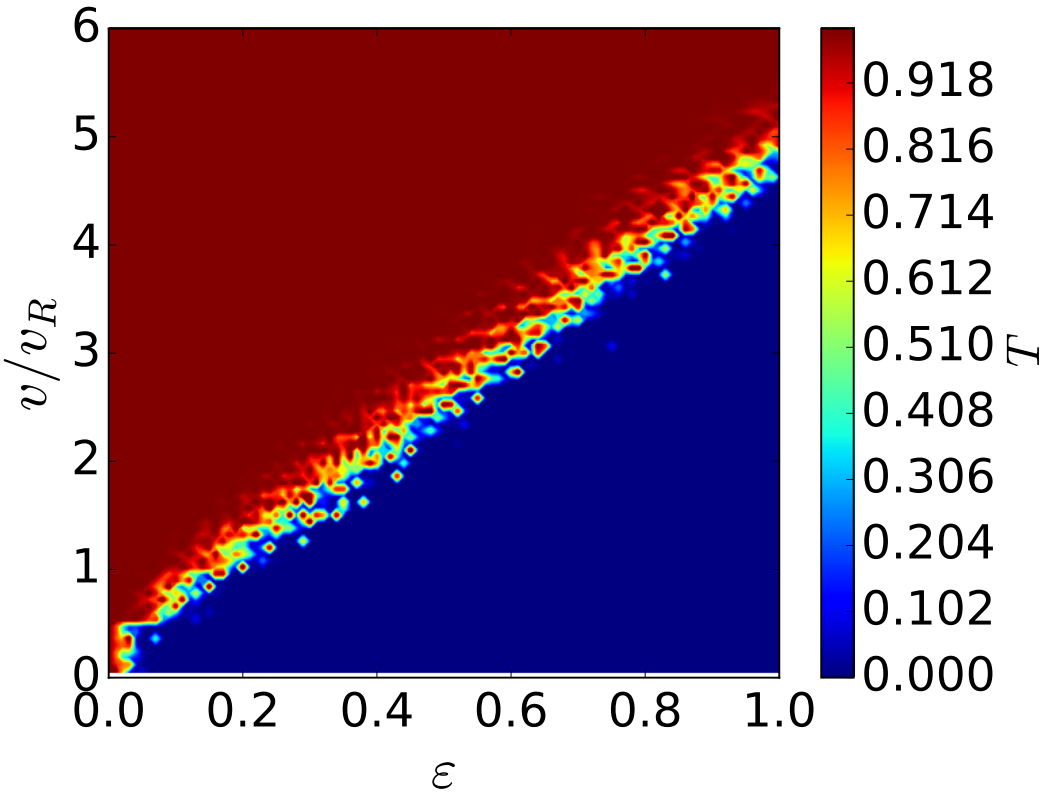

FIGURE 3.7: This figure shows the transmission probability for a standing for the parameters $U_0 = -20E_R$, $\omega_0 = 15\mu$, $F = 0$ and $\lambda = 1064nm$. The areas of total transmission and total reflection are separated by an approximately linear boundary containing fine-grained features of intermediate reflection and transmission.

Furthermore, we have only looked at the case with no filling. Therefore we are going to look at the transmission probabilities for the same parameters except that we vary the filling from $F = 0$ to $F = 1$ in 0.1 increments. The result of this can be seen in Fig. 3.8. The sub figures of it are Fig. 3.8a for $F = 0.2$. It is still very similar to $F = 0$. However, a small spike forms in the top right and corner around $v = 5v_R$ and $\varepsilon = 0.9$. From here with increasing f we see that the number, and distinctiveness of these spikes increase as shown by the Fig.3.8b, 3.8c, and 3.8d, which have the fillings of $F = 0.4$, $F = 0.6$ and $F = 1.0$ respectively. Another difference is that the regions for total transmission and total reflection stop being separated by a straight line and become separated by a curve. As seen when one compares Fig. 3.8d and Fig. 3.7. This is due to the nature of the filling, which is a Gaussian potential. As such its effects are stronger in the central region than the edges of the beam-splitter. Therefore, the linear separation becomes curved as different regions inside the beam-splitter have a different impact on the transmission probability depending on the velocity of the atoms.

These spikes have a similar to the example of the parabolic potential, see Fig. 2.10. Hence they could be understood to come from resonant frequencies.

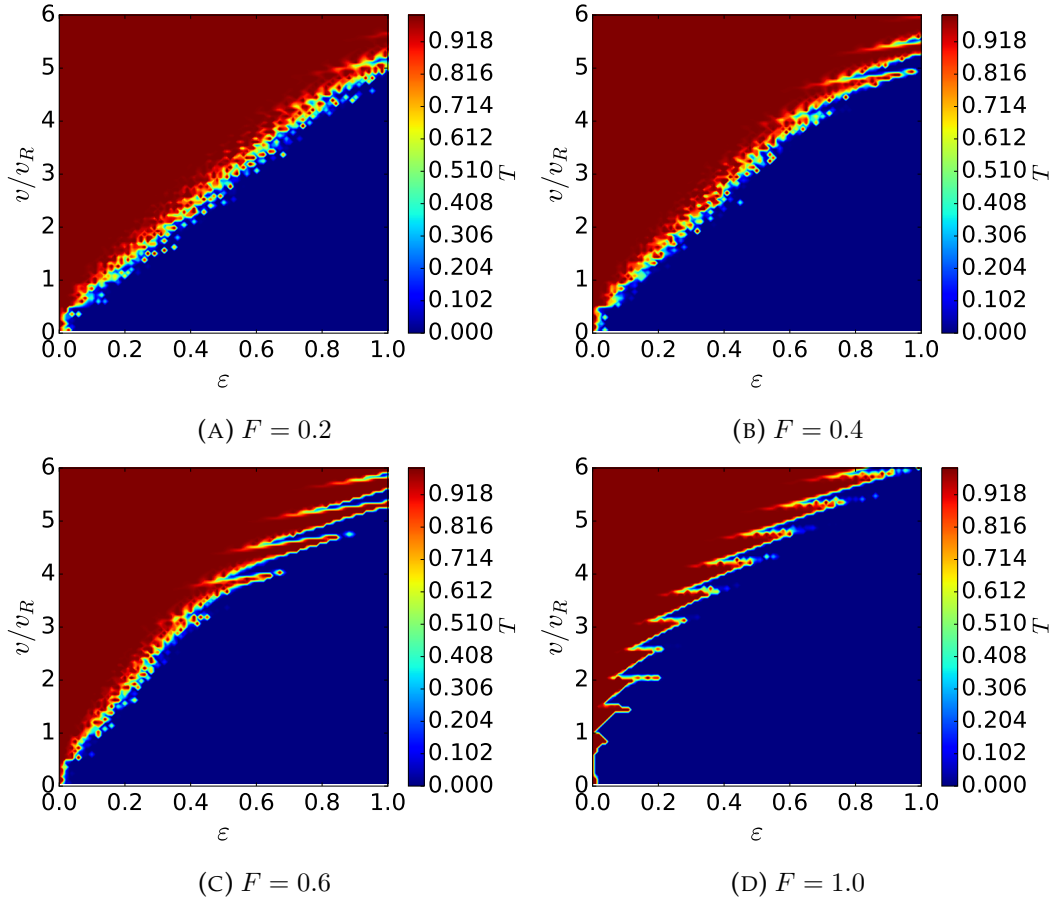

(A) $F = 0.2$ (B) $F = 0.4$

(C) $F = 0.6$ (D) $F = 1.0$

FIGURE 3.8: These figures show the transmission probabilities for the filling, $F = 0.2$(A), $F = 0.4$(B), $F = 0.6$(C) and $F = 1.0$(D). They show clearly that by increasing the the filling the linear boundary between total reflection and total transmission starts developing spikes and the separation between the areas becomes rounded. The other parameters are $U_0 = -20E_R$, $\omega_0 = 15\mu m$ $\lambda = 1064nm$.

3.2.2 Atoms Inside the Beam-Splitter

Further, we could calculate the probability of the wave-function inside the beam-splitter via

$$BS = \int_{-x_m in}^{x_m ax} \psi^*(x)\psi(x)dx. \tag{3.26}$$

It should be noted that we are dealing with plane waves and thus this probability would not be normalised. Nonetheless, we could gain some information by comparing it with the probability of the incident wave over the same area without a potential, which is labelled as P_I. From this ratio, we could see an increase or decrease of the number of atoms inside the beam-splitter. Looking at the corresponding graph, see Fig. 3.9 and comparing to the one for the transmission Fig. 3.7 we see that the area of total transmission is homogeneous, which is to be expected as the wave simply travels through the beam-splitter without being altered. More interesting is the region for total reflection. Cases with a value below unity can be understood to

have the wave reflected shortly after entering the beam-splitter, while values above unity indicated later and/or more complex reflection behaviour from various areas. Furthermore, the spike pattern that was only becoming visible for higher filing is shown here, showing a resonance depending on the velocity of the atoms and the fringe spacing of the optical lattice. However, these calculations do not provide any additional information regarding the determination of suitable splitting parameters and thus are will not be investigated further.

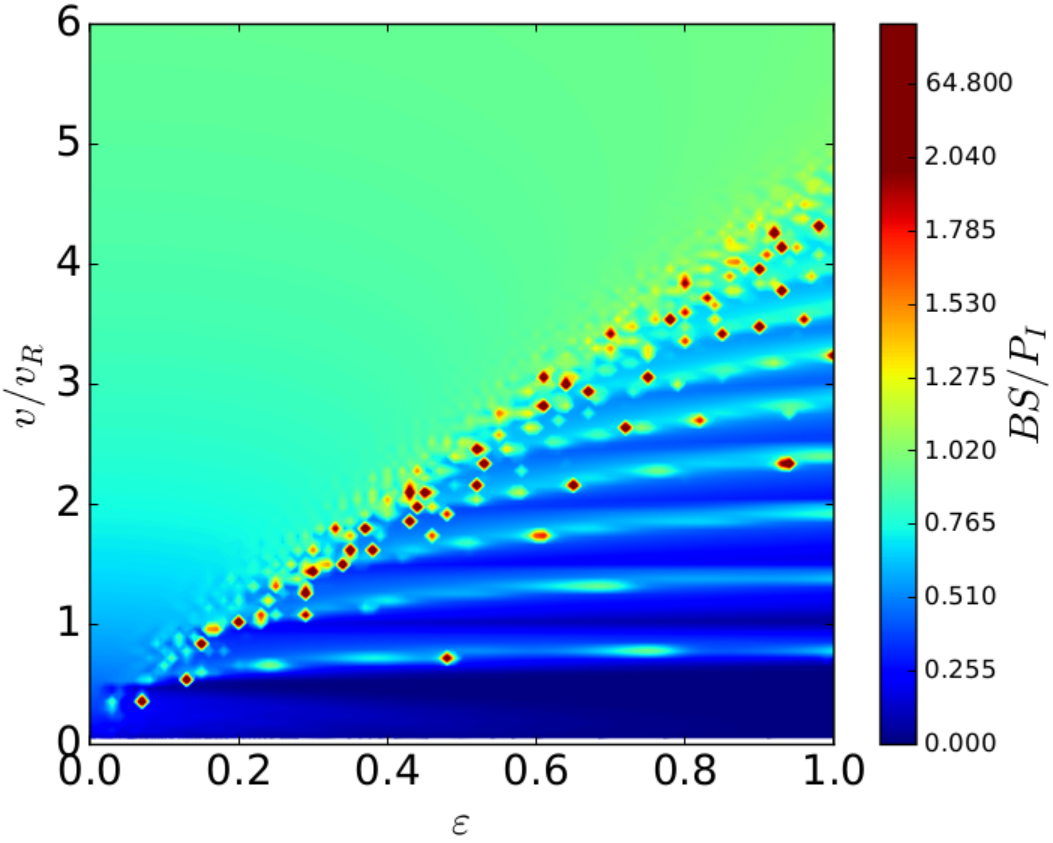

FIGURE 3.9: This figure shows the increase of the wave inside the beam-splitter for the parameters $U_0 = -20E_R$, $\omega_0 = 15\mu$, $F = 0$ and $\lambda = 1064nm$.

3.2.3 Narrower Waveguides

Besides the filling there are other methods to change the splitting behaviour. For this we change the depth U_0, width ω_0 and the wavelength of our $\lambda = 720nm$. The reasons behind these changes can be found in Sect. 4.5. It is not possible to use the band-gap method for these parameters as the numbers of fringes will be reduced drastically and it is one of the reasons for the need to solve the transmission probability for arbitrary potentials, discussed previously in this section.

Parameters: $U_0 = -2E_R$ and $\omega_0 = 1\mu m$

The first case we are focusing on is the case where $U_0 = -2E_R$ and $\omega_0 = 1\mu m$. For these calculations we are going to vary the velocity from $v = 0v_R$ to $v = 5v_R$, the polarisation from $\varepsilon = 0$ to $\varepsilon = 1$ and the filling $F = 0$ to $F = 1$, which are increased in $0.5v_R$, 0.05 and 0.1 increments respectively. Resulting in the transmission probabilities seen in Fig. 3.10, where A is for $F = 0$, it shows a very roughly linear relation for areas of 50:50 splitting. When of is increased this relation becomes more rounded as seen in B, C, and D which are the transmission probabilities for $F = 0.4$, $F = 0.6$ and $F = 1$ respectively. They also have spike that form for higher filling values but not as strong as in the previous case with $U_0 = -20E_R$, $\omega_0 = 15\mu m$ and $\lambda = 1064nm$. Furthermore, there are smaller regions of total transmission inside the total reflection are due to resonant frequencies.

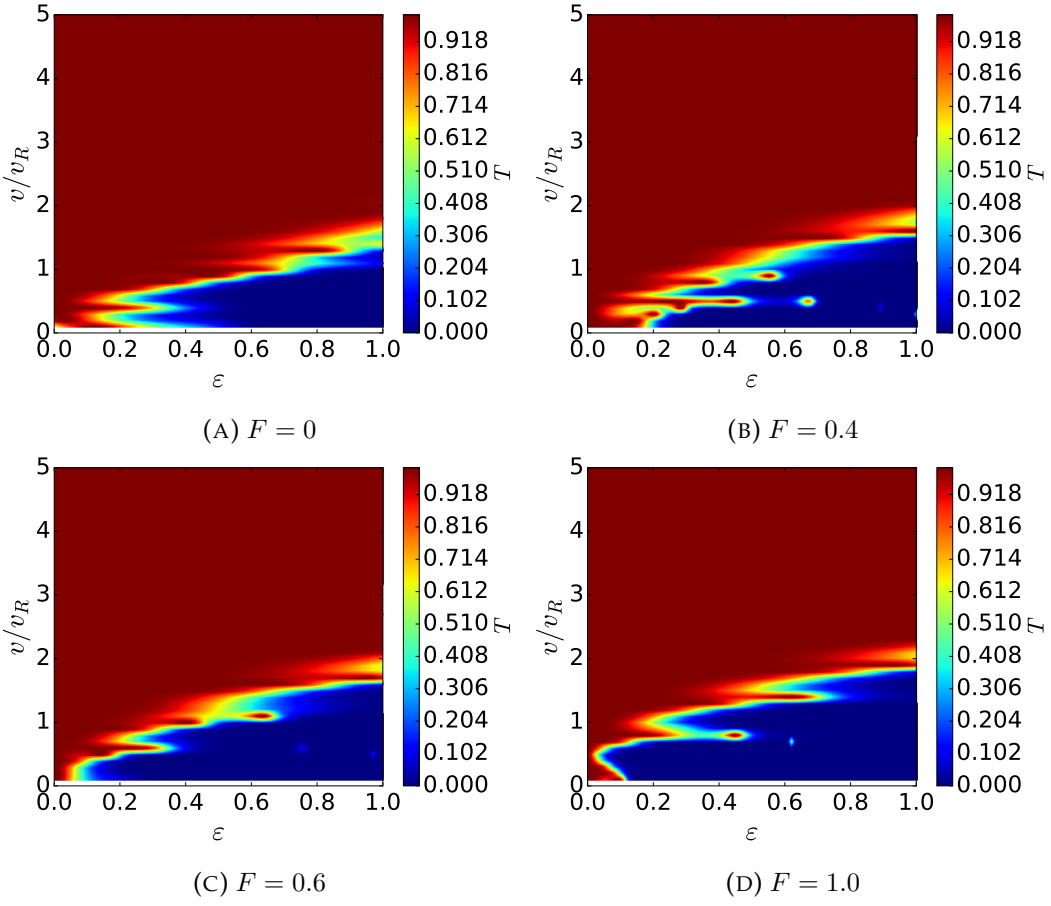

(A) $F = 0$ (B) $F = 0.4$

(C) $F = 0.6$ (D) $F = 1.0$

FIGURE 3.10: These figures show the transmission probability for $U_0 = -2E_R$ and $\omega_0 = 1\mu m$, for the filling, $F = 0$(A), $F = 0.4$(B), $F = 0.6$(C), $F = 1.0$(D). There is a rough straight line separating the case where $F = 0$. This becomes more curved when the filling is increased as shown by comparing A and F directly. The other parameters are $U_0 = -2E_R$, $\omega_0 = 1\mu m$ $\lambda = 720nm$.

Parameters: $U_0 = -2E_R$ and $\omega_0 = 1.5\mu m$

For the next case we increase the width from $\omega_0 = 1\mu m$ to $\omega_0 = 1.5\mu m$. The rest of the parameters stay the same. For this case as well we will vary the velocity $v = 0v_R$ to $v = 5v_R$, the polarisation from $\varepsilon = 0$ to $\varepsilon = 1$ and the filling $F = 0$ to $F = 1$, with the step size for the velocity being $v = 0.5v_R$, for the polarisation 0.05 and the filling 0.1. Giving us the splitting probabilities in Fig. 3.11. The splitting probabilities do not change drastically from the case, where $\omega_0 = 1.5\mu m$. For this case as well the boundary between the total transmission and total reflection regions starts off linear and then becomes curved for increasing filling.

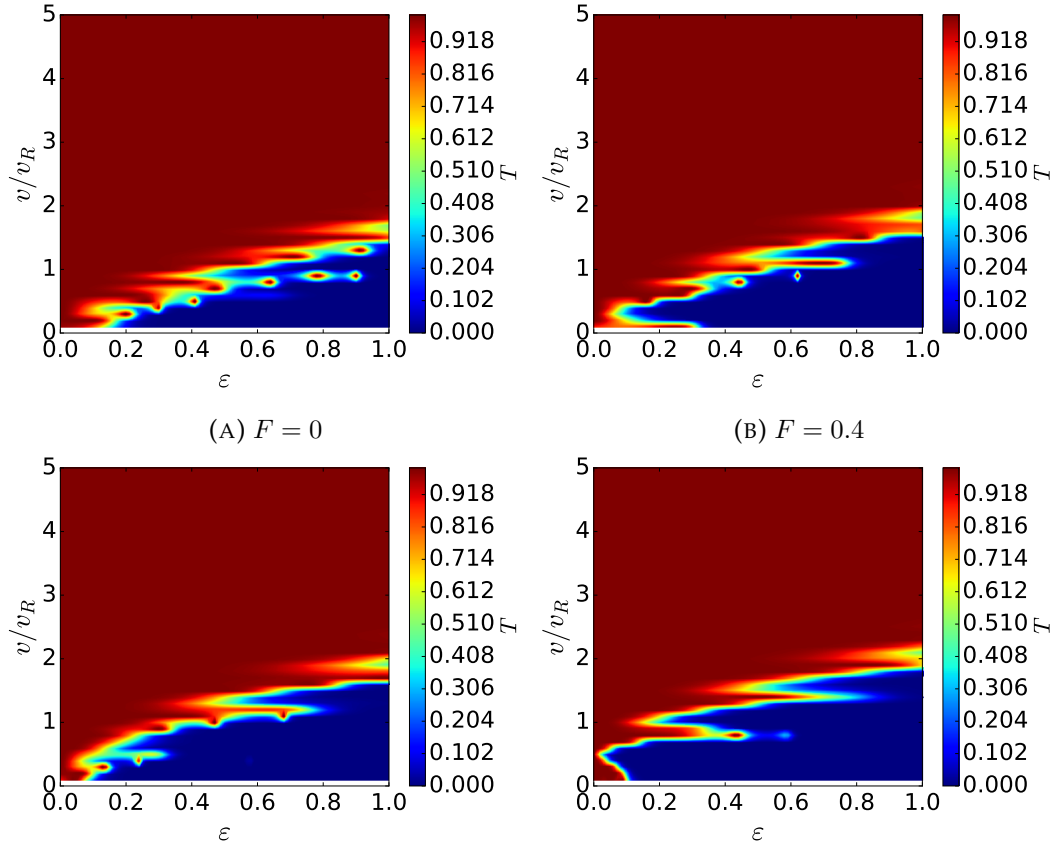

(A) $F = 0$ (B) $F = 0.4$

(C) $F = 0.6$ (D) $F = 1$

FIGURE 3.11: The transmission probabilities for the fillings, $F = 0$, $F = 0.4$, $F = 0.6$ and $F = 1$ are shown in A to E prospectively, while the other parameters are $U_0 = -2E_R$, $\omega_0 = 1.5\mu m$ $\lambda = 720nm$. There is a linear septation between the transmission in A which becomes a curved one when the filling is increased.

Parameters: $U_0 = -5E_R$ and $\omega_0 = 1\mu m$

In the previous case we increased the laser width from $\omega_0 = 1\mu$ to $\omega_0 = 1.5\mu$. In this case we go back to $\omega_0 = 1\mu$ but increase the potential depth of our beam-splitter from $U_0 = -2E_R$ to $U_0 = -5E_R$. The rest of the fixed and variable parameters stay the same. Giving us the transmission probabilities seen in Fig. 3.12. In comparison to the previous case this example allows for overall higher velocities for splitting. It

also has a linear separation for the reflection and transmission and low filling which becomes curved for higher fillings.

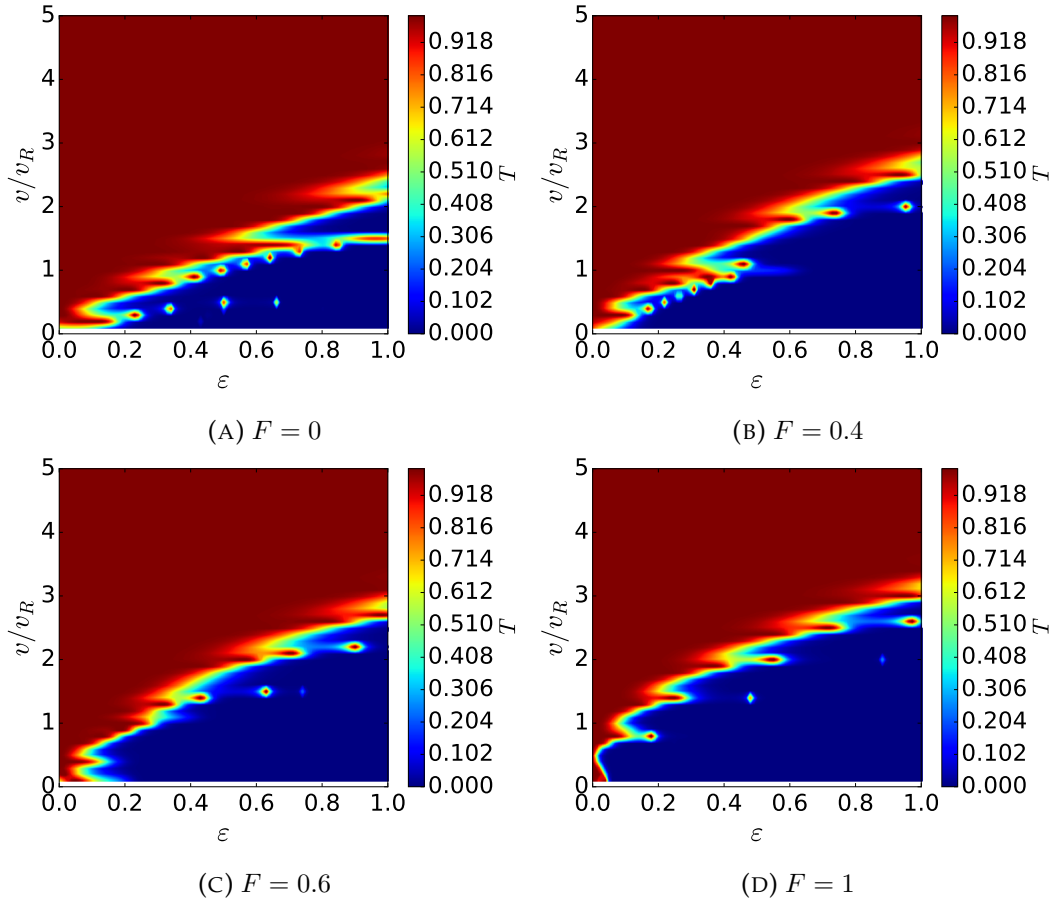

(A) $F = 0$ (B) $F = 0.4$

(C) $F = 0.6$ (D) $F = 1$

FIGURE 3.12: A to D show the transmission probabilities for the fillings $F = 0$ $F = 0.4$, $F = 0.6$ and $F = 1$. The other parameters are $U_0 = -2E_R$, $\omega_0 = 1.5\mu m$ $\lambda = 1064nm$. Here as well the see that the linear boundary between the transmission and reflection area becomes curved for higher filling.

3.3 Split-Step Fourier Method

Additionally, to the band-gaps analysis and the standing wave we can also calculate the propagation of a wave-packet through the beam-splitter, via the split-step Fourier method described in Sec. 2.3.3[100–102]. For this method we need to define a few parameters. Firstly, we need to set the limits of our simulation area so that the wave-function has enough room to properly propagate through the beam-splitter, which depends on the starting width of the wave-packet, position and velocity. The velocity is one of the main factors to determine how long the simulation will run. The others are the approximate final width, which comes from the diffusion of the free wave-packet and the requirement that the wave packet has left the beam-splitter region completely. The step size for the time is $\Delta t = 0.5\mu s$. Furthermore, the starting position of the wave-packet is chosen to be far enough away from the beam-splitter

that any overlap is negligible, but not too far away as this would result in an increase of the runtime. We also need to make sure that the k-space for our calculation is sufficiently large by considering the starting momentum and the maximum momentum it could get from the potential depth in the beam-splitter. Additionally, the separation between the datapoints in the position space is chosen so that there are at least 10 points for every period in the fringes.
The reflection,R and transmission,T probabilities can be obtained by integrating the probability density over the regions before and after the beam-splitter. In comparison to the standing wave some of the atoms can be trapped inside the beam-splitter, BS. Thus there are three regions to take into consideration to find the a viable region for splitting, the region for transmission, the beam-splitter and the region for the reflection. However, the overall probability of finding the wave in all the regions should be unity and thus we actually only need two. Hence it is a good way to check by calculating all three and make sure that they add to unity.

3.3.1 Splitting

For the splitting we begin with defining the actual parameters for our calculations. As in the previous sections our beam-splitter has a depth of $U_0 = -20E_R$, $\omega_0 = 15\mu m$, $\lambda = 1064nm$ and $\theta = 90°$. However, additionally to those we also need to examine the starting form of our wave-packet, which is a Gaussian of the form

$$\psi(x) = \frac{1}{\sigma\sqrt{\sqrt{\pi}}} e^{-\frac{(x-x_0)^2}{2\sigma^2}} e^{ikx}, \tag{3.27}$$

where k is the wavenumber which has the same numerical value as the velocity in recoil units, x_0 is the starting position, and σ is the variance of Gaussian. The starting position is automatically calculated by our program and this procedure will be shown in the appendix A. The variance for this calculation will be $10\mu m$. From these we can calculate now the propagation of a wave though the beam-splitter, where an example is given in Fig. 3.13 for $v = 3v_R$ and $\varepsilon = 0.6$.

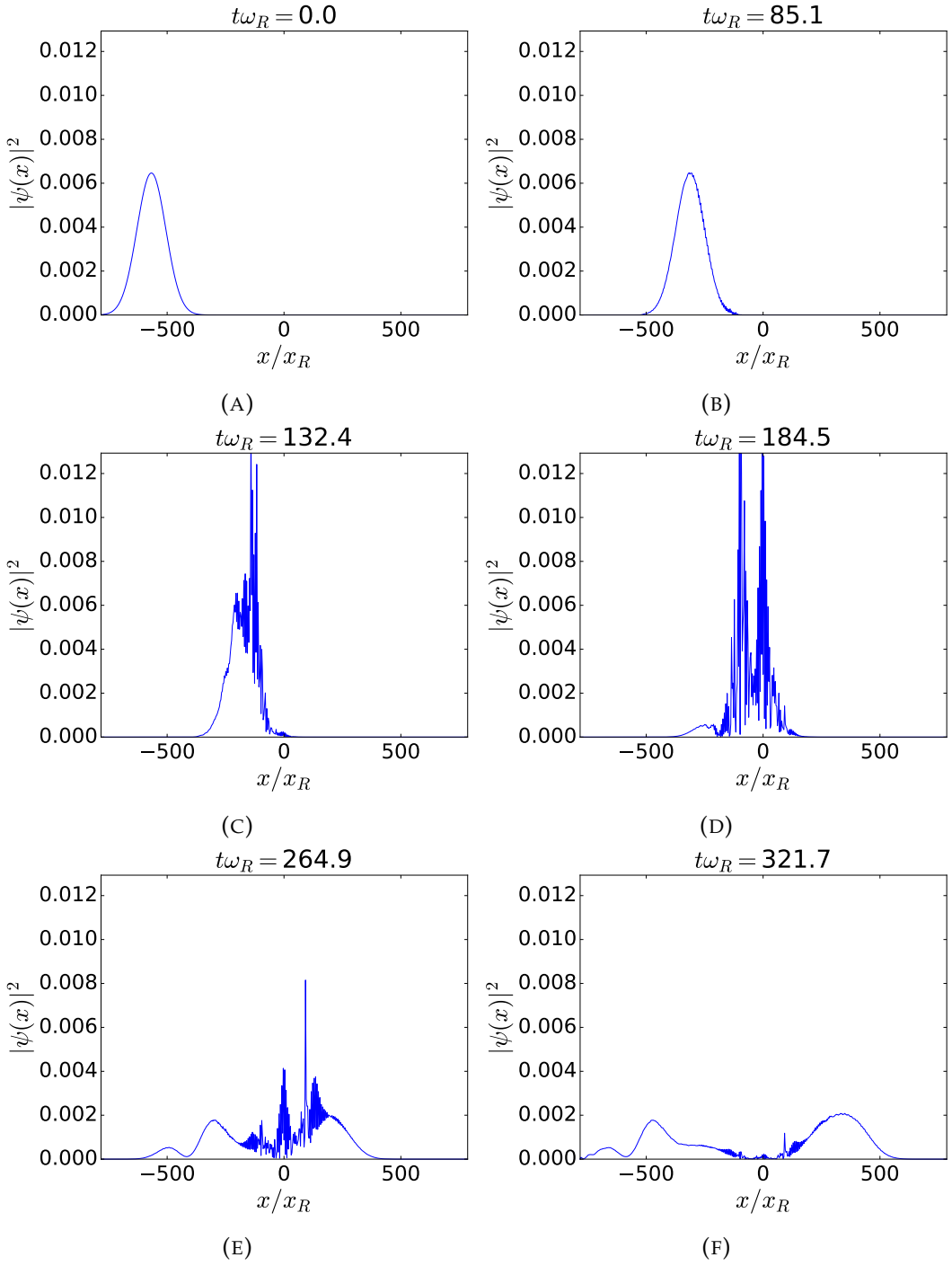

FIGURE 3.13: These figures show the evolution of the wave-packet through a beam-splitter, where the parameters are $v = 3v_R$, $\varepsilon = 0.6$, $U_0 = -20E_R$, $\omega_0 = 15\mu m$, $\lambda = 1064nm$, $\theta = 90°$, $F = 0$ and $\sigma = 10\mu m$. The wave starts off in A and then travels forwards until it reaches the beam-splitter at B. From this point on it propagates through the beam-splitter as shown in C, D, E and leaves it in F. The exiting wave-packets are slightly distorted but their overall shape is still reasonable. The reflected packet is more distorted and looks a bit like a superposition of multiple packets, whereas the transmitted packet is much more like a single packet.

In this A shows the starting position of the wave, which moves forward and starts interacting with the beam-splitter at B. Afterwards it travels through the beam-splitter

as seen in C,D,E, where the splitting starts to become visible at D. Finally leaving the beams-splitter at F. The exciting wave-packets are slightly distorted but have still overall Gaussian shapes. However, some of the wave gets stuck inside the beam-splitter. Similarly, to this example we will repeat this calculation for varying values of the velocity and polarisation, ranging from $v = 0.5v_R$ to $v = 5v_R$ and $\varepsilon = 0$ to $\varepsilon = 1$, respectively. The velocity is increased in $0.5v_R$ increments and the polarisation in 0.1 ones. From this we can compute the transmission probability and the probability of the atoms being trapped inside the beam-splitter shown in Fig. 3.14. This trapping is different to the standing wave as this is the probability of the atoms being getting trapped inside the beam splitter, while the one for the standing wave shows only an increase of atoms depending on the atom density of the input. Thus they cannot be compared. The part for the transmission look similar to the one from the standing wave seen in Fig. 3.7. Due to the nature of a Gaussian wave-packet being an superposition of standing waves the edges between transmission and reflection are smoothed out. Nonetheless, this is not the only factor that creates this smoother edge, the other one is the wide separation of datapoints. However, besides the transmission probability we need to take the fraction of trapped atoms into consideration and from this we see that the best value for the polarisation is in the region of $\varepsilon = 0.6$ to $\varepsilon = 0.8$. The corresponding velocity can then be picked from the transmission probability plot.

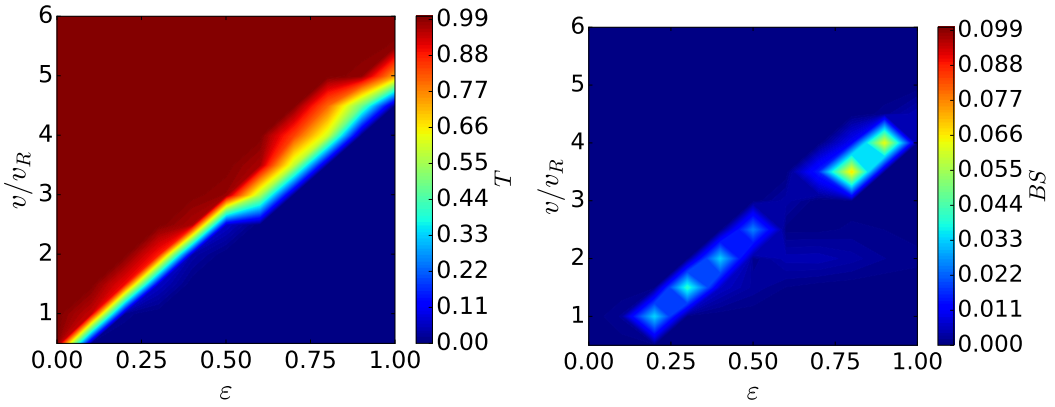

(A) Transmission (B) Beam-Splitter

FIGURE 3.14: These figures shows the transmission probability and the probability of trapped atoms for the a travelling wave-packet with the parameters, $\sigma = 10\mu m$, $U_0 = -20E_R$, $\omega_0 = 15\mu m$, $\lambda = 1064nm$, $\theta = 90°$, $F = 0$. The areas of total transmission and reflection are separated linearly, where one would find the 50:50 splitting ratio. The other tapped atoms show which areas to avoid and thus the best splitting without having atoms being stuck inside the beam-splitter is between $\varepsilon = 0.6$ and $\varepsilon = 0.8$.

3.3.2 Filler

We can expand on these calculation by introducing the the filling, which we will vary between $F = 0$ to $F = 1$ in 0.1 increments. For this we will then calculate the transmission probabilities via allowing the wave-packet to propagate through

the beam-splitter using the the split-step Fourier method. An example of this can be seen in Fig. 3.15, where we set the velocity to $v = 5v_R$, the polarisation to $\varepsilon = 0.6$ and the filling to $F = 1$. The wave-function is starts off in A and then travels towards the beam-splitter, B. Afterwards, it travels through the beam-splitter in C,D,E and leaves it in F. The exciting wave-functions have overall good shapes.

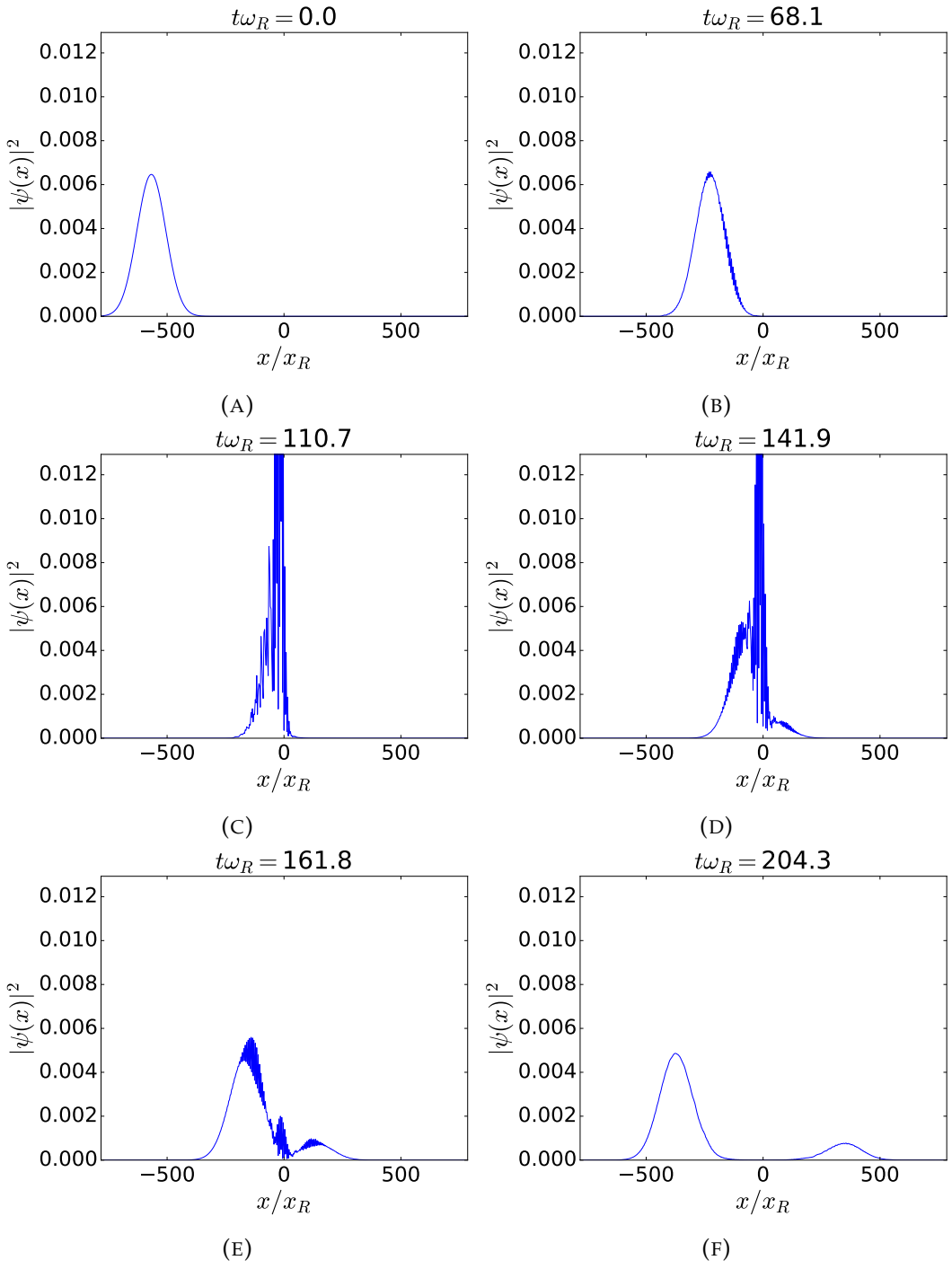

FIGURE 3.15: The wavefuntion propagates through the beam-splitter in alphabetical order: A→B→C→D→E→F. For the parameters $v = 5v_R$, $\varepsilon = 0.6$ $\sigma = 10\mu m$, $U_0 = -20E_R$, $\omega_0 = 15\mu m$, $\lambda = 1064nm$, $\theta = 90°$ and $F = 1$. The splitting is not equal in this case. However, the overall shape of the exiting wave-functions appear to be Gaussian.

From these we can calculate the transmission probabilities for a broad range of velocities, polarisation and fillings as discussed before. Giving us the Fig. 3.16f. These graphs show similarities to the standing waves case Fig. 3.8. Both of which show that the linear boundary between transmission and reflection becomes a curve when the filling is increased. However, it does not have the spikes due to the Gaussian and broad data points separation, as mentioned before.

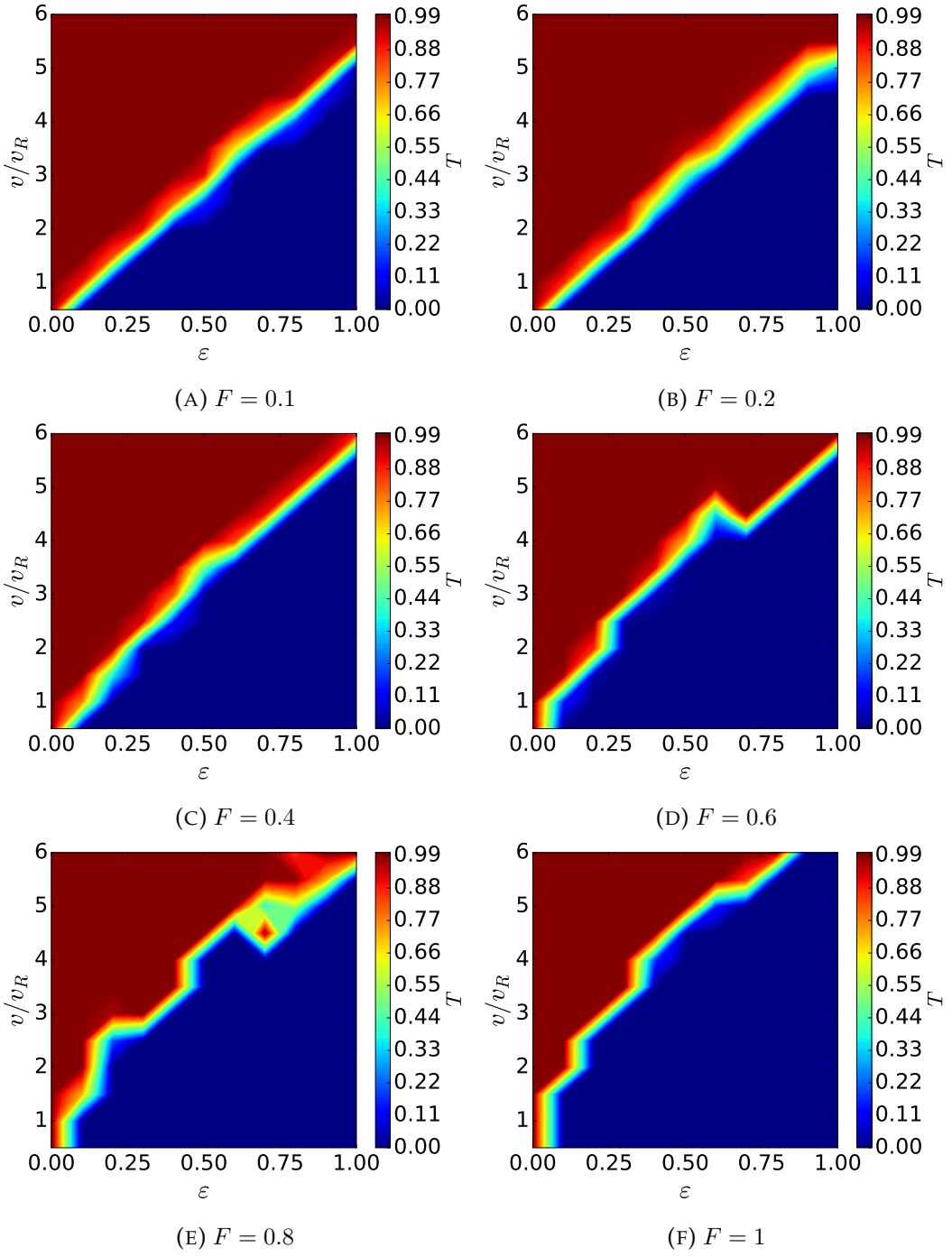

(A) $F = 0.1$ (B) $F = 0.2$

(C) $F = 0.4$ (D) $F = 0.6$

(E) $F = 0.8$ (F) $F = 1$

FIGURE 3.16: These figures show how the splitting behaviour for $\sigma = 10\mu m$, $U_0 = -20E_R$, $\omega_0 = 15\mu m$, $\lambda = 1064nm$ and $\theta = 90^\circ$, change when the filling is increased. The separation between transmission and reflection starts of linear and becomes more and more curved for higher filling.

Additionally, we also need to examine how many atoms are trapped inside the beam-splitter, see Fig. 3.17. In this we see that the area for which atoms are trapped gets reduced as we increase the filling, which is to be expected as the filling is there to reduce the potential depth and thus the atoms can exit the beam-splitter more easily.

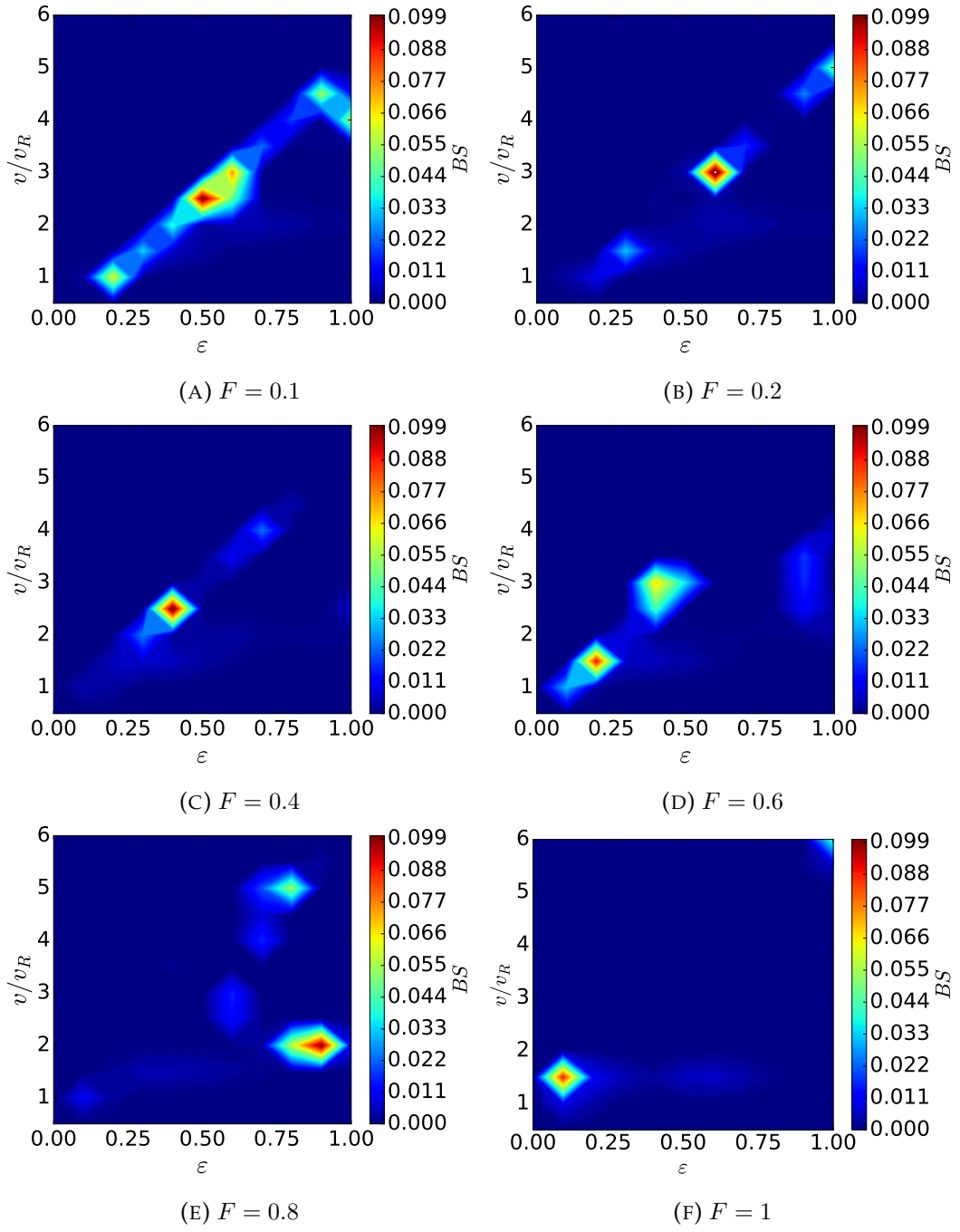

(A) $F = 0.1$ (B) $F = 0.2$

(C) $F = 0.4$ (D) $F = 0.6$

(E) $F = 0.8$ (F) $F = 1$

FIGURE 3.17: These figures shows the probability of atoms being trapped inside the beam-splitter for the parameters $\sigma = 10\mu m$, $U_0 = -20E_R$, $\omega_0 = 15\mu m$, $\lambda = 1064nm$ and $\theta = 90°$. The difference between these figures and goes from $F = 0.1$, $F = 0.2$, $F = 0.4$, $F = 0.6$, $F = 0.8$ and $F = 1$ in alphabetical orders. Regions of significant atom-trapping should be avoided for a beam-splitter.

3.3.3 Shallower and Narrower Waveguides

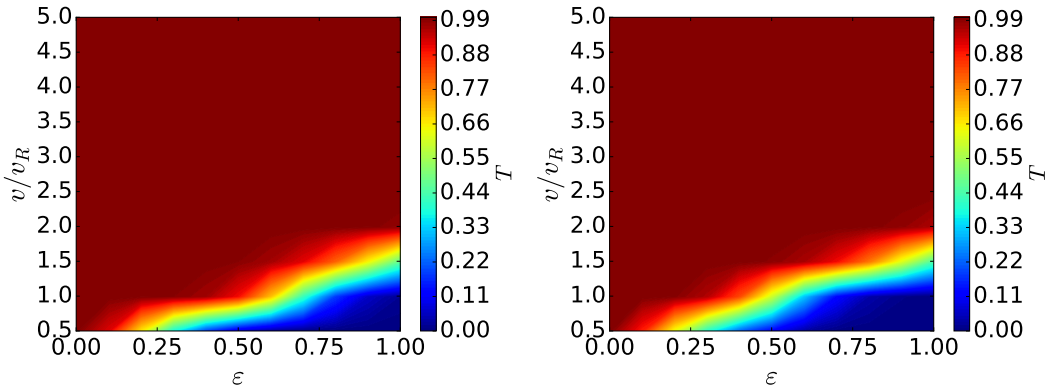

(A) $F = 0$

(B) $F = 0.2$

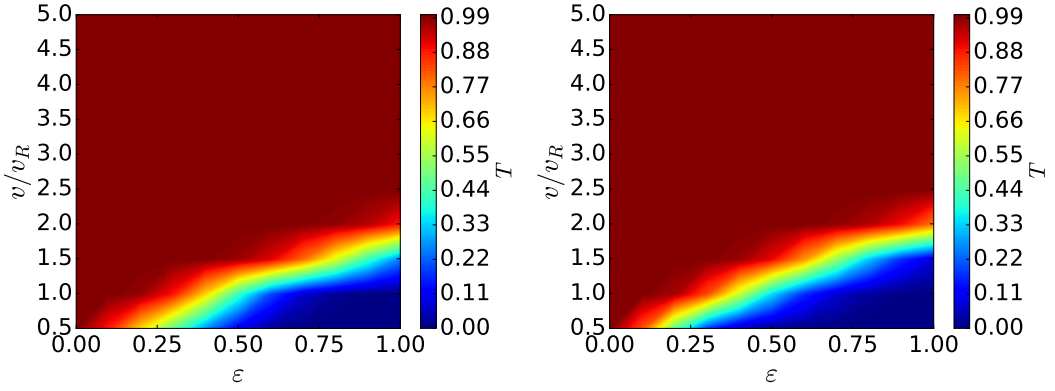

(C) $F = 0.4$

(D) $F = 0.6$

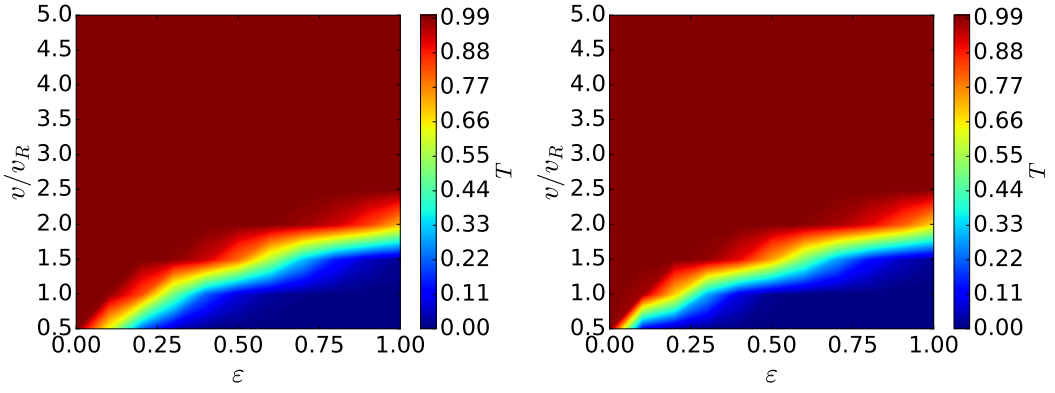

(E) $F = 0.8$

(F) $F = 1$

FIGURE 3.18: The transmission probability for different filling levels are depicted in these figures for different filling levels mentioned below the respected figures. The separation between transmission and reflection is roughly a straight line and $F = 0$ and becomes curved for higher filling. The other parameters are $\sigma = 0.73\mu m$, $U_0 = -2E_R$, $\omega_0 = 1\mu m$, $\lambda = 720nm$ and $\theta = 90°$.

The next step for us is now to apply the split-step Fourier method to the cases with lower waveguide depth and width. Starting off with the depth of $U_0 = -2E_R$, the laser width $\omega_0 = 1\mu m$, its wavelength of $\lambda = 720nm$ and the crossing angle of $\theta = 90°$. For our wave-packet the variance will be $0.73\mu m$. The velocity will be

varied from $v = 0.5v_R$ to $5v = v_R$, the polarisation from $\varepsilon = 0$ to $\varepsilon = 1$ and the filling $F = 0$ to $F = 1$, increments of $0.5v_R$, 0.1 and 0.1, respectively. This allows us to calculate the transmission probabilities, see Fig. 3.18. Again, these are similar to the standing wave, where the reflection and transmission are linearly divided and this division becomes a curve when we increase the filling. Additionally, we need to look at the trapped atom in the band-gaps, see Fig. 3.19, for which it becomes clear that the areas of most trapped atoms are not in regions of 50:50 splitting.

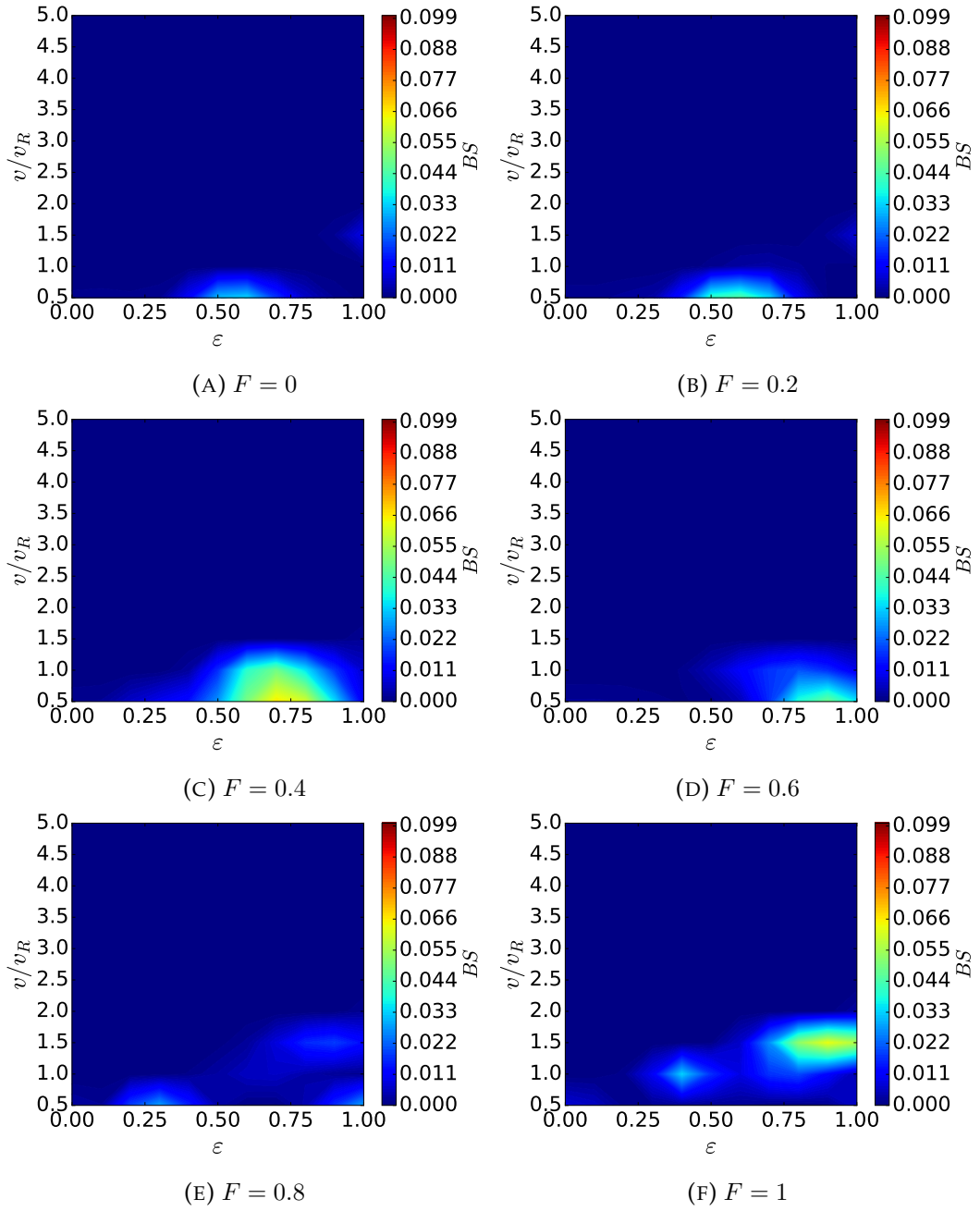

(A) $F = 0$ (B) $F = 0.2$

(C) $F = 0.4$ (D) $F = 0.6$

(E) $F = 0.8$ (F) $F = 1$

FIGURE 3.19: These figures show the amount of atoms being trapped for different filling level, $F = 0$, $F = 0.2$, $F = 0.4$, $F = 0.6$, $F = 0.8$ $F = 1$, as shown in A, B, C, D, E and F, respectively. The other parameters are $\sigma = 0.73\mu m$, $U_0 = -2E_R$, $\omega_0 = 1\mu m$, $\lambda = 720nm$ and $\theta = 90°$. The area of significant trapped atoms has generally no real overlap with the areas of 50:50 splitting.

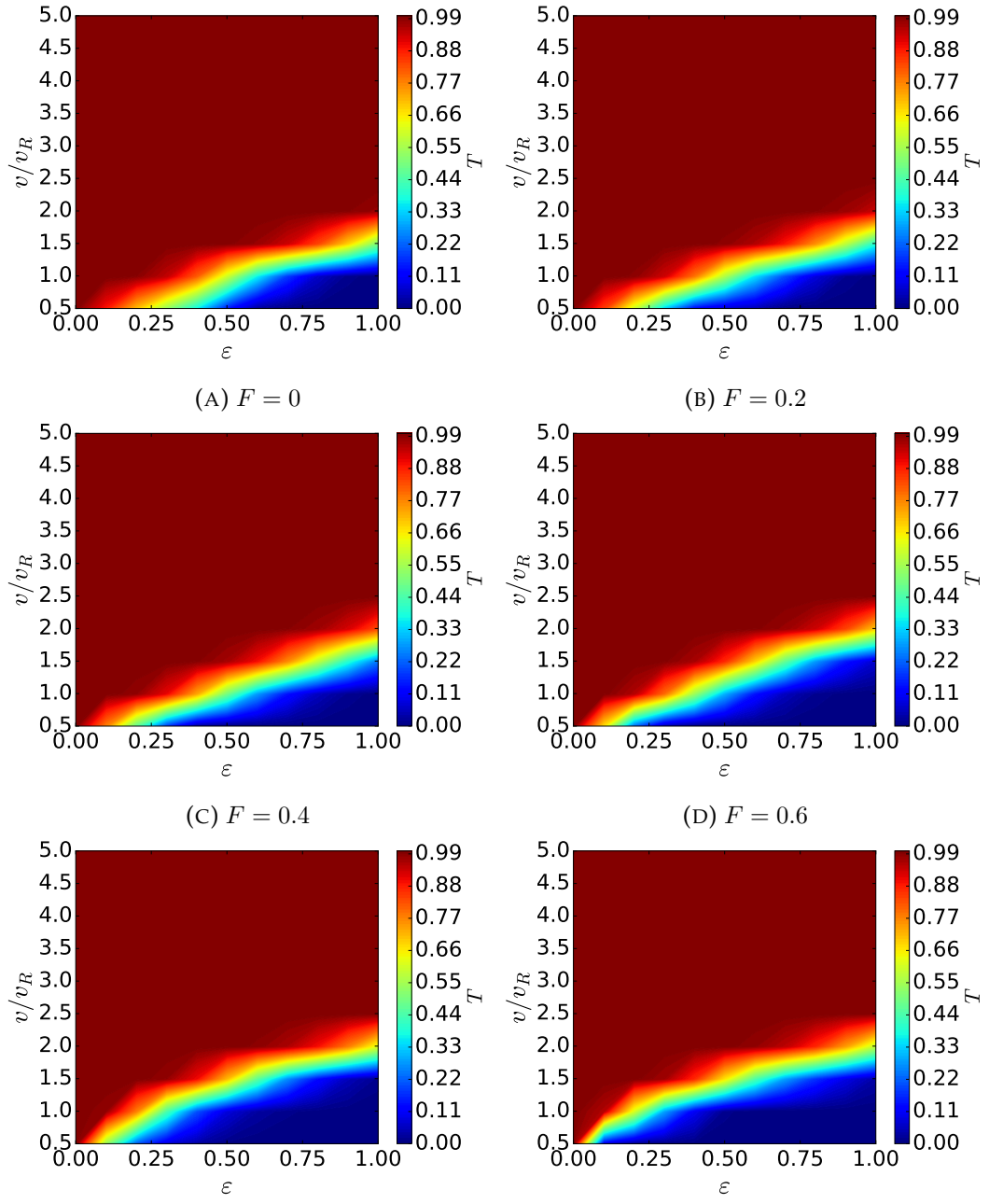

(A) $F = 0$ (B) $F = 0.2$

(C) $F = 0.4$ (D) $F = 0.6$

(E) $F = 0.8$ (F) $F = 1$

FIGURE 3.20: The transmission probabilities for a travelling Gaussian wave-packet though our beam-splitter for the parameters $\sigma = 0.73\mu m$, $U_0 = -2E_R$, $\omega_0 = 1.5\mu m$, $\lambda = 720nm$. In this case as well the separation between the reflection and transmission starts of linearly for low filling as seen in A and becomes round when the filling is increased see B→C→D→E→F. The difference between this case and $\omega_0 = 1\mu m$ is small.

From here we will increase the with of the waveguides to $\omega_0 = 1.5\mu m$ and keep all other parameters the same. Giving us the transmission probabilities as seen in Fig. 3.20. These also correspond well with the ones from the standing waves 3.11. The boundary between transmission is smoothed out but otherwise they show a very similar splitting behaviour. As for this case the regions for total transmission and total reflection are divided by a straight line for $F = 0$ that becomes curved when

the filling is increased.
The regions in which the atoms are trapped does not overlap significantly with good splitting region and thus does not play a significant role in finding the right parameters, see Fig. 3.21. However, it is to be expected that the amount of trapped atoms slightly increases for a wider laser beam as this is seen here.

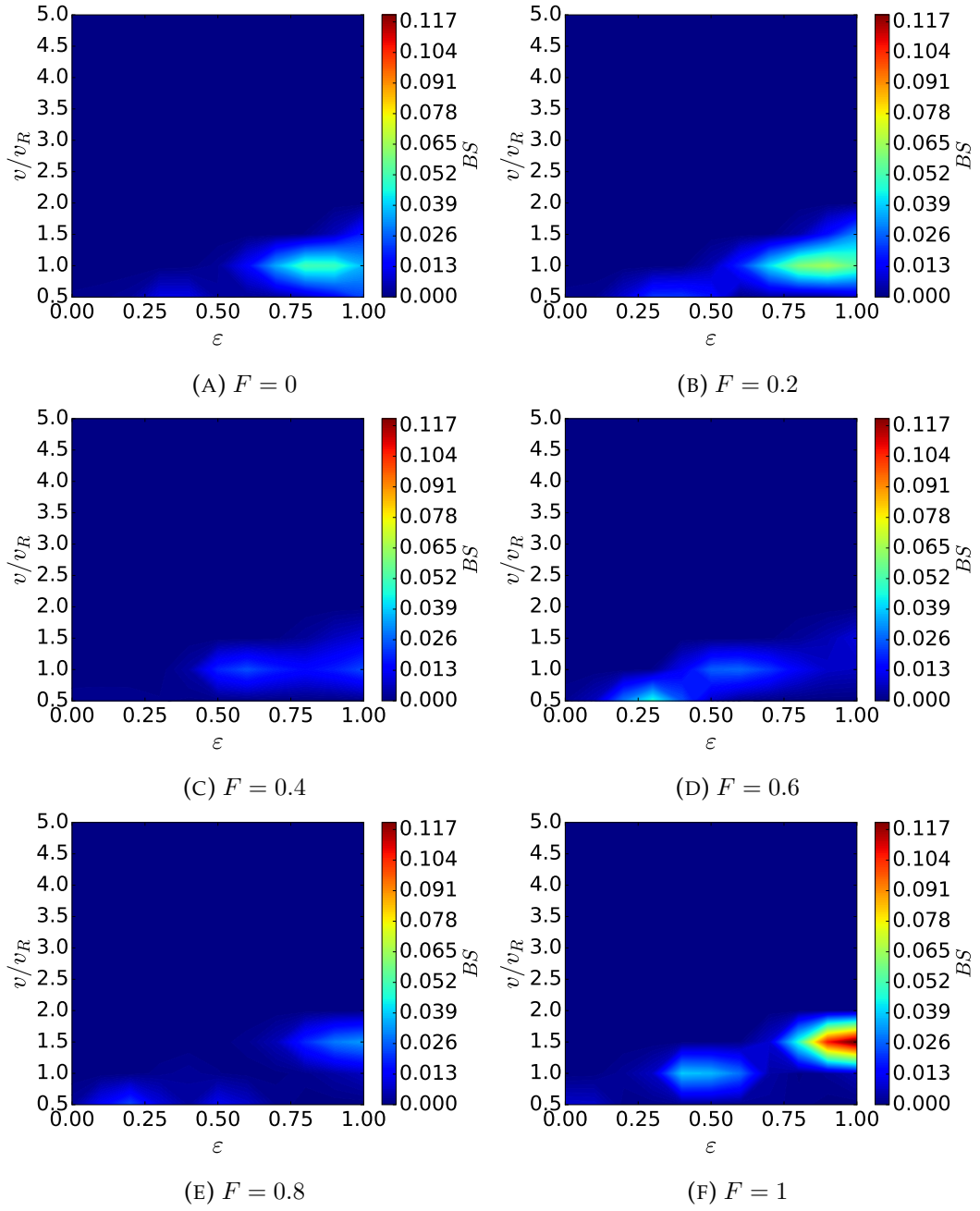

(A) $F = 0$ (B) $F = 0.2$

(C) $F = 0.4$ (D) $F = 0.6$

(E) $F = 0.8$ (F) $F = 1$

FIGURE 3.21: The amount of trapped atoms for a travelling Gaussian wavepacket is depicted for different filling levels, with the other parameters being $\sigma = 0.73\mu m$, $U_0 = -2E_R$, $\omega_0 = 1.5\mu m$, $\lambda = 720nm$. The overlap of trapped atoms and equal splitting is minimal.

Our last case focuses on a deeper waveguide with a depth of $U_0 = -5E_R$ and a width of $\omega_0 = 1\mu m$. All the other parameters stay the same. For which we see the splitting

probabilities in Fig. 3.22. Overall these parameters would allow us to use higher velocities for 50:50 splitting in comparison to the case of $U_0 = -2E_R$. Otherwise it is quite similar with same pattern of having a linear boundary between total reflection and total transmission at lower fillings which becomes curved in favour of reflection for higher filling.

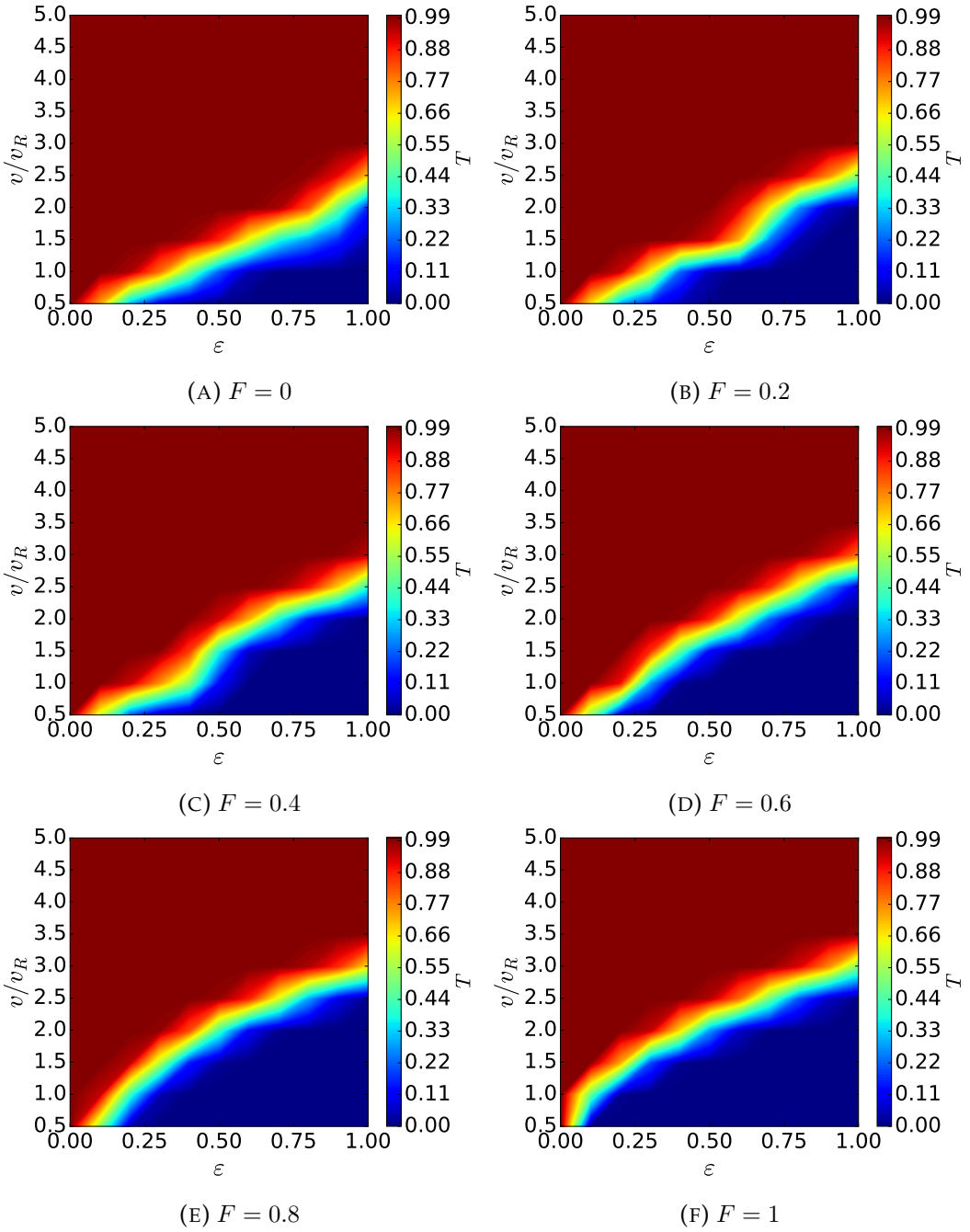

(A) $F = 0$ (B) $F = 0.2$

(C) $F = 0.4$ (D) $F = 0.6$

(E) $F = 0.8$ (F) $F = 1$

FIGURE 3.22: The transmission probabilities for different fillings for the parameters are depicted by these figures for the parameters $\sigma = 0.73\mu m$, $U_0 = -5E_R$, $\omega_0 = 1\mu m$, $\lambda = 720nm$. For this case as well the separation between transmission and reflection is linear and becomes curved for higher fillings in favour for reflection.

In addition to the transmission we also calculated the probability of atoms being

trapped inside the beam-splitter, see Fig. 3.23. In connection with the transmission probability we see that the overlap of equal splitting probabilities and trapped atoms in minimal. Hence, it is not a deciding factor for velocities, polarisation and filling to choose. However, as this beam-splitter is deeper than the one for $U_0 = -2E_R$, more atoms get trapped.

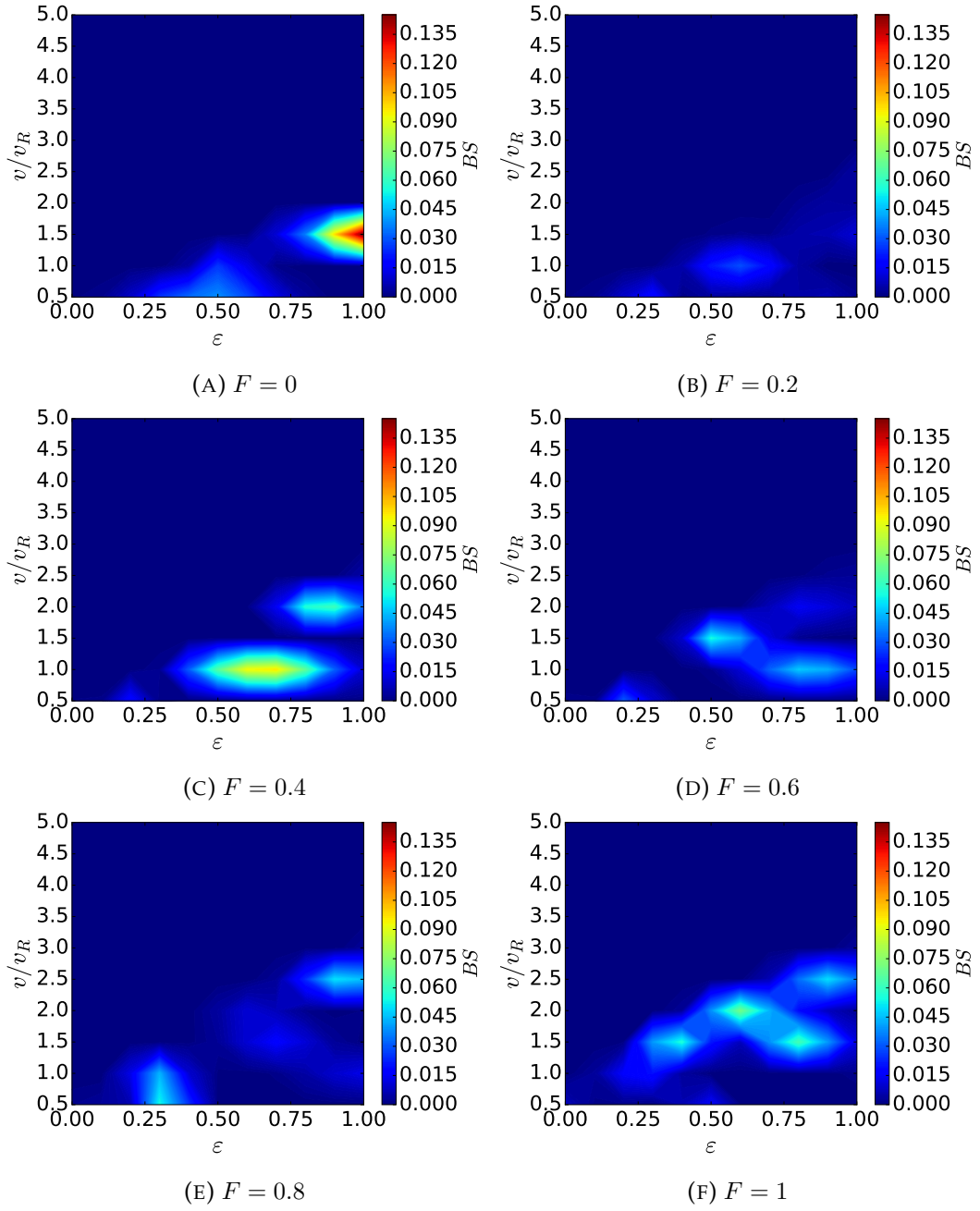

(A) $F = 0$ (B) $F = 0.2$

(C) $F = 0.4$ (D) $F = 0.6$

(E) $F = 0.8$ (F) $F = 1$

FIGURE 3.23: These figures show the probabilities of atoms being trapped inside the beam-splitter for different filling levels for the parameters $\sigma = 0.73\mu m$, $U_0 = -5E_R$, $\omega_0 = 1\mu m$, $\lambda = 720nm$. None of these overlap significantly with the region of desired splitting probabilities.

3.4 Summary

In this chapter we discussed and analysed the splitting probabilities for our one-dimensional beam-splitter, which is just the cross-section of our two dimensional one. Firstly, we used the band-gap method. For this we calculated the individual band-gaps and transmission probabilities and these band-gaps act as regions of forbidden energy and thus atoms need to tunnel through them. We only looked at the parameters of the potential depth of $U_0 = -20E_R$, the laser width $\omega_0 = 15\mu m$ and the laser wavelength of $\lambda = 1064nm$ and expanded on this with a filling parameter, the reason for which will be discussed in the next chaster. However, our lattice does not have enough fringes to actually calculate the band-gaps, which was shown by the contradictory picture provided by the next two methods.
The next method used was for standing waves, where by integrating backwards through the beam-splitter we calculated the transmission probabilities. For $U_0 = -20E_R$, the laser width $\omega_0 = 15\mu m$, the laser wavelength of $\lambda = 1064nm$ and a filling of $F = 0$ we saw that the transmission and reflection areas were linearly divided and when we increased the filling this division becomes curved on favour of reflection with spikes. This is due to atoms with different velocities being reflected by different regions inside the beam-splitter. The Gaussian shape of the filling, fills the central region stronger than the outer, leading to a curved shape between the boundaries. Additionally, we look at how the number of atoms inside the beam-splitter changed depending on velocity and polarisation. Unfortunately, the results do not allow us to narrow down the parameters. Afterwards, we changed the width, depth and wavelength of our laser to $U_0 = -2E_R$, $\omega_0 = 1\mu m$ and $\lambda = 720nm$, respectively. It also started of with a linear divide which become curved when the filling was increased. However, it did not have formation of new spikes. Additionally, to this we also looked at cases with the parameters of $U_0 = -5E_R$, $\omega_0 = 1\mu m$ and $\lambda = 720nm$ and $U_0 = -2E_R$, $\omega_0 = 1.5\mu m$ and $\lambda = 720nm$. Also, there were regions of total transmission inside the region of total reflection due to resonant frequencies. Both of which shows similar behaviour to the previous mentioned case.
The last method we used is the split-step Fourier method for a Gaussian wave-packet travelling though the beam-splitter. We used the same cases as before and saw that they agree with the previous one, for which we calculated the transmission via integrating backwards. The main difference between them is that the border between total reflection and transmission is smoothed out. There are two primary reasons behind this. The first being less data points as the split-step Fourier method takes longer to calculate. The other one being that the Gaussian wave-packet can be written as a sum of standing waves and thus its transmission probability comes from summing the transmission probabilities of different individual standing waves.

Chapter 4

Beam-Splitter Properties in Two-Dimensions

In the previous chapter we have discussed the properties of the beam-splitter in one dimension. Following from there we are looking at the two dimensional properties in this chapter, see Fig. 4.1 for an example potential of the beam-splitter with waveguides labelled for their functions. For this we will discuss in this chapter the Fourier transform in two dimensions, the transverse ground state we use for the starting wave-packet of the atoms, how we calculate the splitting probabilities from the final numerical wave-function. Afterwards we will look at different parameters for our beam-splitter to find desirable splitting probabilities.

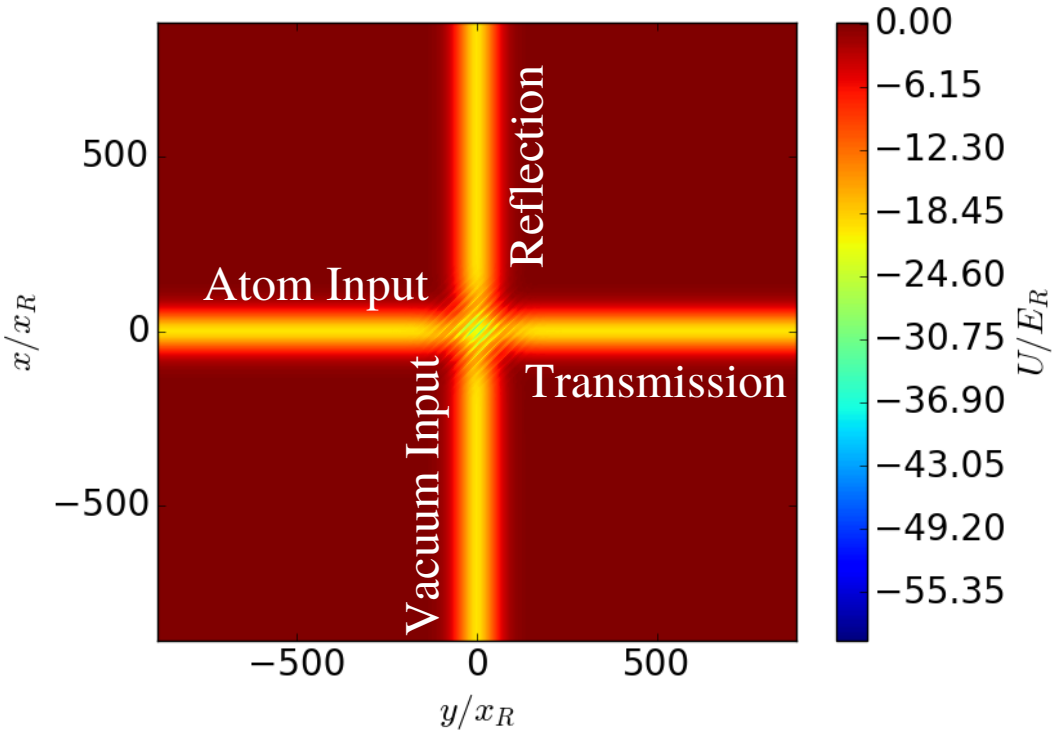

FIGURE 4.1: An example potential of the beam-splitter with the individual waveguides labelled after their function.

4.1 2D Fourier Transform

As we will be working with two dimensional waves from now on we will need to modify the the split-step Fourier method [100–102], Sec. 2.3.3, for this case. Starting off with the definition of the 2D Fourier transform

$$\tilde{\psi}(k_x, k_y, t) = \frac{1}{2\pi} \int_{y_{min}}^{y_{max}} \int_{x_{min}}^{x_{max}} \psi(x, y, t) e^{-i(k_x x + k_y y)} dx dy, \tag{4.1}$$

which is in effect two separate 1D Fourier transforms for each of the coordinates,

$$\tilde{\psi}(k_x, k_y, t) = \mathcal{F}_x \left(\mathcal{F}_y \left(\psi(x, y, t) \right) \right). \tag{4.2}$$

This is similar to the discrete Fourier transform which is also only two 1D transforms over each coordinate

$$g(n\Delta\omega_1, l\Delta\omega_2) = \sum_{q=0}^{L-1} \sum_{m=0}^{N-1} f(m\Delta t_1, q\Delta t_2) e^{-i2\pi n \frac{m}{N}} e^{-i2\pi l \frac{q}{L}}. \tag{4.3}$$

Now we need to change our two continuous Fourier transforms into a discrete form

$$\tilde{\psi}(k_{x,n}, k_{y,l}, t) \simeq \frac{1}{2\pi} \sum_{q=0}^{L-1} \sum_{m=0}^{N-1} \psi(x_m, y_q, t) e^{-ik_{x,n} x_m} e^{-ik_{y,l} y_q} \Delta x \Delta y, \tag{4.4}$$

which we will rearrange to fit our discrete Fourier transform,

$$\begin{aligned} \left[\tilde{\psi}(k_{x,n}, k_{y,l}, t) e^{inx_{min}\Delta k_x} e^{ily_{min}\Delta k_y} \right] \simeq \sum_{q=0}^{L-1} \sum_{m=0}^{N-1} \left[\frac{\Delta x \Delta y}{2\pi} \psi(x_m, y_q, t) e^{-ik_{x,min} x_m} e^{-ik_{y,min} y_q} \right] \\ \times e^{-i2\pi n \frac{m}{N}} e^{-i2\pi l \frac{q}{L}}. \end{aligned} \tag{4.5}$$

This equation show us how to modify our wave-functions to use the 2D discrete Fourier transform to compute the continuous Fourier transform. The same can be done for the inverse, where we begin with the 2D continuous inverse Fourier Transform

$$\psi(x, y, t) = \frac{1}{2\pi} \int_{k_{y,min}}^{k_{y,max}} \int_{k_{x,min}}^{k_{x,max}} \tilde{\psi}(k_x, k_y, t) e^{i(k_x x + k_y y)} dk_x dk_y, \tag{4.6}$$

that will be written into a discrete form

$$\psi(x_m, y_q, t) \simeq \frac{1}{2\pi} \sum_{l=0}^{L-1} \sum_{n=0}^{N-1} \tilde{\psi}(k_{x,n}, k_{y,l}, t) e^{ik_{x,n} x_m} e^{ik_{y,l} y_q} \Delta k_x \Delta k_y. \tag{4.7}$$

Now we need the 2D inverse discrete Fourier transform

$$f(m\Delta t_1, q\Delta t_2) = \frac{1}{NL}\sum_{l=0}^{L-1}\sum_{n=0}^{N-1} g(n\Delta\omega_1, l\Delta\omega_2)e^{i2\pi m\frac{n}{N}}e^{i2\pi q\frac{l}{L}}, \tag{4.8}$$

to rearrange the Eq. 4.7 into

$$\left[\frac{\Delta x\Delta y}{2\pi}\psi(x_m, y_q, t)e^{-ik_{x,min}x_m}e^{-ik_{y,min}y_q}\right] \simeq \sum_{n=0}^{N-1}\left[\tilde{\psi}(k_{x,n}, k_{y,l}, t)e^{inx_{min}\Delta k_x}e^{ily_{min}\Delta k_y}\right] \times e^{i2\pi m\frac{n}{N}}e^{i2\pi q\frac{l}{L}}. \tag{4.9}$$

Now we have a way to solve the continuous Fourier transform and its inverse in two dimensions, which allows us to use the split-step Fourier method to investigate the splitting probabilities of our beam-splitter. The algorithm is roughly the same as given in Sec. 2.3.3, where we have now changed the Fourier transforms to solve the 2D problems. For this the initial wave-function and the potential are now set to 2D. A brief overview for the one-dimensional case can be seen in appendix B.

4.2 Ground State

The waveguides in the two dimensional problems restrict the movement of the atoms along their transverse direction only allowing longitudinal movements . For our simulation we assume that the atoms are in the transverse ground state of the waveguides. A reasonable assumption for the ground state in our Gaussian waveguide would be to set it equal to the ground state in a harmonic oscillator, where the errors of ground state will only be in the tail of the Taylor expansion where the magnitude of the wave-function is very small,

$$\begin{aligned}\psi_0(x) &= \left(\frac{m\omega_{HMO}}{\pi\hbar}\right)^{\frac{1}{4}} e^{-\frac{m\omega_{HMO}x^2}{2\hbar}} \\ &= \frac{1}{\sqrt{\sigma\sqrt{\pi}}}\left(e^{-\frac{x^2}{2\sigma^2}}\right),\end{aligned} \tag{4.10}$$

where the variance of the wave-function is

$$\sigma = \sqrt{\frac{\hbar}{m\omega_{HMO}}}. \tag{4.11}$$

To obtain the angular frequency for this approximation to work we need to Taylor expand the potential for our waveguide

$$U(x) = U_0 e^{-\frac{x^2}{\omega^2}} \approx U_0\left(1 - \frac{x^2}{\omega^2}\right) + \cdots. \tag{4.12}$$

We need to compare this equation with the one from the harmonic oscillator, which is

$$U_{HMO}(x) = \frac{1}{2} m\omega_{HMO}^2 x^2. \tag{4.13}$$

From this can get now

$$\frac{1}{2} m\omega_{HMO}^2 x^2 = |U_0| \frac{x^2}{\omega^2}, \tag{4.14}$$

which needs to be rearranged into

$$\omega_{HMO} = \sqrt{\frac{2|U_0|}{m\omega^2}}, \tag{4.15}$$

leading to the variance of

$$\sigma = \sqrt{\frac{\hbar\omega}{\sqrt{m2|U_0|}}}. \tag{4.16}$$

This approximation can be justified by comparing to the numerical results from the shooting method[99], Sec. 2.3.4, to calculate the fidelity of the approximation with the numerical result. For example the fidelity between the approximation and the shooting method is $\langle \psi_{approx} | \psi_{shoot} \rangle = 0.99140$ for the parameters $\theta = 90°$, $\omega_0 = 1\mu m$, $U_0 = -5E_R$ and $\lambda = 720nm$.

4.3 Variables for the Simulations

Before we start to discuss the 2D simulations we need to explain the general parameters of the calculations. Firstly, the step size in time for our calculations is set to $\Delta t = 0.5\mu s$, while the overall time for the simulations mainly dependence on the velocity of the atoms and the diffusions of their wave-function to make sure they can propagate through the whole beam-splitter. Furthermore, we need to make sure that the potential has enough data points to give a decent image for the fringes. Therefore, the minimum separation between the points is $\Delta x = d/10$, where d is the anticipated length of one fringe period Sec. 2.3.3. The dimension of the position space is so that the wave-function can be completely inside a waveguide without coming into contact with the beam-splitter or the edges of the simulation area. However, this is only the condition in position space. Hence, we need to make sure that there are enough data points available to allow for the momentum change of the wave-function in the beam-splitter. Remembering that the length of the k-space is directly dependent on Δx via $K = \frac{2\pi}{\Delta x}$, where K is the total length of the k-space with a separation of the data points being $\Delta k_x = \frac{2\pi}{N_x \Delta x}$. This relation comes directly from the discrete Fourier transform and thus the only way for us to increase the size k-space is to reduce Δx by increasing the number of data points and keeping X the same.

Additionally, the discretisation of the Fourier transforms via the approximation of the integral as

$$\int dx \approx \sum \Delta x, \tag{4.17}$$

is rather crude. Therefore, we need to have a way of determining when this leads to errors. A good way to do this is to look at variables which should stay constant over the whole simulation. Leading us to the use of the normalisation in position-space,

$$\int_{y_{min}}^{y_{max}} \int_{x_{min}}^{x_{max}} \psi(x,y,t)\psi^*(x,y,t)dxdy = 1, \tag{4.18}$$

in k-space

$$\int_{k_{y,min}}^{k_{y,max}} \int_{k_{x,min}}^{k_{x,max}} \tilde{\psi}(k_x,k_y,t)\tilde{\psi}^*(k_x,k_y,t)dk_xdk_y = 1 \tag{4.19}$$

and the expectation of the energy

$$\begin{aligned}\langle E\rangle &= \langle\psi|\hat{V}+\hat{T}|\psi\rangle = \langle\psi|\hat{V}|\psi\rangle + \langle\psi|\hat{T}|\psi\rangle \\ &= \int_{y_{min}}^{y_{max}} \int_{x_{min}}^{x_{max}} \psi^*(x,y,t)U(x,y)\psi(x,y,t)dxdy \\ &\quad + \int_{k_{y,min}}^{k_{y,max}} \int_{k_{x,min}}^{k_{x,max}} \tilde{\psi}(k_x,k_y,t)\frac{(k_x^2+ky^2)\hbar^2}{2m}\tilde{\psi}^*(k_x,k_y,t)dk_xdk_y,\end{aligned} \tag{4.20}$$

$\hat{T}$ is the operator for the kinetic energy and $\hat{V}$ is the operator for the potential energy. A significant change in any of these values will indicate that errors are growing in the calculations, which therefore need further investigation an example of this is given in Fig. 4.2.

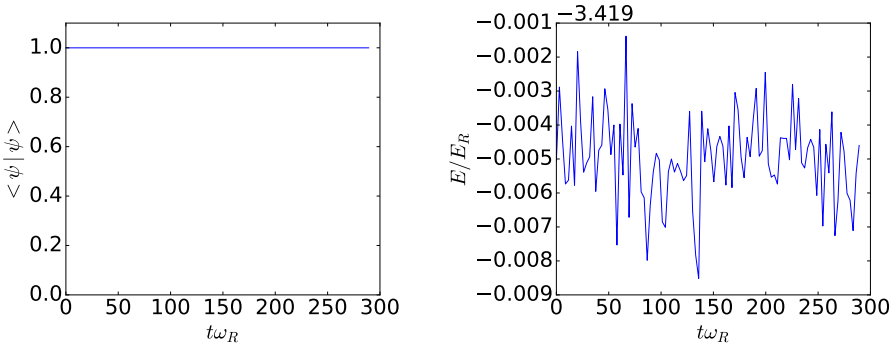

(A) Normalisation (B) Energy

FIGURE 4.2: Figure A depicts the normalisation and its change in time and B shows the energy of the atoms and its change in time. The biggest changes come from numerical errors. They are used to find issues with the simulation and as long as they do not show any significant change they can be neglected. This example is given for the parameters $\theta = 90°$, $\omega_0 = 15\mu m$, $\sigma_x = 10\mu m$, $U_0 = -20E_R$, $\lambda = 1064nm$, $v = 4v_R$, $\varepsilon = 0.5$

4.3.1 Probability Calculations

From here onwards we also need to define how we calculate the probabilities of finding the atoms in a specific arms. This will be done by simply integrating over a certain region inside our simulation area,

$$P = \int_{y_-}^{y_+} \int_{x_-}^{x_+} \psi(x, y, t)\psi^*(x, y, t)dxdy. \tag{4.21}$$

For example to calculate the transmission probability we would set the lower limit x_- to be the end of the beam-splitter and the upper limit x_+ to be the limit of the position space x_{max}. The limits for y are chosen to be $\pm 1.5\omega_0$, where ω_0 is the waist of the waveguide. A smaller range in y can exhibit probability oscillations, due to transverse oscillations of the wave-packet in the wave-guide that develop during the evolution (as will be discussed in Sec. 4.4). The range of y is therefore chosen so that probability does not oscillate transversely out of the range. This method allows us to define 6 regions over, which we can integrate: The input waveguide for the atoms, normally labelled as $I1$, the vacuum input $I2$, the reflection waveguide, R, the transmission guide, T, the beam-splitter, BS and finally the area outside the bounds of the waveguides and beam-splitter, which we define as loss. Additionally, it is of importance to determine the coherence of our outputs. As a reminder, our definition of the coherence is that atoms occupy the transverse ground state and the longitudinal momentum state of their respective waveguide, given by Eq. 1.20 which is

$$|g, k; 0, 0\rangle \rightarrow \frac{1}{\sqrt{2}} \left(|g, k; 0, 0\rangle + |0, 0; g, k\rangle\right), \tag{4.22}$$

where $|g, k\rangle$ is the states with the atom in the longitudinal ground state and the momentum state corresponding to the wave-number k. For this notation, $|0, 0\rangle$ is the vacuum. During our simulation, we constantly monitored the number of atoms in the longitudinal ground state in their respective waveguides. For this, we calculated the probability amplitude between the state and the ground state

$$A(x, t) = \int_{y_-}^{y_+} \psi_0^*(y)\psi(x, y, t)dy, \tag{4.23}$$

where $\psi_0(y)$ is the wave-function of the ground state. From this, we get the probability density as a function of x via

$$\rho(x, t) = |A(x, t)|^2. \tag{4.24}$$

Integrating over the length of the waveguides gives the probability of finding the atoms in the ground state of their respected waveguides,

$$P_0(t) = \int_{x_-}^{x+} |A(x,t)|^2 dx. \tag{4.25}$$

However, this value is for the total wave-function and thus we will only give its ratio with regard to the probability of finding the atoms in the waveguide regardless of their state. This value will give information about the splitting quality with the desired values of P_0(normalised by the total probability) being unity.

4.4 Beam-Splitter Simulations

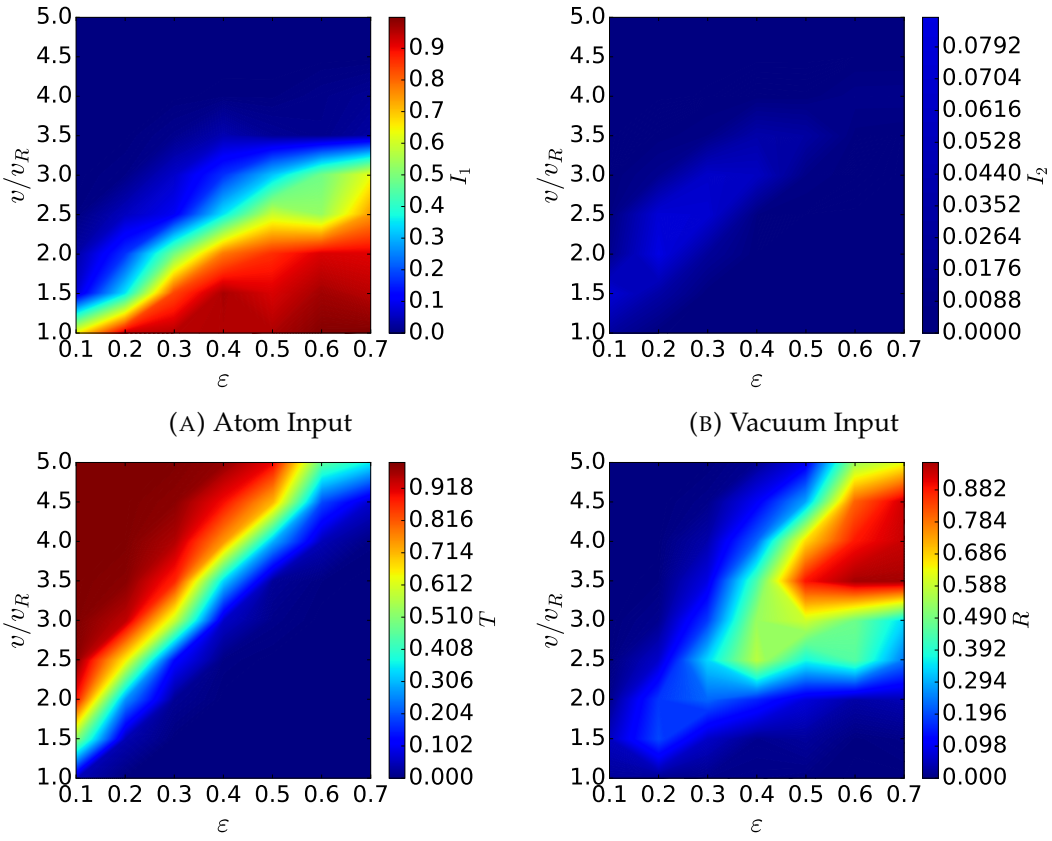

(A) Atom Input

(B) Vacuum Input

(C) Transmission

(D) Reflection

FIGURE 4.3: These plots depict the probability of finding the atoms in the respected waveguides, where A is the input into which the atoms are scattered back if they do not have enough kinetic energy. To have a good functioning beam-splitter any back-scattering into the atom input should be negligible. B shows the vacuum input. In the ideal case it should be mostly empty and thus any significant scattering probability into it is unfavourable for the desired splitting. The transmission probability is depicted in C and it should be chosen to be roughly 50%. Lastly, D shows the reflection and it should be similar to the transmission probability to have an even split.

Now that we have discussed the necessary definitions we will present selected results from our simulations, all the animation can be found as described in appendix A. The two parameters for the simulations that are the easiest to control are the velocity of the atoms, v and the polarisation of the beams, ε, while the other parameters are kept constant. These parameters are the angle at which the Gaussian beams cross, $\theta = 90^{\circ}$, their width $\omega_0 = 15\mu m$, the variance of the incoming wave-packet along the longitudinal direction $\sigma_x = 10\mu m$, the transverse direction is in the ground state of the waveguide, the depth of the waveguide $U_0 = -20E_R$ and the wavelength of the Gaussian beams $\lambda = 1064nm$, Sec. 2.1. Our aim is to find a suitable region for coherent and balanced splitting as such we will investigate the velocity over a range of $1v_R$ to $5v_R$, using the a step size of $0.5v_R$ and epsilon will be varied from 0.1 to 0.7 with the step size of 0.1. During these runs we will measure the probability of finding the wave-packet in the respective waveguides to determine the the reflection and transmission probabilities. In the case of an vacuum in the waveguide it is defined as 0. Additionally, it will be refereed to the coherent.
The plot for them can be seen in Fig. 4.3, where A(4.3a) is the probability of the atoms being reflected back into their input. Any substantial probability of this happening means that these parameters are not suitable for the desired splitting properties of the beam-splitter. Next we have the sub figure B(4.3b), which is the vacuum input and thus it should stay a vacuum for the entire splitting process and any non-negligible scattering into it is unsuitable for the beam-splitter. Next we have the transmission and reflection probability, C(4.3c) and D(4.3d) respectively. These should have roughly a 50:50 splitting for an ideal beam-splitter.
Nonetheless, the shape of the wave-function after the splitting is still as important as the ratio, as they are going to re-interfere in a interferometer. For this we need to take a look at the simulation of the wave through the beam-splitter. Looking at Fig. 4.3, we choose the appropriate values for a roughly even split, which in this case are a velocity of $v = 4v_R$ and $\varepsilon = 0.5$, which can be seen in Fig. 4.4, where the probability density of the wave-function is depicted at different selected points in time, while it is traversing through the beam-splitter, in alphabetic order respectively. The wave-function for these properties gets excited into higher transverse modes of the waveguides. In the reflection band it forms a number of individual smaller wave-packets which disperse and recombine while travelling through the waveguide, which can be seen in E(4.4e) and F(4.4f) . On the other hand, the wave in the transmission waveguide stays more contiguous than in the reflected case. However, it is split in two distinct wave-packages and it is elongated compared to the reflected case and it also has a stronger longitudinal momentum than it. This will make it harder to have interference when the wave-functions are recombined as only certain parts of both wave-functions will be recombined in the beam-splitter instead of having a perfect overlap between these two.

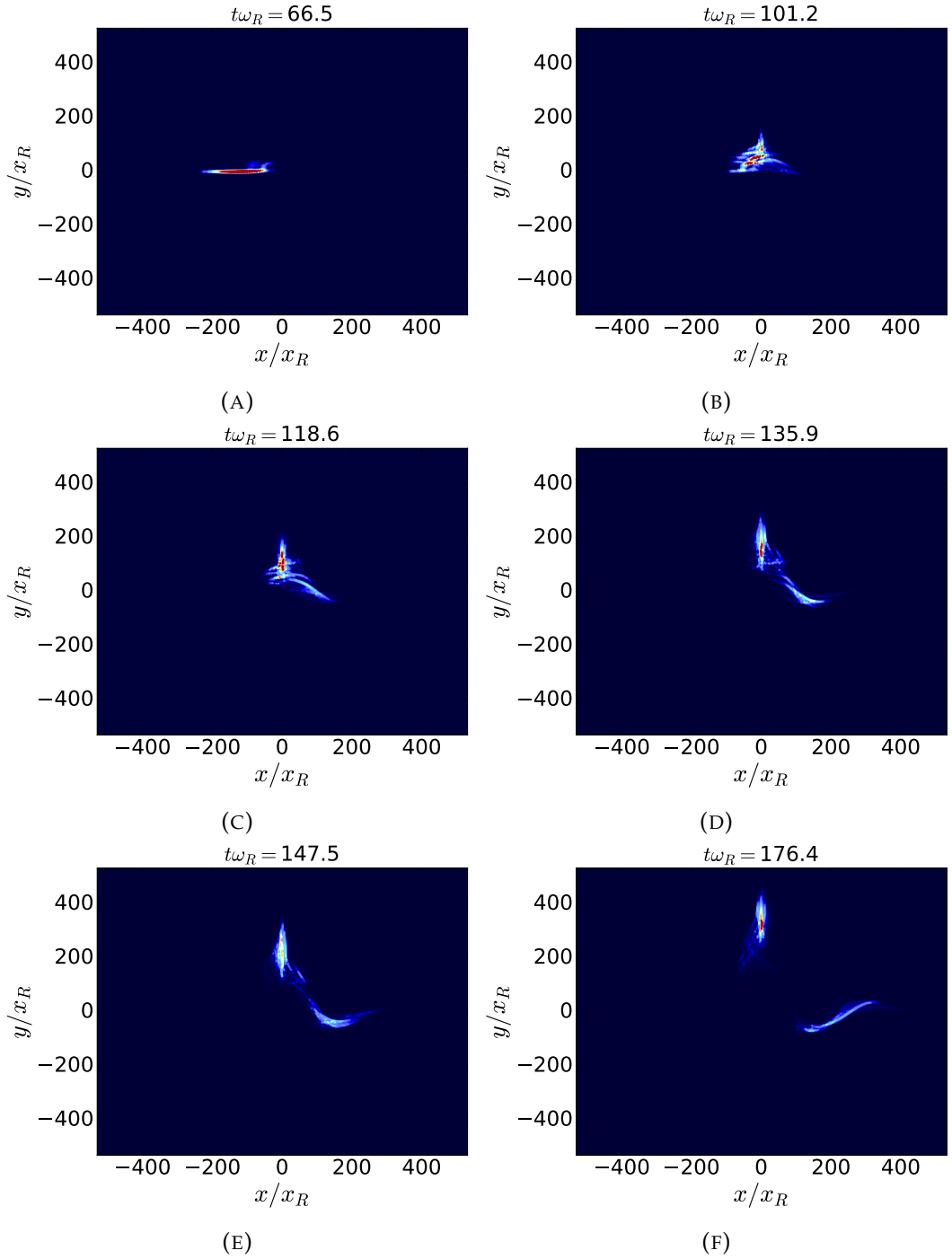

FIGURE 4.4: These figures illustrate the atoms with a velocity of $4v_R$ moving through a beam-splitter with a polarisation of $\varepsilon = 0.5$, to have a roughly even split. The atoms travel through the optical waveguide until they reach the beam-splitter at A. From there they propagate through the beam-splitter as shown in B, C, and D and finally leave the beam-splitter at E with the last time stamp of the simulation shown at F.

Additionally, we looked at the percentage of finding the atoms in the ground state of the transmission(blue dotted line) and reflection(red dashed line) waveguides after the splitting, see Fig. 4.5. Interestingly, even though the wave inside the reflection waveguide is split into more smaller wave-packets, they stay close together and thus

roughly 40% of the wave is in the ground state. Furthermore, while the wave in the transmission guide is more contiguous here is no significant part of it that is in the ground state.

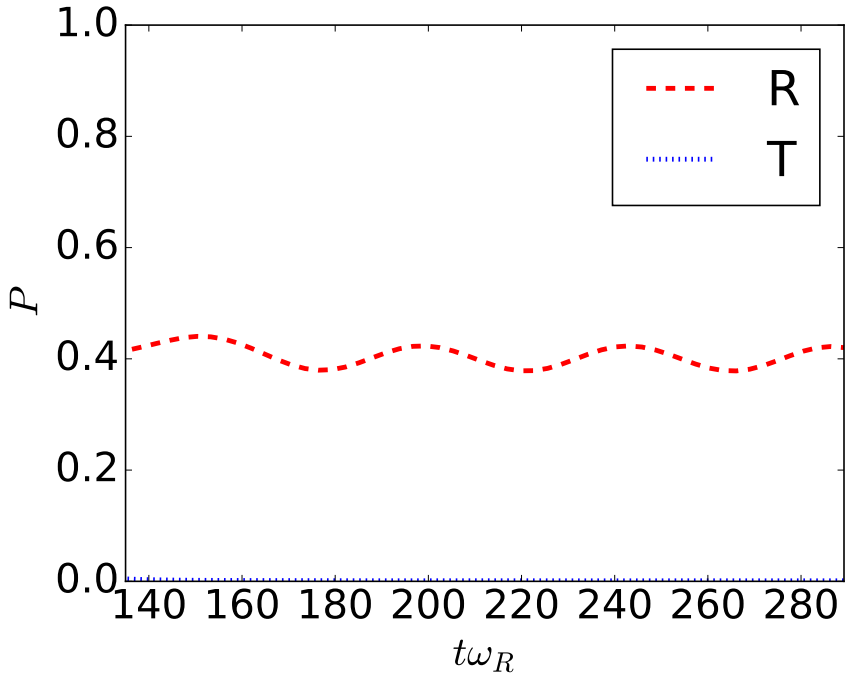

FIGURE 4.5: Shows the per cent of the wave inside the transmission(blue dotted line) and reflection(red dashed line) waveguides being inside the ground state after the splitting. For a wave-function with a velocity of $v = 4v_R$ and a polarisation of $\varepsilon = 0.5$.

Similar behaviour could be seen in all simulations, where the majority is scattered into the reflection and transmission waveguides. Due to, the splitting is non-central and takes part not just in one region of the beam-splitter, which leads to the multitude of smaller Gaussian wave-packets in the transmission and reflection waveguides. This is especially true for the reflection waveguide as most of the smaller wave-packets get reflected inside it while the packet in the transmission waveguide stays more together with a different direction of the momentum. In regards to the momentum change of the atom and the conservation of momentum, the momentum is conserved in the sense that the change of its direction can be accounted for in the momentum of the optical lattice and the photons. This recoil is however negligible for the lattice, as the optical lattice state is effectively a classical state of uncertain photon number containing a very large average photon number, and thus we can treat the potential of the optical lattice seen by the atoms as constant.

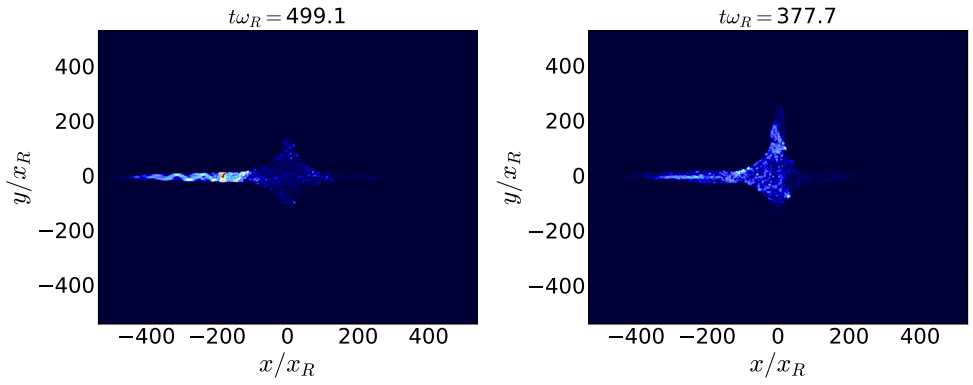

(A) (B)

FIGURE 4.6: These figures depict cases with undesirable splitting probabilities where in case for A the velocity is $v = 1v_R$ and $\varepsilon = 0.1$ and for B $v = 1.5v_R$ and $\varepsilon = 0.2$.

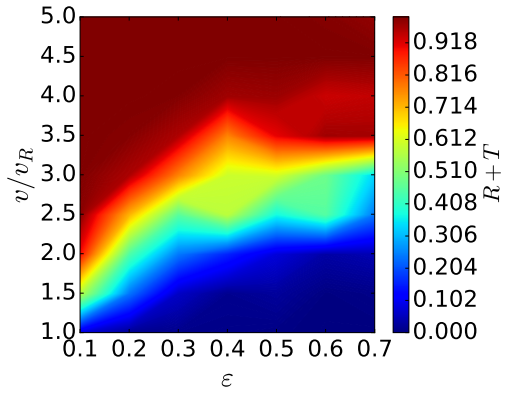

(A) Combination of Reflection and Transmission

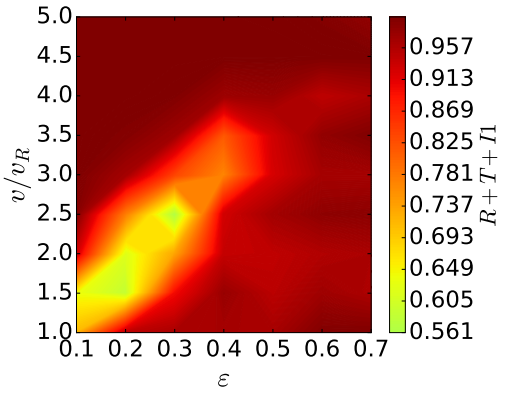

(B) Combination of Reflection, Transmission and Atom Input

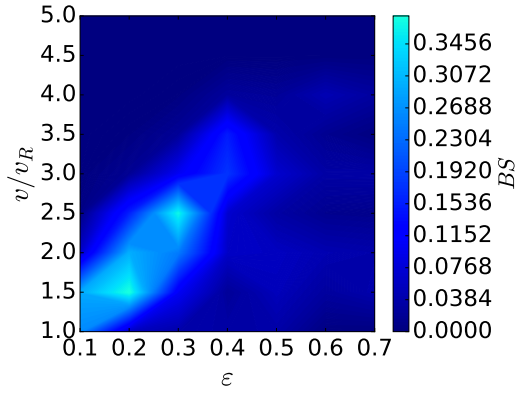

(C) Beam-Splitter

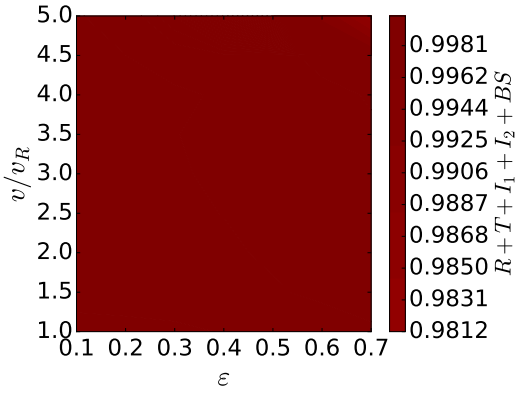

(D) All Waveguides and the Beam-Splitter

FIGURE 4.7: The plot in A shows the combination of reflection and transmission probability. It should be around unity for a decent beam-splitter. B shows the combination of reflection, and transmission and scattering back into the input. There are major probability gaps in here which come from atoms being trapped in the beam-splitter, as shown in C. Lastly, we add up the probability of finding the atoms in the waveguides and the beam-splitter. The discrepancy here comes from atoms escaping.

For cases where the initial velocity is insufficient for the packet to travel through

the beam-splitter we get that the majority is reflected back into the input. However, additionally to getting reflected back into the waveguide, a part of the wave-function gets trapped. As seen in Fig. 4.6, which depicts two cases of this happening. In sub Fig. 4.6a most of the wave-function get reflected back into the atom input and only some of it gets trapped. However, in sub Fig. 4.6b we see that some parts of the wave escapes into the reflection guide. Hence, we always need to consider the form of the wave in addition to the splitting. Nonetheless, we can use this as a criterion to filter out ineffective splitting behaviour by checking how much of the packet is still in the beam-splitter, see Fig. 4.7. In this Figure we see the combination of the reflection and transmission probabilities A(4.7a), which is then combined with the input probability, B(4.7b), the probability of finding the atoms in the beam-splitter can be seen in C(4.7c) and the loss, D(4.7d). These figures in combination with Fig. 4.3 gives a good ansatz to find suitable splitting parameters. However, none of the observed splitting have been coherent and thus the overall fringe quality will be lowered. Nonetheless, they could be used in an multi mode atom interferometer if desired.

4.5 Changes to the Beam-Splitter

The chosen parameters of the last section did not lead to any desirable splitting values, mainly due to the excitation of the wave-packet into higher transverse states. An effect that gives rise to this is the large number of transverse modes in our waveguides, which have relatively close eigen energies. The biggest gap in energy separation between the eigenstates is between the ground state and the first excited state, which is comparable to the one found in the harmonic oscillator. Unlike the harmonic oscillator, the level separation then decreases with increasing energy[105], making transitions to higher states easier to occupy several different eigen states. Additionally, the atoms receive additional kinetic energy when they enter the beam-splitter due to its potential depth, which is created by the overlap of the two Gaussian lasers. This extra kinetic energy could facilitate the occupation of higher energy states inside the beam-splitter, as the energy levels, there are lower than those of the waveguides. Making it easier for the beam-splitter to excite the atoms into higher eigenstates due to non-coherent splitting. From which they get transferred to the higher eigenstates of the waveguide when leaving the beam-splitter. This reduces the kinetic energy along the longitudinal directions of the outputs in comparison to the input.This can be reduced by narrowing our waveguides, which then raises the energy separation between the the modes[105], and also reducing the depth of the potential. This would reduce the energy the atoms could gain from the depth of the beam-splitter and thus would make it harder for the atoms to reach higher transverse energy levels. A schematic for this can be seen in Fig. 4.8. The combination of two modifications could potentially improve the splitting probabilities[106].

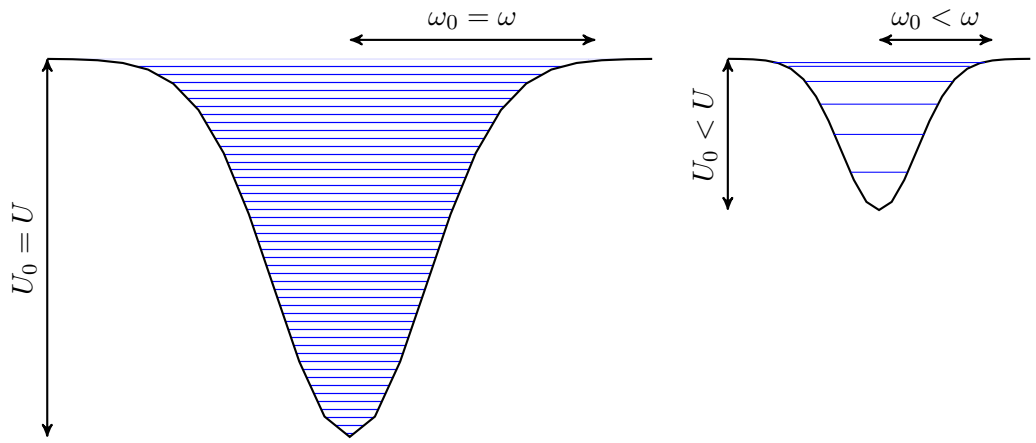

FIGURE 4.8: A representation of the transverse energy levels and their relation to the form of the waveguide. Generally speaking a narrower waveguide has bigger spacing separation between the energy levels and hence less energy levels.

4.5.1 Parameters: $U_0 = -2E_R$ and $\omega_0 = 1\mu m$

From here on we start changing the the width of our waveguides to $\omega_0 = 1\mu m$ and their depth to $U_0 = -2E_R$. However, we also change the wavelength of the laser beams to $720nm$ to accommodate more fringes in the beam-splitter. For this cases we will look at a range of velocity between $v = 0.4v_R$ and $v = 1.4v_R$, the epsilon varies between 0.1 to 0.5 and their step sizes are $0.2v_R$ and 0.1 respectively. From these individual runs we can obtain valuable insight for suitable splitting parameters. Fig. 4.9 shows how many atoms are in the inputs for atoms(A) and the vacuum(B), the reflection probability(C), transmission probability(D), the probability of atoms being trapped in the beam-splitter(E) and the combination of reflection and transmission(F). The plots show us that the velocity must be above $v = 1.2v_R$ and the polarisation value must be above $\varepsilon = 0.3$.
Two examples for this would be $v = 1.2v_R$ and $\varepsilon = 0.4$, and the other one could be $v = 1.4v_R$ and $\varepsilon = 0.5$, which can be seen in Fig. 4.10. The form of the wave-function in the transmission guide is similar for both cases. However, more of the wave-function get trapped in the cases where $v = 1.2v_R$ and $\varepsilon = 0.4$. On the other hand Fig. 4.10b has a higher loss, as more of the wave-functions escape.

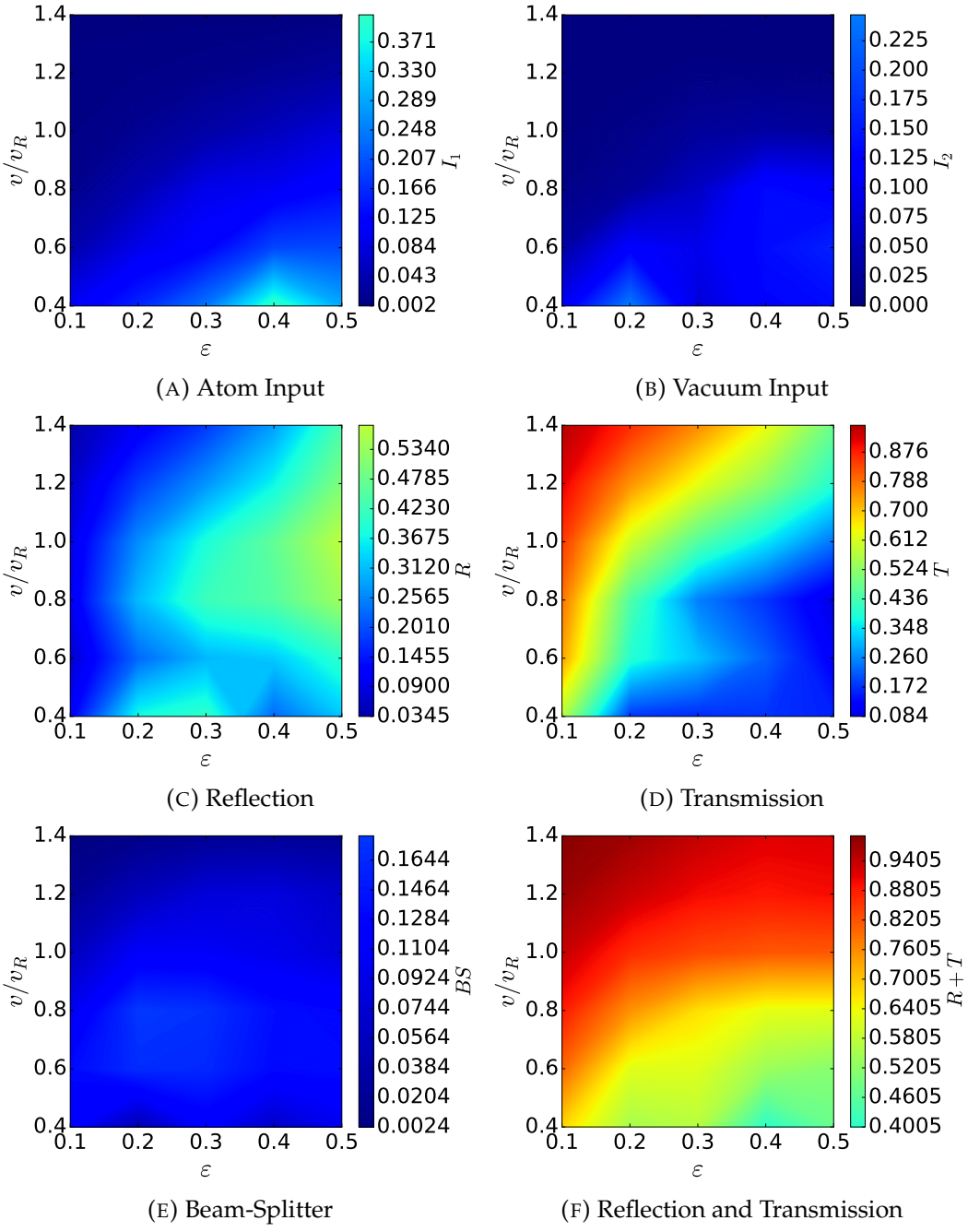

(A) Atom Input (B) Vacuum Input

(C) Reflection (D) Transmission

(E) Beam-Splitter (F) Reflection and Transmission

FIGURE 4.9: These figures show the probabilities of finding the atoms at the end of the simulations in atom input (A), vacuum input (B), reflection waveguide(C), reflection(D), beam-splitter(E) and reflection and transmission together(F). All of these together determine areas of interest for potentially suitable splitting regions.

However, looking at Fig. 4.11 we see that the coherence has improved due to shrinking and narrowing the waveguides. This is especially noticeable for the transmission wave(blue dotted line and green dash-dotted), which was previously minuscule, see Fig. 4.5. Also, the coherence of the reflection improved for both cases, while for $v = 1.2v_R$ and $\varepsilon = 0.4$ it only went up slightly(red dashed line) for the $v = 1.4v_R$ and $\varepsilon = 0.5$ it improved greatly(cyan solid).

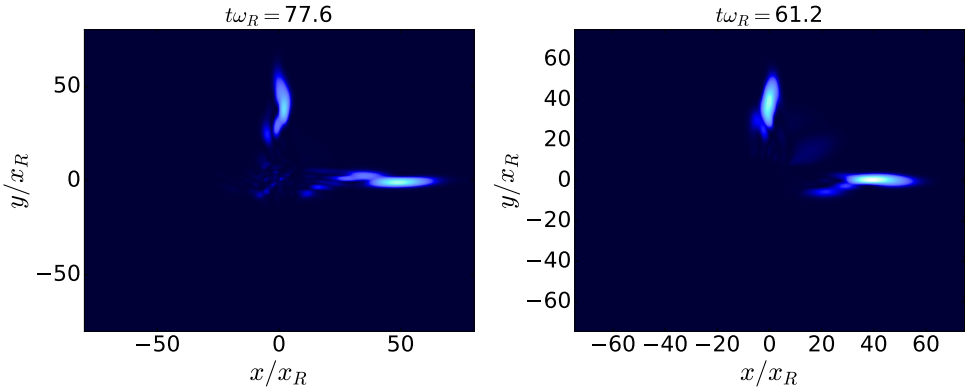

(A) (B)

FIGURE 4.10: These figures show the wave-function at the end of the simulation. The constant parameters for these calculations are , $\theta = 90°$, $\omega_0 = 1\mu m$, $\sigma_x = 0.73\mu m$, $U_0 = -2E_R$, $\lambda = 720nm$. The individual parameters are $v = 1.2v_R$ and $\varepsilon = 0.4$ for A and $v = 1.4v_R$ and $\varepsilon = 0.5$ for B. The forms of the wave-functions that get scattered into the reflection and transmission guide are similar for both. However, they differ in that more atoms get trapped in A while more can escape in B.

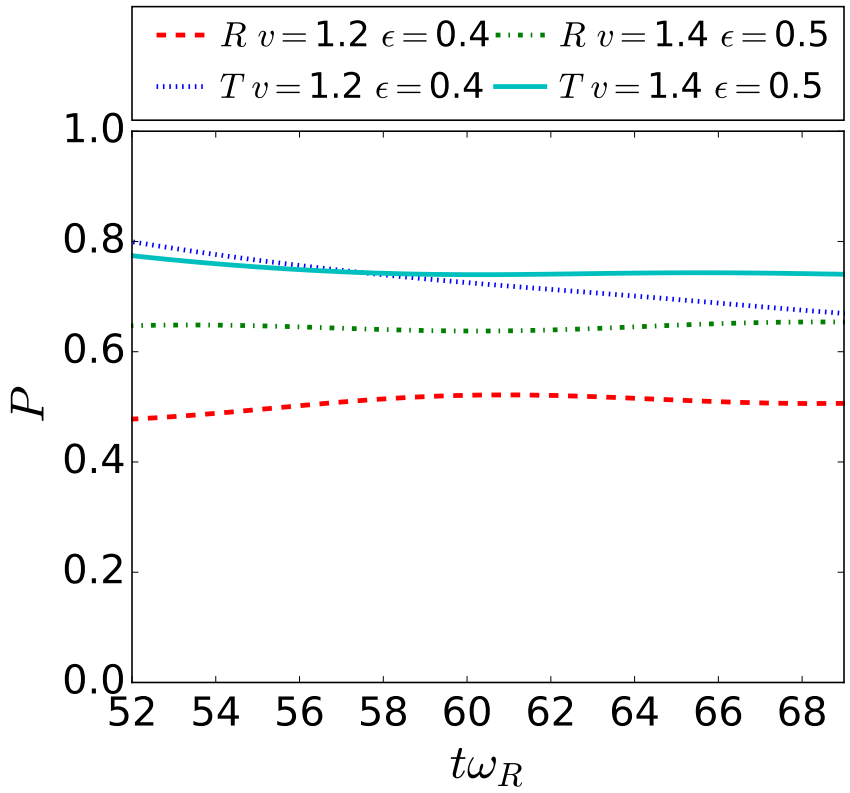

FIGURE 4.11: Plots showing the percentage of the wave-function inside transmission and reflection waveguide being in the ground state as the wave travels inside them after the splitting. For the cases with $v = 1.2v_R$ and $\varepsilon = 0.4$(reflection red dashed and transmission blue dotted) and $v = 1.4v_R$ and $\varepsilon = 0.5$(reflection green dot-dashed and transmission solid cyan)

Nonetheless, the splitting should still be improved, because the recombination will reduce the output quality further for an interferometer. Additionally, the number

of fringes in the beam-splitter has been reduced so dramatically that we are now dealing with splitting behaviour due to potential barriers of each fringe, instead of due to lattices. Hence, we increase the width of the waveguide to $\omega_0 = 1.5\mu m$, see Fig. 4.12.

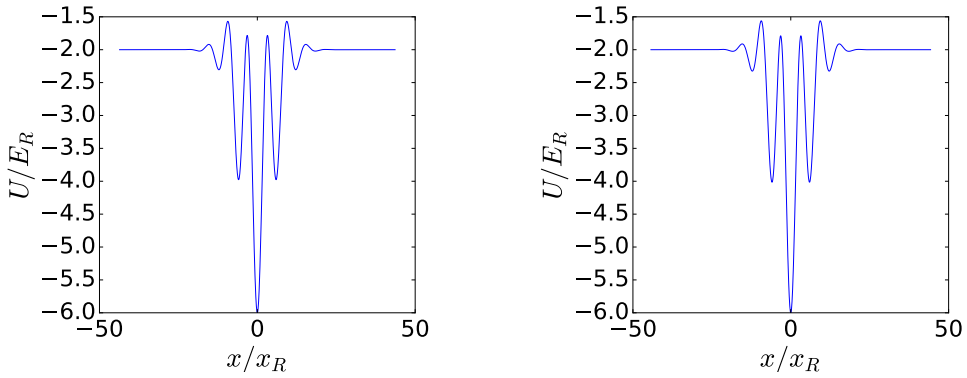

(A) $\omega_0 = 1\mu m$ (B) $\omega_0 = 1.5\mu m$

FIGURE 4.12: Plots showing the cross-section of the potential for a $U_0 = -2E_R$, $\theta = 90°$, $\varepsilon = 0.5$, $\lambda = 720nm$ $\omega_0 = 1\mu m$(A) and $\omega_0 = 1.5\mu m$(B).

4.5.2 Parameters: $U_0 = -2E_R$ and $\omega_0 = 1.5\mu m$

The splitting probabilities for an increase in the Gaussian laser beam's width to $\omega_0 = 1.5\mu m$ can be seen in Fig. 4.13. From these graphs we can deduce that the parameters necessary for decent splitting probabilities. A suitable combination of parameters would be $v = 1.4v_R$ and $\varepsilon = 0.4$. A velocity of $1.2v_R$ has too much of the wave being trapped inside the beam-splitter. However, we can also use this to directly compare how the change in the width of the waveguides influences the splitting probabilities. The first point to notice is that more atoms get reflected back into the input, which is to be expected as there are more fringes for $1.5\mu m$, making is harder for the atoms to tunnel through. On the other hand, the fringes in the beam-splitter are aligned at an $45°$ angle in comparison to the waveguide, thus extra fringes reduce the number of atoms that get scattered into the vacuum input. This can also be seen in the transmission and reflection probability, where the probabilities for transmission is reduced while the reflection probability is increased.

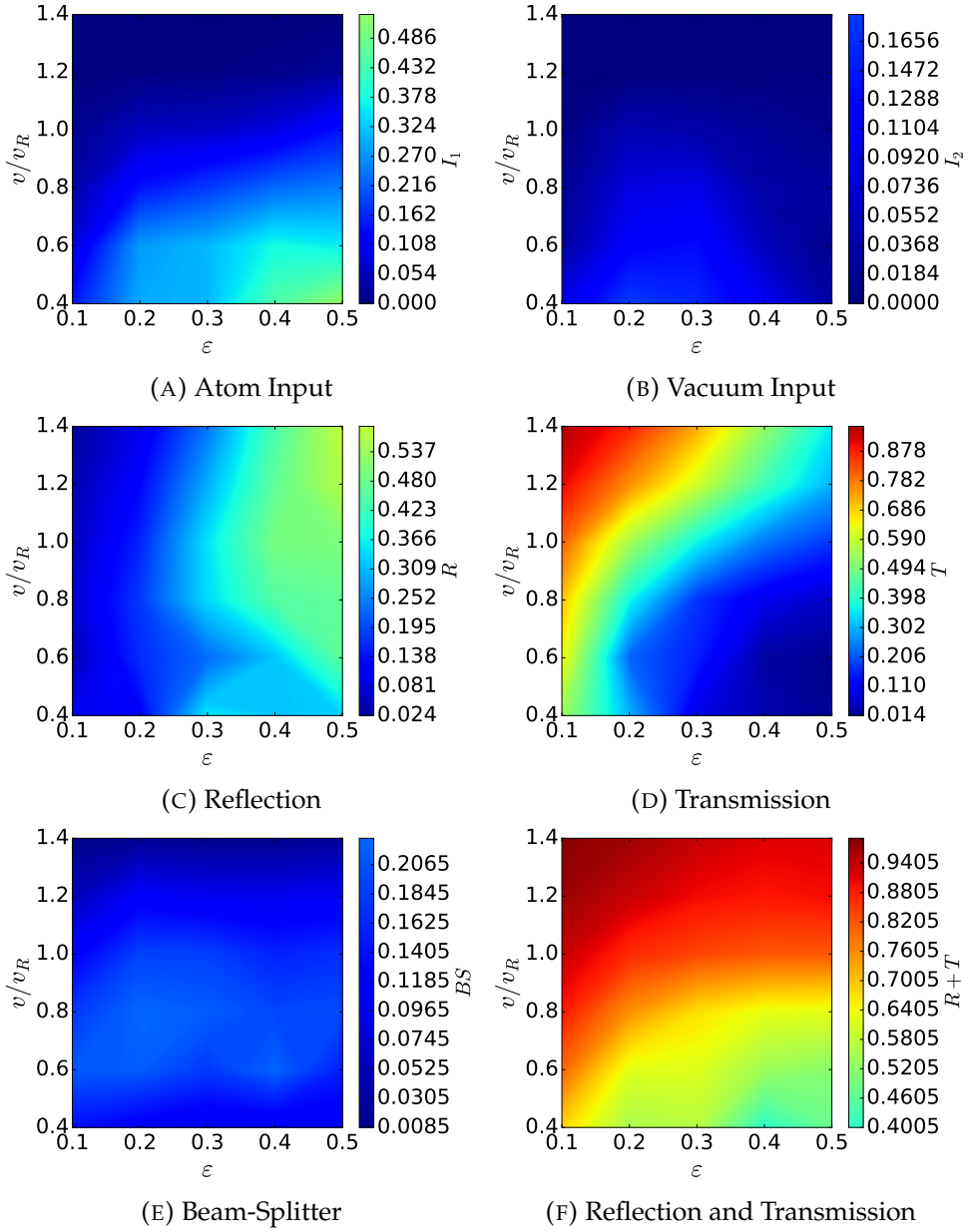

(A) Atom Input (B) Vacuum Input

(C) Reflection (D) Transmission

(E) Beam-Splitter (F) Reflection and Transmission

FIGURE 4.13: Probabilities of finding the atoms in specific regions of the simulations. The parameters for these calculations are $U_0 = -2E_R$, $\theta = 90°$, $\varepsilon = 0.5$, $\lambda = 720nm$ and $\omega_0 = 1\mu m$.

After having calculated the probabilities, it is important to have a direct look at the wave-functions for suitable candidate splitting probabilities. Fig. 4.14 shows the absolute square of the wave-functions for different parameters at the end of the simulation and Fig. 4.15 shows the percentage of the wave-function inside the reflection and transmission waveguide being in the ground state.

Fig. 4.14 show the wave-functions of four different simulations, where Fig. 4.14a is for $v = 1.2v_R$ and $\varepsilon = 0.4$. From this, it is clearly visible that some of the wave-function gets trapped inside the beam-splitter. It is only marginally better than the case for $\omega_0 = 1\mu m$, seen Fig. 4.12a. Also, the coherence in this instant is not the best

especially for the transmission, see red dashed line Fig. 4.15. Increasing the polarisation from this to $\varepsilon = 0.5$ can be seen in Fig. 4.14b, which is very similar to to the previous polarisation. This can also be seen in the coherence, see the blue dotted line in Fig. 4.15, which overlaps with the line for $v = 1.2v_R$ and $\varepsilon = 0.4$. This is due to the relationship of the fringe hight to the potential depth of the waveguide. This means that an increase of the polarisation of 0.1 increase the fringe hight only minimally and unless the wave travels through a fringe now instead of over it we will not see any significant difference. On the other hand, when the velocity is increased to $v = 1.4v_R$ the wave-function in the transmission waveguide slightly decreases, see Fig. 4.14c and green dash-dotted line Fig. 4.15. Lastly, we look at the case with increased polarisation and velocity, being $\varepsilon = 0.5$ and $v = 1.4v_R$, respectively, see solid cyan line Fig. 4.15, which is figurative identical to line of with a lower polarisation. Hence, the best cases for the parameters used were $\varepsilon = 0.4$ and $v = 1.2v_R$ and $\varepsilon = 0.5$ and $v = 1.2v_R$. However, both of these still have a significant amount of loss which can also be seen in their wave-function.

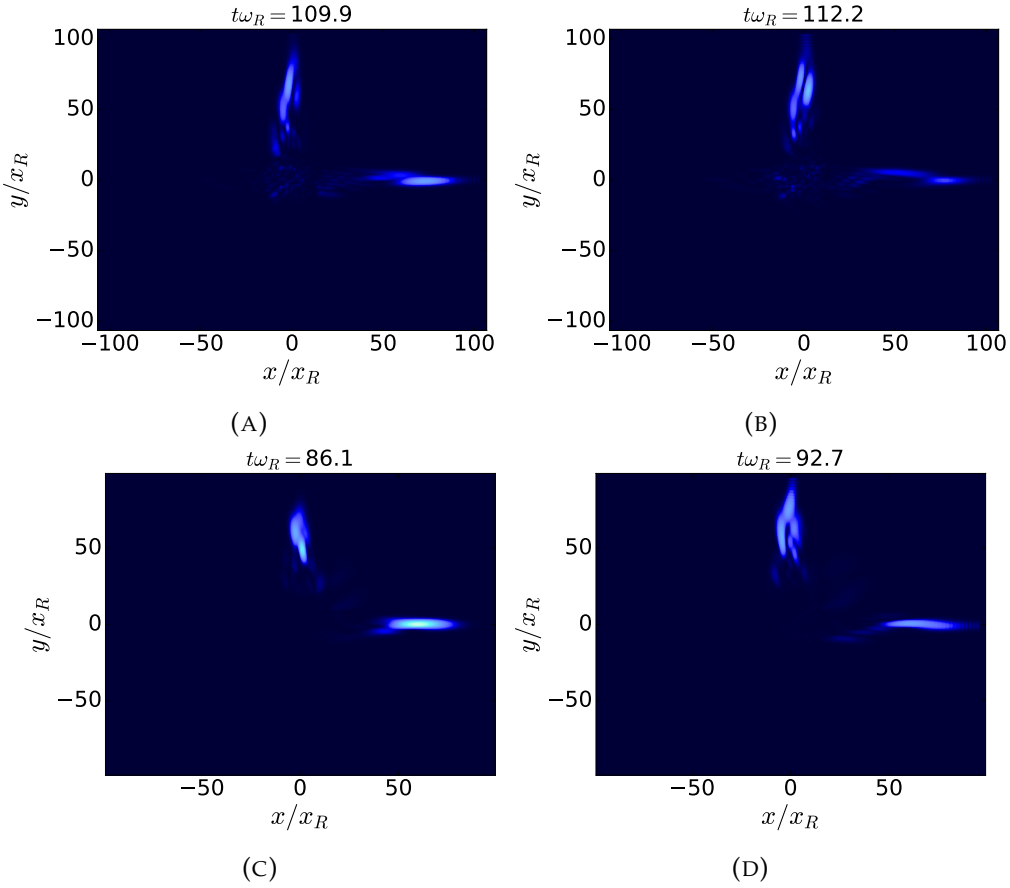

FIGURE 4.14: The wave-function at the end of the simulations, where A is $v = 1.2v_R$ and $\varepsilon = 0.4$, B is $v = 1.2v_R$ and $\varepsilon = 0.5$, C is $v = 1.4v_R$ and $\varepsilon = 0.4$ and lastly, D is $v = 1.4v_R$ and $\varepsilon = 0.5$. The other parameters are $U_0 = -2E_R$, $\theta = 90°$, $\lambda = 720nm$ $\omega_0 = 1.5\mu m$.

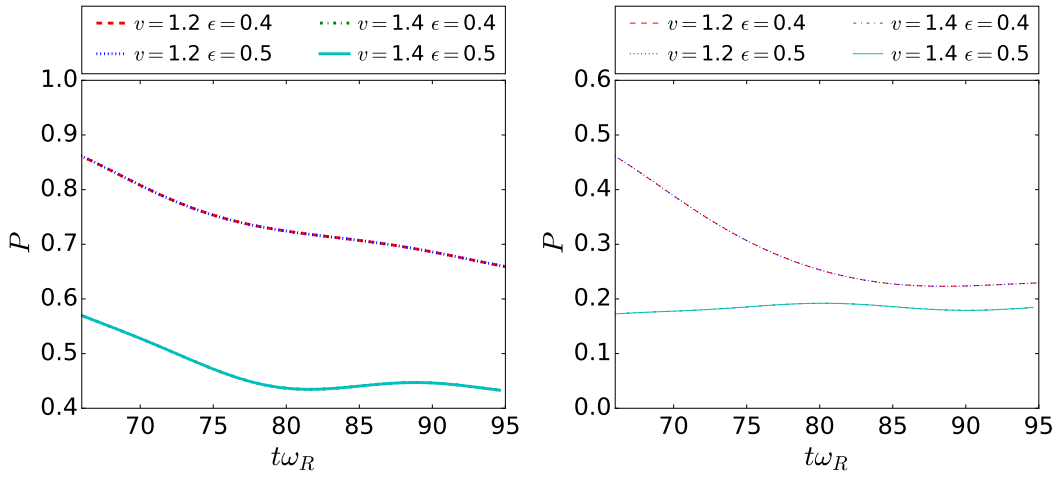

FIGURE 4.15: A shows the percentage of the atom being in the ground state of the transmission waveguide and B shows the same for the reflection waveguide for the cases $v = 1.2v_R$ and $\varepsilon = 0.4$(red dashed), $v = 1.2v_R$ and $\varepsilon = 0.5$(blue dotted) $v = 1.4v_R$ and $\varepsilon = 0.4$(green dash-dotted) and, $v = 1.4v_R$ and $\varepsilon = 0.5$(cyan solid), with the other parameters being $U_0 = -2E_R$, $\theta = 90°$, $\lambda = 720nm$ $\omega_0 = 1.5\mu m$.

4.5.3 Parameters: $U_0 = -5E_R$ and $\omega_0 = 1.0\mu m$

A way of reducing this loss is the increasing of the waveguide depth. However, we may not want to increase it too much as this energy could lead to even higher transverse excitations in the splitting. Therefore, we will change it from $U_0 = -2E_R$ to $U_0 = -5E_R$ and go back to $\omega_0 = 1.\mu m$ for the width of the waveguides. The variable parameters for this run will be a velocity with the range of $0.6v_R$ to $3.0v_R$, going in $0.2v_R$ steps. The other parameters stay the same. From this we calculate the splitting probabilities: probability of finding the atoms in their input, Fig. 4.16a, in the vacuum input, Fig. 4.16b, in the reflection probability, Fig. 4.16c, transmission probability, Fig. 4.16d, atoms trapped inside the beam-splitter, Fig. 4.16e and the combination of reflection and transmission probabilities, Fig. 4.16f. From these plots we see that the minimum velocity should be $v = 2v_R$ and the minimum for the polarisation is $\varepsilon = 0.3$.

Hence, sets of parameters for desirable splitting behaviour are $v = 2v_R$ and $\varepsilon = 0.4$ and $v = 2v_R$ and $\varepsilon = 0.5$. For these, we take a closer look at their wave-functions. Additionally, we could compare them with the example wave-functions for the cases where $U_0 = -2E_R$. The outputs can be seen in Fig. 4.17, where Fig. 4.17a has a velocity of $v = 1.2$ and a polarisation of $\varepsilon = 0.4$. The wave-function gets scattered into all waveguides with the biggest proportion going into the reflection. This is quite different from the case with $U = -2E_R$, seen in Fig. 4.10a, where most got either reflected or transmitted and only some got trapped inside the beam-splitter. This difference comes from the increased beam-splitter fringe size. The size of these fringes is dependent on the depth of the beam-splitter and the polarisation and hence increasing the depth increase the fringe height, making it harder for the wave-function to tunnel

through. Additionally, looking at red dashed and blue dotted line for the coherence of the reflection of the transmission perspectively in Fig. 4.18a shows us that overall coherence decreased when compared with the calculation for $U_0 = -2E_R$, see Fig. 4.11. The same behaviour can bee seen in Fig. 4.17b and the green dash-dotted and solid cyan line in Fig. 4.18a , which has a velocity of $v = 1.4$ and a polarisation of $\varepsilon = 0.5$, where the $U = -2E_R$ counterpart can be seen in Fig. **??** and the green dash-dotted and solid cyan line in Fig. 4.11.

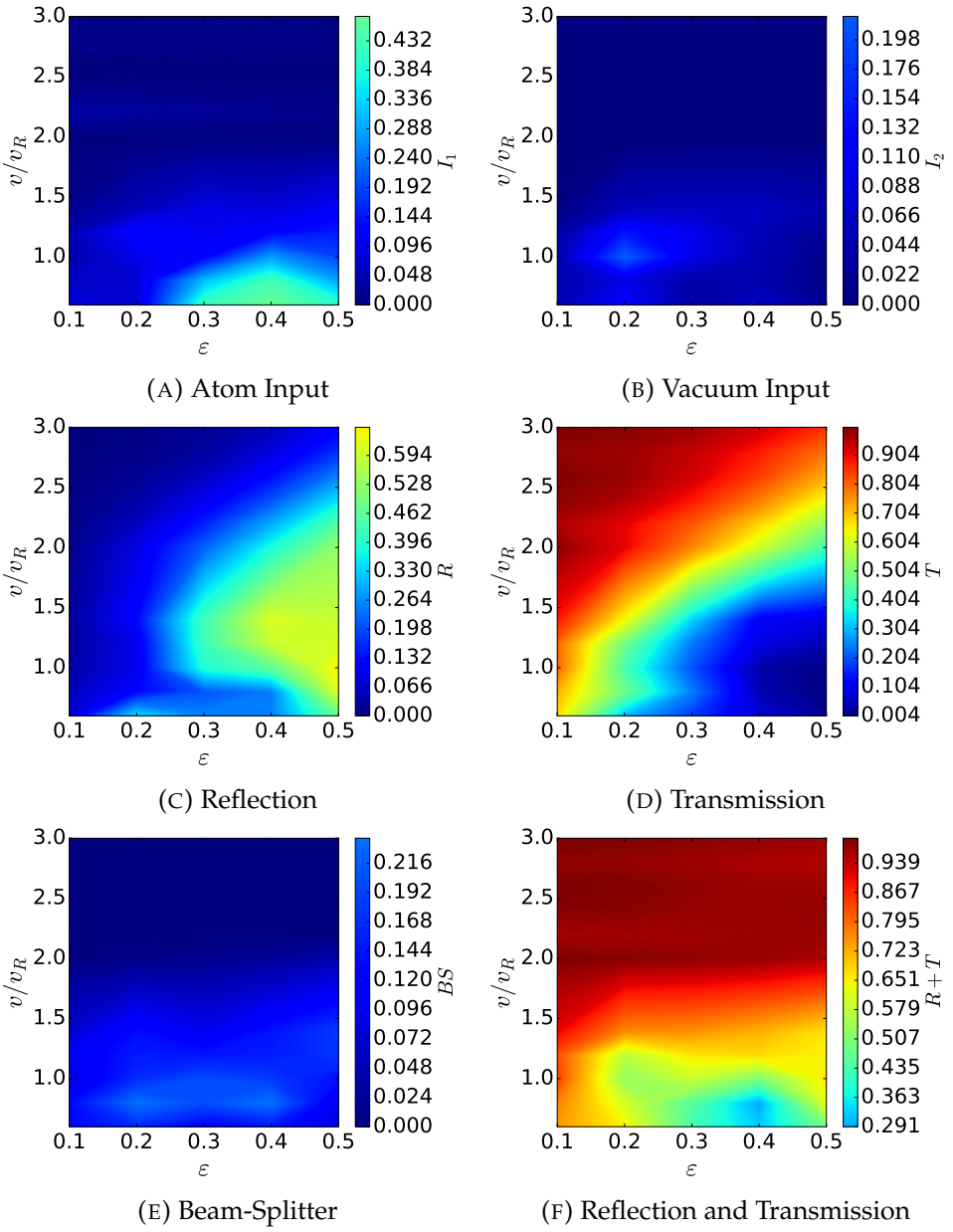

(A) Atom Input (B) Vacuum Input

(C) Reflection (D) Transmission

(E) Beam-Splitter (F) Reflection and Transmission

FIGURE 4.16: The probabilities of finding the atoms in the waveguides for, A atom input, B vacuum input. C displays the reflection probability, D the transmission probability, E shows the percentage of atoms being trapped inside the beam-splitter and F combines reflection and transmission probability. The other parameters used are $\omega_0 = 1.\mu m$, $U = -5E_R$, $\theta = 90^\circ$ and $\lambda = 720nm$.

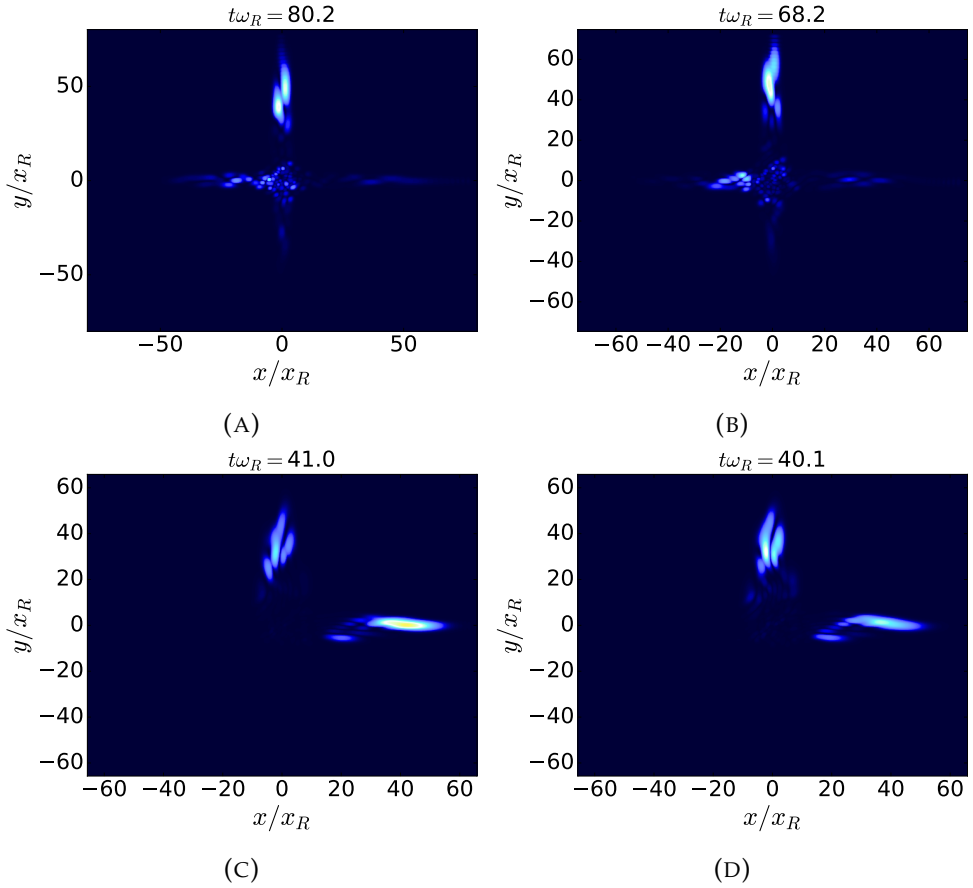

FIGURE 4.17: The wave-function at the end of the simulations for A $\varepsilon = 0.4$ and $v = 1.2v_R$, B $\varepsilon = 0.5$ and $v = 1.4v_R$, C $\varepsilon = 0.4$ and $v = 2.0v_R$ and D $\varepsilon = 0.5$ and $v = 2.0v_R$. The other parameters are $\omega_0 = 1.\mu m$, $U = -5E_R$, $\theta = 90°$ and $\lambda = 720nm$.

Lastly, we are looking at the cases which have the most desirable splitting properties in our parameter space $v = 2v_R$ and $\varepsilon = 0.4$, $v = 2v_R$ and $\varepsilon = 0.5$, these can be seen in Fig. 4.17c and Fig. 4.17d, respectively. Their coherence can be seen in Fig. 4.18b. The first one has more balanced splitting than the second. However, in both cases, the reflected wave-function is still distorted. The coherence for parameters with a more even splitting is worse.

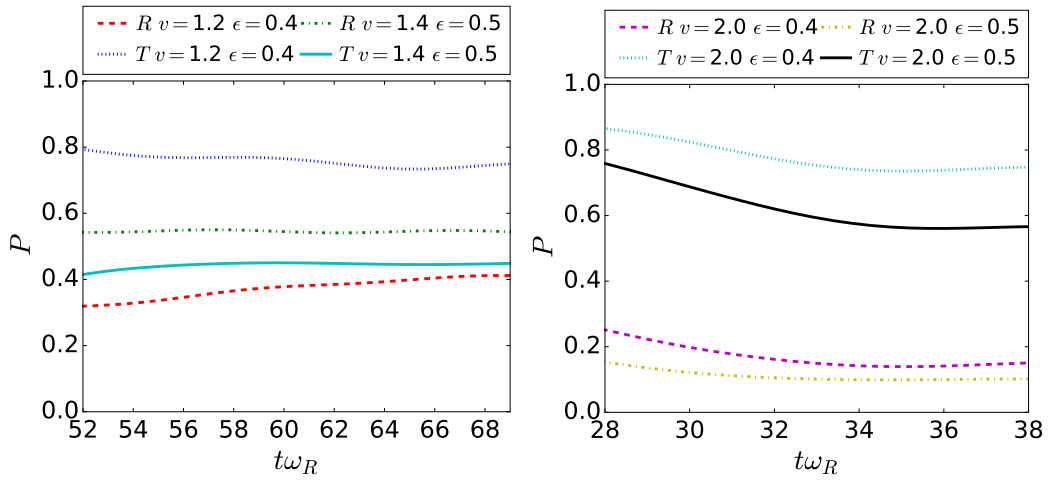

(A) (B)

FIGURE 4.18: A shows the percentage of the atoms being in the reflection and transmission waveguide, for $\varepsilon = 0.4$ and $v = 1.2v_R$(red dashed for reflection and blue dotted for transmission) and $\varepsilon = 0.5$ and $v = 1.4v_R$(green dash-dotted for reflection and cyan solid for transmission). B shows the same for $\varepsilon = 0.4$ and $v = 2.0v_R$(magenta dashed for reflection and cyan dotted for transmission) and $\varepsilon = 0.5$ and $v = 2.0v_R$(yellow dash-dotted for reflection and black solid for transmission). For the parameters $\omega_0 = 1.\mu m$, $U = -5E_R$, $\theta = 90^\circ$ and $\lambda = 720nm$.

4.6 Small Angle

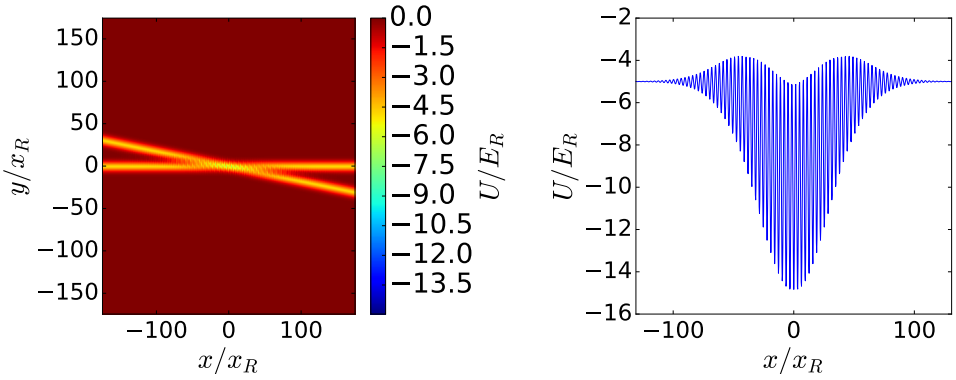

(A) Potential (B) Cross-section

FIGURE 4.19: The figures depict the potential(A) for $\omega_0 = 1.\mu m$, $U = -5E_R$, $\theta = 90^\circ$, $\varepsilon = 0.5$, $\lambda = 720nm$ and its the cross-section(B).

Having looked at the a crossing angle of $\theta = 90^\circ$ for low potential depth in the last section, we are not able to find coherent splitting for any of the parameters. The low energy narrow beam-splitter had overall only a few fringes and thus the splitting behaviour can be mostly directly attributed to tunnelling instead of interactions with a optical lattice. However, to have Bragg diffraction we will need more fringes.One way to increase the number of fringes would be to increase the width of

the waveguides, which we intentionally tried to reduce, to increase the energy spacing between the transverse eigenstates. However, we can also increase the number of fringes by changing the crossing section between our Gaussian laser beams to $\theta = 170°$. Additionally, to just increase the fringe number, such a beam-splitter has also the advantage of not changing the direction of the momentum too drastically compared to the $\theta = 90°$ case. The potential for the beam-splitter can be seen in Fig. 4.19a with its cross-section in Fig. 4.19b, for the parameters $\omega_0 = 1.\mu m$, $U = -5E_R$, $\theta = 90°$, $\varepsilon = 0.5$ and $\lambda = 720nm$.

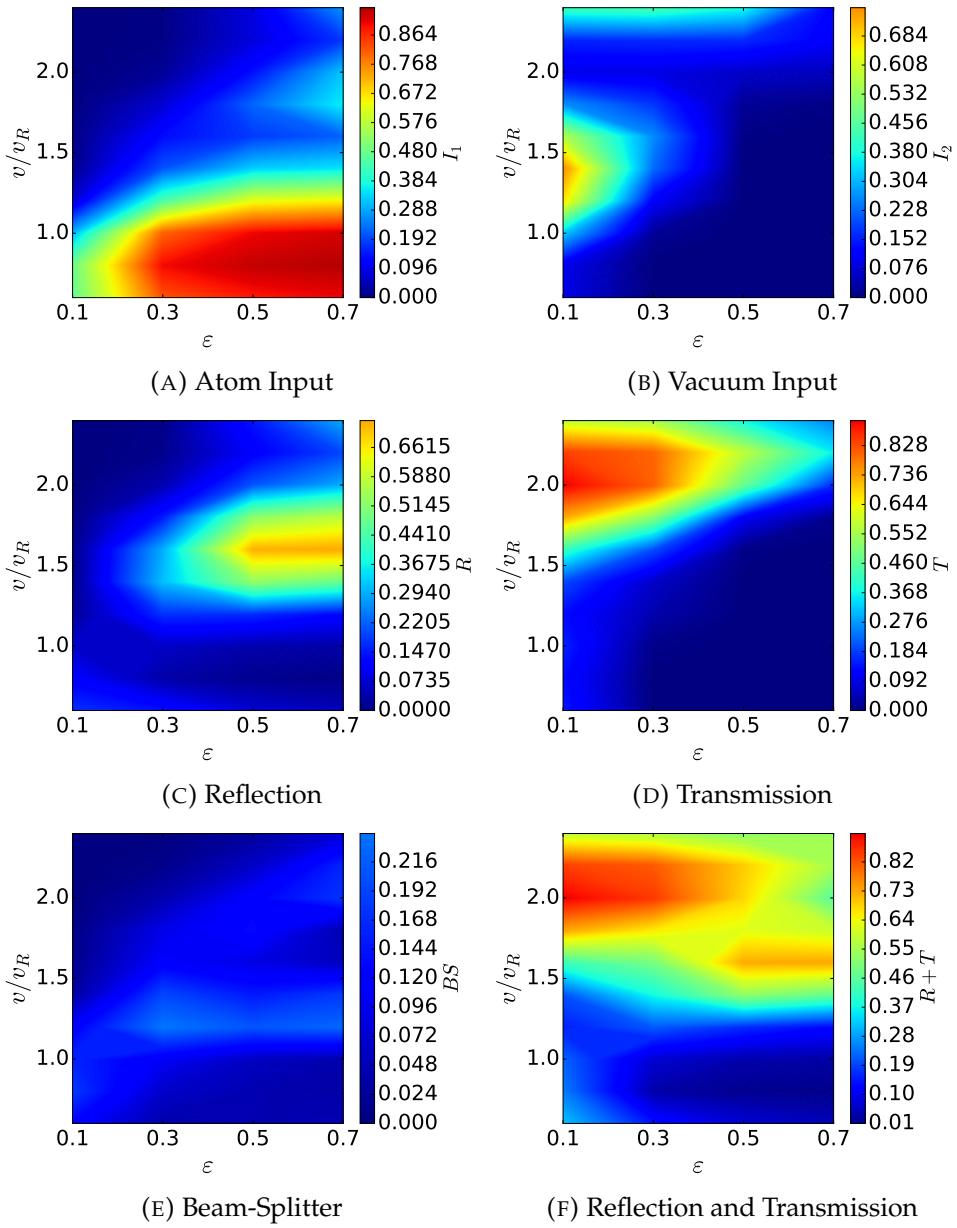

(A) Atom Input (B) Vacuum Input

(C) Reflection (D) Transmission

(E) Beam-Splitter (F) Reflection and Transmission

FIGURE 4.20: These are the probabilities for finding the atoms in the atom input(A), vacuum input(B), reflection waveguide(C), transmission waveguide(D), beams-splitter(E) and a combination of the reflection and reflection(E). For the parameters $\omega_0 = 1\mu m$, $U = -5E_R$, $\theta = 170°$, and $\lambda = 720nm$.

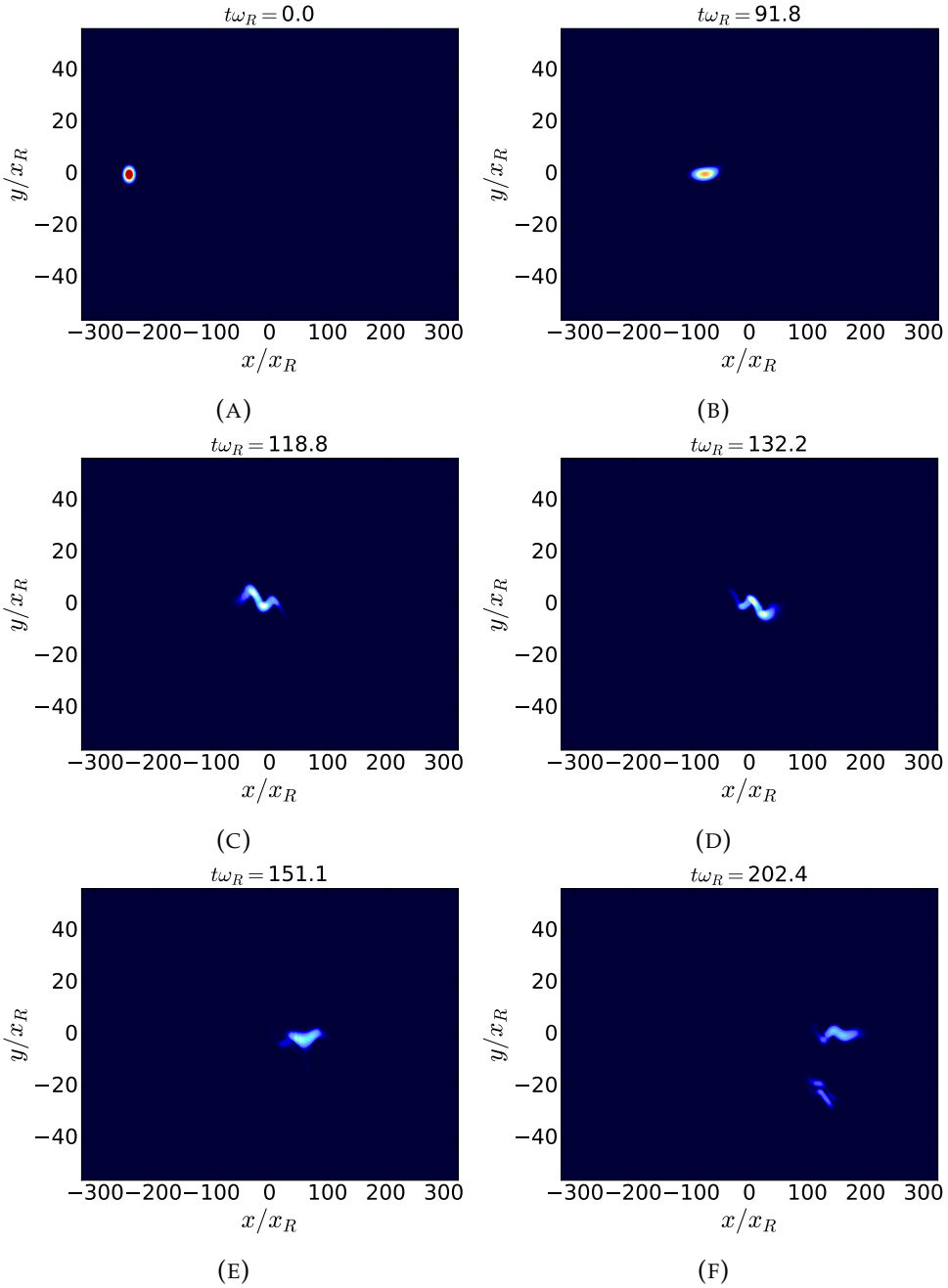

FIGURE 4.21: The Figures show the propagation of the atoms through the beam-splitter for for parameters of $v = 1.8v_R$ and $\varepsilon = 0.1$ $\omega_0 = 1.\mu m$, $U = -5E_R$, $\theta = 90°$, and $\lambda = 720nm$.

Similarly, to previous simulations we will alter the velocity from $v = 0.6v_R$ to $v = 2.4v_R$ in $0.2v_R$ intervals. The polarisation also ranges from $\varepsilon = 0.1$ to $\varepsilon = 0.7$, going in 0.2 intervals. Up until now we have defined the top waveguide as the reflection one due to the shape of the fringes as they are positioned at an $45°$ angle allowing for the atoms to be reflected into upwards into the top waveguide, for the Gaussian beams cross at $\theta = 90°$ angle. However, for $\theta = 170°$ angle that is not necessarily the case as getting reflected back into the upper waveguide would result in a much stronger directional change for the momentum. Keeping that in mind we stick to the

previous definition but we look now at the vacuum input as a potential reflection and thus it does not necessarily needs to be close to zero. Setting the other variables to $\omega_0 = 1\mu m$, $U = -2E_R$, $\theta = 170°$, and $\lambda = 720nm$, we get the probabilities seen in Fig. 4.20, where we can see that there is a substantial reflection backwards into the atom input for nearly all parameters, see Fig. 4.20a. Additionally, a lot of the wave gets trapped inside the beam-splitter.
One of the few possible possible value ranges for which we can potentially achieve good splitting would be a velocity of $v = 1.6v_R$ to $v = 1.8v_R$ and $\varepsilon = 0.1$ to $\varepsilon = 0.2$. For this case, the vacuum input would be the reflection output. Looking at the specific case $v = 1.8v_R$ and $\varepsilon = 0.1$, we see the propagation through the beam-splitter in Fig. 4.21. Starting at Fig. 4.21a the wave travels through the waveguide until it reaches the beam-splitter Fig. 4.21b. From here on out it propagates through the beam-splitter, Fig. 4.21c, 4.21d, 4.21e, and is separated. Leaving the wave-function in the state seen in Fig. 4.21f. Unfortunately, this does not improve the overall coherence of wave, see Fig. 4.22 as the wave-packet is still oscillating inside the waveguide. Similar behaviour can be seen for the other potential parameters. The increase of the angle would increase the area of the final atom interferometer. However, inferring from the wave-function shape it does not provide a substantial benefit.

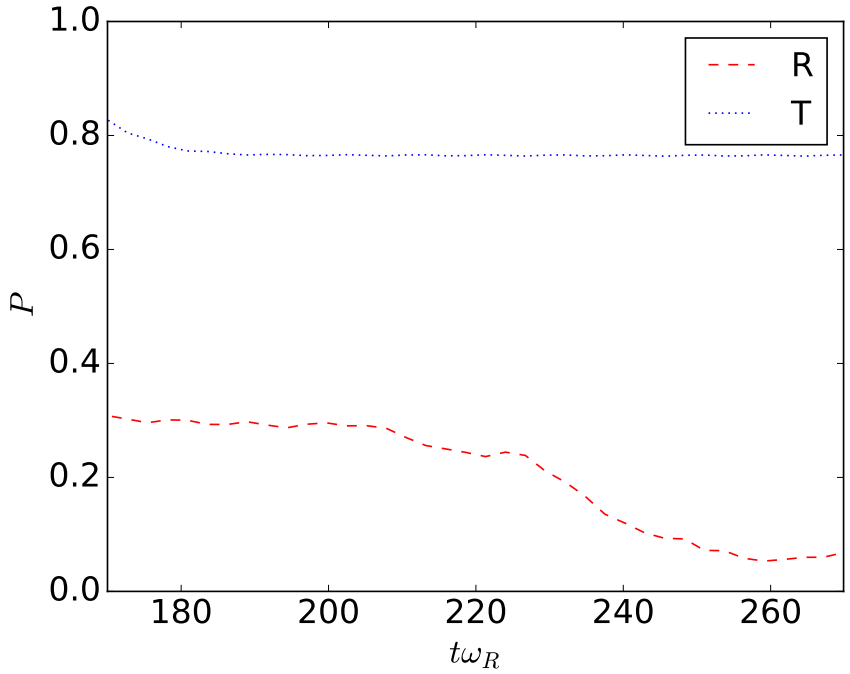

FIGURE 4.22: Plots showing the percentage of the wave being in the ground state of transmission(blue dotted) and reflection(red dashed line) waveguide after the splitting for $v = 1.8v_R$, $\theta = 170°$, $\varepsilon = 0.1$, $\omega_0 = 1\mu m$, $\sigma_x = 0.73\mu m$, $U_0 = -5E_R$, $\lambda = 1064nm$ and $F = 1$.

4.7 Modifications to the Beam-Splitter via a Third Beam

Our beam-splitter potential has a Gaussian dip in its centre due to the nature of the two over-lapping Gaussian beams, Sec. 2.1[94, 107]. The size of this dip can lead to a momentum shift in the atoms, which is a potential cause for the excitation of the higher transverse modes after the splitting. This could well be cancelled out by the overlap of a third Gaussian beam which would be blue-detuned[72, 106], in comparison to the two red-detuned beams that provide the wave-guides. This blue-detuned beam would work as a reflector (and so provide positive potential) as opposed to an attractor (negative potential). This will only be done to the case, where the angle between the two original beams is $90°$, as this is the case with the most symmetrical potential. For our simulation we will simply add a counter potential, that fills in the Gaussian well so that the cross-section of the potential is zero for the case with no fringes. To find this potential we look at our original beam-splitter, Eq. 2.8 and set $y = 0$, $\epsilon = 0$ and $\theta = 90°$, giving us

$$x' = \cos(\frac{\pi}{4})x, \tag{4.26}$$

$$y' = -\sin(\frac{\pi}{4})x, \tag{4.27}$$

$$U_0(x', y') = -2U_0 e^{-\left(\frac{1}{\omega_0^2}\right)\times((1-\cos\left(\frac{\pi}{2}\right))x'^2+\left(1+\cos\left(\frac{\pi}{2}\right)\right)y'^2)}, \tag{4.28}$$

$$A(x', y') = \cosh(2\sin(\frac{\pi}{2})\left(\frac{x'y'}{w_0^2}\right)), \tag{4.29}$$

which can be simplified to

$$U_0(x', y') = -2U_0 e^{-\left(\frac{x}{\omega_0}\right)^2}, \tag{4.30}$$

$$A(x', y') = \cosh(\frac{x^2}{w_0^2}). \tag{4.31}$$

These can then be substituted into the equation for the potential

$$U(x', y') = -U_0(x', y')A(x', y'), \tag{4.32}$$

to gain

$$U(x', y') = 2U_0 e^{-\left(\frac{x}{\omega_0}\right)^2}\cosh(\frac{x^2}{w_0^2}), \tag{4.33}$$

$$U(x', y') = U_0 e^{-\left(\frac{x}{\omega_0}\right)^2}\left(e^{\left(\frac{x}{\omega_0}\right)^2} + e^{-\left(\frac{x}{\omega_0}\right)^2}\right), \tag{4.34}$$

$$U(x', y') = U_0 e^{-2\left(\frac{x}{\omega_0}\right)^2} + U_0. \tag{4.35}$$

From this we can see that the potential to counter the dip must be

$$-U_0 e^{-2\left(\frac{x}{\omega_0}\right)^2}, \tag{4.36}$$

as the second term only shows the depth of the potential from one of the Gaussian beams. Following from here we can write our new 1D beam-splitter potential as

$$U(x',y') = 2U_0 e^{-\left(\frac{x}{\omega_0}\right)^2}\left(\cosh(\frac{x^2}{w_0^2}) + \varepsilon\left(\frac{2\pi y'}{d}\right)\right) - FU_0 e^{-2\left(\frac{x}{\omega_0}\right)^2}, \tag{4.37}$$

and for the 2D case

$$\begin{aligned} U(x',y') =& 2U_0 e^{-\left(\frac{1}{\omega_0^2}\right)\times\left((1-\cos\left(\frac{\pi}{2}\right))x'^2+\left(1+\cos\left(\frac{\pi}{2}\right)\right)y'^2\right)} && (4.38)\\ &\times\left(\cosh(2\sin(\frac{\pi}{2})\left(\frac{x'y'}{w_0^2}\right)) + \varepsilon\left(\frac{2\pi y'}{d}\right)\right) && (4.39)\\ &-FU_0 e^{-2\left(\frac{x^2+y^2}{\omega_0}\right)}, && (4.40) \end{aligned}$$

where

$$x' = \cos(\frac{\pi}{4})x + \sin(\frac{\pi}{4})y, \tag{4.41}$$

$$y' = -\sin(\frac{\pi}{4})x + \cos(\frac{\pi}{4})x, \tag{4.42}$$

and F is a new coefficient, introduced so we can vary the degree of filling. It is thus directly correlated with the intensity of the third Gaussian beam that is responsible for the filling.

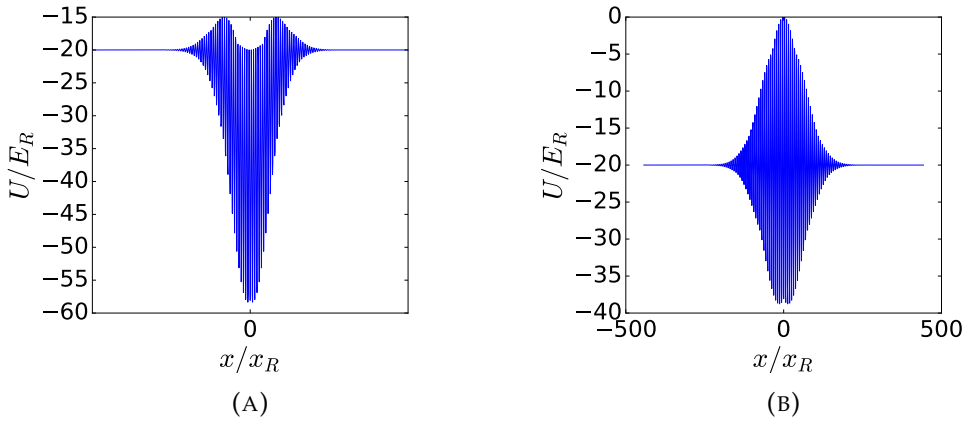

FIGURE 4.23: These Figures depict the cross-section of the beam-splitter with $F = 0$ (A) and $F = 1$ (B). The potential with the filling is symmetric around the energy value of $-20E_R$ as this is the depth of the waveguides. Additionally, in the case with filling there will be more reflection coming directly from tunnelling through the fringes instead of reflection from a well. The rest of parameters for this graphs are $\theta = 90°$, $\omega_0 = 15\mu m$, $U_0 = -20E_R$, $\lambda = 1064nm$.

However, it should be noted that this filling only applies to the case where the beams

cross at $90°$. The change in potential can be seen in Fig. 4.23, where we show two cross-sections for the beam-splitter potential one with $F = 0$ and the other one with $F = 1$. The filling lifts up the fringes so there will be more reflection coming directly from tunnelling through the fringes instead of reflection from a well.

4.7.1 Full-Filling Beam-Splitter

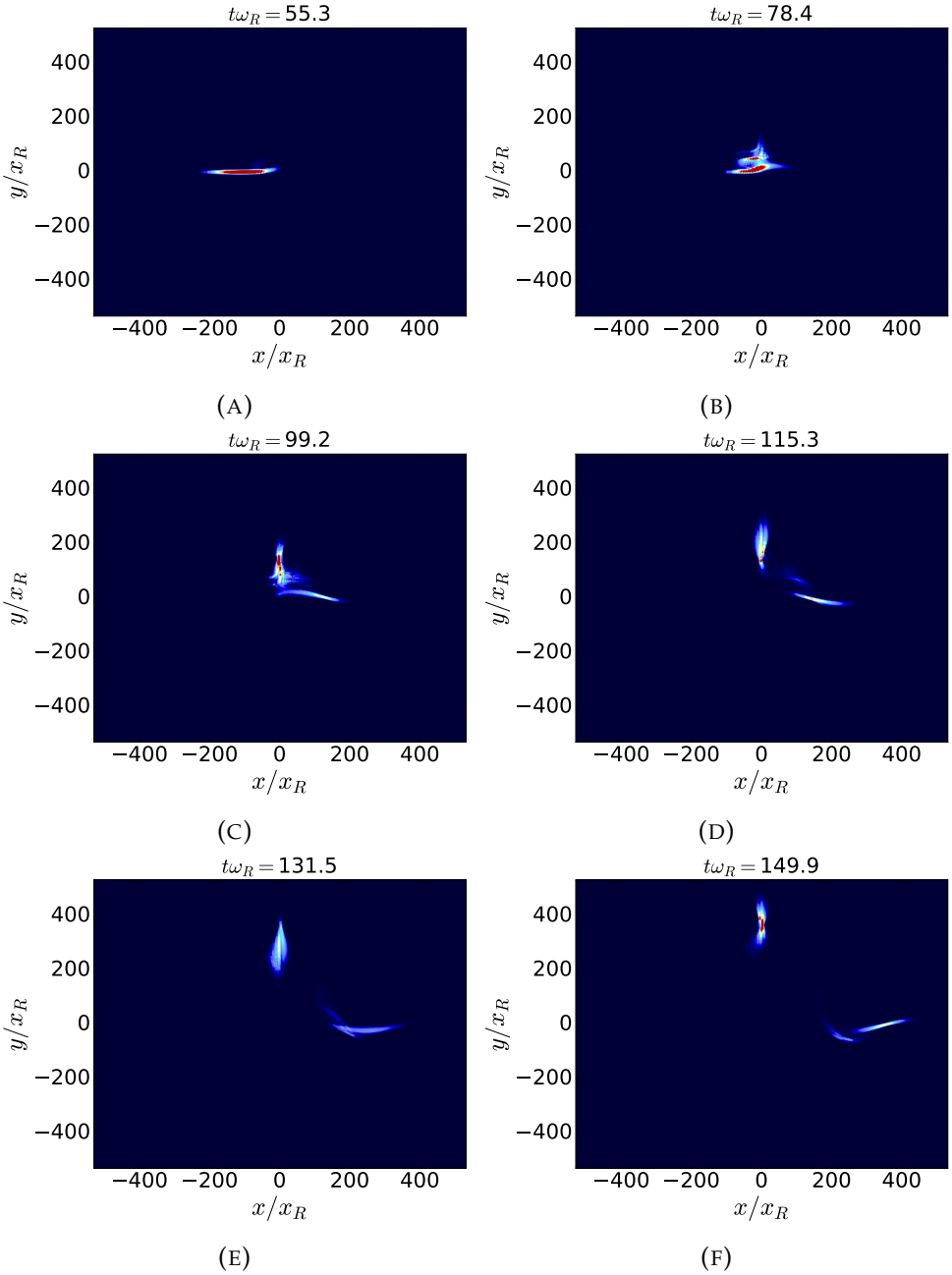

FIGURE 4.24: These graphs show the evolution of the wave-packet through the beam-splitter, for the parameter of $v = 5v_R$, $\theta = 90°$, $\varepsilon = 0.5$, $\omega_0 = 15\mu m$, $\sigma_x = 10\mu m$, $U_0 = -20E_R$, $\lambda = 1064nm$ and $F = 1$. Our wave travels through the waveguide until it comes into contact with the beam-splitter at A. Now the wave starts to travel through the beam-splitter, where it is being split in B,C and D Finishing with the wave-packet leaving the beam-splitter at E and F.

After we have derived the expression for the filling of our beam-splitter, we perform a systematic search over several velocity ranging from $1v_R$ to $6v_R$ separated by a step size of $1v_R$. The same is done for the polarisation, ε, which varies from 0 to 0.7 with a step size of 0.1. The other parameters for this are kept constant and are the following: $\theta = 90°$, $\omega_0 = 15\mu m$, $\sigma_x = 10\mu m$, $U_0 = -20E_R$, $\lambda = 1064nm$ and $F = 1$. An example of this splitting can be seen in Fig. 4.24, where the velocity and polarisation are $v = 5v_R$ and $\varepsilon = 0.5$, respectively. The wave-packet then evolves through the beam-splitter as shown in A, B, C, D and E. Leaving, the beam-splitter at F. The splitting via this beam-splitter is not coherent, see Fig. 4.25, as the wave is split into a multitude of modes. However, this does not mean that it cannot be used for interferometers. This kind of interferometer would be one that uses more than one mode for recombination. Nonetheless, it would be inferior in comparison to one that would only split the packet into the ground state mode of each waveguide.

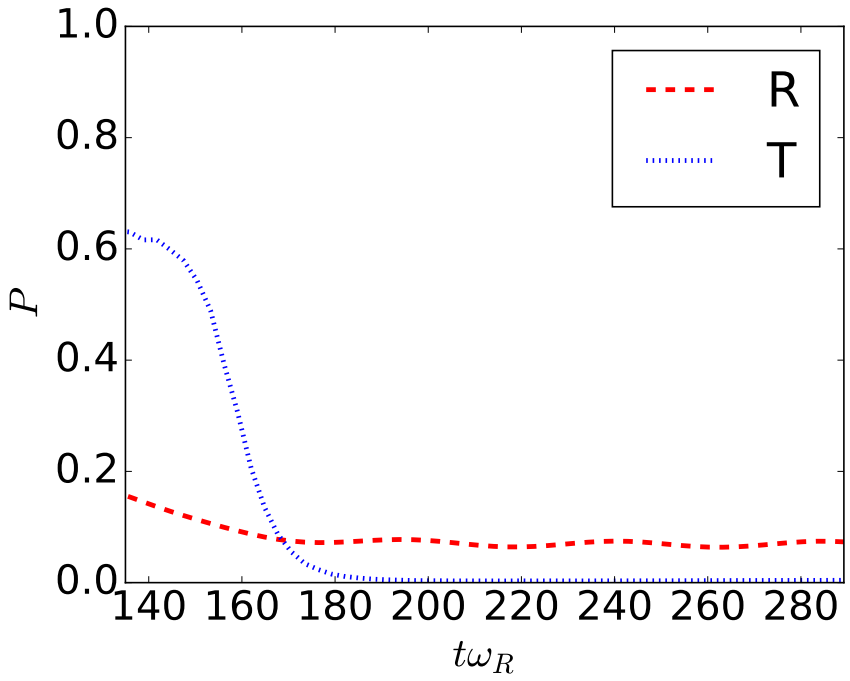

FIGURE 4.25: Plots showing the percentage of the wave-function inside transmission(blue dotted) and reflection(red dashed line) waveguide being in the ground state after the splitting for $v = 5v_R$, $\theta = 90°$, $\varepsilon = 0.5$, $\omega_0 = 15\mu m$, $\sigma_x = 10\mu m$, $U_0 = -20E_R$, $\lambda = 1064nm$ and $F = 1$.

In the same manner as we have done for the simulation depicted Fig. 4.24, we are simulating over the aforementioned range of velocity and polarisation $1v_R - 6v_R$ and $0 - 0.7$, respectively. We can deduce the probability of finding the atoms in each waveguide by integrating over each of them separately after the simulation has finished. Leaving us not only with the transmission and reflection probability, but also the information of how much is in the input arms, Sec. 4.3.1. This is presented in Fig. 4.26, where A(4.26a) is the atom input with the wave-packet in it, B(4.26b) is the vacuum input, C(4.26c) is the transmission probability and D(4.26d) is the

reflection probability. If the velocity is too low with respect to the polarisation it will get reflected back into the atom input. Once we get over that threshold, we see that the beam-splitter is splitting the incoming wave into the reflection and transmission arms. However, the area for 50;50 splitting is not smooth. This comes from the change of resonant frequency. Nonetheless, we observed something similar with the one-dimensional numerical calculation for the transmission and reflection, which also generated these regions of decent splitting probabilities.

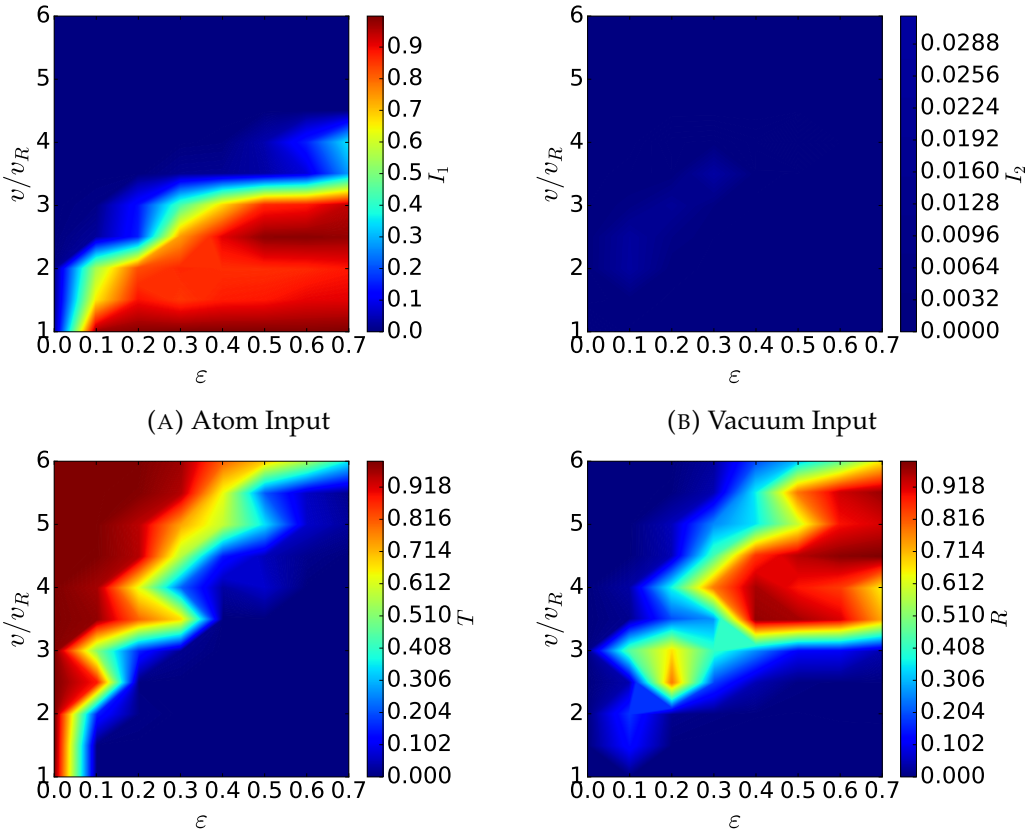

(A) Atom Input

(B) Vacuum Input

(C) Transmission

(D) Reflection

FIGURE 4.26: These graphs show the probability of finding the atoms after the splitting in the input from where the atoms started(A), the vacuum input(B), the transmission probability(C) and the reflection probability(D). From this we see that if the the velocity is too low for certain polarisation it will get reflected backwards into the waveguide where it came from. Additionally, nearly nothing gets scattered into the vacuum input, as desired. The boundary between total transmission and total reflection is more ragged which comes from the shift in the resonant frequencies.

Besides looking at the probabilities individually we can also add them together to see how closely they sum to unity, and thus how much atom loss is present. This is done to see potential loss of atoms. Looking at Fig. 4.27, where A(4.27a) is the probability of reflection and transmission added together and B(4.27b) where we have additionally added the probability of atom input. From these plot we see that we are missing a substantial fraction of the atoms, up to roughly 20%. This is due to the loss of atoms inside the beam-splitter, as the third-laser beam has lowered the

potential boundary around the edges of the beam-splitter, allowing for more atoms to escape. This can also bee seen in Fig. 4.24 in G(4.24f), where a part of the wave escapes in between the waveguides. From all this information we are able to to infer useful velocity and polarisation values for use in interferometers.

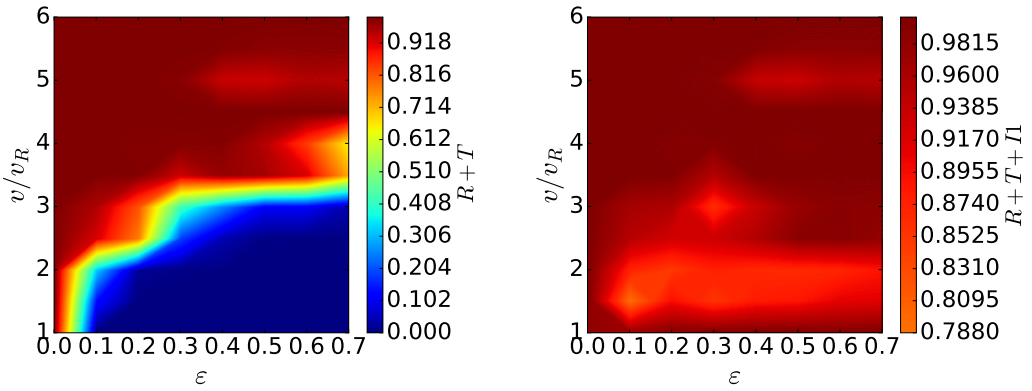

(A) Transmission and Reflection

(B) Transmission, Reflection and Atom Input

FIGURE 4.27: A shows the combination of the transmission and reflection probability and B shows the compilation of the probabilities for transmission, reflection and atom input waveguide. Nonetheless, in some cases these probabilities do not add up to unity, which is due to some atoms being lost, because the added filling potential has lowered the boundary potential of the beam-splitter making it easier for atoms to escape.

4.7.2 Beam-Splitter for Different Fillings

In the last section we have varied the velocity and the polarisation. However, we could also vary the degree of filling by adjusting F. It is varied in the range from 0 to 1 in 0.05 increments. The other parameters are as follow: $v = 5v_R$, $\theta = 90°$, $\varepsilon = 0.5$, $\omega_0 = 15\mu m$, $\sigma_x = 10\mu m$, $U_0 = -20E_R$ and $\lambda = 1064nm$. We already have an example with $F = 1$ in the last section, see Fig. 4.24, hence we will be referring back to it in this section. In addition to this, we will have a closer look at the case of $F = 0.5$, to get a better picture of how the beam-splitter splits the wave-function, instead of just looking at the splitting probabilities, see Fig. 4.28. In this simulation the wave-function goes through the beam-splitter in A(4.28a), B(4.28b), C(4.28c),D(4.28d) and exits into the respective waveguides from the beam-splitter in E(4.28e), F(4.28f). However, it is not coherent, see Fig. 4.29. A main difference between different F values lies in the shape of the wave-packet exiting the beam-splitter into the transmission waveguide. Looking at the case where $F = 0$ we see that most of the wave tunnels through the beam-splitter creating two distinct wave-packets in the transmission waveguide. One of which stays approximately the transverse ground state, while the other bounces around in the waveguide, due to transverse excitation. When the F value is increased, the reflection probability also

rises, as expected. However, the ratio between the two wave-packets in the transmission arm changes, from mostly being in the ground state to the one occupying higher modes, until it is the only wave-packet at $F = 1$.

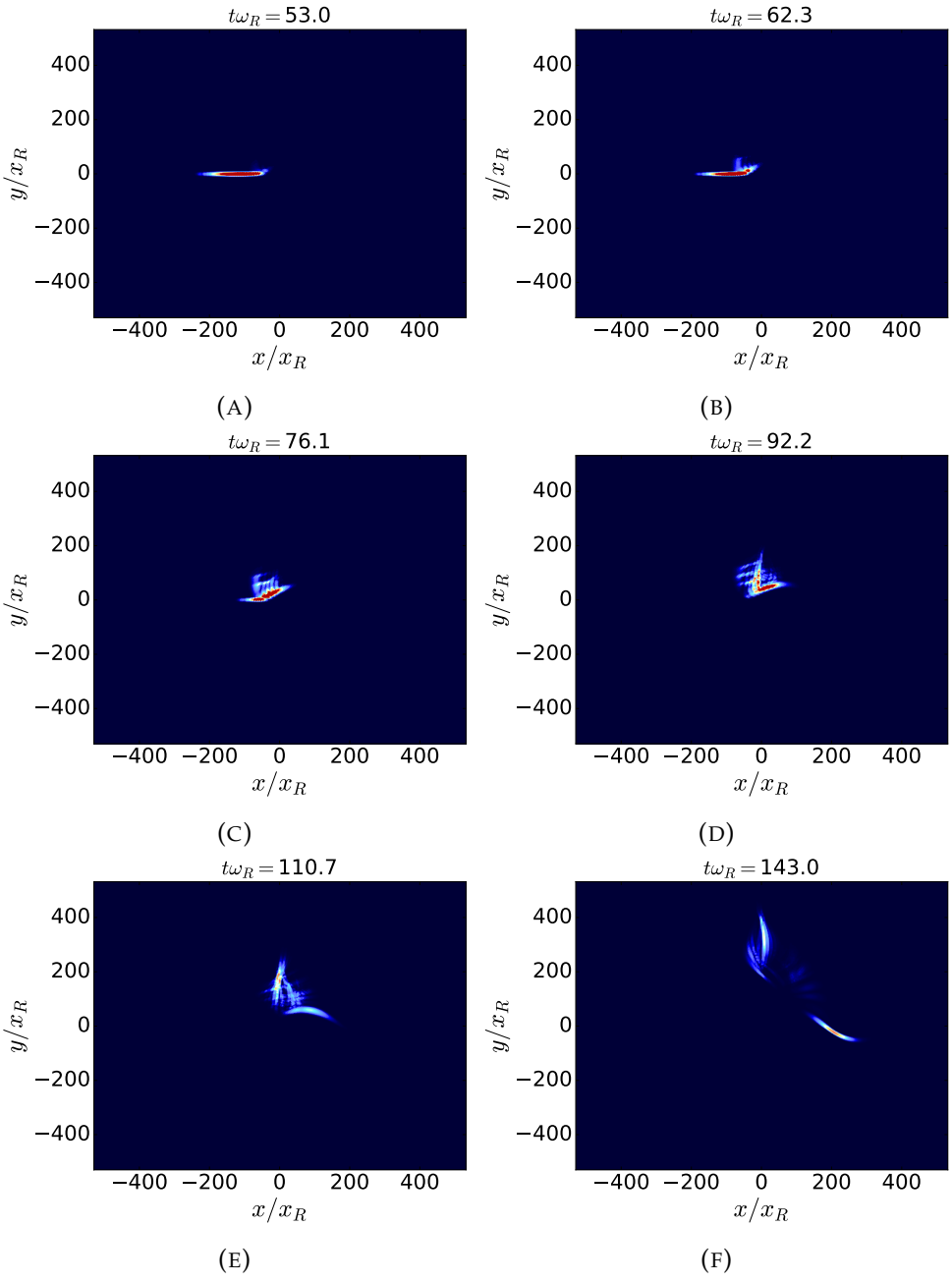

FIGURE 4.28: The evolution of the wave-packet through the beam-splitter is depicted by these figures, for the parameter of $v = 5v_R$, $\theta = 90^\circ$, $\varepsilon = 0.5$, $\omega_0 = 15\mu m$, $\sigma_x = 10\mu m$, $U_0 = -20E_R$, $\lambda = 1064nm$ and $F = 0.5$. The wave-function starts at A from which it evolves in chronological order $A \rightarrow B \rightarrow C \rightarrow D \rightarrow E \rightarrow F$.

After having looked at the form of the wave-packet we will now look at the transmission and reflection probability over the aforementioned F values. Looking at Fig. 4.30 we see that transmission is overall decreasing and reflection is increasing for increasing F values, which is to be expected. The rising of the fringes reduces

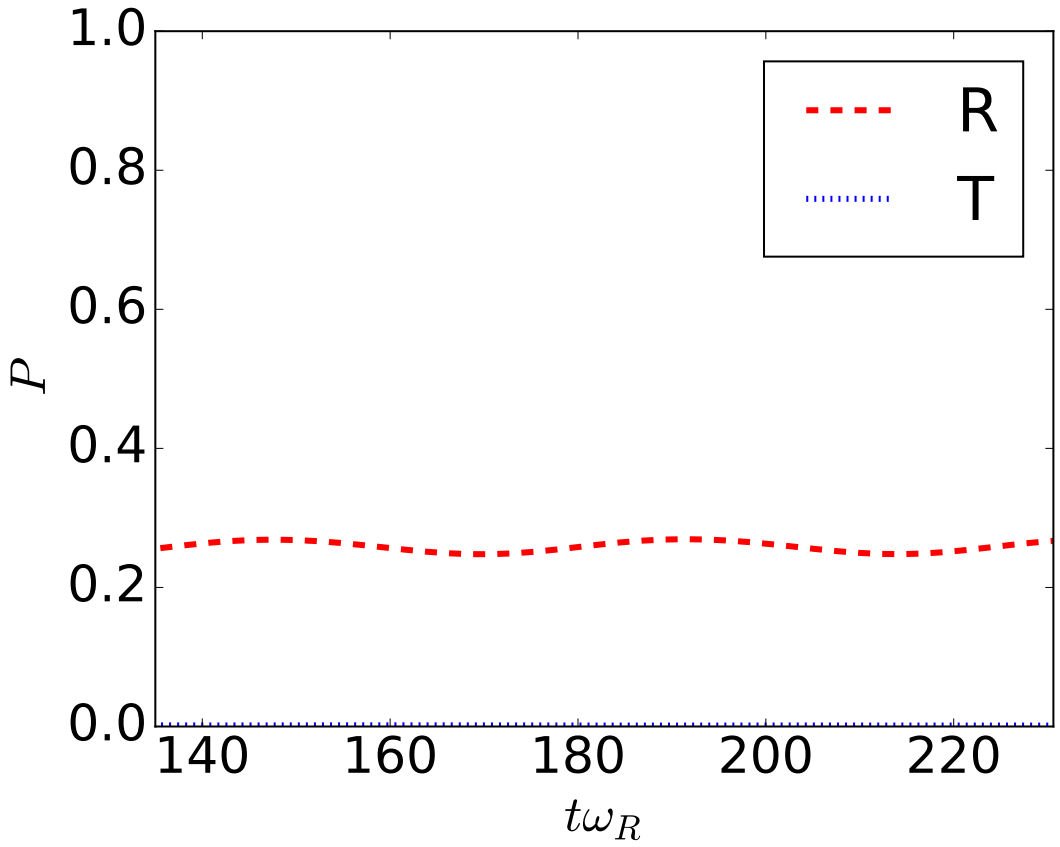

FIGURE 4.29: Showing the percentage of the wave-function inside transmission(blue dotted) and reflection(red dashed line) waveguide being in the ground state after the splitting for $v = 5v_R$, $\theta = 90°$, $\varepsilon = 0.5$, $\omega_0 = 15\mu m$, $\sigma_x = 10\mu m$, $U_0 = -20E_R$, $\lambda = 1064nm$ and $F = 0.5$.

the difference between the energy of the atoms and the peaks of the fringes until they eventually lead into tunnelling. Thus increasing the reflection probability, similarly to the behaviour seen from a potential well. Additionally, we also see direct tunnelling through the fringes now that they have been raised. However, the probability plots are not monotonic and have local minima and maxima as a function of F. This come from the change in the resonance frequencies. A similar behaviour has also been observed in the one dimensional time-independent case for standing waves. It should be easy to find a decent splitting condition for certain F parameters. However, anything between the value of 0 and 1 for F creates a substantial superposition in the transmission waveguide. This superposition will make it harder for fringes to appear in an interferometer as it would be hard to have interference between the wave-packet in the reflection waveguide and both wave-packets in the transmission as they are more spread out. Hence, only a smaller portion of them would have overlap and thus interference which would reduce the overall fringes in the final interferometer measurement.

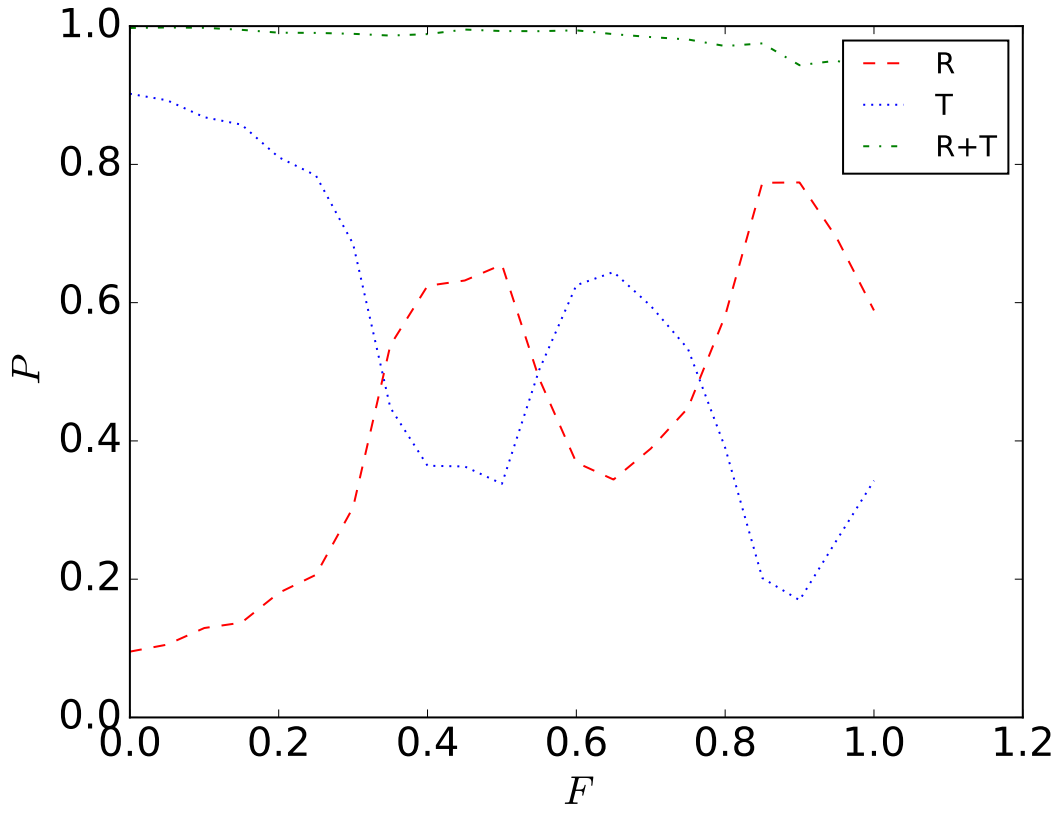

FIGURE 4.30: This figure shows the change of transmission probability(red dash), reflection probability(blue dot) and their combination (green dash-dot), in correspondence to a change in the filling level F. The functions for the transition are not monotonic and have local maxima and minima, which can be attributed to changes in the position of resonances.

4.8 Summary

In this chapter we discussed the probabilities of splitting in two dimensions. For this we expanded our step-split Fourier method into a form for two dimensions. For the simulations in two dimensions we had to make sure the the incoming atoms were in the transverse ground state of the waveguide which can roughly be approximated by the ground state of the harmonic oscillator.

Afterwards we then considered several cases for the beam-splitter. As our desire is to create a generally compact interferometer we mostly focussed on the cases where the crossing section between the two laser beams is at $\theta = 90°$. The first case being for the fixed parameters of $\theta = 90°$, $\omega_0 = 15\mu m$, $\sigma_x = 10\mu m$, $U_0 = -20E_R$, $\lambda = 1064nm$. The velocity and polarisation were varied until roughly 50:50 splitting were observed. One of those parameters is the velocity of $4v_R$ and the polarisation of $\varepsilon = 0.5$. Even though these parameters had decent splitting probabilities the splitting itself was not coherent and the out-coming atoms occupied higher level transverse modes in the reflection and transmission waveguides.

To improve the coherence we reduced the depth of the waveguides and their width. This was done because reducing the width increases the energy spacing between

the eigenstates and reducing the depth would reduce the potential energy available for the atoms to occupy higher energy levels. For this regime we examined three cases. The first being the one where the fixed parameters were $\theta = 90°$, $\omega_0 = 1\mu m$, $\sigma_x = 0.73\mu m$, $U_0 = -2E_R$, $\lambda = 720nm$. We varied the velocity and polarisation for this and the most suited parameters were $v = 1.4v_R$ and $\varepsilon = 0.5$. The overall coherence was improved however, it is still likely inadequate for interference in a full interferometer. Further, due to the lower depth of the waveguides some atoms were able to escape and the number of fringes was reduced drastically due to the width of the waveguides. To counter this we reduced the wavelength of the lasers to $\lambda = 720nm$. For the next case we increased the width to $\omega_0 = 1.5\mu m$ to have something more similar to an optical lattice. The best splitting for this case was observed to be for $v = 1.2v_R$ and $\varepsilon = 0.4$. Nonetheless, the consistency did not decrease compared to the case with a width of $\omega_0 = 1\mu m$. The last case we investigated is the one where we increased the depth of the waveguide a little to reduce the number of atoms being able to escape. The width for this case was $\omega_0 = 1\mu m$. The increase in the depth did decrease the coherence of the atoms further but it reduced the loss of the atoms. Regardless, we still do not have coherent splitting.

The next step was to change the angles to increase the interaction region between the two Gaussian laser beam by letting them cross at a narrow angle of $\theta = 170°$. This bigger interaction area increases the number of fringes drastically and due to the narrow angle the momentum change in the atoms would be less drastically. An example for a good splitting parameter for this case would be $v = 1.8v_R$ and $\varepsilon = 0.1$. However, this did not improve the coherence and as our goal is to create a interferometer with a small area we will no longer discuss this case in the next chapter.

As the aforementioned approaches did not improve the splitting too much we returned to our original parameter values and introduced a third laser beam. This laser is tuned in such a way that it acts as a reflector for atoms and thus allows us to fill the dip in the beam-splitter, which is created by the overlap of the two Gaussian beams. Similarly to the reduced depth of the waveguides, this allows us to reduce the energy that is available for the atoms from the depth of Gaussian dip of the beam-splitter to reach higher energy levels. The degree of filling can be controlled by varying the intensity of the third beam. For our case we simply give it an F value from 0 to 1, where the case of 0 means that their is no filling from the third beam and the case, where $F = 1$ means that the cross-section is completely filled.

The cases which we studied the most were the extremal cases of $F = 0$ and $F = 1$. The $F = 0$ case is the same as the one without the third laser and thus will not be discussed again. On the other hand the case where $F = 1$ provides a good range of decent splitting probabilities. An example of this would be $v = 5v_R$ and $\varepsilon = 0.5$. This was chosen because the atoms have a slower overall velocity, allowing for a longer interaction time with the signal. Nonetheless, even for the case of $F = 1$ the coherence did not improve. Furthermore, the third laser beam reduces the boundary potential for the beam-splitter, making it easier for atoms to escape. Additionally, the

parameter region of decent splitting is more ragged than the one for the case without the third laser. This is similar to the 1D case with standing waves.
Lastly we varied the F value while the other parameters stayed fixed, where these parameters were $\theta = 90^\circ$, $\omega_0 = 15\mu m$, $\sigma_x = 10\mu m$, $U_0 = -20E_R$, $\lambda = 1064nm$, $v = 5v_R$ and $\varepsilon = 0.5$. We noticed that increasing the F value generally decreases the transmission probability, as one would expect. On the other hand the function describing the transmission probability is not monotonic due to resonance shift. However, increasing F generally does not improve the coherence in splitting.
All the cases we have looked at have shown that the beam-splitter does not split the atoms coherently. Nonetheless, it is possible to to create a multi mode atom interferometer, which we will discuss in the next chapter.

Chapter 5

Interferometer

In this chapter we are going to discuss the combining properties of our beam-splitter. As discussed in Sec. 1.2, the overall aim is to create a Mach-Zehnder[26, 27, 88] interferometer with a continuous atom laser for the input. However, to study the combining properties with numerical simulations it is more convenient to use the Michelson interferometer[88, 108] as its implementation is easier. As has be seen in chapter 4, our splitting is not coherent so we need to create a multimode interferometer[109, 110]. Furthermore, this Michelson interferometer requires a smaller area for the simulation and thus more computational runs can be accomplished at the same time. We simulate the phase shift by moving the mirror in the respective arms of the interferometer, see Fig. 5.1, where x_{mr} and x_{mt} are the mirror positions in the reflection and transmission waveguide. At the output, we will measure the atom number depending on the mirror position. The most desired output would be a periodic pattern that ranges from 0 to 1, which are the measurement fringes.

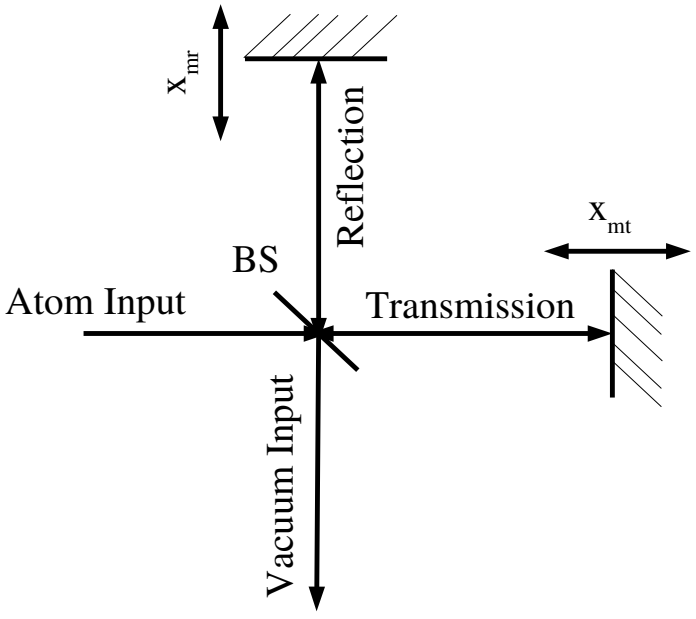

FIGURE 5.1: Schematic of our Michelson interferometer and how we create artificial phases by moving the mirror positions where x_{mr} and x_{mt}.

5.1 Mirror Types

For the creation of a Michelson interferometer a mirror is needed which is a type of potential barrier in our case. There are three types considered. The first one being a linear potential. To test the behaviour of the mirror we set one wave-packet into the transmission guide, which then travels towards the mirror and gets reflected back into the beam-splitter. This can be seen in Fig. 5.2, where the wave starts at A, travels towards and interacts with mirror potential in B, gets reflected and travels backwards towards, C, the beam-splitter and then interacts with it, D. This is done for example for the parameters $v = 2v_R$, $\varepsilon = 0$, $\lambda = 720nm$, $\omega_0 = 1\mu m$, $U_0 = -5E_R$ and $\sigma_x = 0.73\mu m$. The mirrors for these simulations are positioned at 60% of the distance from the centre of the simulation to the edge (which is defined as x_0). Hence, they are located at $x_{mr} = x_{mt} = 0.6|x_0|$ in their respected waveguides.

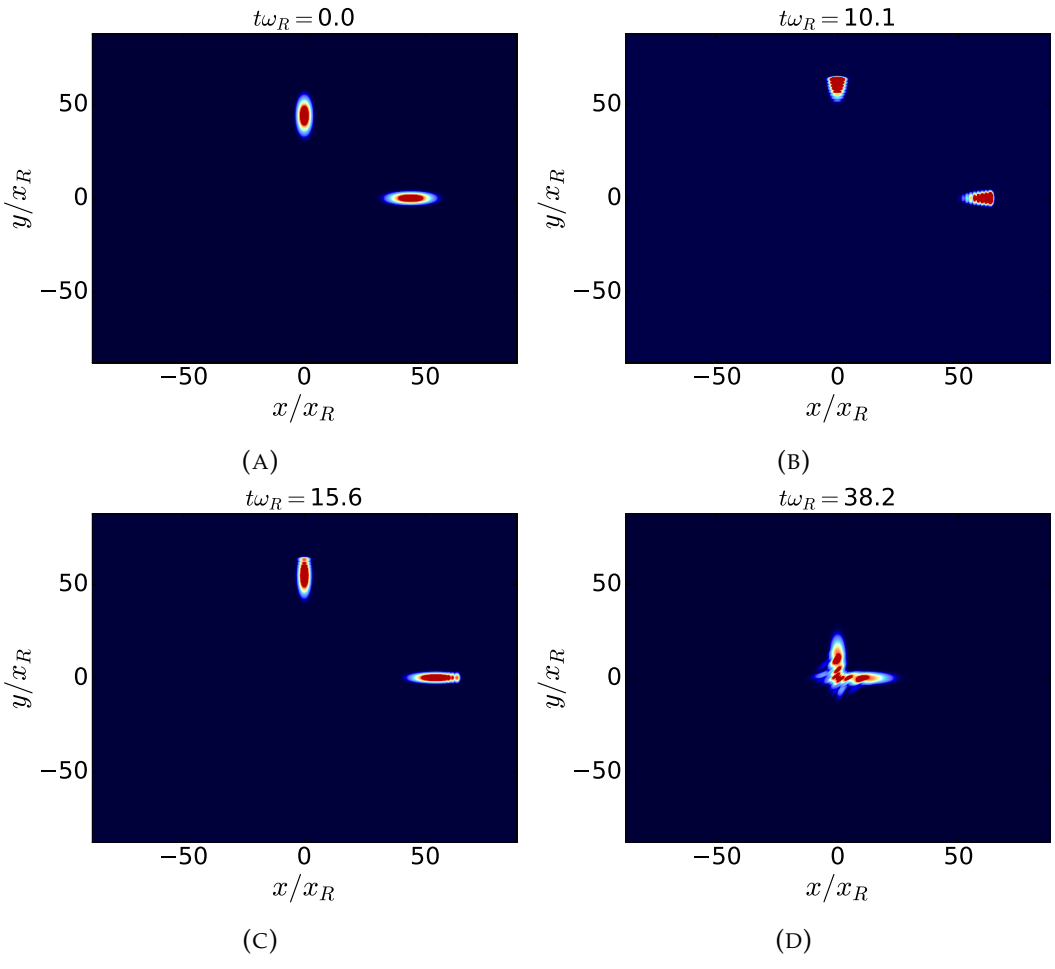

FIGURE 5.2: Mirror test example where the wave starts at A, travels towards and interacts with mirror potential in B, gets reflected and travels backwards towards, C, the beam-splitter and then interacts with it, D. This is done for the parameters $v = 2v_R$, $\varepsilon = 0$, $\lambda = 720nm$, $\omega_0 = 1\mu m$, $U_0 = -5E_R$ and $\sigma_x = 0.73\mu m$.

Looking just at the wave-function suggests that everything is working fine. However, when we look at the energy we see that something is wrong, see Fig. 5.3. The

total energy is increased after the interaction with mirror, while the normalization stays constant. This comes from the discontinuity in the gradient of the potential seen by the atoms. As the energy is increased mainly during the period where the wave-packet interacted with the mirror.

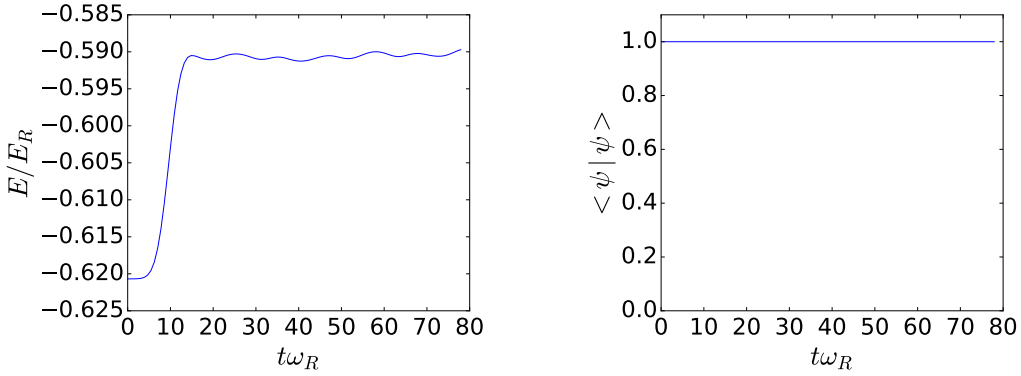

(A) Energy (B) Normalization

FIGURE 5.3: These figures depict the energy(A) and normalization(B) for a linear mirror, for $v = 2v_R$, $\varepsilon = 0$, $\lambda = 720nm$, $\omega_0 = 1\mu m$, $U_0 = -5E_R$ and $\sigma_x = 0.73\mu m$, which increases due to the discontinuity.

The next mirror tested is a quadric mirror, where the energy and normalisation are seen in Fig. 5.4. The dips in the energy show the times the wave-packet interacted with the potential of the mirror, beam-splitter and the cage, which surrounds the simulation to prevent the wave coming in contact with the edge of the simulation. These dips in energy are overall negligible due to their size.

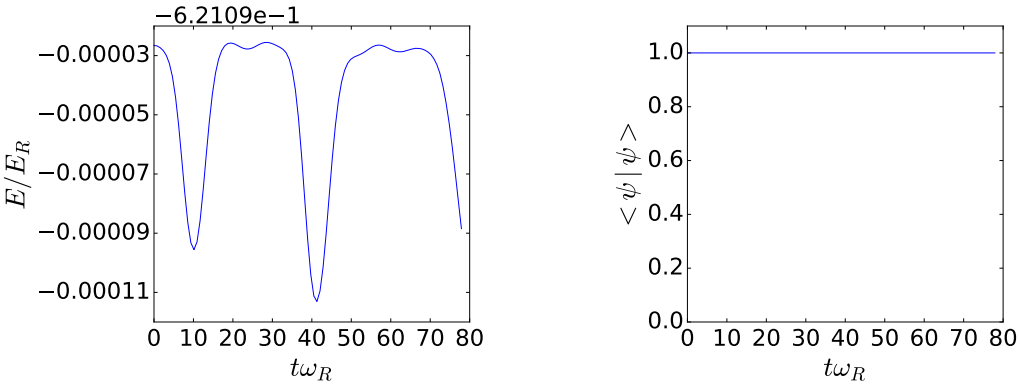

(A) (B)

FIGURE 5.4: These figures show the mean energy(A) and normalisation(B) for a quadric mirror, where the dips come from the interaction with the mirror, cage and beam-splitter.

The last mirror is created by a Gaussian reflective potential.It shows similar dips in energy at the same points as the quadratic mirror, which are again therefore negligible on the overall scale of the energy, see Fig. 5.5. This potential is chosen to be

the one used in the simulation, as it is both continuous (in potential and potential gradient) and it could be possibly implemented by the use of a blue-detuned[72] Gaussian laser beam.

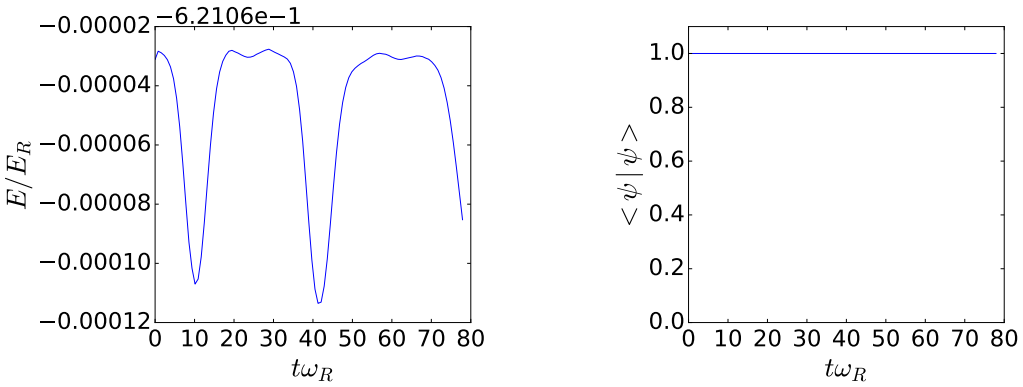

(A) (B)

FIGURE 5.5: These figure shows the mean energy(A) and normalisation(B) for a Gaussian shaped potential acting as a mirror.

5.2 Mirror Position

As our beam-splitter excites the atoms to higher transverse states in the waveguides we need to examine the mirror position. The reason for this is that the two wave-packets exiting the beam-splitter are not necessarily excited in the same fashion and hence might have slightly different average velocity and path length. As such it is important to investigate the positions of the mirrors relative to the beam-splitter. For this we will use coarse movement of the mirrors to adjust interfering packet overlap and to achieve a good fringe height. Then fine mirror movement away from these set positions can be used to produce the phase shift to vary the output probabilities.

5.2.1 Filling

We begin with the case where we have full filling with $F = 1$, $\theta = 90°$, $\omega_0 = 15\mu m$, $\sigma_x = 10\mu m$, $U_0 = -20E_R$ and $\lambda = 1064nm$. We start off by setting our mirrors at 60% of the length of the reflections and transmission waveguides and allow the one in the transmission to be moved. This movement will create a path difference twice the distance that the mirror has moved. The atoms have a velocity of $5v_R$ and the fringes are $\varepsilon = 0.5$. This movement ranges from $-0.48\lambda_{DB}$ to $0.43\lambda_{DB}$, where λ_{DB} is the De Broglie wavelength of the atoms in regard to their average velocity, and the potential fringes can be seen in Fig. 5.6, where the fringes in the atom input can be seen Fig. 5.6a and for the vacuum input in Fig. 5.6b. From these we see that there are only tiny fringes in the atom input. However, there are no fringes in the vacuum input. The mirror position in the reflection guide will be labelled as x_{mr} and the one in the transmission x_{mt}.

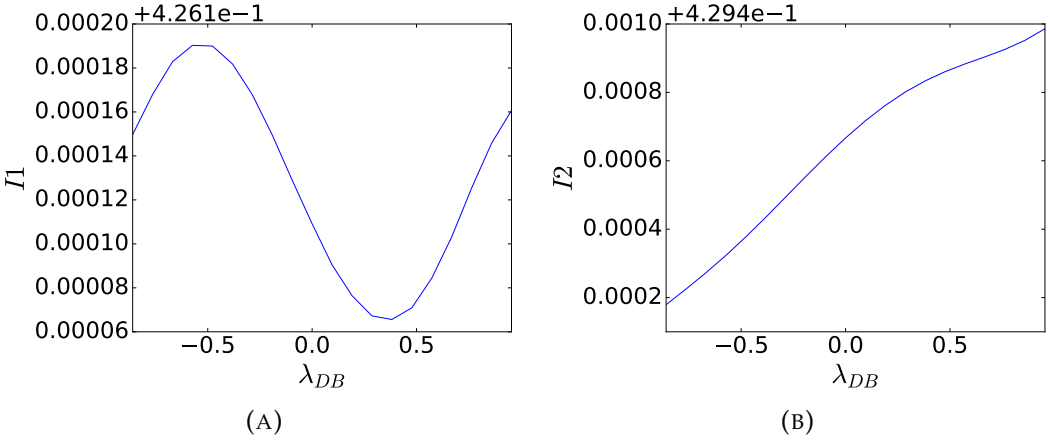

(A) (B)

FIGURE 5.6: The probabilities of finding the atoms in the atom input(A) and vacuum input(B) in regards to additional path difference, where the other parameters of this simulations are $F = 1$, $\theta = 90°$, $\omega_0 = 15\mu m$, $\sigma_x = 10\mu m$, $U_0 = -20E_R$, $\lambda = 1064nm$, $v = 5v_R$, $\varepsilon = 0.5$ and $x_{mt} = x_{mr} = 0.6|x_0|$.

As for the reason why this is happening we need to examine the simulation directly. Looking at Fig. 5.7, we that the wave-function travels through the beam-splitter in A. Following this the split packets evolve in their respective outputs and are then reflected backwards to the beam-splitter via the Gaussian mirror potentials, see in B and C. Furthermore, in C we also see that the wave in the reflection waveguide has already arrived at the beam-splitter, while the one in the transmission is still travelling. In D the wave from the reflection get split, while the transmission just arrives at the the beam-splitter. Following from here the wave from the transmission gets split but most of it goes directly input the vacuum input and lastly F shows the final wave-function of the simulation. From this we see that the two do not recombine as they arrive at significantly different times and hence the fringes seen in the atom input, Fig. 5.6a, come most likely only from the interference of the outer areas of the wave-function. These fringes are so small that they are dominated by other effects in the vacuum input Fig. 5.6b.

To investigate this behaviour further we perform full evolution simulations for different static mirror positions chosen in the range $-31.83\lambda_{DB}$ to $-6.37\lambda_{DB}$. This can be seen in Fig. 5.8, where Fig. 5.8a shows the probabilities of finding the atoms in the input in regards to the mirror position and Fig. 5.8b depicts the same for the vacuum input. From these we can see that the position of the mirrors is important.

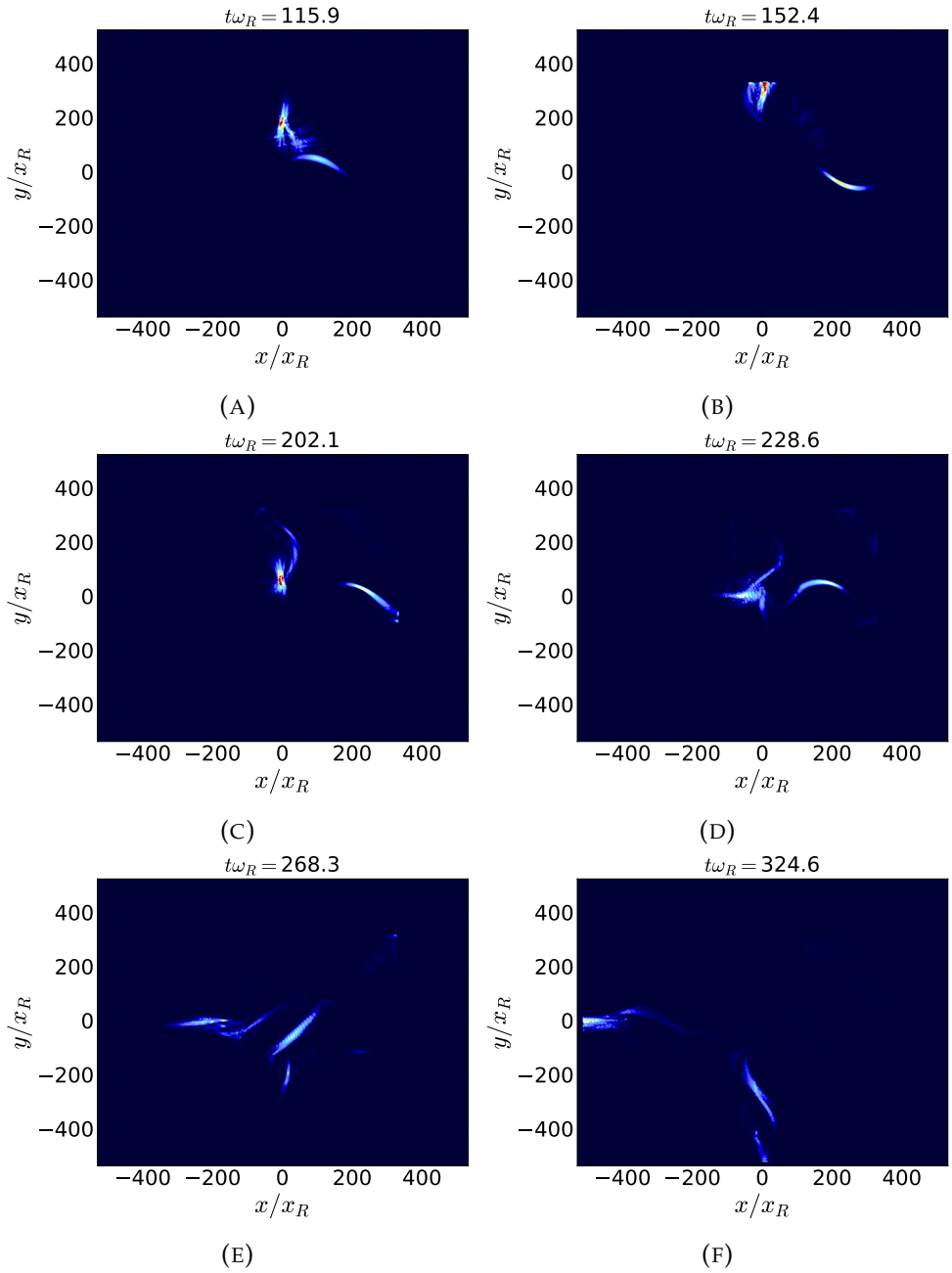

(A) (B) (C) (D) (E) (F)

FIGURE 5.7: This series of figures shows the atomic wave-packet evolving in a Michelson interferometer. The atoms start off at A and then get split by the beam-splitter in B and A. Following from here they get reflected back into the beam-splitter at B, where the wave in the reflection arms reaches the beam-splitter first in C and gets split in D, while the wave from the transmission guide just arrives. This wave then gets as well split by the beam-splitter in E with the final form of the overall wave-function seen in F. The parameters for this simulation are $F = 1$, $\theta = 90°$, $\omega_0 = 15\mu m$, $\sigma_x = 10\mu m$, $U_0 = -20E_R$, $\lambda = 1064nm$, $v = 5v_R$, $\varepsilon = 0.5$, and $x_{mt} = x_{mr} = 0.6|x_0|$. As both waves return at significantly different times the wave are not combined but have two independent splittings.

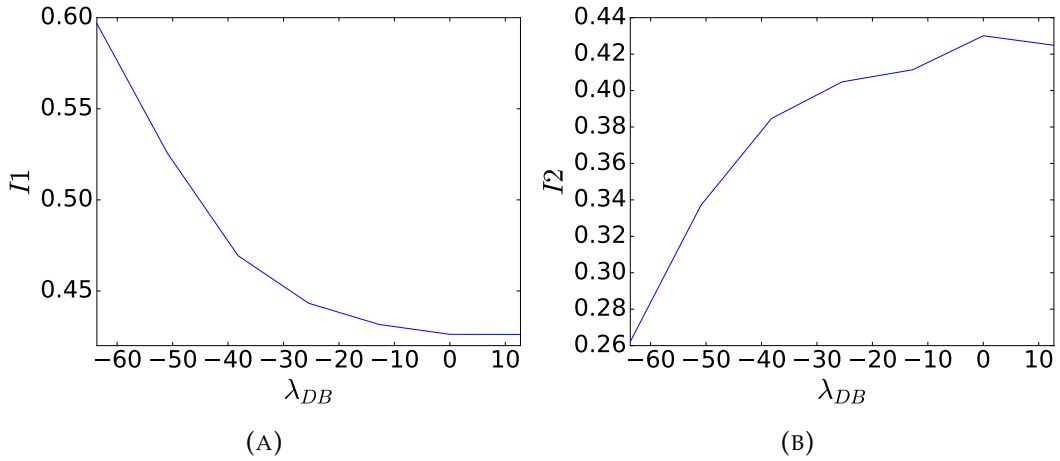

(A) (B)

FIGURE 5.8: Figure A depicts the probability of finding the atoms in the atom input in regards to path difference from the mirror position, while B shows the same for the vacuum input. The mirror is moved over a distance from $-31.83\lambda_D B$ to $-6.37\lambda_D B$, staying static for each run. Even though the mirror moves over this long distance the ration between the output constantly increases. Hence is mirror position is important to finding good splitting.

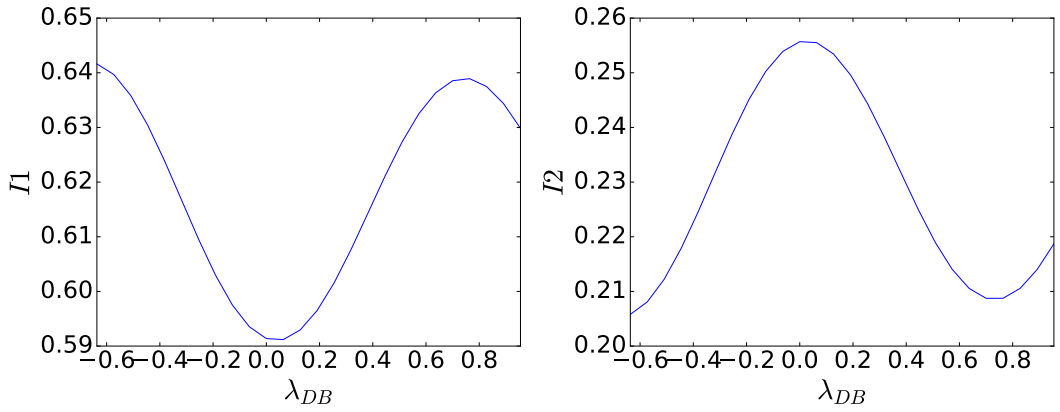

(A) Atom Input (B) Vacuum Input

FIGURE 5.9: These Figures show the changes in the probability of finding the atoms in the, atom input(A) and the vacuum input(B) depending on the path difference from the mirror position in the transmission arm. The probability of finding the atoms in these two waveguides is combined 85%.

Now we examine the case where the mirrors are both moved by $-31.83\lambda_{DB}$ closer to the beam-splitter and the mirror inside the transmission band is moved from $-0.32\lambda_{DB}$ to $0.48\lambda_{DB}$. Fig. 5.9 clearly shows that the measured fringes have increased significantly to 5%. Furthermore, when the fringes in the two inputs are are summed, the total probability remains constant at around 85%, where the rest is lost due to being either trapped inside the beam-splitter, reflected back into the reflection and transmission waveguide or the atom escaped the waveguide during the simulation.

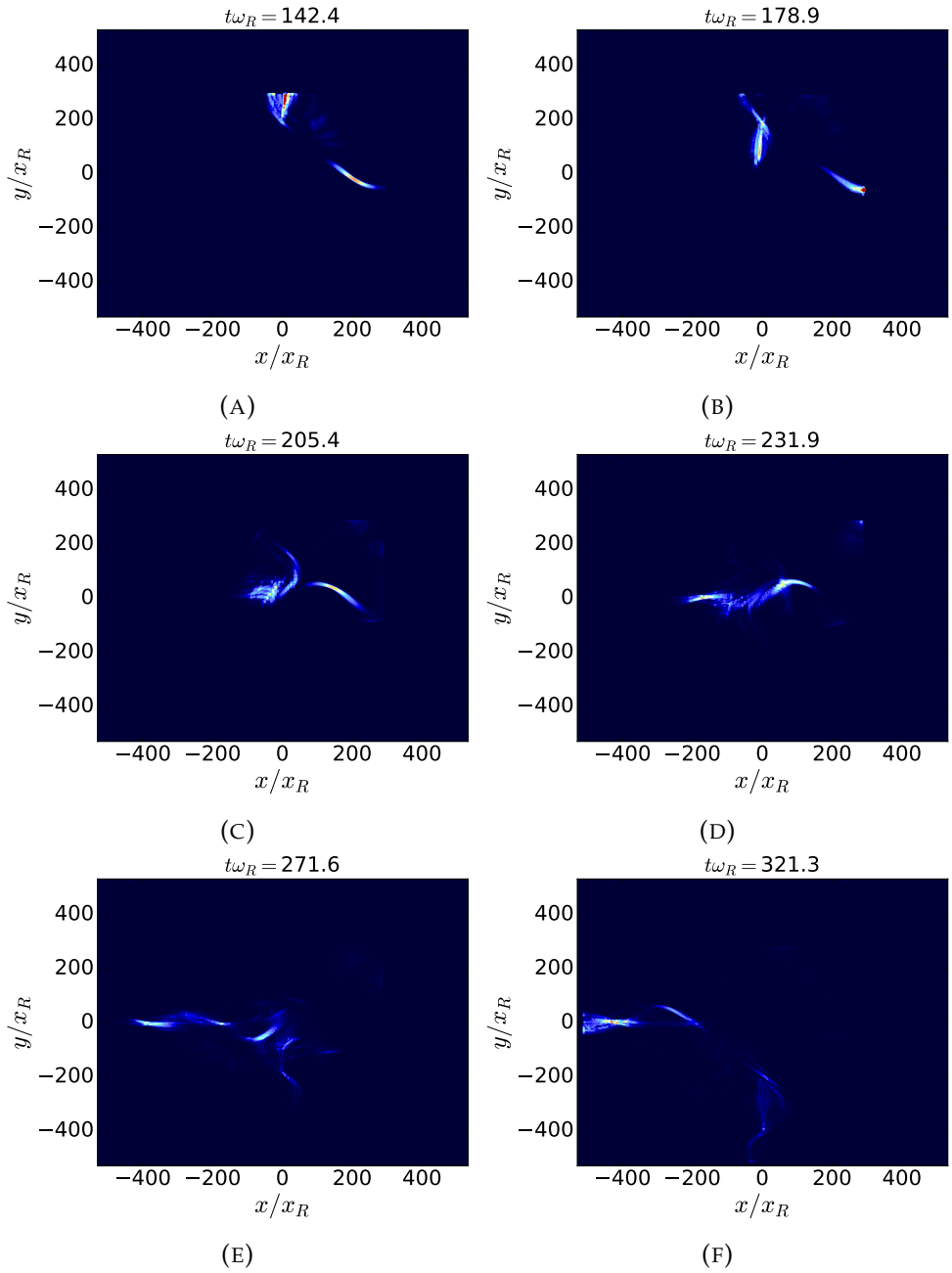

FIGURE 5.10: These figures show the recombination of two wave-packets already split into two which then get reflected backwards into the beam-splitter(A). They travel then towards the beam-splitter(B), get combined(C and D) leave. The other parameters are $F = 1$, $\theta = 90°$, $\omega_0 = 15\mu m$, $\sigma_x = 10\mu m$, $U_0 = -20E_R$, $\lambda = 1064nm$, $v = 5v_R$, $\varepsilon = 0.5$, and $x_{mr} = x_{mt} = 0.6|x_0| - 31.83\lambda_{DB}$.

To find the reasons for this we need investigate the wave-function for this case, see Fig. 5.10. The wave-function has already been split for the first step in Fig. 5.10a and gets reflected in Fig. 5.10b. From here the two waves gets combined starting with Fig. 5.10c, where most of the wave-function from the reflection has already been propagated through the beam-splitter while the wave from the transmission just arrives. This then enters the beam-splitter where it slightly overlaps with the small part from the reflection wave. The waves then start to leave the beam-splitter

in Fig. 5.10d and the form of the wave-function can be seen Fig. 5.10d. The main difference to the previous one is that there is now a small overlap in the waves while in the first case, Fig. 5.8, the wave-functions have virtually no overlap.
Even from this slight overlap we managed to increase the fringes drastically. Moving the two mirrors even further to $39.79\lambda_{DB}$ we see again a decrease in the fringe visibility, see Fig. 5.11. The fringe height falls from 5% to 1.5%, but the total probability in the output waveguides is the same as before 85%.

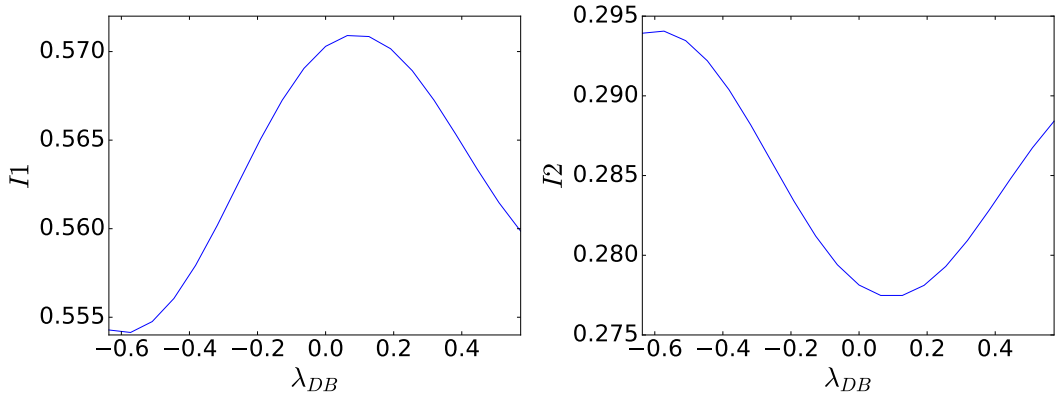

(A) (B)

FIGURE 5.11: The probability of finding the atoms in the atom(A) or vacuum(B) input after the end of the simulation as a function of path difference due to the mirror shift in the transmission guide for the parameters $F = 1$, $\theta = 90^{\circ}$, $\omega_0 = 15\mu m$, $\sigma_x = 10\mu m$, $U_0 = -20E_R$, $\lambda = 1064nm$, $v = 5v_R$, $\varepsilon = 0.5$, and $x_{mt} = x_{mr} = 0.6|x_0| - 39.79\lambda_{DB}$. Both of these probabilities add up to 85%.

To understand the differences we need to have another look at the wave-function where we start off the with the waves already being split by the beam-splitter, see Fig. 5.12a, which then gets reflected back by the mirror in Fig. 5.12b and enters the beam-splitter in Fig. 5.12c, where the wave-function from the reflection waveguide is already halfway through while the transmission waves just enters it. However, source of the difference between cases $31.83\lambda_{DB}$ and $39.79\lambda_{DB}$ can be seen in Fig. 5.12d. For the $31.83\lambda_{DB}$ case parts of the reflection and transmission waves overlap, while for $39.79\lambda_{DB}$ they only cross with a smaller overlap and this having a smaller area for interference. This then leads to the smaller fringes seen in 5.11.

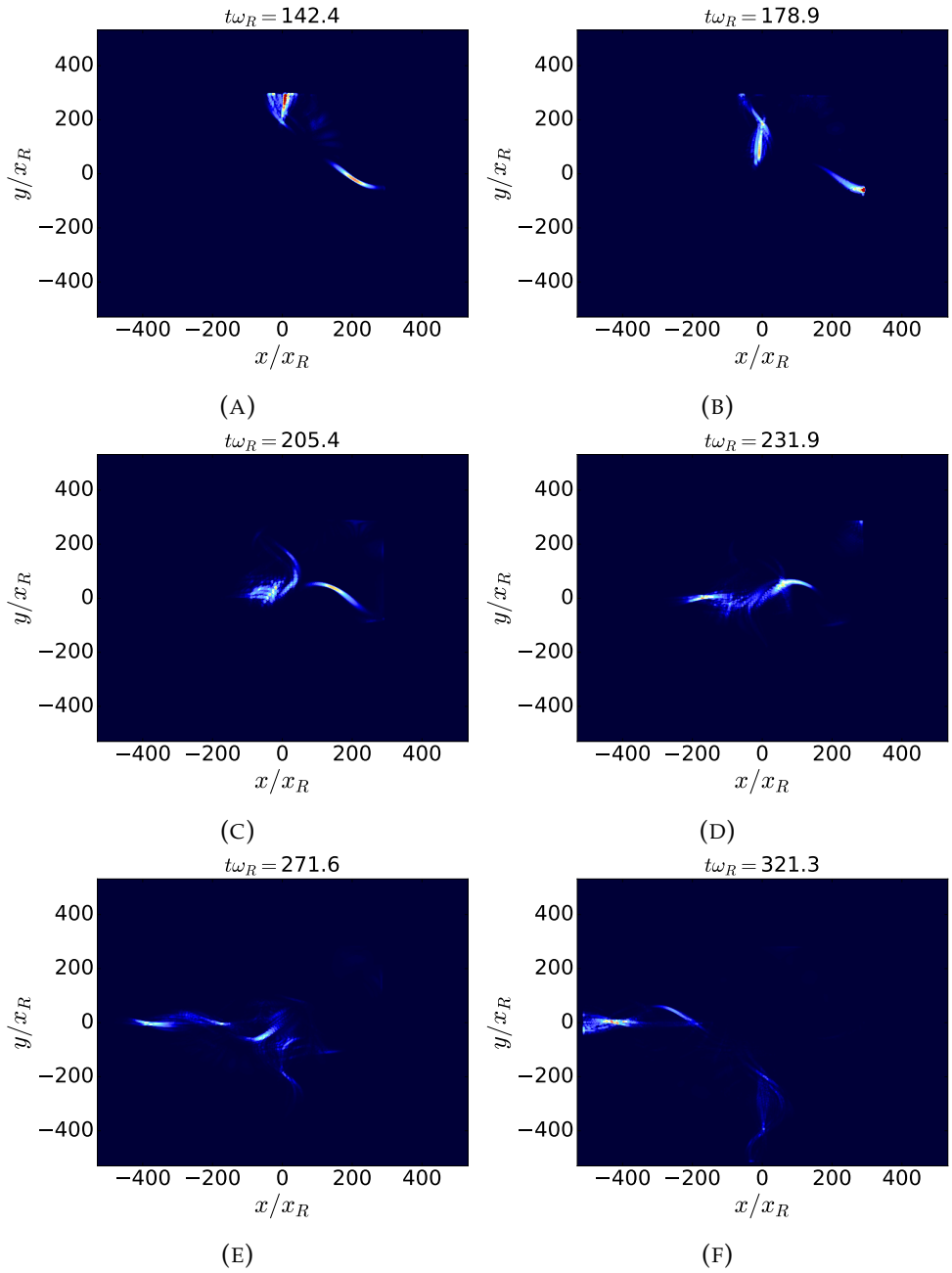

FIGURE 5.12: These figures shows the recombination of two wave-packets. They begin separated(A) and being reflected back by the mirrors(B), where they recombine(C and D) and exit the beam-splitter(E and F), for the parameters $F = 1$, $\theta = 90°$, $\omega_0 = 15\mu m$, $\sigma_x = 10\mu m$, $U_0 = -20E_R$, $\lambda = 1064nm$, $v = 5v_R$, $\varepsilon = 0.5$, and $x_{mt} = x_{mr} = 0.6|x_0| - 39.79\lambda_{DB}$.

These observations show that we need to increase the overlapping area to increase the fringes. Normally, the mirrors are equal distance from the beam-splitter. However, if we were to move the one in the transmission band closer so we could increase the overlap. For this we will move both mirrors to $-31.83\lambda_{DB}$ and the mirror in the transmission will be moved for an additional $-71.62\lambda_{DB}$ in $3.98\lambda_{DB}$ intervals. Using this we can determine the values that provide the most useful overlap. The two solutions which appear to be most useful from an initial inspection are case

$(i)-71.62\lambda_{DB}$ and case (ii) $-75.6\lambda_{DB}$, see Fig. 5.13 and Fig.5.15 ,respectively.

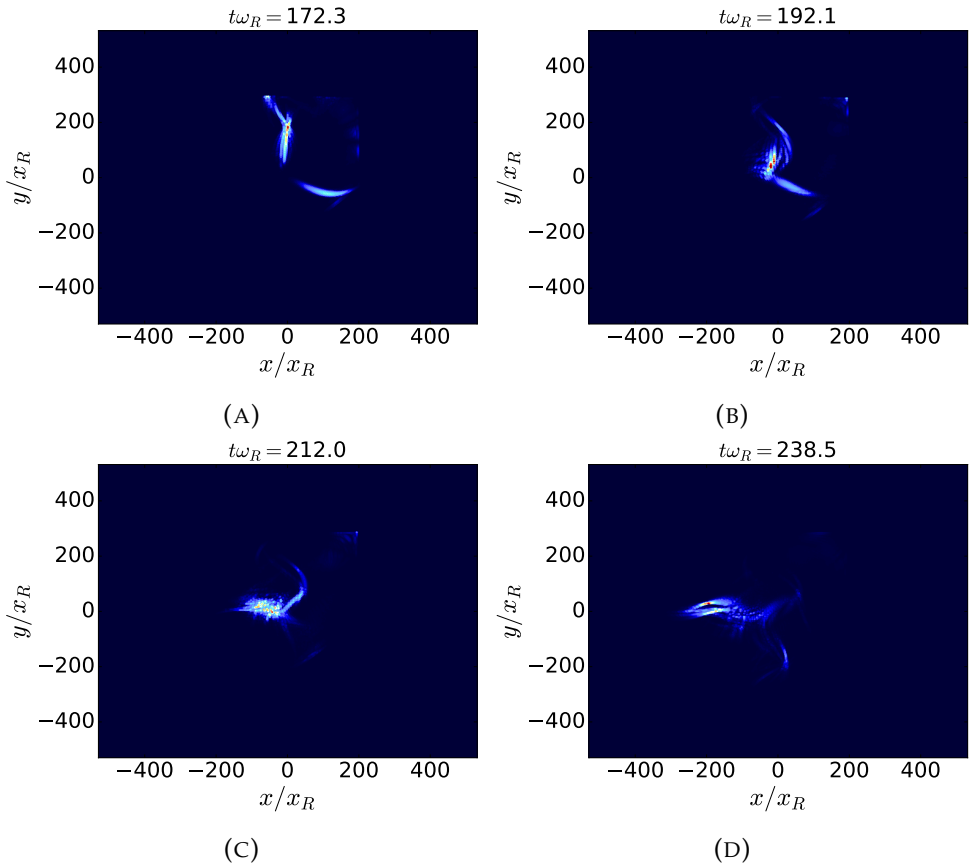

FIGURE 5.13: The recombination of two wave-packets is shown by the figures for the mirror in the reflection being at $x_{mr} = 0.6|x_0| - 31.83\lambda_{DB}$ and the one in transmission in $x_{mt} = 0.6|x_0| - 103.45\lambda_{DB}$. The wave-function starts off split and being reflected by the mirror(A), which then gets recombined(B and C) and leaves the beam-splitter(D). The other parameters are $F = 1, \theta = 90°$, $\omega_0 = 15\mu m$, $\sigma_x = 10\mu m$, $U_0 = -20E_R$, $\lambda = 1064nm$, $v = 5v_R$ and $\varepsilon = 0.5$.

For case (i) the wave-function from the transmission and reflection band enter the beam-splitter for recombination in Fig. 5.13a. From which they then progress into in Fig. 5.13b, combine Fig. 5.13c and leave Fig. 5.13d. From these calculations we can then obtain the the fringes by varying the mirror inside the transmission guide by an additional $-0.48\lambda_{DB}$ to $0.43\lambda_{DB}$. Creating the fringes seen in Fig. 5.14. In these we can see the the fringes observed have been reduced to no visible fringes in our observation frame. The probability in these two waveguides is 88%. The reason for this is mostly due to the nature of our beam-splitter. Meaning that the splitting is non-central inside the beam-splitter and thus the combining is non-central as well. Hence, even though the beams combined, each of them experienced the most important steps of the splitting process individually and they were then combined afterwards.

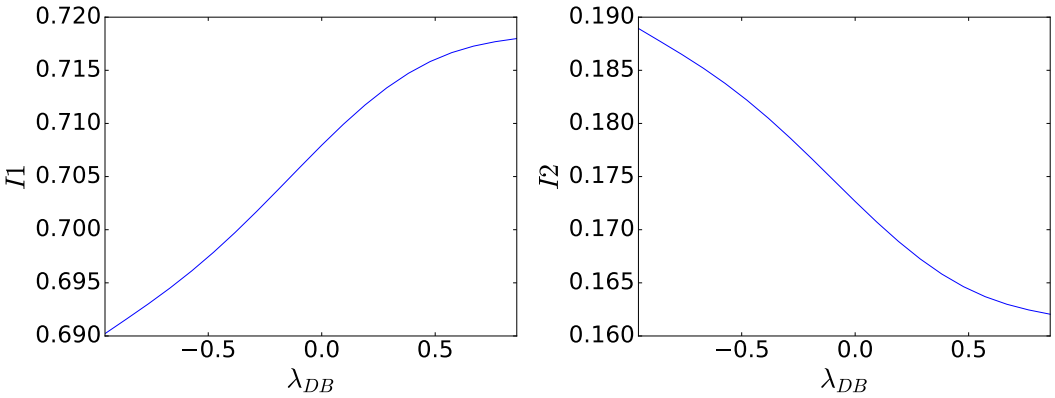

(A) (B)

FIGURE 5.14: These figures show the probability of finding the atoms in the atom input(A) and vacuum input(B) for the parameters $F = 1, \theta = 90°, \omega_0 = 15\mu m, \sigma_x = 10\mu m, U_0 = -20E_R, \lambda = 1064nm, v = 5v_R, \varepsilon = 0.5$, the position of the mirror in the reflection waveguide at $x_{mr} = 0.6|x_0| - 31.83\lambda_{DB}$ and the one in transmission at $x_{mt} = 0.6|x_0| - 103.45\lambda_{DB}$. The probabilities for this case add up to 88%.

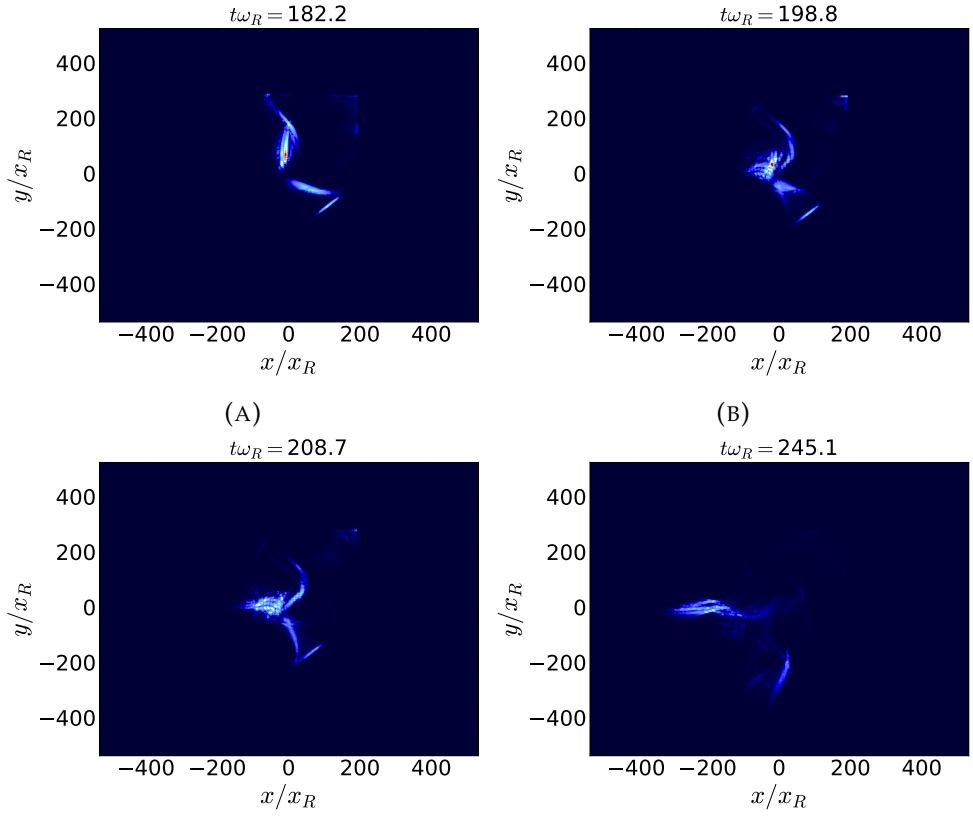

(A) (B)

(C) (D)

FIGURE 5.15: The figures demonstrate the process of recombination for the parameters $F = 1, \theta = 90°, \omega_0 = 15\mu m, \sigma_x = 10\mu m, U_0 = -20E_R, \lambda = 1064nm, v = 5v_R, \varepsilon = 0.5$, the position of the mirror in the reflection waveguide at $x_{mr} = 0.6|x_0| - 31.83\lambda_{DB}$ and the one in transmission at $x_{mt} = 0.6|x_0| - 107.43\lambda_{DB}$. Starting off with the split wave-function travelling back towards the beam-splitter(A), where they get recombined(B and C) and finally leave the beam-splitter(D).

Case (ii) is when we move the mirror by an additional value of $-75.6\lambda_{DB}$ compared to the on in the reflection. So its position would be moved by $-107.43\lambda_{DB}$ in comparison to the $-31.83\lambda_{DB}$. The wave-function starts off being split and reflected backwards into the mirror at Fig. 5.15a. From there the individual parts travel into the beam-splitter and seemingly come into contact in the centre, in Fig. 5.15b. There they combine, Fig. 5.15c and leave Fig. 5.15d.
For this case as well we see that there are no fringes in the chosen area which ranges from $-0.48\lambda_{DB}$ to $0.43\lambda_{DB}$, see Fig. 5.16. The reason for this is the non-central splitting as well which is more visible in this case looking at Fig. 5.15b. The wave-packets meet in the centre but split before they come into direct contact. Thus the most crucial area for the splitting is the entrance area of the beam-splitter.

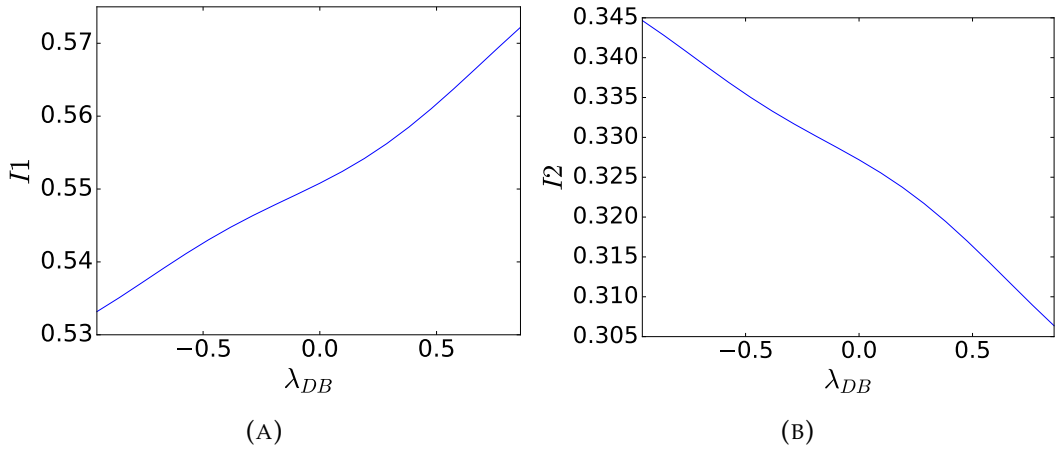

(A) (B)

FIGURE 5.16: The probability of finding the atom in the atom input(A) and vacuum input(B) for the parameters $F = 1$, $\theta = 90°$, $\omega_0 = 15\mu m$, $\sigma_x = 10\mu m$, $U_0 = -20E_R$, $\lambda = 1064nm$, $v = 5v_R$, $\varepsilon = 0.5$, the position of the mirror in the reflection waveguide at $x_{mr} = 0.6|x_0| - 31.83\lambda_{DB}$ and the one in transmission at $x_{mt} = 0.6|x_0| - 107.43\lambda_{DB}$. There are no fringes for this case. Meaning their was not a recombination but an independent splitting of the two different splitting.

Lastly, we are going back to the case where we observed the best fringes for a filled beam-splitter. The case where both mirrors are moved by $-31.83\lambda_{DB}$. However, this time the mirror is moved in the reflection waveguide from $-0.48\lambda_{DB}$ to $0.43\lambda_{DB}$, creating the fringes seen in Fig. 5.17, which has the same fringe separation and high as the one in the transmission waveguide see Fig. 5.9. The probability of finding atoms in the two waveguides stays the same as well, 85%. However, it should be noted the fringe length is not $1\lambda_{DB}$. This stems from the beam-splitter exciting the wave into higher transverse modes of the waveguide and thus lowering their velocity, along the waveguide propagation direction. This is due to the conservation of energy. The kinetic energy from the atoms is transferred to allow atoms to reach higher transverse modes. The momentum change has been discussed in Sec. 4.4. Therefore, they have a different wavelength than the one they started with. Our shifts are based on the starting wavelength and therefore a change in their wavelength will result in a different fringe period length than expected.

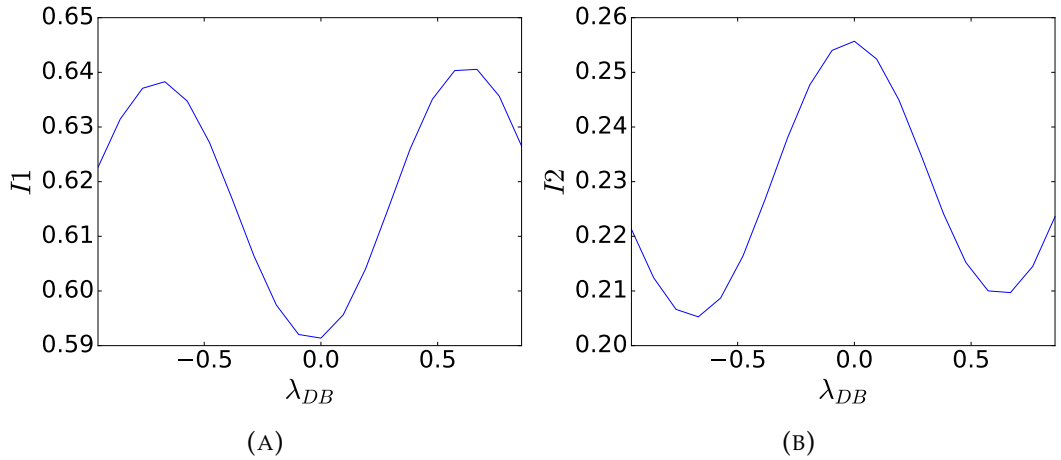

(A) (B)

FIGURE 5.17: The probability of finding the atoms in the atoms and vacuum inputs is shown by these figures as a function of the path difference from the mirror shift inside th reflection waveguide for the parameters parameters $F = 1$, $\theta = 90°$, $\omega_0 = 15\mu m$, $\sigma_x = 10\mu m$, $U_0 = -20E_R$, $\lambda = 1064nm$, $v = 5v_R$, $\varepsilon = 0.5$, the position of the mirror $x_{mt} = x_{mr} = 0.6|x_0|$.The probabilities for this case add up to 85%.

5.2.2 No Filling

After having looked at the case of $F = 1$, we are now looking at $F = 0$, where the other parameters are $\theta = 90°$, $\omega_0 = 15\mu m$, $\sigma_x = 10\mu m$, $U_0 = -20E_R$ and $\lambda = 1064nm$. In Sec. 4.4 we found that the best parameters for even splitting are $v = 4v_R$ and $\varepsilon = 0.5$ which we will use for the simulations. Our mirrors will again be put at 60% of the distance between the centre and the edge of the simulation. Thus the first issue that needs to be addressed is how the wave-functions overlap for these parameters, which can be seen in Fig. 5.18, where the wave-function starts off split, A, and then reflected by the mirrors in B. The wave-packet enters the beam-splitter in C while the one from transmission enters later in D. E and F show the waves leaving the beam-splitter and the last time stamp of the simulation respectively.
However, looking at these it becomes clear that the wave-function overlap is negligible between the two wave-packets. Hence we started to move both mirrors simultaneously. However, we did not find positions where we could make the packets overlap. Therefore, instead of moving both mirrors only the one in the transmission waveguide was moved. The position that was then decided on is $-103.45\lambda_{DB}$, which can be seen in Fig. 5.19. The wave-function starts off at being split and reflected back by the mirrors(5.19a) backwards into the beam-splitter, where the one of the transmission enters the beam-splitter(5.19b) and then gets split by it travelling through the upper part of it(5.19c). The wave-packet from the reflection enters afterwards(5.19d). The two wave-packets then leave the beam-splitter(5.19e and 5.19f).

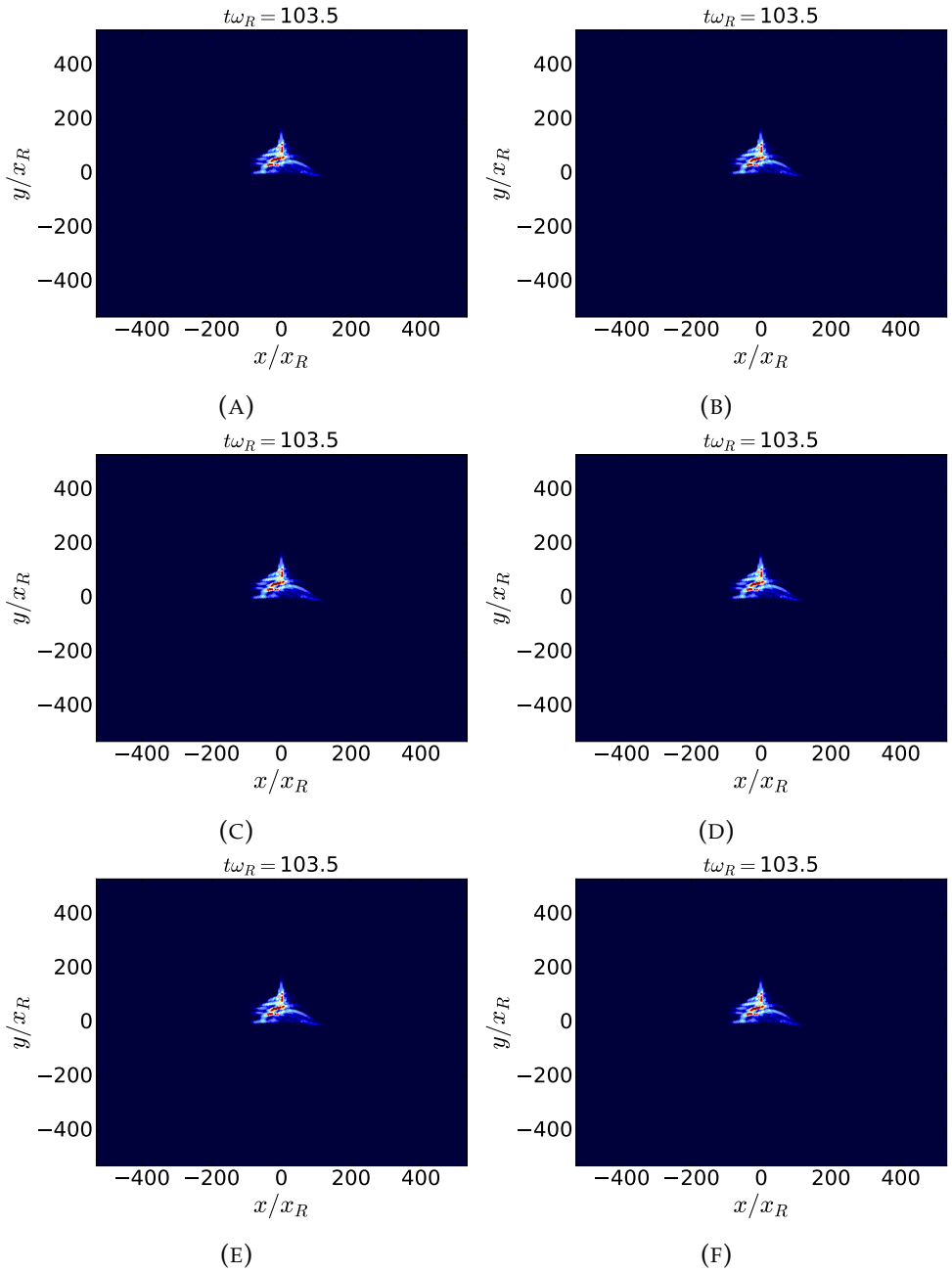

FIGURE 5.18: The propagation of a wave-function through the beam-splitter and subsequent reflection by the mirror and second interaction with the beam-splitter is shown. A shows the splitting of the wave-function which then leaves the beam-splitter in B. Afterwards it gets reflected by the mirror in C. From which it re-enters the beams-splitter in D and then leaves in E and F. For the parameters $F = 0$, $\theta = 90°$, $\omega_0 = 15\mu m$, $\sigma_x = 10\mu m$, $U_0 = -20E_R$, $\lambda = 1064nm$, $v = 4v_R$, $\varepsilon = 0.5$, the position of the mirrors $x_{mt} = x_{mr} = 0.6|x_0|$.

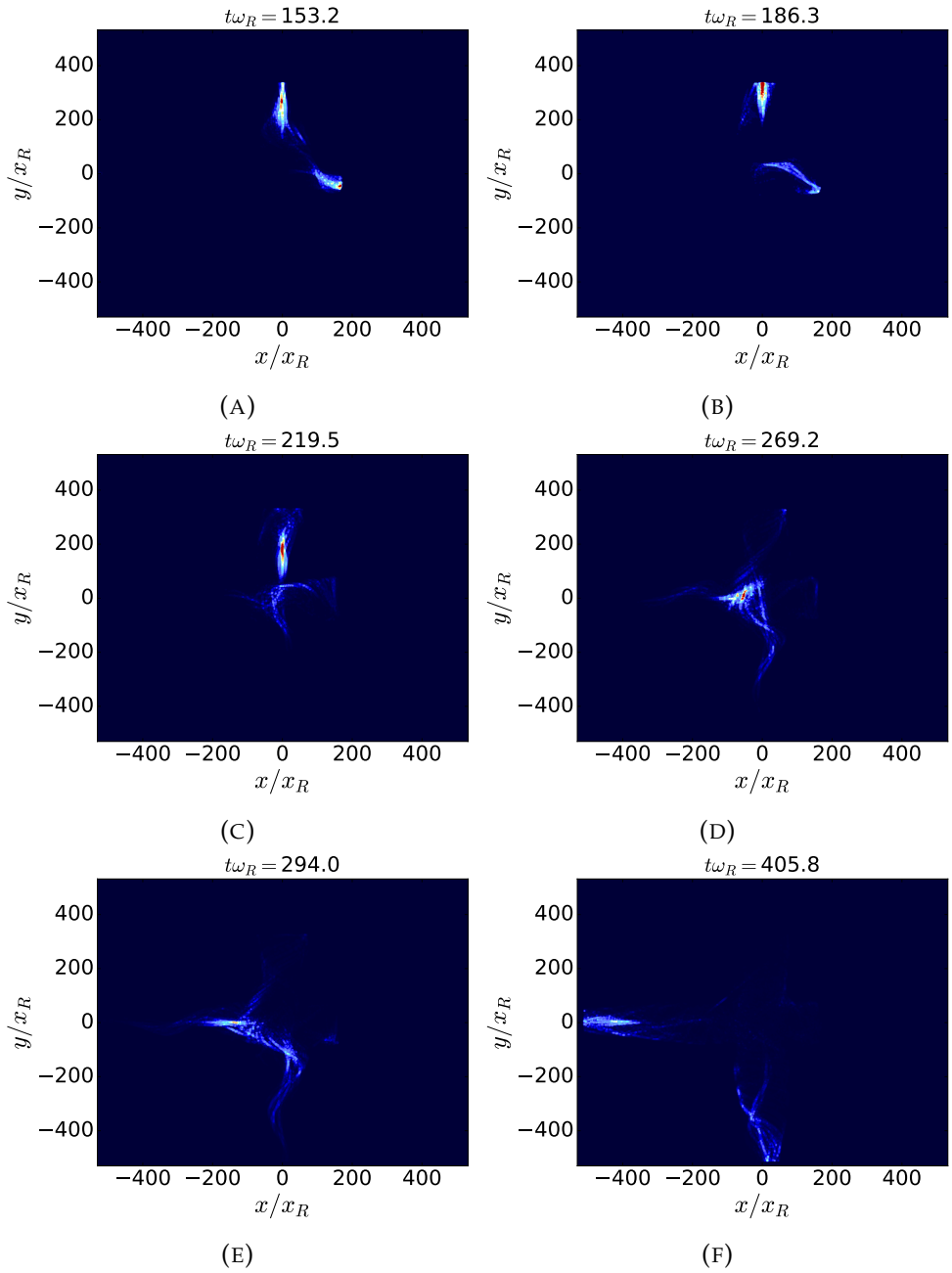

(A) (B) (C) (D) (E) (F)

FIGURE 5.19: For the parameters $F = 0$, $\theta = 90°$, $\omega_0 = 15\mu m$, $\sigma_x = 10\mu m$, $U_0 = -20E_R$, $\lambda = 1064nm$, $v = 4v_R$, $\varepsilon = 0.5$, the position of the mirror inside the reflection guide $0.6|x_0|$ and the one in transmission at $0.6|x_0| - 103.45\lambda_{DB}$. The wave-packet begins to split and then gets reflected back(A), where the wave-packet from the transmission guide reaches the beam-splitter first(B) and travels long through the are of the beam-splitter closes to the reflection guide it upper preliminary, while the reflection just enters(C). Then both waves get split more or less individually(D and E) and leave the beam-splitter(F).

The reason we have chosen these parameters is the wave-packet from the reflection waveguides starts splitting before it reaches the centre. Hence, to have interference between these two it is necessary that the wave-function from the transmission waveguide travels along the upper-side of the beam-splitter. This is possible to due to the wave-packet bouncing around the transmission waveguide while still staying

relatively compact instead of forming several smaller independent wave-packets. Allowing it to come into contact with the beam-splitter at different angles.
Afterwards, the mirror in the reflection guide needs adjusting. Two possible shifts were observed. The first one at $-47.75\lambda_{DB}$ for which the recombination can be seen in Fig. 5.20. The wave-function starts off split and gets reflected back into the mirror(5.20a). The wave-packet from the transmission guide enters first and travels along the upper side of the beam-splitter(5.20b) and thus it allows for the combination with the wave-packet from the reflection guide(5.20c). Finally, leaving the beam-splitter((5.20d)).

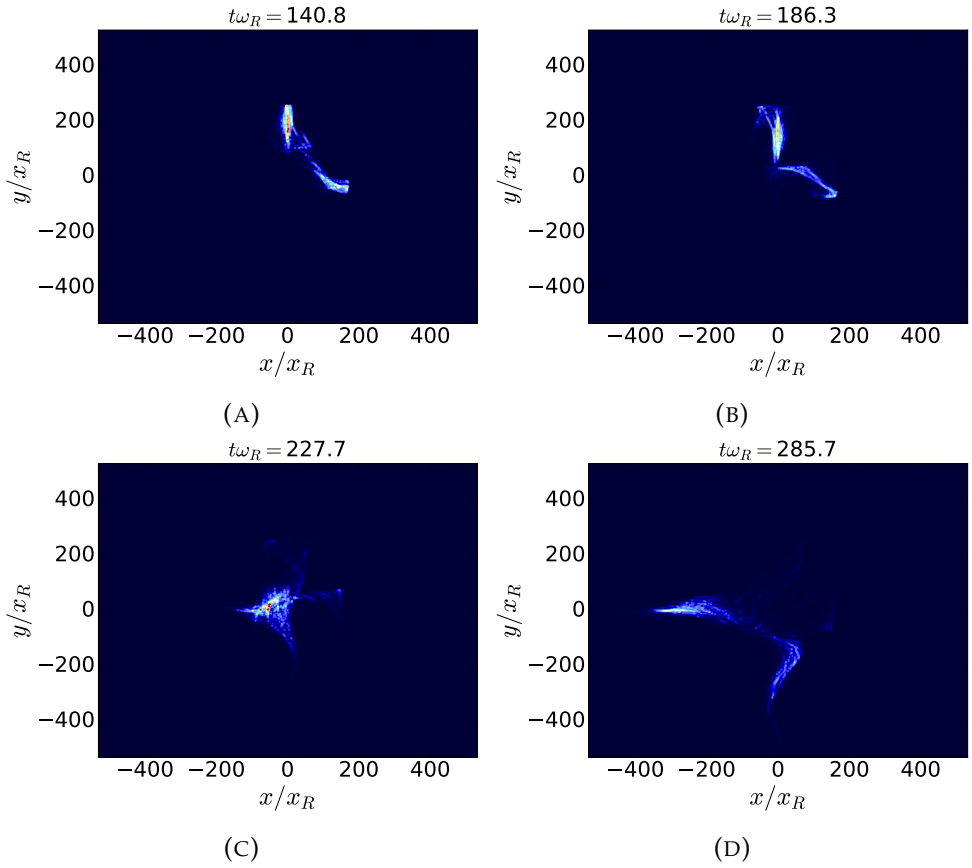

FIGURE 5.20: Starting off with a split wave that get reflected backwards by the mirrors(A), where the wave-packets then re-enter the beam-splitter(B) and then get recombined(C). Following with the departure towards the output(D) for the parameters $v = 5v_R$, $\varepsilon = 0.5$, $F = 0$, $\theta = 90°$, $\omega_0 = 15\mu m$, $\sigma_x = 10\mu m$, $U_0 = -20E_R$, $\lambda = 1064nm$, $v = 4v_R$, $\varepsilon = 0.5$, the position of the mirror inside the reflection guide $0.6|x_0| - 47.75\lambda_{DB}$ and the one in transmission at $0.6|x_0| - 103.45\lambda_{DB}$.

Now the mirror in the transmission guide is varied from $-0.48\lambda_{DB}$ to $0.44\lambda_{DB}$ creating the fringes pattern seen in Fig. 5.21. The fringes size in these is roughly 8% and the combined probability is 91%

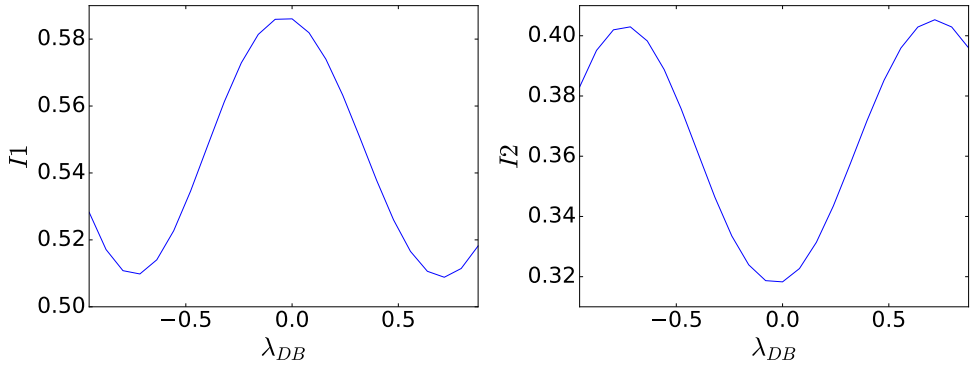

(A) Atom Input (B) Vacuum Input

FIGURE 5.21: The figures show the fringes in the atom and vacuum input for $v = 4v_R$, $\varepsilon = 0.5$, $F = 0$, $\theta = 90^\circ$, $\omega_0 = 15\mu m$, $\sigma_x = 10\mu m$, $U_0 = -20E_R$, $\lambda = 1064nm$, $v = 5v_R$, $\varepsilon = 0.5$, the position of the mirror inside the reflection guide $0.6|x_0| - 47.75\lambda_{DB}$ and the one in transmission at $0.6|x_0| - 103.45\lambda_{DB}$. Where the highest fringe high is about 8% and the total probability in the two waveguides add up to 91%.

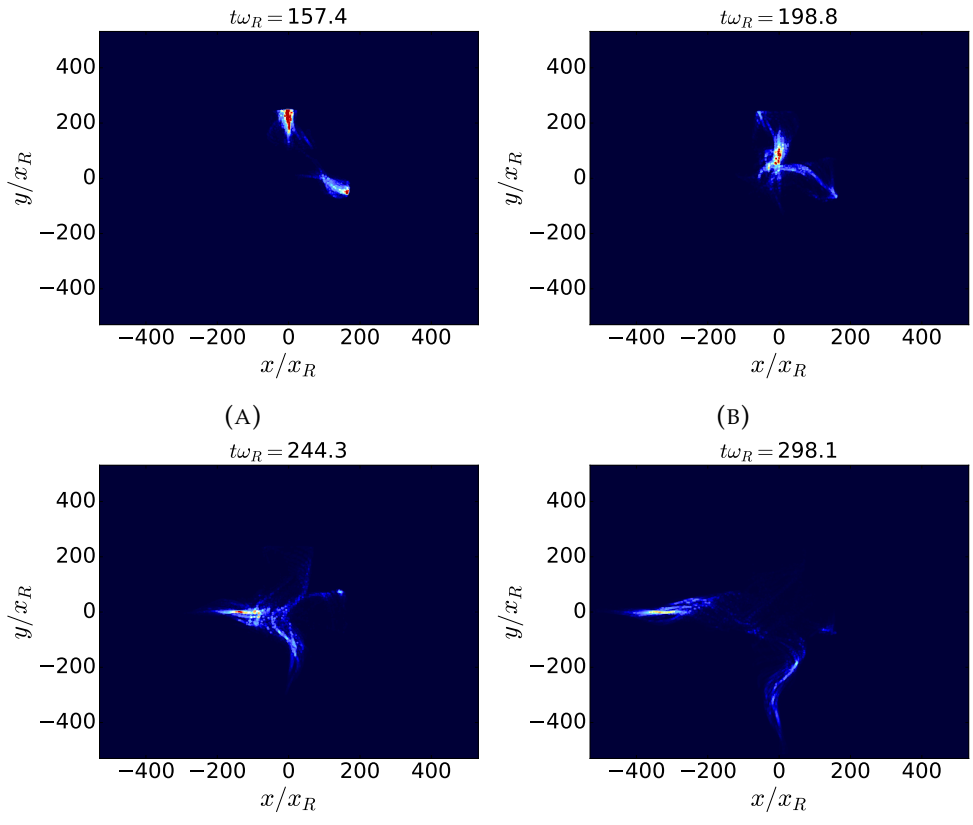

(A) (B)

(C) (D)

FIGURE 5.22: These figures depict the evolution of two wave-packets after they have been split and reflected backwards into the beam-splitter(A), where the recombine(B and C) and leave(D). For the parameters $v = 5v_R$, $\varepsilon = 0.5$, $F = 0$, $\theta = 90^\circ$, $\omega_0 = 15\mu m$, $\sigma_x = 10\mu m$, $U_0 = -20E_R$, $\lambda = 1064nm$, $v = 4v_R$, $\varepsilon = 0.5$, the position of the mirror inside the reflection guide $0.6|x_0| - 55.7\lambda_{DB}$ and the one in transmission at $0.6|x_0| - 103.45\lambda_{DB}$.

The other possible position for the mirror in the reflection waveguide is $-47.75\lambda_{DB}$, see Fig. 5.22. The wave-function starts off split into two different wave-packets inside the reflection and transmission waveguide, respectively, that get reflected back to the beam-splitter by the mirrors(5.22a). Then they get recombined(5.22b and (5.22c)) and leave the beam-splitter((5.22d)).
From these we can get the fringes as seen in Fig. 5.23. They have a maximum height of 10% and which is thus better than the 8% from the case with a shift of $-47.75\lambda_{DB}$, the combined probability is still 91%.

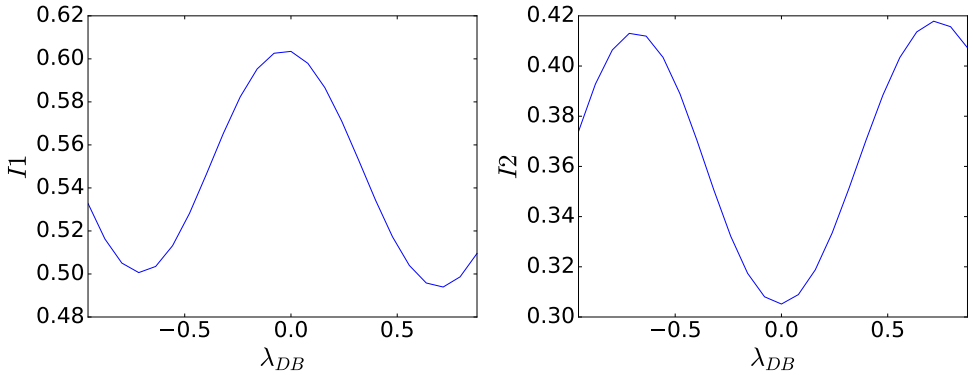

(A) Atom Input (B) Vacuum Input

FIGURE 5.23: The fringes in the atom input(A) and vacuum input(B) are depicted here, where the fringes high is roughly 10% for the parameters $v = 4v_R$, $\varepsilon = 0.5$, $F = 0$, $\theta = 90°$, $\omega_0 = 15\mu m$, $\sigma_x = 10\mu m$, $U_0 = -20E_R$, $\lambda = 1064nm$, $v = 5v_R$, $\varepsilon = 0.5$, the position of the mirror inside the reflection guide $0.6|x_0| - 55.7\lambda_{DB}$ and the one in transmission at $0.6|x_0| - 103.45\lambda_{DB}$. The probability of the two waveguides sum up to 91%.

5.3 Combining

The mirror position has proven important for a waveguide with a depth of $U_0 = -20E_R$ and a width of $\omega_0 = 15\mu m$. However, the main factor for this was that the wave-packet inside the transmission guide is bouncing inside of it, due to excitation to higher lateral modes causing transverse movement of the packet, and the splitting is heavily not central. However, this not as significant for both the narrower and shallower waveguides. For this reason we will investigate over a broader range of parameters for recombination.

5.3.1 Parameters: $U_0 = -2E_R$ and $\omega_0 = 1\mu m$

The first case will be the one where the width of our waveguides is $\omega_0 = 1\mu m$ and their depth is $U_0 = -2E_R$. The other parameters are a filling of $F = 0$, the crossing angle of the laser beams $\theta = 90°$, the width of the wave-packet in the longitudinal direction $\sigma_x = 0.73\mu m$, the wave-length of the lasers $\lambda = 720nm$ and the the position of the mirrors $x_{mr} = x_{mt} = 0.6|x_0|$. For this case the velocity is going to be varied from $v = 1.5v_R$ to $v = 4.0v_R$ varied with a step size of $0.5v_R$. As this is the region

we could trust and below $v = 1.5v_R$ we would have significant reflection back into the input. The polarisation is going from $\varepsilon = 0.3$ to $\varepsilon = 0.6$ with 0.1 increments and lastly the mirror in the transmission band is varied from $-0.48\lambda_{DB}$ to $0.48\lambda_{DB}$ in $0.04\lambda_{DB}$ increments. From these we can calculate the fringes and from these we can then determine the highest fringe size in the atom input and plot this as a function of the velocity and polarisation as done in Fig. 5.24.

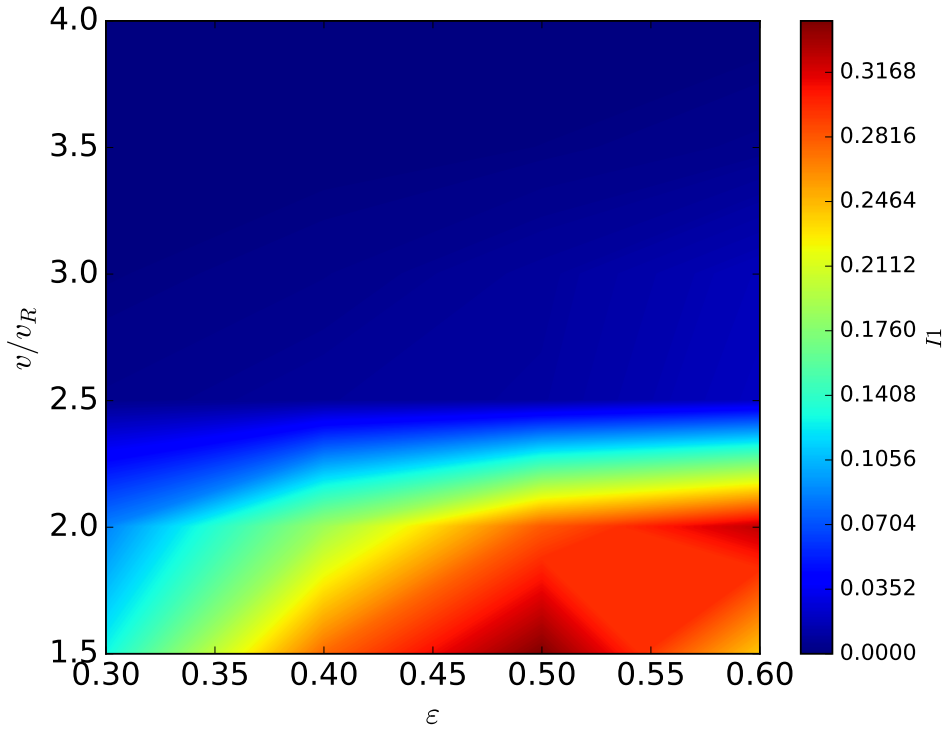

FIGURE 5.24: These figures show the height of the fringes as a function of the velocity and polarisation. The highest fringes were seen at $v = 1.5v_R$ and $\varepsilon = 0.5$ for the parameters. $F = 0$, $\theta = 90^\circ$, $\omega_0 = 1\mu m$, $\sigma_x = 0.73\mu m$, $U_0 = -2E_R$, $\lambda = 720nm$ and $x_{mr} = x_{mt} = 0.6|x_0|$.

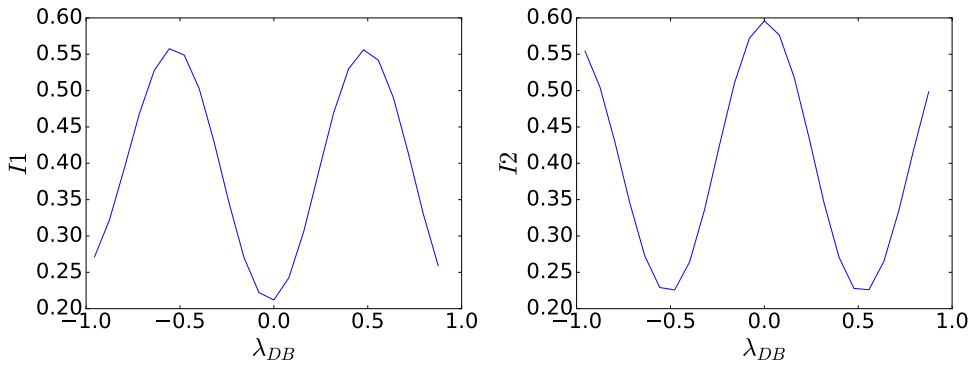

(A) Atom Input (B) Vacuum Input

FIGURE 5.25: The fringes for atom and vacuum inputs for the velocity $v = 1.5v_R$ and $\varepsilon = 0.5$, with the highest fringes being around 32%. The probabilities in the output waveguides add up to 78%.

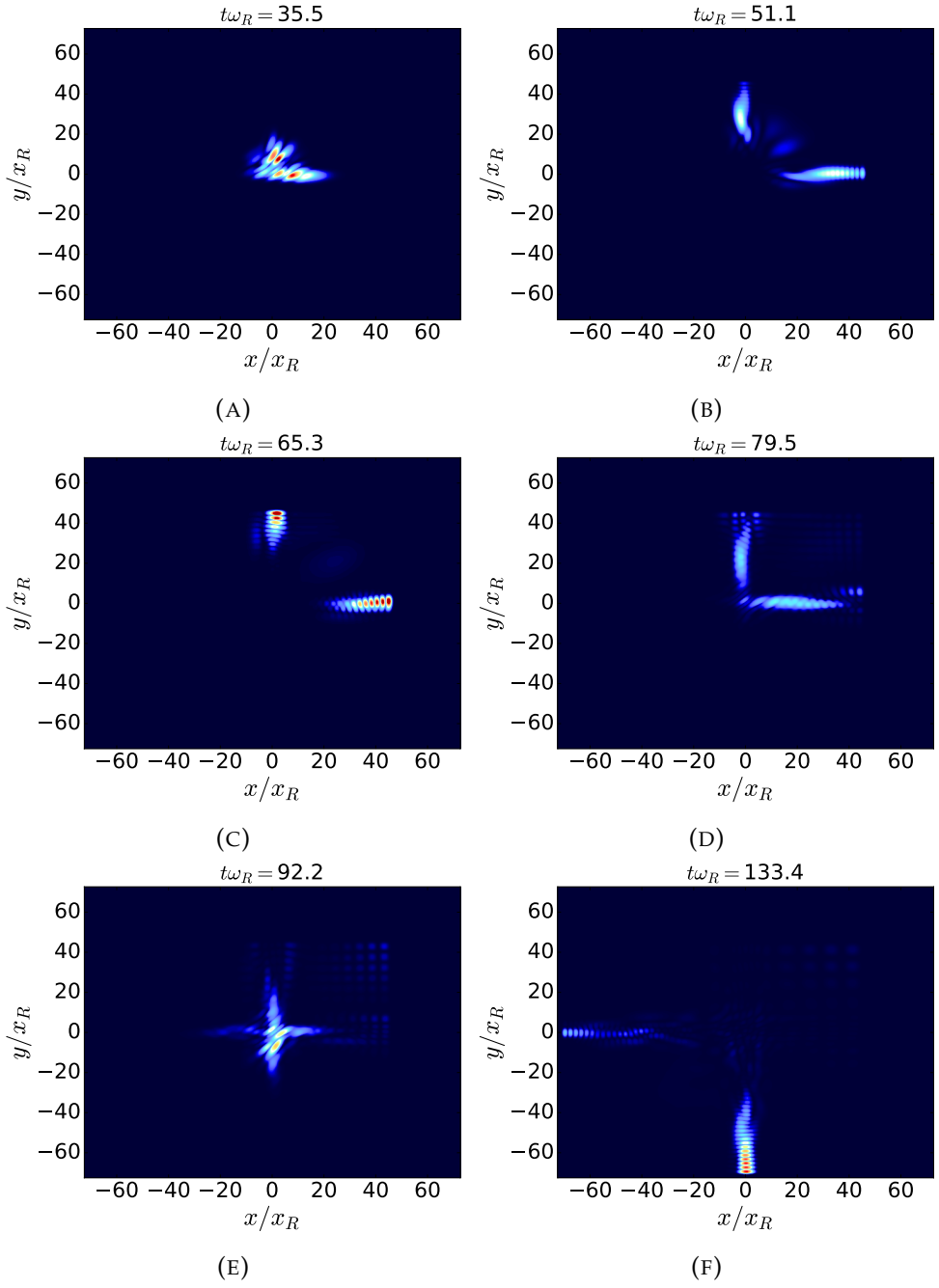

FIGURE 5.26: These figures depict the evolution of the wave-function through the beam-splitter, where the wave-function begins(A) travelling towards the beam-splitter(B) and gets split by it(C). Eventually, leaving the beam-splitter with some loss(D). Afterwards it gets reflected back into it by the mirror(E), where it recombines and(F and G) and finally leaves(H). The parameters for this simulation are $v = 1.5v_R$, $\varepsilon = 0.5$, $F = 0$, $\theta = 90°$, $\omega_0 = 1\mu m$, $\sigma_x = 0.73\mu m$, $U_0 = -2E_R$, $\lambda = 720nm$ and $x_{mr} = x_{mt} = 0.6|x_0|$.

From it we see that the biggest fringes can be found for the parameters of $v = 1.5v_R$ and $\varepsilon = 0.5$, where the actual fringe pattern can be seen Fig. 5.25. They show a fringe height up to 32%, which is significantly greater than the typical values we were able to find for the waveguide discussed in the previous sections. The probability of finding the atoms in the atom and vacuum input combined is 78%.

Lastly, it is worth to have a look at the evolution of the wave-function itself for these parameters. The example chosen is for the case where there is no shift in the mirror, see Fig. 5.26. The wave-functions gets by the beam-splitter split((5.26a)) and leaves at (5.26b), where it can be seen that some of the wave-function escapes creating loss. Now the wave-packets get reflected backwards into the beam-splitter(5.26c), where they recombine closer relative close to the centre((5.26d) and (5.26e)). Lastly, the interfering wave-packets exit the beam-splitter(5.26f).

5.3.2 Parameters: $U_0 = -2E_R$ and $\omega_0 = 1.5\mu m$

The next case we examine is the one where the width of the waveguide is widened to $\omega_0 = 1.5\mu m$. The other parameters stay the same. For this case as well we will vary the velocity from $v = 1.5v_R$ to $v = 4.0v_R$ with a step size of $0.5v_R$. The polarisation is going from $\varepsilon = 0.3$ to $\varepsilon = 0.6$ with 0.1 increments and the mirror in the transmission band is altered from $-0.48\lambda_{DB}$ to $0.48\lambda_{DB}$ by $0.04\lambda_{DB}$ increments.

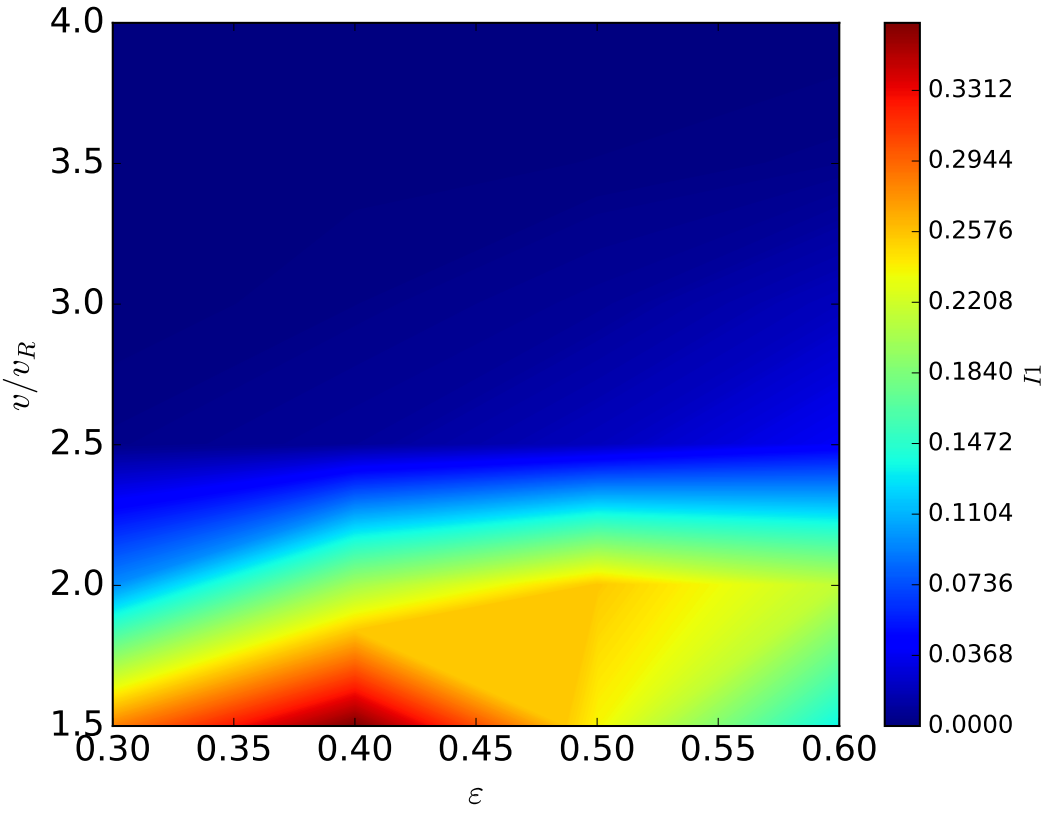

FIGURE 5.27: This graph depicts the maximum observed fringe size in the atom input, for a moving mirror in the transmission guide, which moves from $-3\lambda_{DB}$ to $3\lambda_{DB}$ by $0.25\lambda_{DB}$. The highest fringes were seen for $v = 1.5v_R$ and $\varepsilon = 0.4$ and the other parameters are $F = 0$, $\theta = 90°$, $\omega_0 = 1.5\mu m$, $\sigma_x = 0.73\mu m$, $U_0 = -2E_R$, $\lambda = 720nm$ and $x_{mr} = x_{mt} = 0.6|x_0|$.

For these properties we can calculate the maximum fringes in the atom input, Fig. 5.30. From this we see that the highest fringes can be seen for the velocity of $v = 1.5v_R$ the polarisation $\varepsilon = 0.4$. The fringes for these can be seen in Fig. 5.28. They

have a maximum height of 33% and thus they are the best ones observed so far, with the summed up probability of the relevant waveguides being 90%.

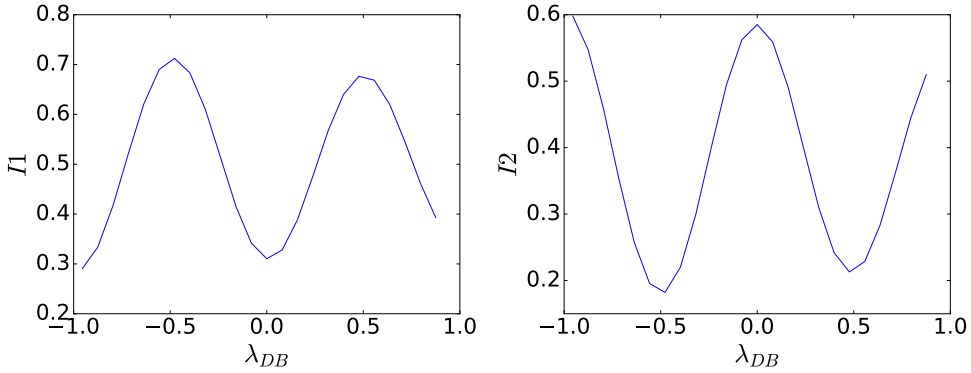

(A) Atom Input (B) Vacuum Input

FIGURE 5.28: The fringes in the atom(A) and vacuum(B) input for the velocity $v = 1.5v_R$ and $\varepsilon = 0.4$, with the highest fringes being around 33% and the summation of the probabilities being 90%.

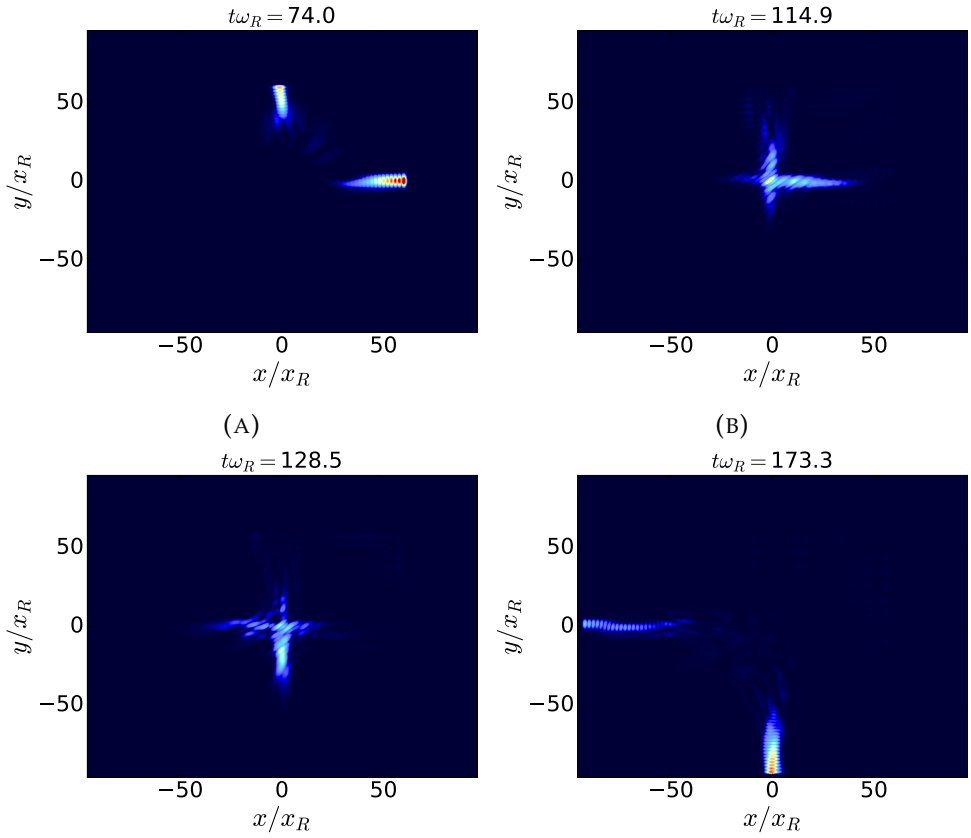

(A) (B) (C) (D)

FIGURE 5.29: The propagation of a wave-function through the beam-splitter for case with the highest fringes for the parameters $v = 1.5v_R$, $\varepsilon = 0.4$, $F = 0$, $\theta = 90°$, $\omega_0 = 1.5\mu m$, $\sigma_x = 0.73\mu m$, $U_0 = -2E_R$, $\lambda = 720nm$ and $x_{mr} = x_{mt} = 0.6|x_0|$. In A the wave-function starts starts by getting reflected from the mirrors, where some loss can be seen due to the splitting. Afterwards, the wave-packets travel back to the beam-splitter, where they get recombined in B and C. Finally, leaving towards the outputs in D.

The last thing to examine for this case is the propagating wave through the beam-splitter at the recombination, see Fig. 5.29. Starting off the with the wave-function being split with some losses, to be reflected by the mirrors(5.29a). They then travel back into the beams-splitter an get recombined5.29b and 5.29c). Lastly, the outputs leave the beam-splitter5.29d). The wave-packet consistency is still a lot better than for the case with $U_0 = -20E_R$ and $\omega_0 = 15\mu m$.

5.3.3 Parameters: $U_0 = -5E_R$ and $\omega_0 = 1\mu m$

The last case is the one where the depth of the lasers is $U_0 = -5E_R$ and their width is $\omega_0 = 1\mu m$. The other parameters stay the same. The other variable range for the velocity from $v = 1.5v_R$ to $v = 4.0v_R$ with an increment size of $0.5v_R$. The polarisation ranges from $\varepsilon = 0.3$ to $\varepsilon = 0.6$ with 0.1 increments and the mirror in the transmission band is moved from $-0.48\lambda_{DB}$ to $0.48\lambda_{DB}$ in $0.04\lambda_{DB}$ increments. From this the height of the fringes in the atom input can be calculated giving us Fig. 5.30, where the highest fringes can be found at $v = 3v_R$ and $\varepsilon = 0.6$.

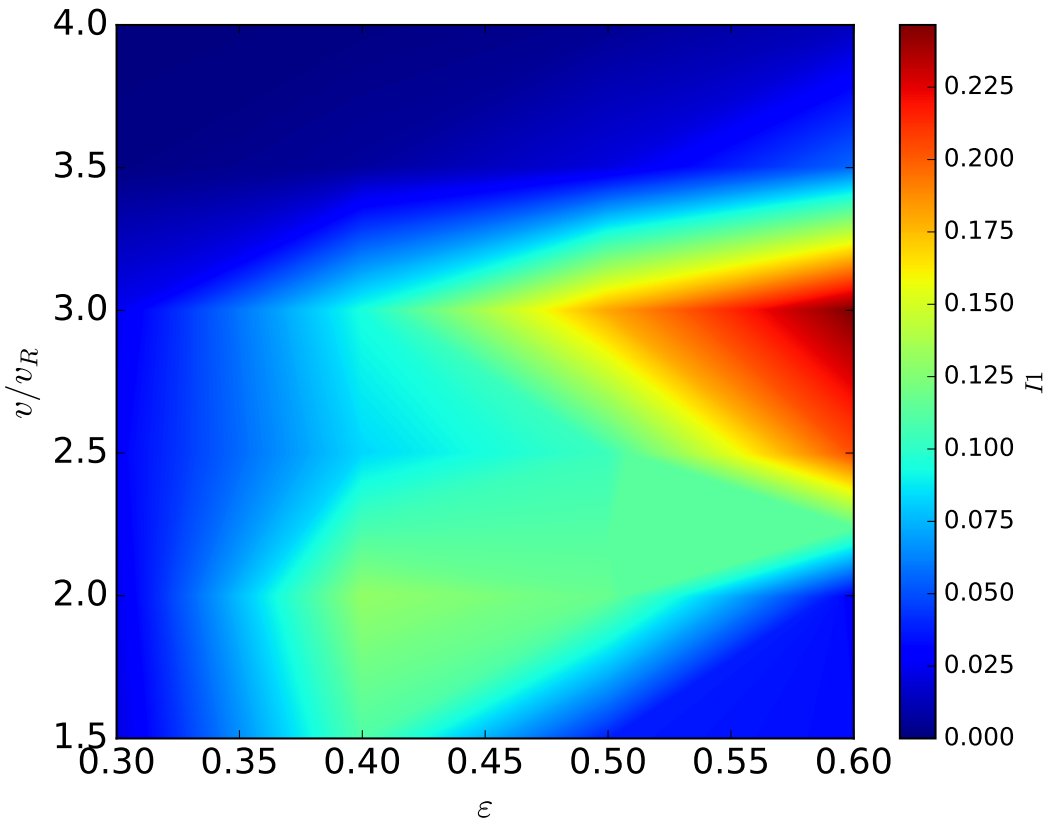

FIGURE 5.30: Showing the fringe height for the atom input at the end of the simulation, where the highest fringes are found to be around $v = 3v_R$ and $\varepsilon = 0.6$. The other parameters are $F = 0$, $\theta = 90°$, $\omega_0 = 1\mu m$, $\sigma_x = 0.73\mu m$, $U_0 = -5E_R$, $\lambda = 720nm$ and $x_{mr} = x_{mt} = 0.6|x_0|$.

For this case the fringes are seen in Fig. 5.31, with a height of 22%, which is thus lower than the two previous cases. For this case as well the fringes are not a de

Broglie wavelength long due to the excitation of the atom into higher transverse modes and thus lowering the overall velocity in the propagation direction of the waveguide.

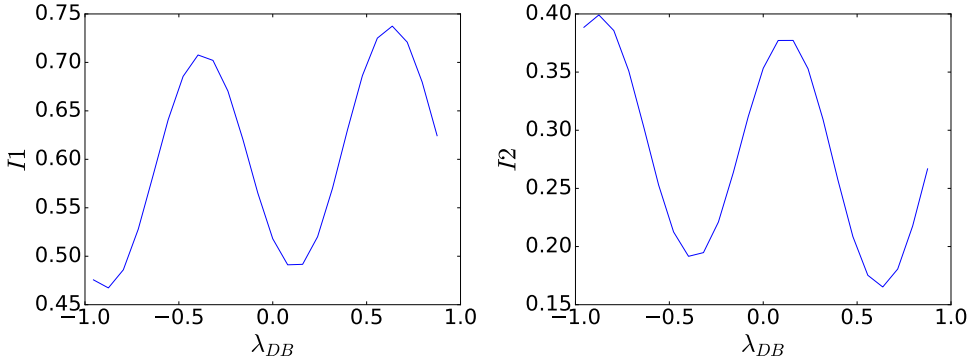

(A) Atom Input (B) Vacuum Input

FIGURE 5.31: The fringes for the atom(A) and vacuum(B) input for the velocity $v = 3v_R$ and the polarisation $\varepsilon = 0.6$, with the highest fringes being around 22%. The sum of these two waveguides sums up to 89%.

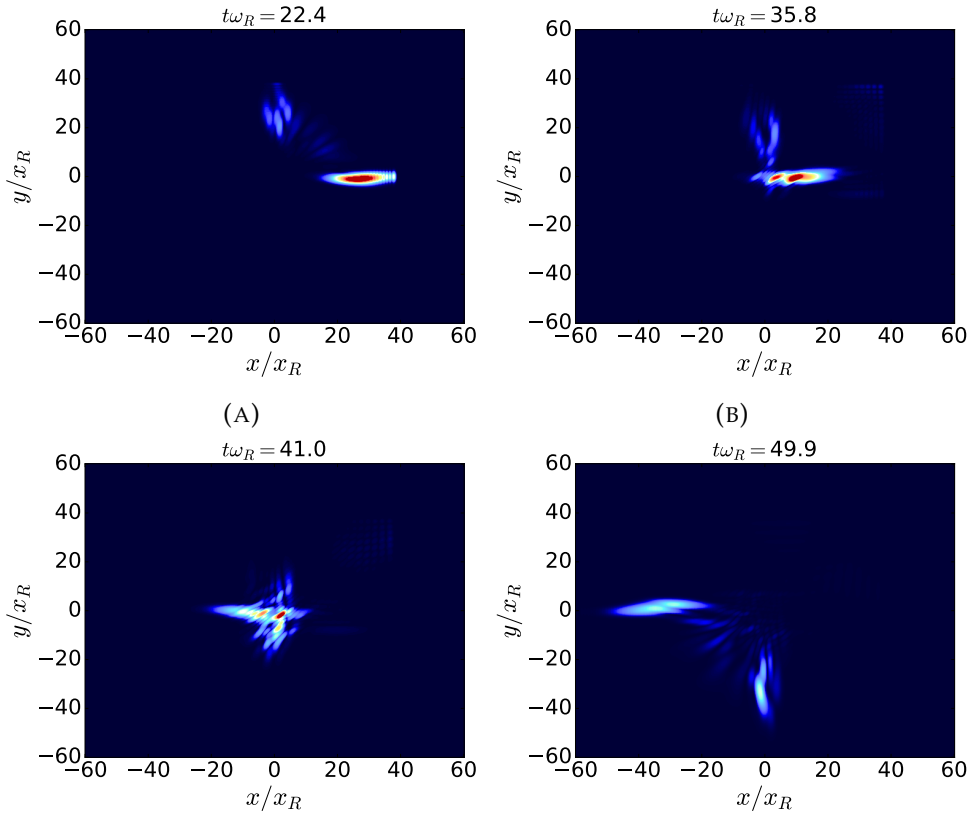

(A) (B)

(C) (D)

FIGURE 5.32: The wave-function leaves the beam-splitter with some loss to be reflected back by the mirror in A. B shows the wave re-entering the beam-splitter to be recombined in C and then exiting in D. The other parameters are $v = 3v_R$, $\varepsilon = 0.6$, $F = 0$, $\theta = 90^\circ$, $\omega_0 = 1\mu m$, $\sigma_x = 0.73\mu m$, $U_0 = -5E_R$, $\lambda = 720nm$ and $x_{mr} = x_{mt} = 0.6|x_0|$.

The last thing to examine is the propagation of the wave-function, Fig. 5.32. The atom starts off leaving the beam-splitter with some loss to get reflected backwards by the mirrors(5.32a). Afterwards, it reaches the beam-splitter(5.32b) and gets recombined (5.32c)). Leaving the beam-splitter with some additional loss(5.32d). Also, the output is again more coherent than the one for a deeper and wider waveguide, this can be inferred from looking at the probability density.

5.4 Summary

In this chapter we investigated the recombination abilities of our beam-splitter by creating a Michelson interferometer where the mirrors are reflective Gaussian potentials that could be created by lasers. One of the mirrors was moved between each run to create artificial fringes.
The first examination was focused on the importance of the mirror position for the case. For this we use coarse movement of the mirrors to adjust interfering packet overlap, and fine movement to produce the phase shift to vary the output probabilities. The parameters that were shared in these investigation were $\sigma_x = 10\mu m$, $U_0 = -20E_R$, $\lambda = 1064nm$, $\varepsilon = 0.5$ and $x_{mr} = x_{mt} = 0.6|x_0|$. Using this we investigated two cases of the filling of the potential well in the beam-splitter, $F = 1$ and $F = 0$. Beginning with $F = 1$ with a velocity of $v = 5v_R$, the mirrors are moved coarsely in parallel until a point was found were the two wave-packets overlapped an example being at $-31.83\lambda_{DB}$. At this point we then performed fine mirror movements in the transmission waveguide to create artificial fringes by rerunning the simulation for each position separately. Giving us the fringe height of 5% with 85% of the wave being in both output waveguides. When both mirrors were slightly moved further to $39.8\lambda_{DB}$ the fringe height collapsed to 1.5% with the combined probability of the waveguides staying the same. Afterwards, we set the mirrors back to $-31.83\lambda_{DB}$ and moved only the transmission guide mirror coarsely to an additional $-71.62\lambda_{DB}$ and $-75.6\lambda_{DB}$ as the wave-packet seemed to meet in the centre. However, beam-splitter recombination is non-central and starts at the edges. Thus when the wave-packets meet in the centre they already have gone through partially being split. Lastly, for this case we varied the mirror in the reflection guide instead of the translation guide to create artificial fringes and these were the same height as for the ones in the transmission waveguide.
The next case was for $F = 0$ with a velocity of $v = 4v_R$. For this case it was not possible to overlap the wave-packets with both mirrors moved simultaneously. As such the mirror in the transmission band was moved so that the wave-packets travel through the upper region of the beam-splitter. Afterwards, the mirror in the reflection was set so that the wave-packet from it could be combined with that from the transmission guide. There were two possible cases found for which we investigated the fringes. These are the ones where the reflection mirror is shifted by $-47.74\lambda_{DB}$

and the one in the transmission by $-103.45\lambda_{DB}$, giving fringes of 8% with a summation of the probabilities being 91%. The other one is $-55.7\lambda_{DB}$ for the reflection mirror and $-103.45\lambda_{DB}$ for the mirror inside the translation waveguide. These gave a fringe height 10% with a combined probability of 91%. Nonetheless, it should be noted that the wavelength of the recombined wave-packets is increased as the average speed of the packet along the waveguide direction really is lowered by the excitation of transverse modes in the waveguide and so there is then less translational kinetic energy in the waveguide propagation direction.

Afterwards, we looked at the cases where the waveguides are narrower and shallower, having the shared parameters $x_{mr} = x_{mt} = 0.6|x_0|$ and $\lambda = 720nm$. As these kinds of beam-splitter are less sensitive to non-central splitting we fixed the mirror and varied the velocity and polarisation over a range of parameters recording the fringe height for each case. Through this investigation we found that for a potential depth of $-2E_R$ and a width of $\omega_0 = 1\mu m$ the heights fringes are 32% and a combined probability at both outputs of 78%. The next one was a potential depth of $-2E_R$ and a width of $\omega_0 = 1.5\mu m$. For this case the fringe height was 33% with a probability at both outputs of 90%. These are the highest fringes that were observed. The last case is for a potential depth of $-5E_R$ and a width of $\omega_0 = 1\mu m$ with fringes of the height of 22% and a probability of 89% to find the atoms at the outputs. Furthermore, for all these cases the wavelength was larger after the splitting. However, it was not massively increased. Hence these parameters would be easier to optimise for than the ones for a deeper depth and a wider width waveguide. Additionally one could potentially infer information about the coherence of the split wave-packets from the wavelength observed at the output. If this is very close to the input wavelength there will be minimal excitation into higher transverse modes in the waveguides and the splitting will be coherent. If the wavelength decreases significantly this will be linked to excitation into higher transverse modes and the splitting will be less coherent.

The maximum sensitivity of an interferometer can be archived by having the output without an unknown phase shift being at the maximum of the slope. Hence it is important to have a feedback system that returns the output to this position. This is done by applying a controlled shift to compensate and return the system to where it was. The unknown phase shift is then the negative of the shift that was applied to remove it. For this process to work it the interferometer must be calibrated, so a known shift can be applied to keep the interferometer output position and the maximum of the slope[111].

Chapter 6

Conclusion

This thesis has focused on the modelling of the beam-splitting properties of an all optical beam-splitter, where the beam-splitter is created by the overlap of two red-detuned Gaussian laser beams that also function as the waveguides for the atomic Bose-Einstein experimental investigations on this system that have been undertaken in the group of Professor Yuri Ovchinnikov at the National Physical Laboratory (NPL) [95]. Throughout, the modelling parameters used in this thesis have been chosen to be compatible with the experimental capabilities, so as to investigate the potential for such interferometers as practical devices. In the simulations we have employed a low density condensate and thus it is only necessary to solve the time dependent Schrödinger equation. However, this also has the disadvantage of being restricted by the Shot noise limit, which is dependent on the number of atoms[27].
The beam-splitting was firstly analysed in one-dimension, where we used the method from Daemon et al. to calculate the band-gap structure[97] and from this the transmission probability for the atoms as a function of velocity and polarisation ε. However, for our chosen parameters did not have enough fringes to work these results were not compatible with those of two other methods which we used to calculate the transmission probability.
Following this, we calculated the transmission probability as a function of velocity and ε by integrating backwards through the beam-splitter for four different cases[104]. The first one being the case being for $U_0 = -20E_R$, $\omega = 15\mu_m$, $\lambda = 1064nm$ and a variety of filling levels. For these parameters the regions of total reflection and total transmission were initially linearly divided. However, when the filling was increased the separation becomes curved. This is due to the nature of the filling, which is a Gaussian potential. As such its effects are stronger in the central region than the edges of the beam-splitter. Therefore, the linear separation becomes curved as different regions inside the beam-splitter have a different impact on the transmission probability depending on the velocity of the atoms. The other cases were for a $\lambda = 720nm$, $U_0 = -2E_R$, $\omega = 1\mu_m$, $U_0 = -2E_R$, $\omega = 1.5\mu_m$ $U_0 = -5E_R$, $\omega = 1\mu_m$. In all of these cases the same phenomenon happened, where the separation was linear for no filling then became curved when filling was added. These three cases are generally very similar where the difference between them is the due to their resonant frequencies which enhances the transmission probability for certain velocities.

The last method that we used was the split-step Fourier method. Furthermore, as these simulations investigated the propagation of the wave-function through the beam-splitter, we found that it is possible that atoms become localised, or trapped, inside the beam-splitter, which is not desirable. In this method we investigated various examples, again starting with the one where $U_0 = -20E_R$, $\omega = 15\mu_m$. Additional to previous parameters our incoming wave-packet as a width of $\sigma = 10\mu m$. The resulting transmission probabilities agreed significantly with the ones from the standing wave calculations, with the caveat that the transition areas between total transmission and total reflection are smoothed out. This comes from the nature that a Gaussian wave-packet is a superposition of monochromatic travelling waves and thus the observed transmission is related to the superposition of the individual transmission probabilities. Additionally, the propagating wave-function could be directly observed and thus how its shape changes due to the action of the beam-splitter. The wave-packets after the splitting are not perfectly Gaussian but reasonably so, indicating a relatively coherent splitting in one-dimension. Indicating a relative coherent splitting in one Dimensions. However, regions of approximate 50:50 splitting were found to have significant overlap with evolutions that resulted in significant trapping probabilities. As for the other three cases $U_0 = -2E_R$, $\omega = 1\mu_m$ $U_0 = -2E_R$, $\omega = 1.5\mu_m$ $U_0 = -5E_R$, $\omega = 1\mu_m$. The width of the wave-packet used in these was $\sigma = 0.73\mu m$. The results from these calculations agreed with those from the standing wave calculations as well, and the observed splittings appeared a little more coherent. Also, the areas of significant atom trapping do not overlap much with those for approximate 50:50 splitting.

After having investigated the one-dimensional properties of the beam-splitter, the second step undertaken was to analyse the propagation of a wave-packet through the beam-splitter in two-dimension,s using the split-step Fourier method. Given two dimensions, there was more scope for the wave-packet propagation to various regions, which are the waveguides for the atom input, vacuum input, reflection, transmission, beam-splitter and outside the waveguides and beam-splitter, which will be counted as a loss of atoms. Our ideal splitting probabilities would be a 50:50 split, with an insignificant number of atoms inside the atom input, vacuum input and beam-splitter as these could potentially lead to additional noise, when these would interact with the atoms coming directly from the atom laser. Therefore having atoms in these regions is used as an execution criteria, while atom loss due to escaped atoms is not ideal as this would lower the precision due to the shot noise limit [27]. The cases studied in two-dimensions were the same as those in one-dimension with the exception that the filling was only used for $U_0 = -20E_R$, $\omega = 15\mu_m$. Thus for the case with $U_0 = -20E_R$, $\omega = 15\mu_m$, the probabilities for finding the atoms in the respective regions were calculated, and the best values were found to be $v = 4v_R$ and $\varepsilon = 0.5$ for balanced splitting with no filling. However, the splitting itself is not

coherent and excites the incoming wave-packet over a range of transverse modes inside the waveguides. Therefore the wave-packets stay generally within the waveguides, but exhibit transverse motion (bouncing) due to the excitation. However, the wave-packet inside the reflection region does not stay together but splits into a significant number of smaller wave-packets bouncing inside the waveguide. To counter this the width and depth of the waveguides were reduced, to lower the beam-splitter potential energy that could increase the kinetic energy of the atoms inside it, and to increase the separation energy between the eigenstates, respectively. Thus making it harder for the atoms to occupy higher modes. This led to the investigation of the cases $U_0 = -2E_R$, $\omega = 1\mu_m$ $U_0 = -2E_R$, $\omega = 1.5\mu_m$ $U_0 = -5E_R$, $\omega = 1\mu_m$. In these cases the splitting was still not coherent enough, but was improved. The transmitted wave-packet stays roughly inside the centre of the waveguide but the wave-packet inside the reflection guide was still split into several wave-packets, but significantly fewer in number. However, the disadvantage to this approach is that the atoms can more easily escape due to inelastic intra-trap collisions[72]. Our next investigation to improve the splitting was with a smaller crossing angle between the beams, in order to reduce the momentum direction change. Despite this reasoning, there was no useful improvement, as the wave-packets still occupy higher states. The last method that was investigated to improve the splitting was the introduction of a third laser beam to act as a reflector[72], which is the source of the above mentioned filling. However, for the case where $U_0 = -20E_R$, $\omega = 15\mu_m$ it did not improve the coherence. Additionally, it should be mentioned that the splitting generated is non-central within the beam-splitter region, especially for $U_0 = -20E_R$, $\omega = 15\mu_m$.
In general our results have shown that the beam-splitting is not coherent and excites higher modes inside the waveguides. However, it can still be used for recombination as a multimode interferometer[109, 110], which is similar to the white light case in optics. The final experimental and technological goal (and thus also modelling goal) is the creation of a Mach-Zehnder interferometer. However it was easier for the present level of modelling investigations to implement a Michelson interferometer to test recombination. For the mirrors Gaussian potentials were used as these could be implemented by blue-detuned Gaussian laser beams[72]. For $U_0 = -20E_R$, $\omega = 15\mu_m$ with zero filling no region could be found to create an interferometer with both mirrors equidistant from the beam-splitter, because the packets in the two wave-guides exhibited different longitudinal speeds. As so both mirror need to be at different positions. Furthermore, as the splitting is mostly non-central it was necessary to choose the mirror position inside the transmission waveguide so that the wave-packet from it is guided to interfere with the wave-packet from the reflection inside the upper part of of the beam-splitter. The best interference fringes found for these parameters exhibited a fringe height of 10%. The next investigations were made for parameters of $U_0 = -20E_R$, $\omega = 15\mu_m$ with $F = 1$ filling. For this case the best fringes were found with height of 5% for the case of both mirrors equidistant from the beam-splitter. Detailed investigations for narrower waveguides were then

undertaken. For the cases the splitting was more central as such instead of looking for mirror position we investigated over a wide parameter space for the largest fringe height, where the highest fringes for $U_0 = -2E_R$, $\omega = 1\mu m$, $U_0 = -2E_R$, $\omega = 1.5\mu m$ and $U_0 = -5E_R$, $\omega = 1\mu m$ are 32% 33% and 22%, respectively. Thus there is a change that could be used to build an interferometer depending on the laboratory results. It should also be mentioned that due to the excitation in the splitting the fringes have a longer period the atom are slowed done due to be excited into higher modes.

However, even though this is the end of the content of this thesis there is still much work that could be done. One interesting development would be the implementation of the Gross-Pitaevskii equation into the split-step Four method with further optimisation of the code[112–122], as this would allow to study higher density BECs allowing for higher precision due to the atom number depends for the shot noise and Heisenberg limit. Furthermore, thus far the mirror position has only been varied for $U_0 = -20E_R$ and $\omega = 15\mu m$. But it could also be varied for the other cases. Additionally, to date only a Michelson interferometer has been simulated. For a closer model to the envisaged experimental scenarios, expansion towards a Mach-Zehnder arrangement would be desirable. However, this would require a significantly larger modelling region to capture the complete evolution of the atomic wave-packet through the complete system. Also, the simulations presented here only demonstrate an artificial interference pattern, generated through a phase shift produced by fine movement of one mirror. Thus it would be desirable to simulate more practical applications, by generating the phase shift through rotation (using some form of time-dependent potential) or inclusion of some realistic phase-shifting material in one arm of the interferometer.

Significant further developments that could be pursued, both from the modelling and the experimental perspectives, could build on the current work to include major additional physics[123, 124]. One direction would be the introduction of noise and other environmental effects using techniques of open quantum systems, and potentially including feedback and control. Another would be the use of non-classical states, for example employing squeezing or entanglement, to push the limits of atomic interferometry and metrology towards the ultimate Heisenberg limit of sensitivity[10, 12, 85, 89, 125–130].

Appendix A

Animations

In addition to the thesis a zip file(AppendixA.zip) has been submitted to give all the relevant background animations. For this we have arranged the animations inside a folder structure A.1. The four sub folders are thesis, which contain all the animations highlights shown in the thesis where the animations are labelled with the number of the figure ,aka "Fig 2.13.pdf". The subfolder Chapter 3 contains all the background animations in subfolders labelled after the appropriate plots, in chapter 3. If one set of animations was used to create several plots it will be labelled by the figure with the lowest number. The same is the case for the folder Chapter 4 and Chapter 5. It should be noticed that they only contain the animations that are from the split-step Fourier method. These animations are generally labelled as such 11.0:E=-20.0_epsilon=0.5_w=15.0_sigx=10.0_v=5.0_theta=90.0_lambda=1064.0_shift=0.0_fill=0.50.mp4, where the first number is a counting integer in the simulation, followed by the energy in E_R, the polarisation ε, the waist of the Gaussian beams in μm, the variance of the wave-packet in μm, the velocity in v_R, the angel between the beams in degrees, the wavelength of the laser beams in nm, the shift of one of the mirrors to create the artificial fringes in $1/k$ where k is the wavenumber of the incoming wave-packet, lastly the same integer number as to can also be at the end instead of the beginning.

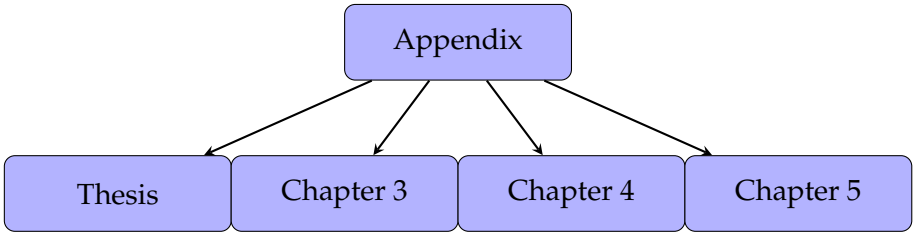

FIGURE A.1: Folder Structure

Appendix B

Code

The appendix contains a general overview of my code for the split-step Fourier method in one-dimensions. The main function iterates over the variable parameters as seen and the number of datapoints needed in k-space, in Fig. B.1.

```
program main
    use omp_lib
    use omp_lib_kinds
    implicit none
    include "fftw3.f"
    !initiating variable
    integer iret
    character(len=50)::f_num,f_folder,folder
    real ( kind = 8 ):: angle_deg,v_x,v_y,ep,k_shift,fill
    integer( kind = 8 )::n,deg,v,e,ks,f
    !set number of threads
    call dfftw_init_threads(iret)
    call dfftw_plan_with_nthreads(4)
    CALL OMP_SET_NUM_THREADS (4)
    CALL omp_set_nested(.true.)
    !counting integer
    n=1


    !iterating of these paramters

    f_folder="1d_split4_720_fill/1d_split4_720_"
    !filling
    fill=0.
    do f= 1,11
        !velocity
        v_x=.5
        do v= 1,10
            !polarisation
            ep=0.
            do e=1,11
                !shift  in the mirror position
                k_shift=0.
                do ks = 1, 1
                    !scrossing angle
                    angle_deg=90.
                    do deg = 1,1
                        write(f_num,*) n

                        folder=(trim(f_folder)//trim(adjustl(f_num)))
                        write(*,*) folder
                        !call the function that manages the caculations for the repectiveruns
                        call sub(angle_deg,folder,v_x,ep,n,k_shift,fill)
                        !plotting
                        call execute_command_line ("python 1d_shift_plot_04_07_2019.py "//trim(folder), wait=.true.)
                        write (*,*) "Marker"
                        call execute_command_line ("python 1d_shift_plot_04_07_2019_2.py "//trim(folder)//" "//trim(f_folder), wait=.true.)

                        angle_deg=angle_deg+0
                        n=n+1
                    end do
                    k_shift=k_shift+0.6
                end do
                ep=ep+0.1
            end do
            v_x=v_x+0.5
        end do
        fill=fill+0.1
    end do
```

FIGURE B.1: This is the main function which gives the variable parameters to for each run.

The individual runs are handled by the subroutine sub, beginning by defining the fixed parameters, size of the simulation area and simulation time in Fig. B.2. The other variables like the steps in position and momentum space to evolve the wavefunction.

```
pi=3.14159265358979323846264338327950288419716939937510582097494459230781640628
mass=86.909180527*1.660538921E-27 !mass of the particle
hbar=1.0545718E-34 ! reduced plank constant
theta=angle/180.*pi !angle of the crossing beams in rads
wave_l=720.
kr=2*pi/(wave_l*1.E-9)!recoil wavenumber
vr=kr*hbar/mass!recoil velocity
!Er=hbar**2.*kr**2./(2.*mass)!recoil energy
!Er=real(0.5*(real( hbar, kind = 8 )*real( hbar, kind = 8 ))**2./real( mass, kind = 8 ),kind=4)
Er=0.5*(hbar*kr)**2./mass
wr=vr*kr!recoil angular frequency
!epsi=0.!polarisation difference between the beams
w0_num=1.5
w0=w0_num*1.E-6*kr!waist of the beams
!vx=vx/vr!vx=8.84!initial velocity in x direction
!vy=0.!initial velocity in y direction
d=pi/(sin(theta*0.5))!fringe spacing in the lattice
sig_num=0.73
sigx=sig_num*1.E-6*kr!waist of the gaussian atom beam in the x direction
u0=-5.!depth of the potential

dt=0.5E-6*wr!time step size
t_number=101!number of time saves
t=(6.*w0*(1.+abs(cos(theta)/sin(theta)))+4.*sigx)/vx!calculates the time
N_t=CEILING(t/dt)!calculates the number of time steps
N_t_small=CEILING(N_t/(t_number-1.))!calculates the number of steps between two time plots
t=N_t*dt!recalculates the time

dx=d/50.!separation between the data points in x direction
xi=-3.*w0*(1.+abs(cos(theta)/sin(theta)))-2.*abs(sqrt((sigx**4.+(t)**2.)/sigx**2.))!stating point of the wavepacked in the x direction
ax=-2.5*abs(sqrt((sigx**4.+(t)**2.)/sigx**2.))-1.*abs(xi)
ax=ax
bx=-ax
dkx=2.*pi/(bx-ax)
kix=vx
!Extra for combine
t=2.5*abs(xi)/vx!calculates the time
N_t=CEILING(t/dt)!calculates the number of time steps
N_t_small=CEILING(N_t/(t_number-1.))!calculates the number of steps between two time plots
t=N_t*dt!recalculates the time
```

FIGURE B.2: Defining the fixed parameters, simulation time and simulation area.

```
!Make sure to have enought k-space
if ((bx-ax)/dx > 2.*(abs(kix)+3./sigx+sqrt(3.*abs(u0)))/dkx) THEN
    nx=int(2**(CEILING(log2((bx-ax)/dx))))
else
    nx=int(2**(CEILING(log2(2.*(abs(kix)+3./sigx+sqrt(3.*abs(u0)))/dkx))))
end if
!reset dx in case nx or ny changed
dx=(bx-ax)/nx
write (*,*) "Stage 1"
!alloocate paramters
allocate(u(nx),psi_x(nx),psi_k(nx),psi_x_mod(nx),psi_k_mod(nx),full_step_x(nx),full_step_k(nx))
allocate(x_arrange(nx),x_1(nx),kx_1(nx))
!creates a list from 0 to nx in integers
CALL arrange(x_arrange,nx)
!1d array for x
x_1=ax+x_arrange*dx
write (*,*) "Stage 2"
kx_1=(-nx/2.+x_arrange)*dkx
!minimum x and k_x
x_0=ax
kx_0=-nx/2.*dkx
write(*,*) "dkx: ",dkx
write(*,*) "kx_0: ",kx_0
deallocate(x_arrange)
!create the potential for the beam-splitter and the cage
Call potential(u,U0,x_1,nx,theta,w0,d,epsi,pi,fill)
allocate(u_r(nx))
Call potential_gaussian_c(u_r,U0,x_1,x_0,dx)
u=u+u_r
deallocate(u_r)
!define the steps for the spli-step fourier method
full_step_x=exp(-0.5*i*u*dt)
full_step_k=exp(-0.5*i*(kx_1**2.)*dt)
write (*,*) "Stage 3"
!create the wave-packet
CALL gaussian_x(psi_x,x_1,kix,sigx,pi,xi,i)
!change it so the discrete fourier transform can use it for our case
CALL mode_psi_x(psi_x,psi_x_mod,x_1,dx,kx_0,pi,i)


write (*,*) "Stage 4"

call system("mkdir -p "//trim(folder))
!define the number of datapoints to be saved
step_x=1
if ((log2(real(nx,kind=8))-9.)>0.) then
    step_x=CEILING(2.**(log2(real(nx,kind=8))-9.))
end if
```

FIGURE B.3: Sets the variables to evolve the wave-function and determines the number of required datapoints.

Then the wave-function is evolved taking snapshots of it and related information at times spaced by set intervals, see Fig. B.4.

```
!defines the points when the program dsaves the state of the wave-function
DO t_count=0,t_number-1
    i_r=0.
    t_r=0.
    e_r=0.

    !needs to chage back the phase shifts
    CALL reverse_psi_x(psi_x,psi_x_mod,x_1,dx,kx_0,pi,i)
    CALL reverse_psi_k(psi_k,psi_k_mod,kx_1,kx_0,x_0,i)
    time=t_count*N_t_small*dt
    !caculate the normalisation in position and k space and the enrgy
    energy=real(sum(CONJG(psi_k)*(kx_1**2)*psi_k)*dkx+sum(CONJG(psi_x)*u*psi_x)*dx,kind=8)
    norm=real(sum(CONJG(psi_x)*psi_x)*dx,kind=8)
    norm_k=real(sum(CONJG(psi_k)*psi_k)*dkx,kind=8)
    write (33,*) time
    write (34,*) energy
    write (35,*) norm
    write (56,*) norm_k


    !save the data
    DO k=step_x,nx,step_x
        write (31,*) real(CONJG(psi_x(k))*psi_x(k),kind=8)
    END DO


    !determined how much of the wave-function is in each region
    DO k=1,nx
        if(x_1(k)<=-1.5*w0*(1.+abs(cos(theta)/sin(theta))))Then
            i_r=i_r+real(CONJG(psi_x(k))*psi_x(k),kind=8)*dx

        else if(x_1(k)>=1.5*w0*(1.+abs(cos(theta)/sin(theta)))) Then
            t_r=t_r+real(CONJG(psi_x(k))*psi_x(k),kind=8)*dx

        else
            e_r=e_r+real(CONJG(psi_x(k))*psi_x(k),kind=8)*dx
        end if
    END DO


    write (36,*) i_r
    write (37,*) t_r
    write (41,*) e_r


    !perfomes the split-step fourier method

    if (t_count<(t_number-1)) THEN
        call ssfm(nx, psi_x_mod, psi_k_mod,full_step_x,full_step_k,N_t_small )
    else
        write(*,*) "End"
    end if


END DO
```

FIGURE B.4: Shows the saving of the data at certain times

The split-step algorithm is in the subroutine ssfm, see Fig. B.5which uses the "Fastest Fourier Transform in the West" (FFTW) for the discrete Fourier transform[131], to follow the method descriptive in Sec. refCha2: The Split-Step Fourier Method for the Schrödinger Equation.

```
subroutine ssfm(nx, psi_x_mod, psi_k_mod,full_step_x,full_step_k,N_t_small)
    !split-step fourier method repeaded N_t_small times
    implicit none
    integer( kind = 8 ),INTENT(IN) :: nx, N_t_small
    complex( kind = 8 ),INTENT(IN) :: full_step_k(:),full_step_x(:)
    complex( kind = 8 ),INTENT(INOUT) ::psi_x_mod(:),psi_k_mod(:)
    integer( kind = 8 )::j,fft_norm

    fft_norm=nx
    !$OMP PARALLEL WORKSHARE
    psi_x_mod(:)=psi_x_mod(:)*sqrt(full_step_x(:))
    !$OMP END PARALLEL WORKSHARE
    DO j=1,N_t_small-1
        call fft1( nx, psi_x_mod)
        !$OMP PARALLEL WORKSHARE
        psi_x_mod(:)=psi_x_mod(:)*full_step_k(:)
        !$OMP END PARALLEL WORKSHARE
        call ifft1( nx, psi_x_mod)
        !$OMP PARALLEL WORKSHARE
        psi_x_mod(:)=psi_x_mod(:)*full_step_x(:)/fft_norm
        !$OMP END PARALLEL WORKSHARE
    END DO
    call fft1( nx, psi_x_mod)
    !$OMP PARALLEL WORKSHARE
    psi_x_mod(:)=psi_x_mod(:)*full_step_k(:)
    !$OMP END PARALLEL WORKSHARE
    call ifft1( nx, psi_x_mod)
    !$OMP PARALLEL WORKSHARE
    psi_x_mod(:)=psi_x_mod(:)*sqrt(full_step_x(:))/fft_norm
    psi_k_mod(:)=psi_x_mod(:)
    !$OMP END PARALLEL WORKSHARE
    call fft1( nx, psi_k_mod)
end subroutine ssfm
```

FIGURE B.5: Implementation of the Split-Step Fourier Method Algorithm

Bibliography

[1] E. Schrödinger. "Quantisierung als Eigenwertproblem". *Annalen der Physik* (Jan. 27, 1926).

[2] M. A. Nielsen and I. L. Chuang. *Quantum Computation and Quantum Information by Michael A. Nielsen*. Cambridge Core. Dec. 2010.

[3] C. H. Bennett and D. P. DiVincenzo. "Quantum information and computation". *Nature* **404**, 6775 (Mar. 16, 2000).

[4] H. Buhrman, R. Cleve, and A. Wigderson. "Quantum vs. Classical Communication and Computation". *arXiv:quant-ph/9802040* (Mar. 12, 1998).

[5] M. D'Angelo and Y. H. Shih. "Quantum imaging". *Laser Physics Letters* **2**, 12 (Sept. 16, 2005).

[6] L. A. Lugiato, A. Gatti, and E. Brambilla. "Quantum imaging". *Journal of Optics B: Quantum and Semiclassical Optics* **4**, 3 (Mar. 27, 2002).

[7] Y. Shih. "Quantum Imaging". *IEEE Journal of Selected Topics in Quantum Electronics* **13**, 4 (July 2007).

[8] S. L. Braunstein and P. van Loock. "Quantum information with continuous variables". *Reviews of Modern Physics* **77**, 2 (May 29, 2005).

[9] V. Giovannetti, S. Lloyd, and L. Maccone. "Quantum Metrology". *Physical Review Letters* **96**, 1 (Jan. 3, 2006).

[10] V. Giovannetti, S. Lloyd, and L. Maccone. "Advances in quantum metrology". *Nature Photonics* **5**, 4 (Apr. 2011).

[11] M. A. Taylor and W. P. Bowen. "Quantum metrology and its application in biology". *Physics Reports*. Quantum metrology and its application in biology **615** (Feb. 23, 2016).

[12] B. M. Escher, R. L. de Matos Filho, and L. Davidovich. "Quantum Metrology for Noisy Systems". *Brazilian Journal of Physics* **41**, 4 (Sept. 10, 2011).

[13] J. Joo et al. "Quantum metrology for non-linear phase shifts with entangled coherent states". *Physical Review A* **86**, 4 (Oct. 18, 2012).

[14] J. Joo, W. J. Munro, and T. P. Spiller. "Quantum metrology with entangled coherent states". *Physical Review Letters* **107**, 8 (Aug. 16, 2011).

[15] A. Einstein. "Quantentheorie des einatomigen idealen Gases". *Sitzungsberichte der Preussischen Akademie der Wissenschaften* **3**, 1 (Jan. 8, 1925).

[16] Bose. "Plancks Gesetz und Lichtquantenhypothese". *Zeitschrift für Physik* **26**, 1 (Dec. 1, 1924).

[17] M. H. Anderson et al. "Observation of Bose-Einstein Condensation in a Dilute Atomic Vapor". *Science* **269**, 5221 (July 14, 1995).

[18] K. B. Davis et al. "Bose-Einstein Condensation in a Gas of Sodium Atoms". *Physical Review Letters* **75**, 22 (Nov. 27, 1995).

[19] C. C. Bradley et al. "Evidence of Bose-Einstein Condensation in an Atomic Gas with Attractive Interactions". *Physical Review Letters* **75**, 9 (Aug. 28, 1995).

[20] D. G. Fried et al. "Bose-Einstein Condensation of Atomic Hydrogen". *Physical Review Letters* **81**, 18 (Nov. 2, 1998).

[21] M.-O. Mewes et al. "Output Coupler for Bose-Einstein Condensed Atoms". *Physical Review Letters* **78**, 4 (Jan. 27, 1997).

[22] I. Bloch, T. W. Hänsch, and T. Esslinger. "Atom Laser with a cw Output Coupler". *Physical Review Letters* **82**, 15 (Apr. 12, 1999).

[23] E. W. Hagley et al. "A Well-Collimated Quasi-Continuous Atom Laser". *Science* **283**, 5408 (Mar. 12, 1999).

[24] N. P. Robins et al. "A pumped atom laser". *Nature Physics* **4**, 9 (Sept. 2008).

[25] N. P. Robins et al. "Atom lasers: Production, properties and prospects for precision inertial measurement". *Physics Reports* **529**, 3 (Aug. 20, 2013).

[26] A. D. Cronin, J. Schmiedmayer, and D. E. Pritchard. "Optics and interferometry with atoms and molecules". *Reviews of Modern Physics* **81**, 3 (July 28, 2009).

[27] J.-F. Schaff, T. Langen, and J. Schmiedmayer. "Interferometry with Atoms". *arXiv:1504.04285 [cond-mat, physics:quant-ph]* (Apr. 16, 2015).

[28] L. Marton. "Electron Interferometer". *Physical Review* **85**, 6 (Mar. 15, 1952).

[29] O. Carnal and J. Mlynek. "Young's double-slit experiment with atoms: A simple atom interferometer". *Physical Review Letters* **66**, 21 (May 27, 1991).

[30] D. W. Keith et al. "An interferometer for atoms". *Physical Review Letters* **66**, 21 (May 27, 1991).

[31] Dunningham Jacob, Burnett Keith, and Phillips William D. "Bose–Einstein condensates and precision measurements". *Philosophical Transactions of the Royal Society A: Mathematical, Physical and Engineering Sciences* **363**, 1834 (July 28, 2005).

[32] R. Trubko et al. "Atom Interferometer Gyroscope with Spin-Dependent Phase Shifts Induced by Light near a Tune-Out Wavelength". *Physical Review Letters* **114**, 14 (Apr. 10, 2015).

[33] T. L. Gustavson, A. Landragin, and M. A. Kasevich. "Rotation sensing with a dual atom-interferometer Sagnac gyroscope". *Classical and Quantum Gravity* **17**, 12 (June 2000).

[34] A. Lenef et al. "Rotation Sensing with an Atom Interferometer". *Physical Review Letters* **78**, 5 (Feb. 3, 1997).

[35] L. Zhou et al. "Measurement of Local Gravity via a Cold Atom Interferometer". *Chinese Physics Letters* **28**, 1 (Jan. 2011).

[36] O. Carraz et al. "Measuring the Earth's gravity field with cold atom interferometers". *arXiv:1506.03989 [physics, physics:quant-ph]* (June 12, 2015).

[37] G. W. Biedermann et al. "Testing gravity with cold-atom interferometers". *Physical Review A* **91**, 3 (Mar. 24, 2015).

[38] D. Becker et al. "Space-borne Bose-Einstein condensation for precision interferometry". *arXiv:1806.06679 [physics.atom-ph]* (June 18, 2018).

[39] M. Kritsotakis et al. "Optimal Matterwave Gravimetry". *Physical Review A* **98**, 2 (Aug. 27, 2018).

[40] *UK Quantum Technology Hub for Sensors and Metrology* -. UK Quantum Technology Hub for Sensors and Metrology. URL: `https://www.quantumsensors.org/`.

[41] L. M. Rico-Gutierrez, T. P. Spiller, and J. A. Dunningham. "Quantum-enhanced gyroscopy with rotating anisotropic Bose–Einstein condensates". *New Journal of Physics* **17**, 4 (Apr. 14, 2015).

[42] P. W. Graham et al. "Dark matter direct detection with accelerometers". *Physical Review D* **93**, 7 (Apr. 20, 2016).

[43] P. Hamilton et al. "Atom-interferometry constraints on dark energy". *Science* **349**, 6250 (Aug. 21, 2015).

[44] B. Elder et al. "Chameleon dark energy and atom interferometry". *Physical Review D* **94**, 4 (Aug. 25, 2016).

[45] C. Burrage, E. J. Copeland, and E. A. Hinds. "Probing dark energy with atom interferometry". *Journal of Cosmology and Astroparticle Physics* **2015**, 3 (Mar. 24, 2015).

[46] C. Burrage and E. J. Copeland. "Using atom interferometry to detect dark energy". *Contemporary Physics* **57**, 2 (July 16, 2016).

[47] R. Geiger. "Future Gravitational Wave Detectors Based on Atom Interferometry". *arXiv:1611.09911 [gr-qc, physics:physics]* (Nov. 29, 2016).

[48] J. B. Fixler et al. "Atom Interferometer Measurement of the Newtonian Constant of Gravity". *Science* **315**, 5808 (Jan. 5, 2007).

[49] P. Cheiney et al. "Realization of tunnel barriers for matter waves using spatial gaps". *EPL (Europhysics Letters)* **103**, 5 (Sept. 25, 2013).

[50] R. Delhuille et al. "Some theoretical and experimental aspects of three-grating Mach–Zehnder atom interferometers". *Comptes Rendus de l'Académie des Sciences - Series IV - Physics* **2**, 4 (June 2001).

[51] C. M. Fabre et al. "Realization of a Distributed Bragg Reflector for Propagating Guided Matter Waves". *Physical Review Letters* **107**, 23 (Nov. 29, 2011).

[52] P. J. Martin et al. "Bragg scattering of atoms from a standing light wave". *Physical Review Letters* **60**, 6 (Feb. 8, 1988).

[53] C. Ryu and M. G. Boshier. "Integrated coherent matter wave circuits". *New Journal of Physics* **17**, 9 (Sept. 21, 2015).

[54] G. L. Gattobigio et al. "Optically Guided Beam Splitter for Propagating Matter Waves". *Physical Review Letters* **109**, 3 (July 19, 2012).

[55] D. W. L. Sprung. "Scattering by a finite periodic potential". *American Journal of Physics* **61**, 12 (1993).

[56] J. F. Annett. *Superconductivity, Superfluids and Condensates*. Oxford University Press, Aug. 11, 2005.

[57] W. Ketterle. "Nobel lecture: When atoms behave as waves: Bose-Einstein condensation and the atom laser". *Reviews of Modern Physics* **74**, 4 (Nov. 20, 2002).

[58] T. W. Hänsch and A. L. Schawlow. "Cooling of gases by laser radiation". *Optics Communications* **13**, 1 (Jan. 1975).

[59] H. J. Metcalf and P. van der Straten. *Laser cooling and trapping*. Graduate texts in contemporary physics. Springer-Verlag New York, 1999.

[60] G. Giuliani. "Conservation laws and laser cooling of atoms". *European Journal of Physics* **36**, 6 (Aug. 28, 2015).

[61] D. J. Wineland and W. M. Itano. "Laser cooling of atoms". *Physical Review A* **20**, 4 (Oct. 1, 1979).

[62] J. T. Mendonça and H. Terças. *Physics of Ultra-Cold Matter: Springer Series on Atomic, Optical, and Plasma Physics 70*. 2013th ed. Springer Series on Atomic, Optical, and Plasma Physics 70. Springer Verlag, 2013.

[63] F. Dalfovo et al. "Theory of Bose-Einstein condensation in trapped gases". *Reviews of Modern Physics* **71**, 3 (Apr. 1, 1999).

[64] V. Bolpasi et al. "An ultra-bright atom laser". *New Journal of Physics* **16**, 3 (Mar. 28, 2014).

[65] F. Gerbier, P. Bouyer, and A. Aspect. "Quasicontinuous Atom Laser in the Presence of Gravity". *Physical Review Letters* **86**, 21 (May 21, 2001).

[66] J. Jeffers et al. "Bound mode of an atom laser". *Physical Review A* **62**, 4 (Sept. 11, 2000).

[67] N. P. Robins et al. "Limits to the flux of a continuous atom laser". *Physical Review A* **72**, 3 (Sept. 29, 2005).

[68] G. M. Moy, J. J. Hope, and C. M. Savage. "Atom laser based on Raman transitions". *Physical Review A* **55**, 5 (May 1, 1997).

[69] P. Meystre. *Atom optics*. Springer series on atomic, optical, and plasma physics 33. New York ; London: Springer, 2010.

[70] J. Rogel-Salazar. "The Gross-Pitaevskii Equation and Bose-Einstein condensates". *European Journal of Physics* **34**, 2 (Jan. 9, 2013).

[71] C. E. Wieman, D. E. Pritchard, and D. J. Wineland. "Atom cooling, trapping, and quantum manipulation". *Reviews of Modern Physics* **71**, 2 (Mar. 1, 1999).

[72] R. Grimm, M. Weidemüller, and Y. B. Ovchinnikov. "Optical Dipole Traps for Neutral Atoms". *Advances In Atomic, Molecular, and Optical Physics*. Ed. by B. Bederson and H. Walther. Vol. 42. Academic Press, 2000.

[73] H. Ott et al. "Bose-Einstein Condensation in a Surface Microtrap". *Physical Review Letters* **87**, 23 (Nov. 13, 2001).

[74] B. T. Wolschrijn et al. "Guiding of cold atoms by a red-detuned laser beam of moderate power". *New Journal of Physics* **4** (Sept. 27, 2002).

[75] B. M. Garraway and V. G. Minogin. "Theory of an optical dipole trap for cold atoms". *Physical Review A* **62**, 4 (Sept. 15, 2000).

[76] C. Jönsson. "Elektroneninterferenzen an mehreren künstlich hergestellten Feinspalten". *Zeitschrift für Physik* **161**, 4 (Aug. 1961).

[77] C. Jönsson. "Electron Diffraction at Multiple Slits". *American Journal of Physics* **42**, 1 (Jan. 1974).

[78] H. Kurz and H. Rauch. "Beugung thermischer Neutronen an einem Strichgitter". *Zeitschrift für Physik A Hadrons and nuclei* **220**, 5 (Oct. 1, 1969).

[79] D. W. Keith et al. "Diffraction of Atoms by a Transmission Grating". *Physical Review Letters* **61**, 14 (Oct. 3, 1988).

[80] Y. B. Ovchinnikov et al. "Diffraction of a Released Bose-Einstein Condensate by a Pulsed Standing Light Wave". *Physical Review Letters* **83**, 2 (July 12, 1999).

[81] O. Morsch and M. Oberthaler. "Dynamics of Bose-Einstein condensates in optical lattices". *Reviews of Modern Physics* **78**, 1 (Feb. 27, 2006).

[82] E. M. Rasel et al. "Atom Wave Interferometry with Diffraction Gratings of Light". *Physical Review Letters* **75**, 14 (Oct. 2, 1995).

[83] N. W. Ashcroft and N. D. Mermin. *Solid state physics*. Belmont CA, New York: Brooks/Cole, Cengage Learning, Holt, Rinehart and Winston, 1976.

[84] C. C. Gerry and P. Knight. *Introductory quantum optics*. Cambridge: University Press, 2005.

[85] B. Lücke et al. "Twin Matter Waves for Interferometry Beyond the Classical Limit". *Science* **334**, 6057 (Nov. 11, 2011).

[86] Y. Shin et al. "Atom Interferometry with Bose-Einstein Condensates in a Double-Well Potential". *Physical Review Letters* **92**, 5 (Feb. 6, 2004).

[87] N. Mielec et al. "Atom interferometry with top-hat laser beams". *Applied Physics Letters* **113**, 16 (Oct. 18, 2018).

[88] C. A. Bennett. *Principles of physical optics*. Hoboken, N.J. ; Chichester: Wiley, 2008.

[89] V. Giovannetti, S. Lloyd, and L. Maccone. "Quantum-Enhanced Measurements: Beating the Standard Quantum Limit". *Science* **306**, 5700 (Nov. 19, 2004).

[90] M. Zwierz, C. A. Pérez-Delgado, and P. Kok. "General Optimality of the Heisenberg Limit for Quantum Metrology". *Physical Review Letters* **105**, 18 (Oct. 27, 2010).

[91] W. Heisenberg. "Über den anschaulichen Inhalt der quantentheoretischen Kinematik und Mechanik". *Zeitschrift für Physik* **43**, 3 (Mar. 1927).

[92] N. Margolus and L. B. Levitin. "The maximum speed of dynamical evolution". *Physica D: Nonlinear Phenomena* **120**, 1 (Sept. 1, 1998).

[93] M. Napolitano et al. "Interaction-based quantum metrology showing scaling beyond the Heisenberg limit". *Nature* **471**, 7339 (Mar. 24, 2011).

[94] Y. B. Ovchinnikov. "Beam splitters". U.S. pat. 10297358B2. N. M. Ltd. May 21, 2019.

[95] V. Guarrera et al. "Distributed quasi-Bragg beam splitter in crossed atomic waveguides". *Scientific Reports* **7**, 1 (July 6, 2017).

[96] J. Alda. "Laser and Gaussian Beam Propagation and Transformation". *Encyclopedia of Optical Engineering* (Jan. 1, 2003).

[97] F. Damon et al. "Band-gap structures for matter waves". *Physical Review A* **92**, 3 (Sept. 16, 2015).

[98] E. T. Whittaker. *A Course of Modern Analysis*. 4 Reprint edition. Cambridge; Tennessee: Book Jungle, Mar. 14, 2009.

[99] P. L. DeVries and J. E. Hasbun. *A First Course in Computational Physics*. 2nd Revised edition edition. Sudbury, Mass: Jones and Bartlett Publishers, Inc, May 2, 2010.

[100] *Time-Dependent Schrödinger equation via the Split-Step Fourier method — PyCav*. URL: `https://pycav.readthedocs.io/en/latest/api/pde/split_step.html`.

[101] J. Vanderplas. *Quantum Python: Animating the Schrodinger Equation*. URL: `https://jakevdp.github.io/blog/2012/09/05/quantum-python/`.

[102] D. A. Steck. *Quantum and Atom Optics*. revision 0.12.6. Apr. 23, 2019.

[103] C. Cohen-Tannoudji. *Quantum Mechanics*. In collab. with B. Diu and F. Laloe. New York, etc., Wiley, etc.: New York, etc, Wiley, etc, 1977.

[104] A. Rundquist. "Directly integrating the Schroedinger to determine tunneling rates for arbitrary one-dimensional potential barriers" (Jan. 13, 2011).

[105] S. Nandi. "The quantum Gaussian well". *American Journal of Physics* **78**, 12 (Nov. 18, 2010).

[106] Y. Ovchinnikov. *Internal Communication*.

[107] W. Guerin et al. "Guided Quasicontinuous Atom Laser". *Physical Review Letters* **97**, 20 (Nov. 13, 2006).

[108] Y.-J. Wang et al. "Atom Michelson Interferometer on a Chip Using a Bose-Einstein Condensate". *Physical Review Letters* **94**, 9 (Mar. 11, 2005).

[109] W. Li, T. He, and A. Smerzi. "Multimode Kapitza-Dirac Interferometry with Trapped Cold Atoms". *Physical Review Letters* **113**, 2 (July 7, 2014).

[110] E. Andersson et al. "Multimode Interferometer for Guided Matter Waves". *Physical Review Letters* **88**, 10 (Feb. 26, 2002).

[111] T. P. Spiller. *Internal Communication*.

[112] Xueming Liu and Byoungho Lee. "A fast method for nonlinear Schrodinger equation". *IEEE Photonics Technology Letters* **15**, 11 (Nov. 2003).

[113] R. Deiterding et al. "A Reliable Split-Step Fourier Method for the Propagation Equation of Ultra-Fast Pulses in Single-Mode Optical Fibers". *Journal of Lightwave Technology* **31**, 12 (June 15, 2013).

[114] L. Shu-Guang et al. "Adaptive split-step Fourier method for simulating ultrashort laser pulse propagation in photonic crystal fibres". *Chinese Physics* **15**, 2 (Feb. 2006).

[115] J. Shao, X. Liang, and S. Kumar. "Comparison of Split-Step Fourier Schemes for Simulating Fiber Optic Communication Systems". *IEEE Photonics Journal* **6**, 4 (Aug. 2014).

[116] C. Bayindir. "Compressive Split-Step Fourier Method". *TWMS Journal of Applied and Engineering Mathematics* **5**, 2 (2015).

[117] J. R. Costa, C. R. Paiva, and A. M. Barbosa. "Modified split-step Fourier method for the numerical simulation of soliton amplification in erbium-doped fibers with forward-propagating noise". *IEEE Journal of Quantum Electronics* **37**, 1 (Jan. 2001).

[118] O. V. Sinkin et al. "Optimization of the split-step Fourier method in modeling optical-fiber communications systems". *Journal of Lightwave Technology* **21**, 1 (Jan. 2003).

[119] S. M. Zoldi et al. "Parallel Implementations of the Split-Step Fourier Method for Solving Nonlinear Schrödinger Systems". *arXiv:physics/9711012* (Nov. 14, 1997).

[120] T. R. Taha and X. Xu. "Parallel Split-Step Fourier Methods for the Coupled Nonlinear Schrödinger Type Equations". *The Journal of Supercomputing* **32**, 1 (Apr. 2005).

[121] E. Faou, L. Gauckler, and C. Lubich. "PLANE WAVE STABILITY OF THE SPLIT-STEP FOURIER METHOD FOR THE NONLINEAR SCHRÖDINGER EQUATION". *Forum of Mathematics, Sigma* **2** (July 1, 2014).

[122] A. Willinger and G. Eisenstein. "Split Step Fourier Transform: A Comparison Between Single and Multiple Envelope Formalisms". *Journal of Lightwave Technology* **30**, 18 (Sept. 15, 2012).

[123] H.-P. Breuer and F. Petruccione. *The Theory of Open Quantum Systems*. Oxford University Press, 2007.

[124] C. Gardiner, P. Zoller, and P. Zoller. *Quantum Noise: A Handbook of Markovian and Non-Markovian Quantum Stochastic Methods with Applications to Quantum Optics*. Springer Science & Business Media, Aug. 27, 2004.

[125] T. L. S. Collaboration et al. "A gravitational wave observatory operating beyond the quantum shot-noise limit". *Nature Physics* **7**, 12 (Dec. 2011).

[126] L. M. Rico-Gutierrez, T. P. Spiller, and J. A. Dunningham. "Engineering entanglement for metrology with rotating matter waves". *New Journal of Physics* **15**, 6 (June 10, 2013).

[127] C. Gross et al. "Nonlinear atom interferometer surpasses classical precision limit". *Nature* **464**, 7292 (Apr. 22, 2010).

[128] M. Xiao, L.-A. Wu, and H. J. Kimble. "Precision measurement beyond the shot-noise limit". *Physical Review Letters* **59**, 3 (July 20, 1987).

[129] M. Jarzyna and R. Demkowicz-Dobrzański. "True precision limits in quantum metrology". *New Journal of Physics* **17**, 1 (Jan. 9, 2015).

[130] D. W. Hallwood et al. "Measuring atomic NOON-states and using them to make precision measurements". *New Journal of Physics* **11**, 10 (Oct. 26, 2009).

[131] *FFTW Home Page*. URL: `http://www.fftw.org/`.